University of Nevada, Reno

Tectonic Controls, Timing and Geochemistry of Supergene Enrichment of the Tyrone Porphyry Copper Deposit, Grant County, New Mexico

A dissertation submitted in partial fulfillment of the

requirements for the degree of Doctor of Philosophy in

Geology

by

Craig J. Mach

Dr. Tommy B. Thompson/Dissertation Advisor

December, 2008

University of Nevada, Reno
Statewide • Worldwide

THE GRADUATE SCHOOL

We recommend that the dissertation
prepared under our supervision by

CRAIG J. MACH

entitled

Tectonic Controls, Timing And Geochemistry Of Supergene Enrichment Of The Tyrone Porphyry Copper Deposit, Grant County, New Mexico

be accepted in partial fulfillment of the
requirements for the degree of

DOCTOR OF PHILOSOPHY

Tommy B. Thompson, Ph.D., Advisor

Greg B. Arehart, Ph.D., Committee Member

Richard A. Schweickert, Ph.D., Committee Member

Alan R. Wallace, Ph.D., Committee Member

Victor R. Vasquez, Ph.D., Graduate School Representative

Marsha H. Read, Ph. D., Associate Dean, Graduate School

December, 2008

ABSTRACT

The Tyrone porphyry copper deposit is located in the Big Burro Mountains 16 km (10 miles) southwest of Silver City, New Mexico, and is part of the Laramide porphyry copper province in the southwestern US and northern Mexico. The deposit is associated with the Tyrone stock, a composite stock of granodiorite, monzonite porphyry, and quartz monzonite porphyry that intrudes Proterozoic granite. The Tyrone stock has been dated by Phelps Dodge (unpublished) at 55.8 Ma to 52.1 Ma by $^{40}Ar/^{39}Ar$ on magmatic biotite and orthoclase. Hypogene copper grades average 0.09% Cu in chalcopyrite; supergene ore currently averages 0.3% for run-of-mine leach material, but chalcocite ore averaging 2-3% Cu was mined historically.

The supergene copper deposit is laterally zoned. The northern and northeastern parts of the deposit are characterized by a well-developed chalcocite blanket, whereas the southwestern part of the deposit is characterized by an enriched copper oxide zone over a thin, poorly-developed chalcocite blanket. The chalcocite enrichment blanket is tilted 7-9° to the northeast due to Basin and Range extensional faulting. Copper-bearing ferricrete and ferruginous conglomerate units derived from erosional unroofing of the deposit overlie unconformities at two stratigraphic horizons. The older of these units occurs in the southern Little Burro Mountains to the northeast of the deposit and is interbedded with upper Eocene-Oligocene volcanic rocks of the Mogollon-Datil volcanic field. The younger unit lies at the base of Miocene-Pleistocene basin-fill gravels associated with Basin and Range extension, and occurs within northeast-trending paleochannels that extend over 3.2 km (2 mi) from the mine site into the Little Burro Mountains.

The research reported here addresses formation of the Tyrone supergene system and had five main objectives: 1) determine the number and timing of uplift, unroofing and supergene enrichment events; 2) assess the lateral variations in hypogene sulfide content and alteration assemblage across the district and the controls they exercised on formation of the laterally-zoned

supergene system; 3) map the distribution of limonite minerals that reflect the supergene ore types; 4) determine the amount of erosion of the hypogene copper-bearing system and the extent of northeast copper flux in the supergene environment; and 4) assess the groundwater conditions during supergene enrichment.

Tyrone underwent extensive supergene sulfide enrichment during the Tertiary. Detailed $^{40}Ar/^{39}Ar$ dating for this study has resolved three stages of supergene enrichment, which record the progressive unroofing of the deposit. The first stage of supergene enrichment is represented by the copper-bearing ferruginous conglomerate unit in the southern Little Burro Mountains. Its age is bracketed by upper Eocene-Oligocene tuffs dated by $^{40}Ar/^{39}Ar$ at 35.7 and 31.6 Ma. This early supergene enrichment event is not represented by supergene alunite in the deposit because the Eocene enrichment blanket was probably leached and removed by erosion during Miocene uplift. Mass balance calculations indicate the upper 250 m (820 ft) of the hypogene system has been eroded.

$^{40}Ar/^{39}Ar$ age determinations on alunite indicate that main-stage enrichment occurred in the Miocene between 22.2 and 8.7 Ma. The Miocene enrichment event was related to initiation of Basin and Range normal faulting that probably began as early as 26 Ma. The copper-bearing ferricrete unit at the base of the Miocene-Pleistocene basin-fill gravels is 12.1 million years old based on $^{40}Ar/^{39}Ar$ dating of cryptomelane cement. The ferricrete formed in northeast-trending paleochannels as the deposit was tilted during extensional faulting. The Miocene enrichment event is related to displacements on the northwest-striking Treasure Mountain and Knight Peak faults. These are regional Basin and Range normal faults that resulted in uplift of the Big Burro Mountains horst and formation of the San Vicente half graben.

A third, minor supergene enrichment event occurred in the Pliocene-Pleistocene with uplift of the Little Burro Mountains on the Mangas fault, a northwest-striking Basin and Range normal fault that separates the Big Burro and Little Burro mountains. A sample of supergene

alunite from the southern Little Burro Mountains yielded an age of 4.6 Ma. Supergene enrichment diminished in the Pliocene with the onset of arid conditions, and the chalcocite blanket underwent widespread in-situ oxidation as pyrite was consumed in the oxidizing column.

Drill hole logs indicate that the hypogene system in the northeastern part of the district is characterized by a thick, nonreactive phyllic alteration asemblage, pyrite:chalcopyrite averaging ~11:1, and hypogene sulfide content of 2-5 vol. %. The leached cap in the northeastern part of the district is dominated by hematite and overlies a thick, well-developed chalcocite blanket with a poorly-developed, mostly late-stage copper oxide zone. The hypogene system in the southwestern part of the deposit is characterized by a reactive potassic alteration assemblage, pyrite:chalcopyrite averaging ~7:1, and low total hypogene sulfide content of 0.5-2.5 vol. %. The leached cap is dominated by goethite and overlies a well-developed copper oxide zone and a thin, poorly-developed chalcocite blanket.

The unreactive phyllic alteration assemblage, high pyrite:chalcopyrite, and high total hypogene sulfide content in the northeastern part of the district resulted in strongly acidic conditions during supergene enrichment, thorough copper leaching, and strong enrichment. In contrast, the reactive potassic alteration assemblage and lower content of acid-producing hypogene sulfides in the southwestern part of the district resulted in weak leaching and poor enrichment. The copper oxide zone in the southwestern part of the district formed in part during active enrichment. The northeast to southwest lateral zoning of the hypogene system is due in large part to approximately 20° of northeast tilt of the deposit that elevated the potassic zone in the southwestern part of the district while depressing and preserving the phyllic zone in the northeastern part of the district.

Copper mass balance calculations indicate that prior to erosion, the top of the hypogene copper-bearing system was at an average elevation of 2,150 m (7,050 ft). The pre-mine topography was at an average elevation of 1,900 m (6,200 ft); therefore, ~250 m (820 ft) of

leached material have been removed by erosion. Calculations of lateral flux of copper indicate a geochemical sink for supergene copper in the northeastern part of the district in the graben between the northeast-striking Burro Chief-West Main fault zone and east-northeast-striking Virginia-Racket fault zone. This geochemical sink is also apparent in chalcocite grade x thickness maps of the district. Northeast-directed copper flux was due to northeast tilting of the deposit and movement of copper-bearing solutions on northeast-striking faults. Negative copper flux anomalies in the northern part of the district indicate that as much as 370,000 metric tons of copper may have exited the deposit by lateral flux into exotic copper deposits. However, most of the copper that underwent lateral transport was probably captured in the sink between the Burro Chief-West Main and Virginia-Racket fault zones.

The $\delta^{34}S$ values of supergene alunite range from -0.6 to 2.4‰ (VCDT), within the range for hypogene sulfides in porphyry copper deposits of the southwestern US, indicating that alunite formed from supergene oxidation of hypogene sulfides. The $\delta^{18}O_{SO4}$ and δD ratios of alunite (7.4 to 9.7‰ and -85 to -46‰, respectively (VSMOW)) demonstrate that alunite formed in unsaturated conditions, reflecting a water table at depth and seasonal recharge in the semi-arid Miocene climate.

Malachite is common but not abundant in the Tyrone deposit as there are no carbonate host rocks in the district. The $\delta^{18}O_{CO3}$ of malachite ranges from 22.6 to 23.3‰ (VSMOW) and $\delta^{18}C$ values range from -13.5 to -11.4‰ (VPDB). These values are characteristic of speleothem carbonates derived from plant-respired CO_2, and reflect the common occurrence of malachite as a late-stage oxidation product of chalcocite.

Tyrone is one of few deposits in the Laramide porphyry copper province with clear evidence for both Eocene and Miocene supergene enrichment events that have been dated by $^{40}Ar/^{39}Ar$. The Tyrone data indicate that evidence for Eocene supergene enrichment in these deposits is probably often destroyed by Miocene uplift, leaching, and erosion.

ACKNOWLEDGEMENTS

I would like to sincerely thank the Tyrone mine geology staff for their assistance with the field investigation, and for preparing and providing geologic data that in many cases required considerable time and effort over and above their normal duties. Conversations with Phelps Dodge geologists including Ralph Stegen, Bill Seibert, John Brummer, Cal Callahan, and Jim Bussman added much to the ideas presented here. Bill Seibert provided technical data and photographs and descriptions of the ferricrete in inaccessible/mined areas of the pit. Cal Callahan produced the grade x thickness maps and the structure contour map of the base of the basin-fill gravels. John Brummer completed the interpretive geologic map of the Tyrone mine. Bonnie Ertel-Arfsten assisted with collection of alunite samples.

Dr. Simon Poulson of the Nevada Stable Isotope Laboratory at the University of Nevada, Reno, directed the stable isotope work and completed most of the analyses. Dr. Terry Spell and the staff at the Nevada Isotope Geochronology Laboratory at the University of Nevada, Las Vegas, completed the $^{40}Ar/^{39}Ar$ analyses. Dr. John McCormack at the University of Nevada, Reno assisted with the Scanning Electron Microscope.

Financial support from the Ralph J. Roberts Center for Research in Economic Geology (CREG) at the University of Nevada, Reno is gratefully acknowledged; without it my graduate studies would have been impossible. Grants from the Women's Auxiliary to the AIME, Society of Economic Geologists, Nevada Petroleum Geologists Society, Society of Mining Engineers, and an Education Grant from the Sertoma Club are also sincerely appreciated. Ralph Stegen of Phelps Dodge initiated and oversaw the project along with my advisor and Director of CREG, Dr. Tommy Thompson. I sincerely thank them both for their ideas and their help. Finally, thanks to my family for hanging in there through the long haul.

TABLE OF CONTENTS

LIST OF TABLES

LIST OF FIGURES

LIST OF APPENDICES

LIST OF PLATES

CHAPTER 1: INTRODUCTION

OBJECTIVES OF STUDY

The Tyrone porphyry copper deposit is located in Grant County, New Mexico, 16 km (10 mi) southwest of Silver City (Fig. 1). Tyrone is part of the Laramide porphyry copper province in the southwestern U.S. and northern Mexico, which includes approximately 50 deposits (Fig. 2). The timing of supergene enrichment of the Laramide porphyry copper deposits, as well as of several older Mesozoic porphyry copper deposits in the region, has been a matter of debate since the early 1900s. Within individual deposits the timing of initiation of supergene enrichment and the number of events is controversial.

In many of the deposits, enrichment is believed to have begun in the Eocene during erosion of the orogenic highland that formed during the Laramide orogeny (Livingston et al., 1968; Cook, 1994). In other deposits, there is little evidence for an early Tertiary supergene enrichment event, and supergene enrichment is believed to have begun in the mid Tertiary, either with the onset of low-angle extensional faulting in the Oligocene (some Arizona deposits) or with Basin and Range extensional faulting in the late Oligocene-Miocene (Arizona and New Mexico deposits) (Cook, 1994; Enders, 2000; Sillitoe, 2005).

The timing of mid-Tertiary enrichment events is further complicated because the inception of Basin and Range extensional faulting is diachronous throughout the region. Basin and Range extensional faulting began in the Miocene between 15 and 18 Ma in southeastern Arizona (Dickinson, 1991). In southwestern New Mexico, Basin and Range faulting is thought to have begun earlier in the Basin and Range province proper (as early as late Oligocene, ~26 Ma) than in the Transition Zone (early Miocene, ~20 Ma) between the Basin and Range province and the Colorado Plateau (Mack, 2004). Tyrone lies in the Basin and Range province near the boundary with the southern Transition Zone (Fig. 3). Dating mid-Tertiary supergene enrichment

events in the porphyry copper deposits may thus yield important evidence regarding the timing of inception of Basin and Range extension and uplift in a given area.

Supergene enrichment events may be accurately dated by $^{40}Ar/^{39}Ar$ techniques on supergene K-bearing minerals including alunite, jarosite and K-Mn oxides (Vasconcelos et al., 1994b, 1999). However, prior to the present study, systematic $^{40}Ar/^{39}Ar$ dating of supergene minerals has been conducted in only one deposit in the Laramide porphyry copper province, the Morenci deposit in southeastern Arizona (Enders, 2000). $^{40}Ar/^{39}Ar$ dating by Enders (2000) has shown that supergene enrichment at Morenci took place in the Miocene and Pliocene. In the other Laramide deposits, the timing of supergene enrichment events has been interpreted from geologic relationships and few, relatively imprecise, K-Ar dates of supergene alunite (Sillitoe, 2005; Cook, 1994).

Tyrone is an excellent location for the study of tectonic controls of supergene enrichment in a Laramide porphyry copper deposit. The Little Burro Mountains immediately to the northeast of the deposit (Fig. 4) contain a well-preserved section of Tertiary and Quaternary volcanic and sedimentary rocks that bear a record of Cenozoic tectonic events that resulted in uplift, tilting, and erosional unroofing of the deposit. The volcanic rocks are associated with the late Eocene-Oligocene Mogollon-Datil volcanic field and consist dominantly of rhyolite ash-flow tuffs that are easily dated by $^{40}Ar/^{39}Ar$ techniques. Copper-bearing ferricrete deposits related to erosion and supergene enrichment of the deposit fill northeast-trending paleochannels at the base of Miocene-Pleistocene basin-fill gravels. The ferricrete represents a mid-Tertiary unroofing event, but it had not been dated prior to this study. During the initial phases of field work for this project, a previously unknown copper-bearing ferruginous conglomerate unit was identified overlying an unconformity within upper Eocene-Oligocene volcanic rocks in the southern Little Burro Mountains. This unconformity surface represents an older, undated erosional unroofing event.

The main objective of this research is to carry out a detailed evaluation of the history of supergene enrichment of the Tyrone deposit using $^{40}Ar/^{39}Ar$ techniques to date supergene minerals in the deposit and Tertiary unconformity surfaces exposed at the mine and in the Little Burro Mountains. Questions to be addressed here are: 1) how many erosional unroofing events are represented at Tyrone; 2) was there an Eocene or Oligocene erosional unroofing/supergene enrichment event, and what was the timing of mid-Tertiary erosional unroofing/supergene enrichment events; and 3) can mid-Tertiary events be correlated with specific, local faulting events related to Basin and Range extension?

New $^{40}Ar/^{39}Ar$ dates on both ferricrete units/unconformities from this research provide firm ages for two major erosional unroofing/supergene enrichment events. An outgrowth of this research is that accurate $^{40}Ar/^{39}Ar$ dates on the previously undated ash-flow tuffs in the southern Little Burro Mountains allows these rocks to be correlated with ash-flow tuffs of the Mogollon-Datil volcanic field. This is one of the southwesternmost dated sections of Mogollon-Datil volcanic rocks in New Mexico.

Recent work by Mack (2004) on the timing of formation of structurally-controlled Cenozoic basins in southwestern New Mexico makes it possible to correlate mid-Tertiary enrichment events at Tyrone with displacement on specific basin-bounding faults. This has not been accomplished in any other deposit in the Laramide porphyry copper province.

Several other aspects of the formation of the supergene system at Tyrone deposit are addressed in this study. The supergene system is atypical for a porphyry copper deposit in that it is laterally zoned, with a well-developed chalcocite enrichment blanket in the northeastern part of the district, and a copper oxide zone overlying a poorly-developed chalcocite blanket in the southwestern part of the district. The chalcocite blanket has been tilted to the northeast by Basin and Range extensional faulting.

This study examines the geochemical processes responsible for formation of the laterally-zoned supergene system using new drill hole logs of the leached cap, copper oxide zone, and top of the chalcocite blanket in 86 drill holes across the district. The questions addressed are: 1) how does the zoned supergene system relate to the hypogene sulfide content and alteration assemblages, and 2) how does limonite mineralogy of the leached cap correspond to the underlying supergene ore types? New drill hole logs will also be used to determine if hematite horizons in the leached cap, which represent leached chalcocite blankets, can be correlated to give the number of leaching/enrichment events, and whether there is discernible dip fanning of hematite horizons in the leached cap due to tilting and uplift of the deposit during active enrichment.

Mass balance analysis is used to estimate the amount of erosion of the hypogene copper deposit (i.e., the thickness of copper-bearing material that has been stripped from the top of the deposit), and also the extent and direction of lateral copper flux from the deposit. A question to be answered here is, how was lateral copper flux and formation of exotic copper deposits related to northeast tilting of the deposit? To the author's knowledge, mass balance analysis has been performed on only one other porphyry copper deposit in the Laramide porphyry copper province (Morenci), and has never been used for evaluating copper flux in a deposit that underwent tilting during active supergene enrichment.

The stable isotope composition of alunite is used to characterize groundwater conditions during active enrichment, i.e., was the supergene profile fully saturated or unsaturated with a water table at depth? The groundwater conditions have implications for the Cenozoic paleoclimate during enrichment. Finally, stable isotope analyses of supergene malachite are used to assess the conditions of formation of malachite, most of which appears to have formed during late-stage oxidation of the chalcocite blanket, and the source of carbonate, as there are no carbonate rocks associated with the deposit.

The study will construct a chronology of Cenozoic tectonic and supergene enrichment events at Tyrone and relate supergene enrichment events to specific Basin and Range faulting events. Mechanisms are proposed for development of the zoned supergene system.

LOCATION AND GENERAL GEOLOGY

The Tyrone district lies within the Big Burro Mountains of southwestern New Mexico (Fig. 4). As used in this report, the Tyrone district includes the main part of the porphyry copper deposit that had been mined by open pit as of 2003, an area of approximately 8 km^2 (3 mi^2). The pit area is roughly rectangular in shape, elongated in a southwest-northeast direction, with the Main, Gettysburg, San Salvador, and Copper Mountain pits forming the corners of the rectangle (Fig 5).

The Big Burro and Little Burro Mountains are northwest-trending horst blocks, and consist mainly of Proterozoic granite that has been intruded by the Eocene Tyrone stock. The Big Burro and Little Burro Mountains are separated by the Mangas Valley, a half graben bounded on its northeast side by the northwest-striking, southwest-dipping Mangas fault, a Basin and Range normal fault. The Mangas half graben contains up to 370 m (1,200 ft) of Miocene to Pleistocene basin-fill sediments (Fig. 1). The Big Burro Mountains are bounded on the southwest by the Knight Peak fault, a major northwest-striking, southwest-dipping Basin and Range normal fault (Fig. 1).

The Tyrone mine spans the Continental Divide. Elevations at the mine range from 1,830 to 1,950 m (6,000 to 6,400 ft). The highest elevations in the Big Burro Mountains are on Burro Peak, which reaches an elevation of 2,449 m (8,035 ft) approximately 6 km (4 mi) southwest of the mine area. The Little Burro Mountains attain a maximum elevation of 2,010 m (6,625 feet).

The Tyrone stock is a 52.1-55.8 Ma, multistage intrusion consisting of granodiorite, monzonite porphyry, and quartz monzonite porphyry that crops out over an area of approximately

52 km^2 (20 mi^2) (Fig. 1). The stock was emplaced along a northeast-trending Laramide structural zone known as the Santa Rita lineament. Copper deposits are localized in the northeastern part of the Tyrone stock and are hosted by both the stock and the Proterozoic granite (Fig. 4) (Kolessar, 1982; DuHamel et al., 1995). Basin and Range normal faulting tilted the deposit 10 to 20° (this study) to the northeast, preserving the porphyritic cupola zone of the stock. The Tyrone deposit underwent extensive supergene enrichment during the Cenozoic, and the supergene chalcocite blanket was also tilted 7-9° to the northeast (this study) due to Pliocene-Pleistocene displacement on the Mangas fault.

The Tyrone supergene system is laterally zoned reflecting variations in the hypogene system due in part to tilting of the deposit. Copper-bearing ferricrete deposits occur in northeast-trending paleochannels exposed in the Main, Savanna, and Gettysburg pits, and paleochannel deposits extend from the mine site into the southern Little Burro Mountains. Several small, subeconomic exotic copper deposits have been discovered in the ferricrete deposits north of the Main pit (DuHamel et al., 1995), and exotic copper mineralization has been encountered below basin-fill gravels in drill holes ~1 km (3300 ft) east of the Little Burro Mountains.

MINING HISTORY AND PRODUCTION

Copper and turquoise were first discovered in the Tyrone district in 1871 (Kolessar, 1982). Some small-scale underground mining of supergene ore took place until 1909 when Phelps Dodge purchased the Burro Mountain Copper Company. Phelps Dodge completed acquisitions in the district by 1916, and operated underground mines in high grade ore (2-3% Cu) at between 1,400 and 2,000 tons per day until April, 1921, when mining was suspended due to low copper prices and declining grades. From 1949 to 1958, drilling by Phelps Dodge on a 200-foot grid blocked out an orebody measuring 2.8 km (1¾ miles) by 2 km (1¼ miles) in dimension.

Open-pit mining at the Tyrone mine commenced in 1967, with copper recovery from a concentrator.

Between 1972 and 1979, the mine produced nearly 100,000 tons of copper annually (Kolessar, 1982). A solvent extraction-electrowinning (SX-EW) plant began operation in 1984 to process lower grade ores, and the concentrator was finally shut down in 1992 as copper production changed to 100% SX-EW. In 1991, drilling outlined 100 million tons of mine-for-leach ore with an average grade of 0.35% Cu, and an additional 300 million tons of leachable material at a grade of 0.32% Cu was delineated by drilling in 1997 (Phelps Dodge Annual Reports). Between 1987 and 2007, the mine produced 1.6 million metric tons of copper. Mine-for-leach reserves in 2006 were 94,600,000 tons at a grade of 0.34% (Phelps Dodge 2006 Annual Report). The primary ore minerals produced are chalcocite, chrysocolla, and black copper oxides.

PREVIOUS WORK

Tyrone Geology

Early geologic investigations of the Tyrone copper deposits were conducted by Zalinski (1907), Paige (1911, 1922), Somers (1915), and Emmons (1917) when the underground mines were active. These studies helped to characterize the supergene system at Tyrone. Gillerman (1952, 1964, 1967, 1970) provided modern descriptions of the structural geology and ore deposits of the Burro Mountains, and Kolessar (1970, 1982) summarized the geology of the hypogene and supergene copper deposits. Geology of the four quadrangles surrounding Tyrone was mapped at a scale of 1:24,000 by Hedlund (1978a, 1978b, 1978c, 1978d, 1985). The results of geologic investigations conducted by Phelps Dodge at Tyrone from 1990 to 1992 were reported by DuHamel et al. (1995). These investigations provide the geologic background for the present study. The work of Paige (1911, 1922), Gillerman (1964, 1967, 1970), and Hedlund (1978a,

1978b, 1978c, 1978d, 1985) provides an excellent record of the geology of the district that was known prior to open pit mining.

Tectonic Controls and Timing of Supergene Enrichment, Southwestern US

The timing of supergene enrichment of porphyry copper deposits in the southwestern U.S. has been considered by several workers. Livingston et al. (1968) summarized the post-mineralization histories of sixteen porphyry copper deposits in Arizona, including fifteen Laramide deposits and the Jurassic (~170 Ma) Bisbee deposit. Of the sixteen deposits, thirteen show clear evidence of burial by post-mineral, mid-Tertiary volcanic and sedimentary rocks. Twelve of the deposits show evidence of erosion prior to mid-Tertiary burial, and eight deposits show evidence of leaching and/or enrichment prior to mid-Tertiary burial. Livingston et al. (1968) did not emphasize younger enrichment events or multiple cycles of enrichment.

Cook (1994) summarized the tectonic and supergene enrichment histories of fifteen porphyry copper deposits in Arizona and New Mexico, including the Tyrone deposit, based on geologic relationships and K-Ar dates on supergene alunite, jarosite, and illite. He believed that there were three stages of weathering and supergene enrichment in the tectonic evolution of the region. The first stage began in the Eocene with the dissection of the Mogollon Highlands, and in most cases ended with mid-Tertiary burial of the copper deposits by volcanic and sedimentary rocks. The second stage was initiated by mid-Tertiary normal faulting in the upper plates of detachment faults, and erosional removal of volcanic rocks. This episode of extension was related to formation of metamorphic core complexes. The third stage was initiated by late Miocene normal faulting related to Basin and Range extension.

Enders (2000) studied the history of supergene enrichment at the Morenci deposit, which is approximately 100 km (60 mi) northwest of Tyrone, using sixteen new $^{40}Ar/^{39}Ar$ dates on supergene alunite, jarosite, and K-Mn oxides. He found that erosion, weathering and enrichment of the Morenci deposit also has taken place in three stages. The first stage at Morenci took place

with the initial unroofing of the deposit in the Eocene and early Oligocene (53-30 Ma), and ended when the deposit was buried by volcanic rocks erupted during the mid-Tertiary volcanic event. The first stage involved erosion, but there is no direct evidence of enrichment. The second stage, the primary stage for supergene enrichment, took place in the Miocene and Pliocene (18-2 Ma) after erosion of the volcanic cover as a result of Basin and Range faulting and uplift. Most enrichment appears to have occurred during the Miocene and Pliocene from ~13 Ma to ~4 Ma. The third stage (2 Ma to present) involved leaching and partial destruction of the enrichment blanket due to a drop in base level in the late Pliocene-Pleistocene.

The timing of supergene enrichment of the Tyrone deposit has been discussed by Paige (1922), Hedlund (1985), Cook (1994) and DuHamel et al. (1995). The studies by Cook (1994) and DuHamel et al. (1995) used K-Ar geochronology on supergene alunite and illite. Most of these authors agreed that multiple supergene enrichment events had occurred, but the timing of these events was unclear. Paige (1922) believed supergene enrichment occurred in three stages: 1) before burial of the deposit by volcanic rocks, 2) after erosional removal of the volcanic rocks, and 3) during block faulting that formed the sedimentary basins. Hedlund (1985) believed that most supergene enrichment occurred in the late Oligocene or early Miocene, as evidenced by the ferricrete at the base of the basin-fill gravels. Cook (1994) and DuHamel et al. (1995) indicated that a late Eocene enrichment event had occurred based on K-Ar dating of two samples of illite (46.73 $\pm$ 1.05 Ma and 43.64 $\pm$1.11 Ma), but these dates are suspect as the samples possibly contained hypogene and supergene illite and kaolinite (R. Stegen, pers. comm. 2002). Three K-Ar dates on alunite (19.2 $\pm$0.4 Ma, 16.2 $\pm$0.4 Ma, 8.46 $\pm$0.4 Ma) by Cook (1994) and DuHamel et al. (1995) are viewed here as evidence of early and late Miocene enrichment events.

Geochemical Processes of Supergene Enrichment

The geochemical processes of supergene enrichment have been extensively studied since the late 1800s (e.g., Penrose, 1894; Kemp, 1905; Stokes, 1906, 1907; Emmons, 1917; Locke,

1926). More modern studies by Garrels (1954), Anderson (1955), Garrels and Thompson (1960), Sato (1960a, 1960b), Blanchard (1968), and Bladh (1982) addressed the thermodynamic controls on these processes. Anderson (1982), Titley and Marozas (1995), Chávez (2000), and Sillitoe (2005) have produced excellent modern summaries of supergene processes.

Microbiological processes which drive sulfide oxidation reactions (e.g., Schippers et al., 1996; Banfield and Nealson, 1997; Erlich, 1998), and possibly also the metal and sulfate reduction reactions (Sillitoe et al., 1996; Trudinger et al., 1985; Fortin and Beveridge, 1997) are also important to supergene enrichment processes. However, microbiological processes will not be considered further here.

Numerical geochemical modeling of supergene processes by Kwong et al. (1982), Ague and Brimhall (1989), and Lichtner and Biino (1992) has contributed insights into factors that lead to the formation of supergene sulfide and supergene oxide copper deposits, including the formation of zoned oxide-sulfide deposits. Mass balance methods developed by Brimhall et al. (1985) to evaluate the processes of supergene enrichment in porphyry copper deposits are a powerful tool for estimating the amount of erosion of the hypogene copper deposit and also lateral copper flux. Mote et al. (2001) applied mass balance analysis and copper flux calculations to exploration for exotic copper deposits.

METHODS

The research described herein consists of an evaluation of the tectonic controls, timing and geochemistry of supergene processes at Tyrone. Field and laboratory investigations were conducted using existing geologic data from the Tyrone mine and other published and unpublished data, as well as new geologic, geochronologic and geochemical data. Field work consisted of geologic mapping a 9 km^2 (3½ mi^2) area in the southern part of the Little Burro Mountains (Plt. 1, scale 1:12,000) to document the two unconformities and copper-bearing

ferricrete/ferruginous conglomerate units noted above, and also the structural geology and stratigraphy of the other Cenozoic volcanic and sedimentary rocks in the area. In particular, mapping was focused on identification of angular unconformities or dip fanning in the Tertiary section that would be evidence for uplift/unroofing of the porphyry copper deposit related to faulting events prior to the onset of Basin and Range extension (currently believed to have begun at about 26 Ma in the Basin and Range province (Mack, 2004)).

The ferricrete and ferruginous conglomerate units in the Tertiary section were systematically sampled and analyzed for multiple elements including copper to determine the extent of exotic copper deposits. Two ash-flow tuff units were dated by $^{40}Ar/^{39}Ar$ to bracket the age of the older ferruginous conglomerate. The $^{40}Ar/^{39}Ar$ dates and petrography of the volcanic rocks also allowed correlation of these rocks with units of the Mogollon-Datil volcanic field. The younger ferricrete unit was dated directly by $^{40}Ar/^{39}Ar$ on cryptomelane (K-Mn oxide) cement.

Two geologic cross sections (Plt. 2, scale 1:12,000) were constructed to gain a better understanding of the tectonic history of the area. One cross section (A-A') extends in a northeast direction from the Main pit to the southern Little Burro Mountains. The other (B-B') extends in a northwest direction in the southern Little Burro Mountains from Tyrone Peak to Indian Peak. The cross sections are based on the new geologic mapping in the southern Little Burro Mountains and drill hole information from exploration drilling by Phelps Dodge and Amax in the Tyrone mine, Mangas Valley, and Little Burro Mountains.

Field work in the open pits was mostly limited to collecting samples of supergene alunite and malachite for $^{40}Ar/^{39}Ar$ dating and stable isotope analyses. Alunite vein samples were collected mainly from accessible benches in newer parts of the active Main pit, and from drill core. Malachite samples were collected from the inactive Gettysburg pit. Malachite and other green copper oxide minerals are mined out for the most part and occur sparsely in the district; therefore, samples were difficult to obtain. Older parts of the pits are inaccessible due to highwall

instability in the strongly altered rocks. Furthermore, the pits are largely backfilled with dumps so their geological record is lost except for the existing pit geologic maps, which are thorough and complete.

The leached cap, copper oxide zone, and upper part of the chalcocite enrichment blanket were logged in drill holes on a 370 m x 370 m (1,200 foot x 1,200 foot) grid over the district. Eighty-six holes were logged for a total of 9,035 m (29,643 feet). Drill hole logging was completed to: 1) document the lateral distribution of limonite and copper oxide minerals across the district, and the lateral distribution of hypogene alteration assemblages and hypogene sulfide content; 2) determine the number of enrichment cycles represented in the leached cap by correlating hematite horizons that correspond to the positions of previous chalcocite enrichment blankets; 3) identify, if possible, tilt fanning in the hematite horizons that would reveal the amount of progressive tilting during active leaching and supergene enrichment. As discussed below, because of the strong structural control of the supergene system, correlating hematite horizons was not successful. The geologic logs are included on a compact disc in Appendix C. Example logs are shown on Plate 3, and the thicknesses of the logged limonite intervals in each hole are summarized on Plate 4. Two representative drill hole cross sections showing possible limonite correlations are presented on Plate 5.

Laboratory work for the study consisted of $^{40}Ar/^{39}Ar$ dating, stable isotope analyses, multi-element analyses, and petrography. The $^{40}Ar/^{39}Ar$ dating was completed to determine the timing of erosional unroofing events and supergene enrichment events at Tyrone. Fourteen samples were dated by at the Nevada Isotope Geochronology Laboratory at the University of Nevada, Las Vegas. Dated samples include two ash-flow tuffs and cryptomelane from ferricrete as noted above. A late-stage, unmineralized intrusive rhyodacite plug associated with the Tyrone stock was dated to constrain the age of the end of the intrusive event. Ten samples of supergene

alunite vein material were also dated to determine the age of supergene enrichment events and the timing of uplift. These data are included in Appendix A.

Stable isotope analyses were performed on 19 alunite samples (S, H, sulfate O) and eight malachite samples (C, carbonate O) at the Nevada Stable Isotope Laboratory at the University of Nevada, Reno. The stable isotope analyses of alunite were used to assess the groundwater conditions during supergene enrichment, i.e., whether fully saturated or a groundwater table occurred at depth with intermittent recharge/flushing through the vadose zone. Stable isotope analyses of malachite were used to assess the conditions of formation of malachite and the source of carbonate. Multi-element analyses were completed by ALS Chemex on twenty samples of ferricrete and ferruginous sandstone and conglomerate to determine the copper content of these units and the distribution of exotic copper. In addition, 57 rock and ore samples were examined petrographically.

Copper flux calculations were made using composited copper grades for 180 drill holes shown on ore mineral type cross sections produced by the Tyrone mine geology staff. Calculations are included on an Excel spreadsheet as Appendix D on the compact disc. The mass balance calculations were used to produce a series of three maps (Plts. 8 through 10 duplicated as Figs. 48 through 50) depicting the thickness of the leached zone (pre-erosion), the elevation of the copper-bearing hypogene system prior to uplift, tilting and erosion, and the lateral flux of copper.

As noted above, these studies were used to construct a chronology of Cenozoic tectonism and related supergene enrichment events that have affected the Tyrone deposit. To set the stage for this evaluation, the tectonic history, Cenozoic paleoclimate, and Cenozoic paleogeography of southwestern New Mexico are outlined below.

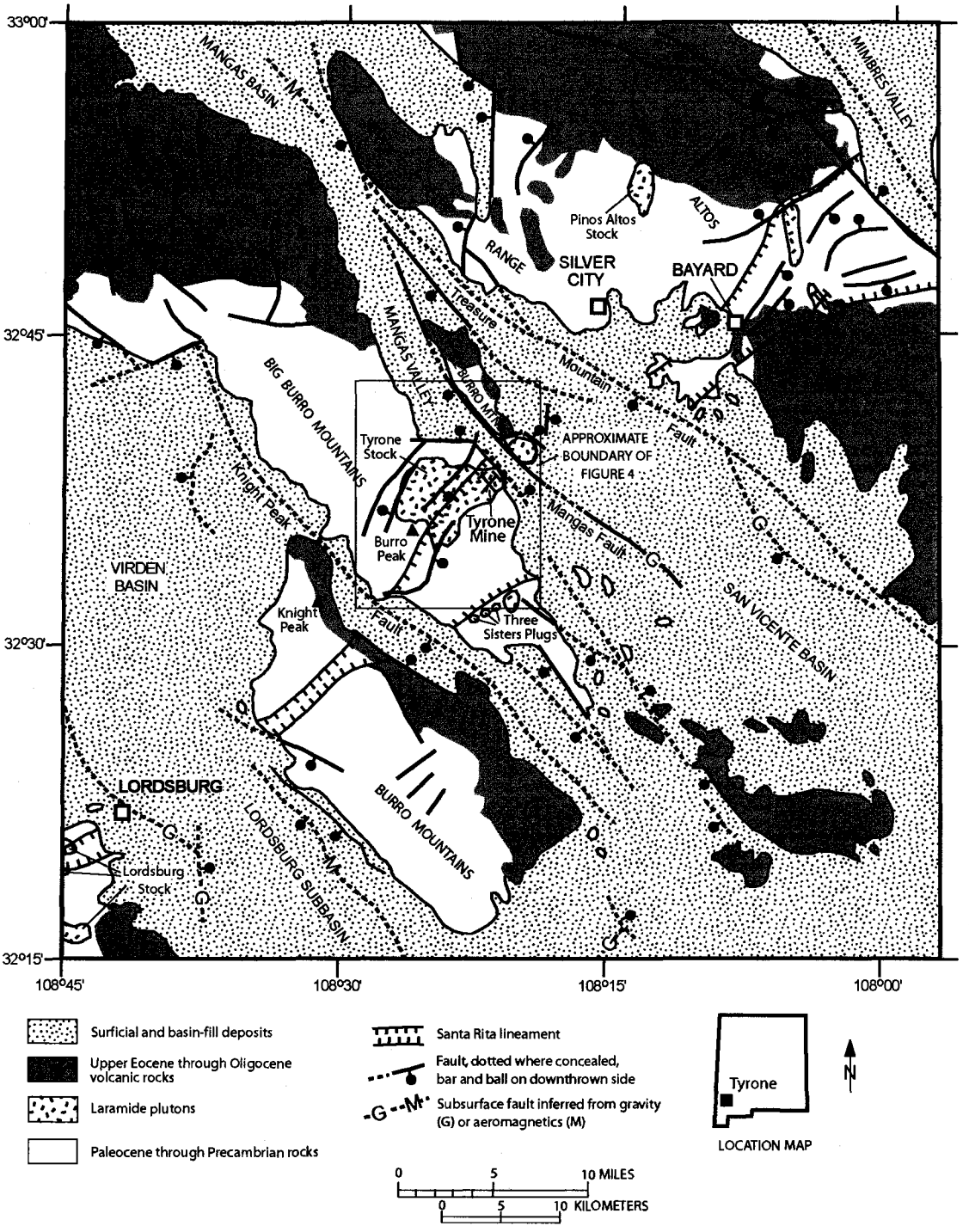

Figure 1. Regional geology of the Tyrone area showing major faults, locations of Laramide intrusions (Lordsburg, Tyrone, and Santa Rita stocks) on the northeast-trending Santa Rita lineament, and the distribution of upper Eocene through Oligocene volcanic rocks. Compiled from Hedlund (1985), Drewes et al. (1985), Gillerman (1970), and Mack (2004).

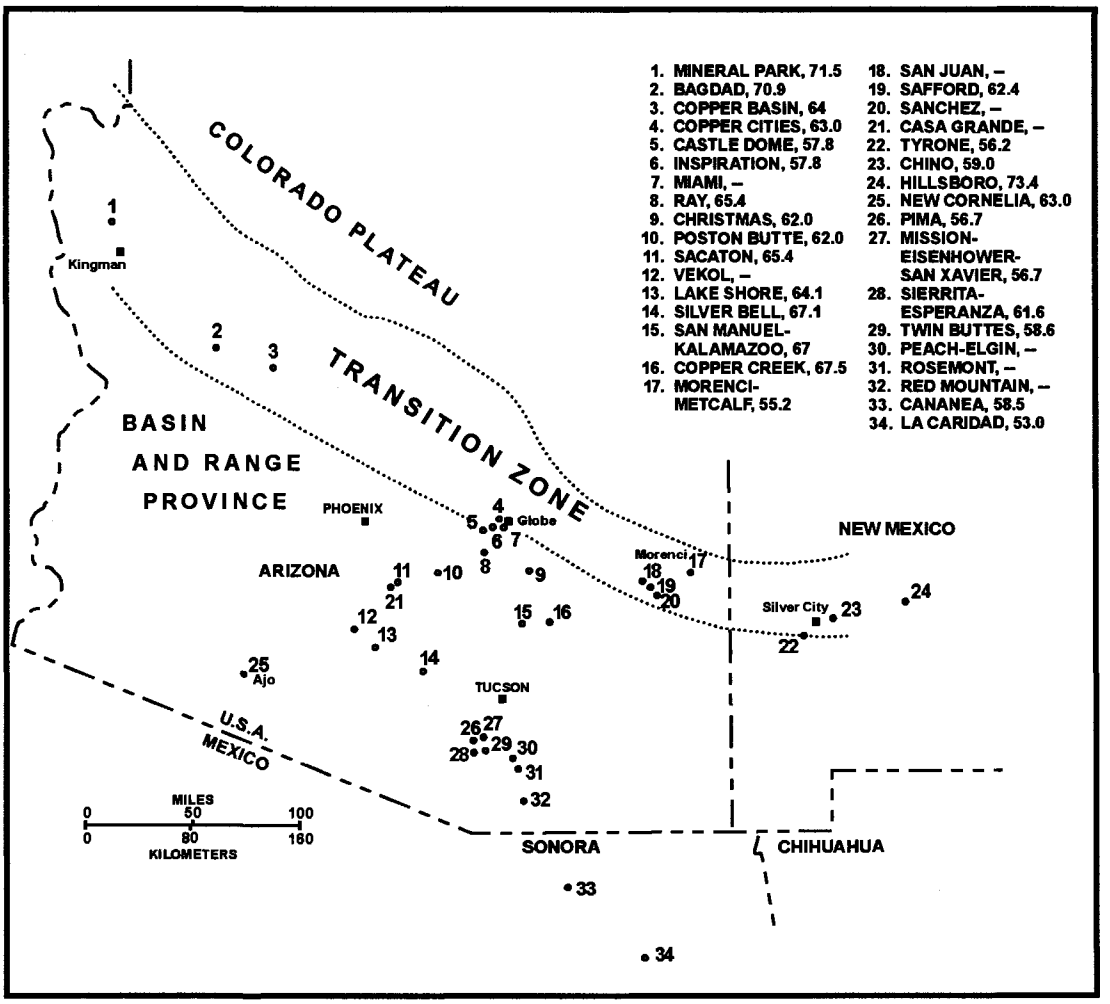

Figure 2. Laramide-aged porphyry copper deposits of Arizona, southwestern New Mexico, and northern Sonora, Mexico. Ages in Ma. Modified from Titley (1982) and Mack (2004).

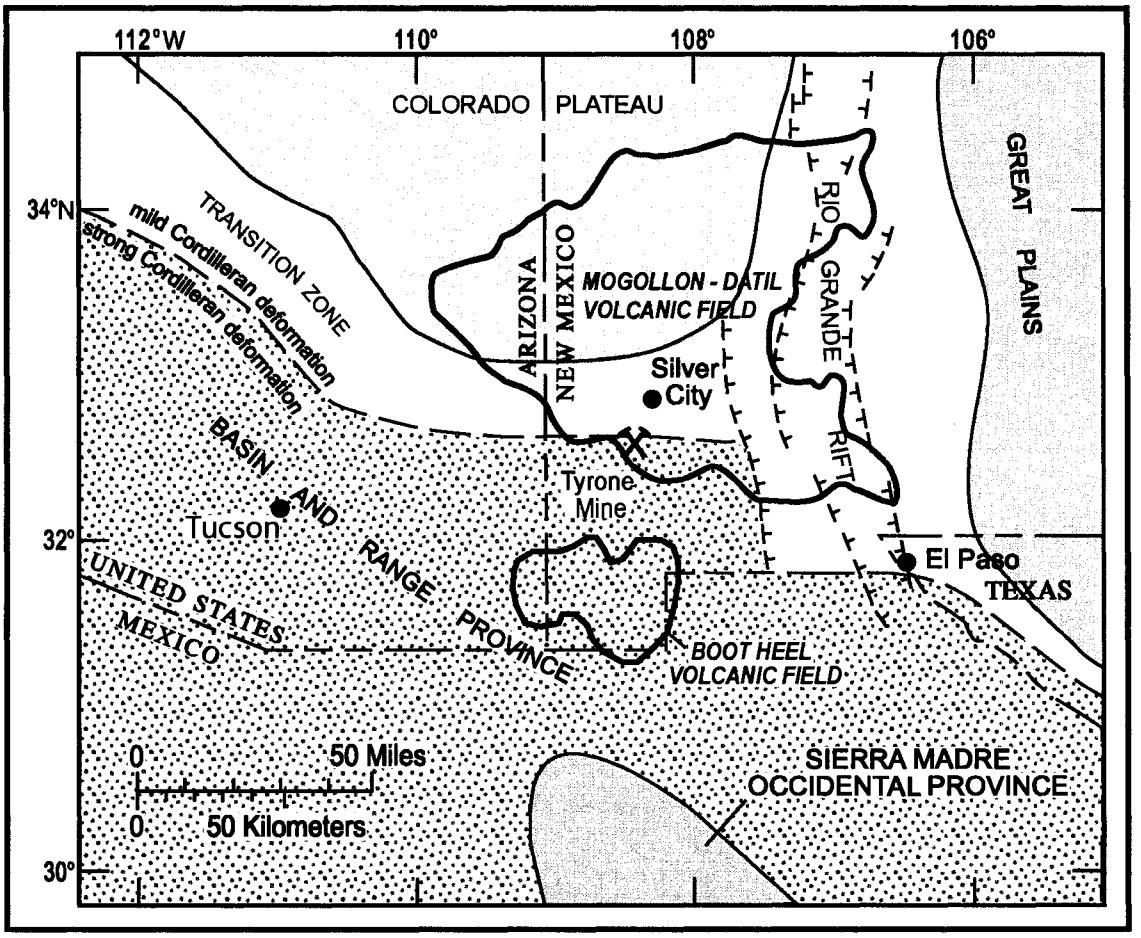

Figure 3. Cenozoic tectonic and physiographic map of southern Arizona and southwestern New Mexico showing the Basin and Range province, Colorado Plateau, Transition Zone, Rio Grande Rift, Mogollon-Datil volcanic field, and Boot Heel volcanic field. Modified from Drewes et al. (1985), Mack (2004), and McIntosh et al. (1992).

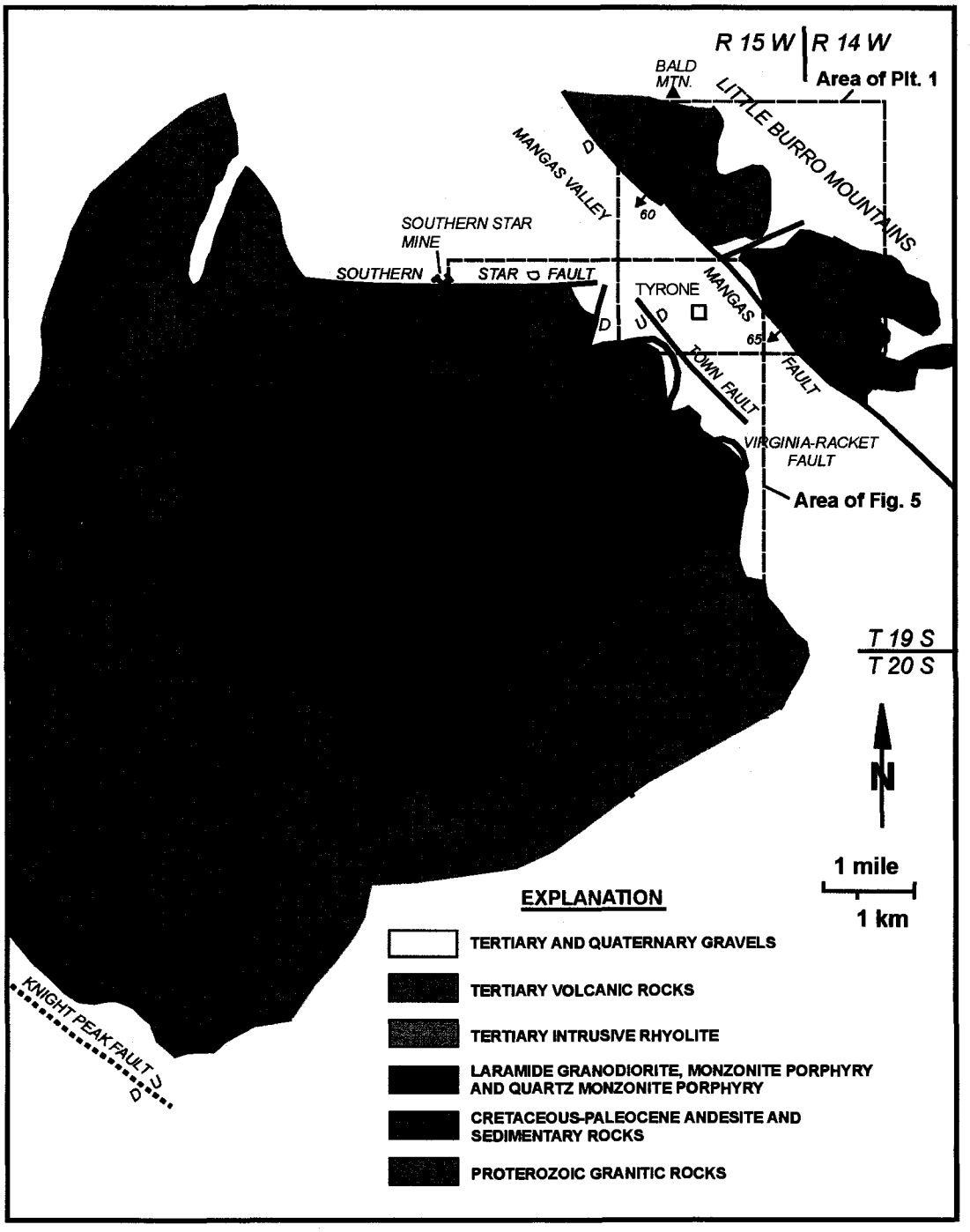

Figure 4. Generalized geologic setting of the Tyrone porphyry copper deposit. Modified from Gillerman (1970) and DuHamel et al. (1995).

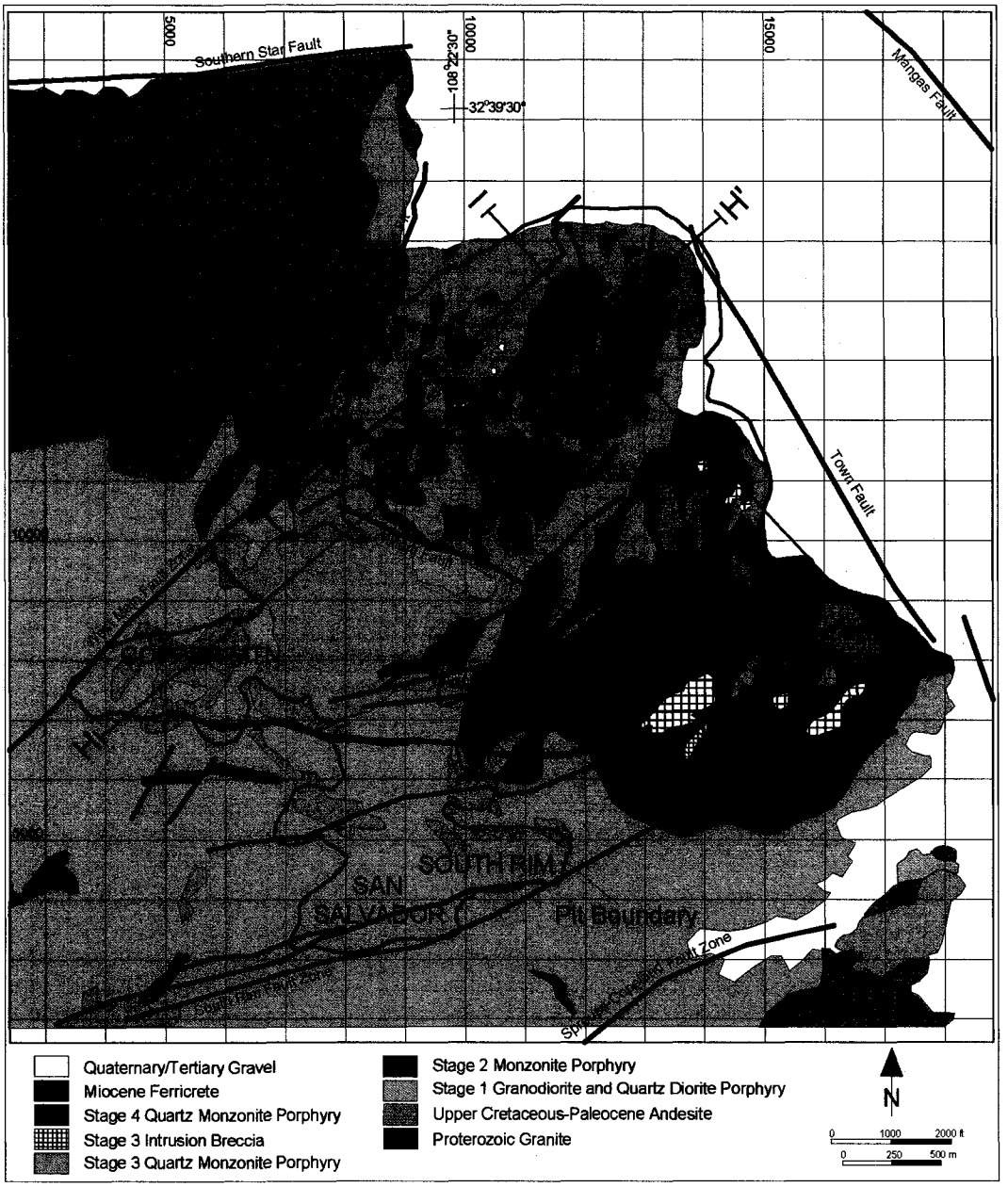

Figure 5. Generalized geologic map of the Tyrone mine, modified from Phelps Dodge Tyrone Geological Services, 2003. Locations are shown for cross sections H-H' and I-I', which are presented in Figure 23.

CHAPTER 2: TECTONIC SETTING, CENOZOIC PALEOGEOGRAPHY AND PALEOCLIMATE

TECTONIC SETTING – SUMMARY OF TECTONIC EVENTS

Proterozoic Through Paleozoic Tectonic Events

The New Mexico portion of the North American craton (Laurentia) formed during the middle to late Proterozoic (1.8 to 1.0 Ga) as microcontinents and arcs were accreted to the southern margin of the craton (Karlstrom et al., 2004; Keller, 2004). At about 1.4 Ga, a belt of magmatism extended across the New Mexico area involving emplacement of granitic plutons. Proterozoic continental growth ended with the Grenville orogeny at 1.2 to 1.0 Ga. Continental rifting between 800 and 550 Ma formed a passive continental margin to the southeast of New Mexico along the southern margin of Laurentia (Karlstrom et al., 2004; Keller, 2004; Dickinson, 1989).

Marine sedimentation occurred along the passive margin during Paleozoic time, and was terminated by the Ouachita-Marathon orogeny from earliest Mississippian through earliest Permian time. Late Pennsylvanian-Early Permian uplift of the Ancestral Rocky Mountains formed fault-bounded uplifts and intervening marine basins in New Mexico. These uplifts and basins were possibly related to subduction or to a transform boundary along the southwestern margin of Laurasia (Kues et al., 2004; Ross and Ross, 1986; Clemons and Mack, 1988).

Mesozoic Tectonic Events

By the Late Triassic, subduction and arc magmatism had been established on the western margins of North and South America (Dickinson, 1989). During the Late Jurassic-Early Cretaceous, backarc rifting in southeastern Arizona and southwestern New Mexico formed the northwest-trending Bisbee basin, a structural arm of the Gulf of Mexico (Fig. 6) (Dickinson, 1989; Lawton, 2004; Keller, 2004). The Precambrian basement-cored Burro uplift, which

included the future Tyrone mine area, formed the northeast shoulder of the Bisbee basin (Fig. 6). Paleozoic sedimentary rocks were eroded from the Burro uplift and Precambrian rocks were exposed by the Early Cretaceous (Lawton, 2004; Seager, 2004). Marine sedimentary rocks onlapped the Burro uplift in southwestern New Mexico during a Late Cretaceous marine transgression (Mack et al., 1988). The Beartooth Quartzite and Colorado Formation in the Little Burro Mountains were deposited at this time.

Laramide Orogeny

Cenozoic tectonism in the southwestern U.S. began with the Laramide orogeny in Late Cretaceous to early Eocene time (80-43 Ma) (Nations et al., 1985; Dickinson, 1989; Seager, 2004, McMillan, 2004). At the onset of the Laramide orogeny, arc magmatism that had been persistent along the western margin of the North America through the Jurassic and most of the Cretaceous gave way to eastward-migrating, calc-alkaline arc magmatism (Fig. 7). This migration of magmatism was possibly due to progressive shallowing of the subducting Farallon slab (Dickinson, 1989, 1991, 2002; Seager, 2004; McMillan, 2004). Along with eastward-migrating magmatism, the effects of the Laramide orogeny were east- to northeast-directed contractional deformation, crustal thickening and uplift.

Magmatism in southwestern New Mexico began by Late Cretaceous time and formed andesite stratovolcanoes, subvolcanic stocks, hypabyssal dike swarms, and granitoid plutons along with rhyolite ignimbrite sheets and associated calderas (Smith et al., 1985; Dickinson, 1989; Seager, 2004). Most of the porphyry copper deposits in Arizona, New Mexico and Sonora, Mexico, including the deposits at Tyrone, Chino (Santa Rita) and Hillsboro, New Mexico, also formed at this time (Fig. 2) (Titley, 1982a; Dickinson, 1989) (Fig 1). Emplacement of porphyry copper deposits in New Mexico was facilitated by the northeast-trending Santa Rita lineament, a Precambrian zone of crustal weakness (Fig. 1) (Hedlund, 1985; Chapin et al., 2004; Heidrick and Titley, 1982). The porphyry copper deposits are associated with calc-alkaline quartz monzonite

to granodiorite stocks emplaced into shallow levels of the crust (1-5 km), possibly in subvolcanic settings beneath andesite to dacite stratovolcanoes (Titley, 1982a; Titley, 1995; Seedorff et al., 2005).

Late Laramide (Paleocene-Eocene) deformation in southwestern New Mexico produced northwest-trending basement-cored uplifts and north-vergent reverse and thrust faults, some with oblique slip (Seager and Mack, 1986; Mack and Clemons, 1988; Seager, 2004) (Fig. 7). By the middle Eocene, southern Arizona and southwestern New Mexico were part of the Mogollon Highlands, an uplift associated with Laramide deformation (Nations et al., 1985; Cather and Johnson, 1986).

The Laramide orogeny was followed by a pronounced lull in arc magmatism in the middle Eocene (50-40 Ma). Widespread erosion occurred in the region at that time resulting in a low-relief erosional surface (Scarborough, 1989; Dickinson, 1991). As discussed above, many porphyry copper deposits in the southwestern U.S. show evidence of supergene enrichment from this erosional event (Livingston et al., 1968; Dickinson, 1989).

Mogollon-Datil Volcanic Field

Cenozoic volcanism peaked volumetrically in southwestern New Mexico in late Eocene to earliest Miocene time (40-21 Ma) with the construction of the Mogollon-Datil volcanic field (MDVF) and Boot Heel volcanic field (BHVF) (Fig. 3) (Chapin et al., 2004; McIntosh et al., 1992). The region was blanketed by a thick accumulation of silicic ignimbrites and intermediate to silicic flows.

Magmatic activity in the MDVF and BHVF occurred during the transition from continental arc magmatism and contractional deformation of the Laramide orogeny to regional extensional deformation in the mid and late Cenozoic. Magmatism in the MDVF and BHVF was accompanied or succeeded by extensional deformation in the southern Rio Grande rift beginning in the latest Eocene at about 35 Ma (Mack, 2004), and by the development of metamorphic core

complexes in southeastern Arizona that began at 28 Ma (Dickinson, 2002). Because rocks of the BHVF do not extend as far north as Tyrone, they are not considered further here.

The MDVF covers ~40,000 km^2 in southwestern New Mexico and southeastern Arizona (Fig. 8). It overlaps the southern boundary of the Colorado Plateau in southwestern New Mexico and extends southward across the Transition Zone separating the Colorado Plateau and Basin and Range province into the Tyrone area (Chapin et al., 2004; McIntosh et al., 1992) (Fig. 3). The porphyry copper deposit at Santa Rita (Fig. 1) is partly concealed beneath rocks of the MDVF (Cook, 1994; Chapin et al., 2004). Volcanic rocks associated with the MDVF crop out extensively in the Little Burro Mountains, but have been removed from the Big Burro Mountains by Miocene erosion.

In the MDVF, intermediate volcanism and eruption of dacite and andesite composite volcanoes in the late Eocene (~46 to 36 Ma) changed in the latest Eocene-early Miocene (36 to 21 Ma) to episodic, bimodal volcanism involving voluminous, high- and low-silica rhyolitic ignimbrites and basaltic andesite flows (McIntosh et al., 1992; Chapin et al., 2004; McMillan, 2004). Thirteen source calderas have been identified for the ignimbrites, although more probably exist; several of the calderas are located 25-50 km northwest, north and east of Tyrone (Fig. 8) (McIntosh et al., 1990, 1992).

Large-scale ignimbrite volcanism occurred in four pulses from 36.2 to 24.3 Ma representing synchronous activity in separate northern and southern caldera complexes (Fig. 8) (McIntosh et al., 1992; Chapin et al., 2004). Volcanism in the southern complex occurred from 36.2 to 28.0 Ma, and in the northern complex from 32.0 to 24.3 Ma (Fig. 8) (McIntosh et al., 1992; Chapin et al., 2004). The first pulse of ignimbrite volcanism in the southern caldera complex occurred between 36.2 Ma and 33.5 Ma (Fig. 8), and involved low-silica rhyolites in thin but widely-dispersed ignimbrites (McIntosh et al., 1992). Eruption of these thin, 'low-aspect ratio' ignimbrites reflects a subdued pre-eruptive topography (i.e. limited fault-controlled

topography) in the late Eocene and high energy or high mobility of the low-silica ash flows (McIntosh et al., 1992). The second pulse of ignimbrite activity spanned only about 0.6 m.y. between 32.0 and 31.4 Ma (Fig. 8) (McIntosh et al., 1992). As shown in this study, the ash-flow tuffs within the Tyrone district were associated with these two pulses of ignimbrite activity.

Mid to Late Cenozoic Extensional Deformation

Extensional tectonism dominated the southwestern United States through the late Cenozoic. This deformation included denudation of metamorphic core complexes (in Arizona) along low-angle detachment faults, block faulting on high-angle normal faults forming horst and graben structures, tilting of strata, basaltic volcanism, and deposition of thick sedimentary fill in fault-bounded terrestrial basins (Dickinson, 1991, 2002). Normal faulting associated with Basin and Range extension produced the modern landscape of basins and ranges in southern Arizona and southwestern New Mexico. Uplift of fault-bounded ranges resulted in tilting and erosion of many of the porphyry copper deposits (Wilkins and Heidrick, 1995).

Southwestern New Mexico is divided into four Cenozoic physiographic and tectonic provinces including the Colorado Plateau, Transition Zone, Basin and Range province, and southern Rio Grande rift (Fig. 3). The Colorado Plateau is an elevated region of stable crust that experienced minimal Cenozoic extension (Nations et al., 1985 Menges and Pearthree, 1989). The Basin and Range province consists of north- to northwest-trending ranges and alluvial valleys that merge imperceptibly into the Rio Grande rift (Mack, 2004). The Transition Zone between the Colorado Plateau and Basin and Range is characterized by rugged relief, dissected alluvial basins, bedrock ranges and plateau remnants (Menges and Pearthree, 1989). The Transition Zone has less structural relief overall than the Basin and Range province or the Rio Grande rift, and it has more deeply incised drainages than the Basin and Range province (Mack, 2004). The Tyrone deposit lies within the northern part of the Basin and Range province (Fig. 3). However, the boundary between the southern Transition Zone and the Basin and Range province is not well

defined (Mack, 2004). The southern Rio Grande rift is distinguished from the Basin and Range province by an asthenospheric upwarp, thinned crust, high heat flow, recently active basaltic volcanoes, deep basins and late Quaternary faulting (Seager and Morgan, 1979). The timing and significance of these provinces is discussed below.

Figure 9 summarizes the timing of middle and late Cenozoic tectonic and magmatic events in southwestern New Mexico. The inception of extensional faulting in southwestern New Mexico occurred from late Eocene to early Miocene time. Faulting began in the southern Rio Grande rift at approximately 35 Ma, followed by the Basin and Range province at approximately 26 Ma, and finally the southern Transition Zone at approximately 20 Ma. Faulting and uplift waned in the Basin and Range province and southern Transition Zone in the late Miocene (Mack, 2004). All three provinces experienced nearly contemporaneous renewed faulting and basin development at about 6-5 Ma, in the latest Miocene and early Pliocene.

Southern Rio Grande Rift

Extensional deformation in the southern Rio Grande rift occurred in two major events (Fig. 9) (Mack, 2004; Mack et al., 1994b). The earlier event which spanned the late Eocene to late Miocene (~35-6 Ma) was characterized by the formation of broad, northwest-trending half grabens and by syntectonic eruptions of basaltic andesite (Seager et al., 1984; Mack, 2004; Dickinson, 2002). The later event began in latest Miocene or early Pliocene (~6 Ma) as a major pulse of extension that continues today. This event is characterized by formation of narrow, deep, north-trending basins and uplifts on high-angle normal faults and by renewed volcanism dominated by alkali-olivine basalt (Seager et al., 1984; Mack, 2004).

Basin and Range Province

Extensional deformation in the Basin and Range province of southern Arizona and southwestern New Mexico varied in timing, style, and extent. Southern Arizona experienced major extension in the middle to late Cenozoic (37-13 Ma). This major extension was dominated

by large displacements on low-angle detachment faults that resulted in exhumation of metamorphic core complexes and highly extended terranes in which upper-plate fault blocks were strongly tilted (Dickinson, 1989, 1991; Spencer and Reynolds, 1989). Cenozoic ash-flow tuff volcanism in southern Arizona is time-transgressive, younging from southeast to northwest. In the late Cenozoic (13-3 Ma), high-angle normal faulting produced gently tilted horsts and grabens. The late Cenozoic faulting event was associated with basaltic magmatism (Nations et al., 1985; Spencer and Reynolds, 1989; Menges and Pearthree, 1989; Menges and McFadden, 1981).

In contrast to southern Arizona, the Basin and Range province in southwestern New Mexico underwent only high-angle normal faulting associated with Basin and Range extension beginning at about 26 Ma (Fig. 9) and lasting into the Holocene (Mack, 2004; Seager et al., 1984). This deformation produced fault block uplifts and complementary basins (horsts and half grabens) (Fig. 10), and was accompanied by basaltic magmatism.

As in the southern Rio Grande rift, the latest Miocene to Pliocene (~6 Ma) was a time of renewed extension in the Basin and Range province of southwestern New Mexico (Fig. 9) (Mack, 2004). Extension continued into the early Pleistocene, with minor activity in the Holocene. During this event, new faults were formed, some existing faults were lengthened, and basins continued to subside and fill with sediment (Fig. 11) (Mack, 2004). Recurrent faulting events are marked by angular unconformities in basin-fill sediments (Mack, 2004).

Southern Transition Zone

The southern part of the Transition Zone experienced middle- to late-Cenozoic normal faulting (Fig. 9) that resulted in uplifts, half grabens and mostly low-angle tilting of volcanic and sedimentary rocks. The southern Transition Zone is dominated by northwest-trending structures regardless of age, indicating reactivation of pre-existing northwest-striking faults (Mack, 2004). Although basaltic andesite volcanism began in the Oligocene, the first phase of extensional

faulting and basin development began in the early Miocene (Mack, 2004). Extensional faulting was accompanied by eruptions of basalt and rhyolite (Fig. 9). A second phase of faulting began at about 5 Ma and continued through Pliocene and early Pleistocene time (Fig. 9) (Mack, 2004).

Basin-fill deposits in the Basin and Range province and southern part of the Transition Zone of southwestern New Mexico consist dominantly of moderately- to poorly-indurated gravel and sand with some basalt (Menges and Pearthree, 1989; Mack, 2004). Most pre-Pliocene basin-fill deposits are poorly exposed so their distribution is not well known, and they are not well dated (Mack, 2004). The oldest dated basin-fill sediments are upper Oligocene, but the exposed sediments are dominantly Miocene to Pliocene in age (Mack, 2004). The basin-fill sediments are part of the Gila assemblage of Scarborough (1989), and have generally been assigned to the Gila Conglomerate regardless of age (Mack, 2004). The Gila assemblage is characterized by low dips and a general lack of internal deformation compared to older Cenozoic sedimentary deposits in southern Arizona (Scarborough, 1989). Most of the basin-fill gravels at Tyrone are alluvial fan deposits (Griffin, 2001), and they are referred to here as alluvial fan gravels.

CENOZOIC PALEOGEOGRAPHY AND PALEOCLIMATE

The Cenozoic paleogeography and paleoclimate of the southwestern New Mexico is important to this study because of the strong control tectonic uplift and climatic conditions have on oxidation and enrichment of porphyry copper deposits. Ideal conditions for supergene enrichment are a warm, semiarid climate resulting in a water table at depth with a well-oxygenated vadose zone and seasonal cycles of precipitation and groundwater recharge. Tectonic uplift also promotes deep oxidation and mature enrichment, as uplift is accompanied by descent of the local groundwater table, leaching of the previously-formed chalcocite blanket, and redeposition and further enrichment of copper below the newly-established groundwater table.

The area of southwestern New Mexico had significant topographic relief following the Laramide orogeny due to uplift of the Mogollon highlands (Fig.7). The Paleocene paleoclimate was humid and warm-temperate to subtropical, and fossil pollen indicate the existence of forests common to subtropical uplands and wet, warm-temperate coastal lowlands (Nations et al., 1985; Scarborough, 1989). Southwestern New Mexico was probably dominated by subdued topography by the late Eocene (Scarborough, 1989; McIntosh et al., 1992). Subtropical to warm-temperate conditions persisted in the Eocene, and fossil pollen from sedimentary basins indicate environments ranging from cool-temperate uplands to subtropical lowlands (Nations et al., 1985; Cather and Johnson, 1986; Schmidt, 1991).

Climatic conditions changed during the Oligocene, and fossil flora resemble modern species. Oligocene plants in southeastern Arizona suggest a drier and more variable climate than during the Eocene and elevations of 1,000 m (3,000 ft) for depositional basins (Nations et al., 1985). With minor exceptions, the dry climates continued through the Neogene. Miocene flora in Arizona indicate higher elevations, above 1,300 m (4,000 ft) but probably less than about 2,200 m (7,200 ft), associated with Basin and Range tectonism (Nations et al., 1985). Elevations of over 2,200 m were achieved during the Pliocene (Nations et al., 1985). In the early Pliocene prior to 3.4 Ma, the climate in southeastern Arizona was arid with seasonal precipitation (Smith, 1994). The climate became wetter until 2.8 Ma, when a return to more seasonal precipitation led to establishment of a dry, monsoonal climate between 1.6 and 0.6 Ma (Smith, 1994; Mack et al., 1994a).

Supergene alunite and jarosite from ore deposits in the southwestern U.S., Chile, and west Africa indicate a common event of deep weathering and supergene enrichment that occurred from the Oligocene until the mid Miocene (>34 Ma to 10-14 Ma) (e.g., Alpers and Brimhall, 1988; Arehart and O'Neil, 1993; Vasconcelos et al., 1994a; Sillitoe and McKee, 1996). Supergene enrichment then diminished as climates became cooler and more arid in the mid-

Miocene. The drying climates may have been influenced by local tectonic uplifts (creating higher elevations and rain shadows), but their world-wide effects indicate that the global climate became more arid in the mid Miocene (Sillitoe and McKee, 1996).

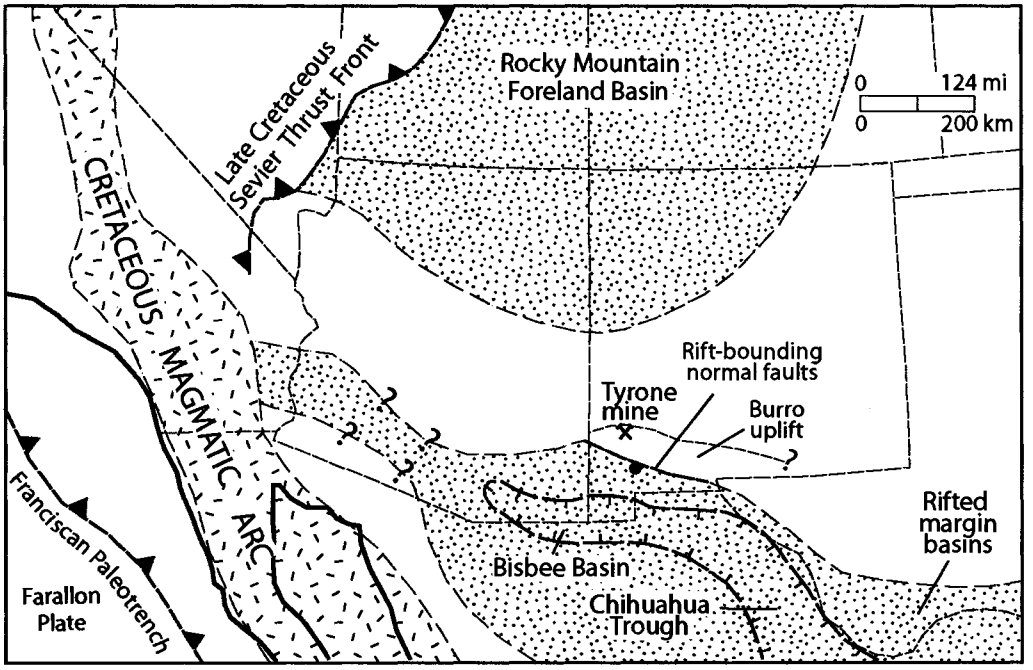

Figure 6. Cretaceous paleotectonic map of Arizona and New Mexico depicting the Bisbee Basin, Burro uplift, and Cretaceous magmatic arc. Modified from Dickinson (1989) and Seager (2004).

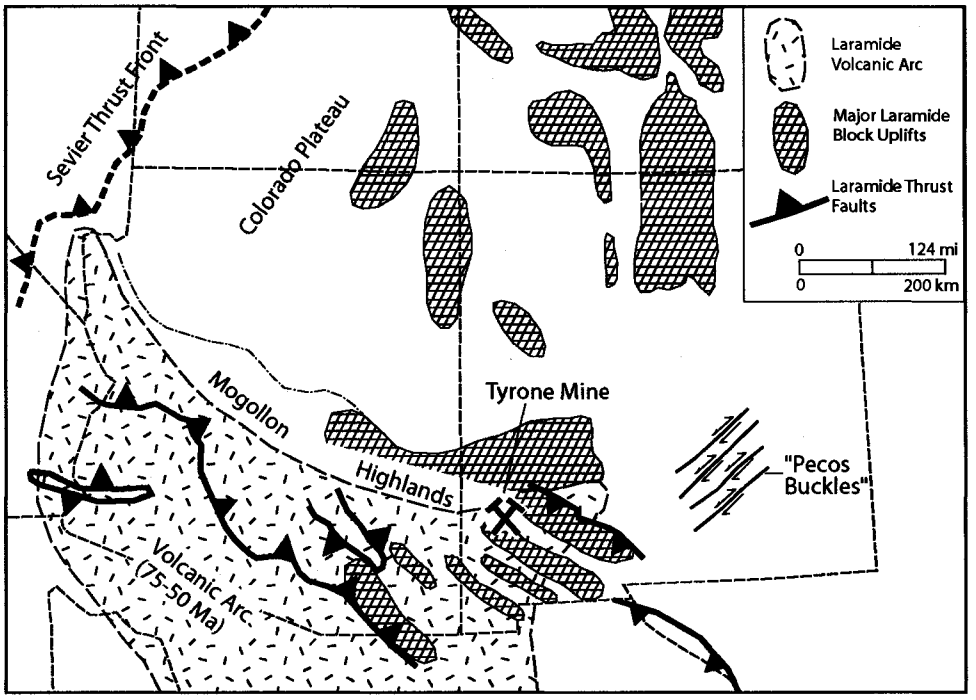

Figure 7. Laramide paleotectonic map of Arizona and New Mexico showing Laramide thrust faults, block uplifts, and the Laramide volcanic arc. Modified from Seager (2004) and Nations et al. (1985).

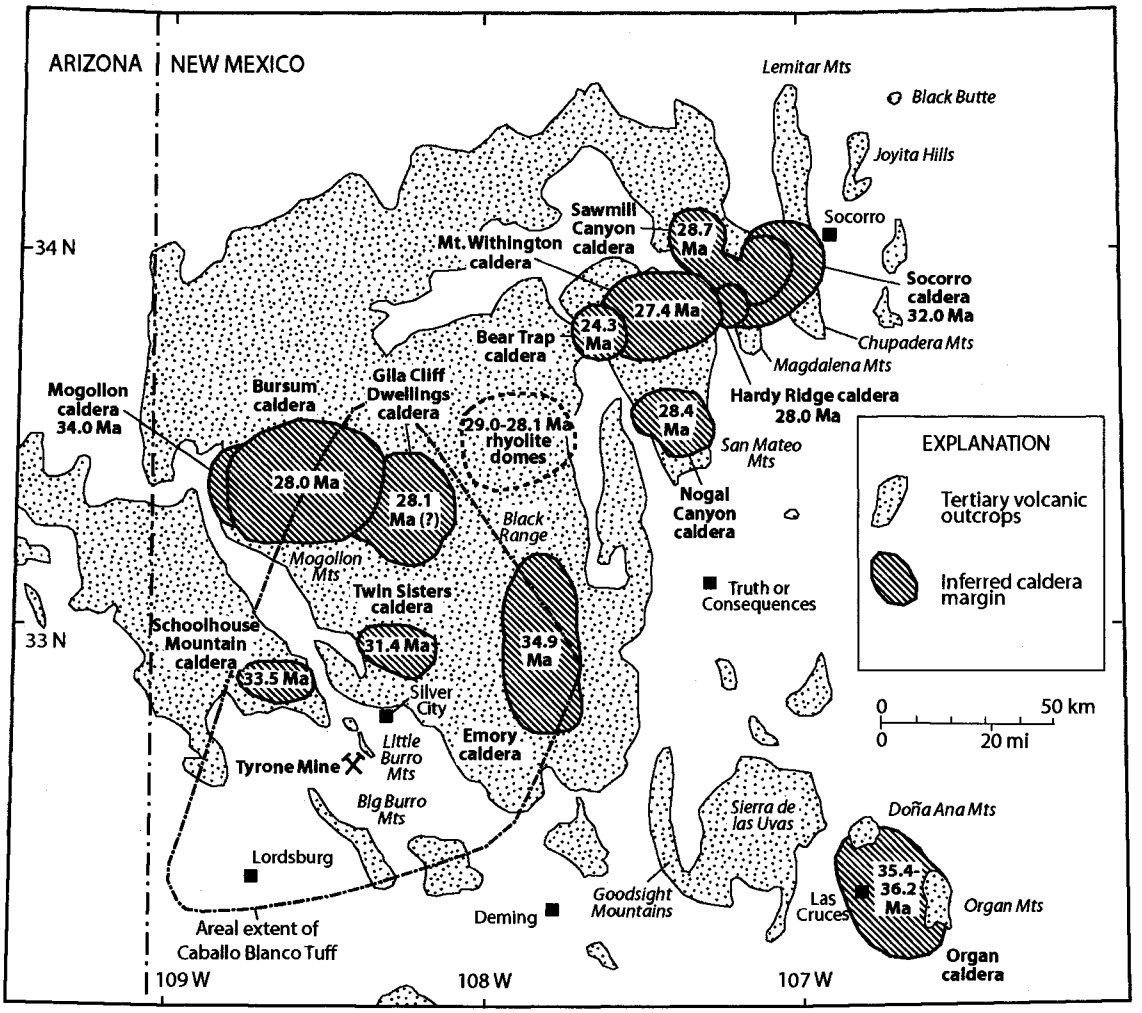

Figure 8. Map of the Mogollon-Datil volcanic field depicting locations of inferred calderas, caldera ages, generalized outcrop distribution of upper Eocene-Oligocene volcanic rocks, and areal extent of the Caballo BlancoTuff (31.65 + 0.06 Ma (McIntosh et al., 1992)). One possible source for the Caballo Blanco Tuff is the Twin Sisters caldera. Modified from McIntosh et al. (1992), Drewes et al. (1985), and Chapin et al. (2004).

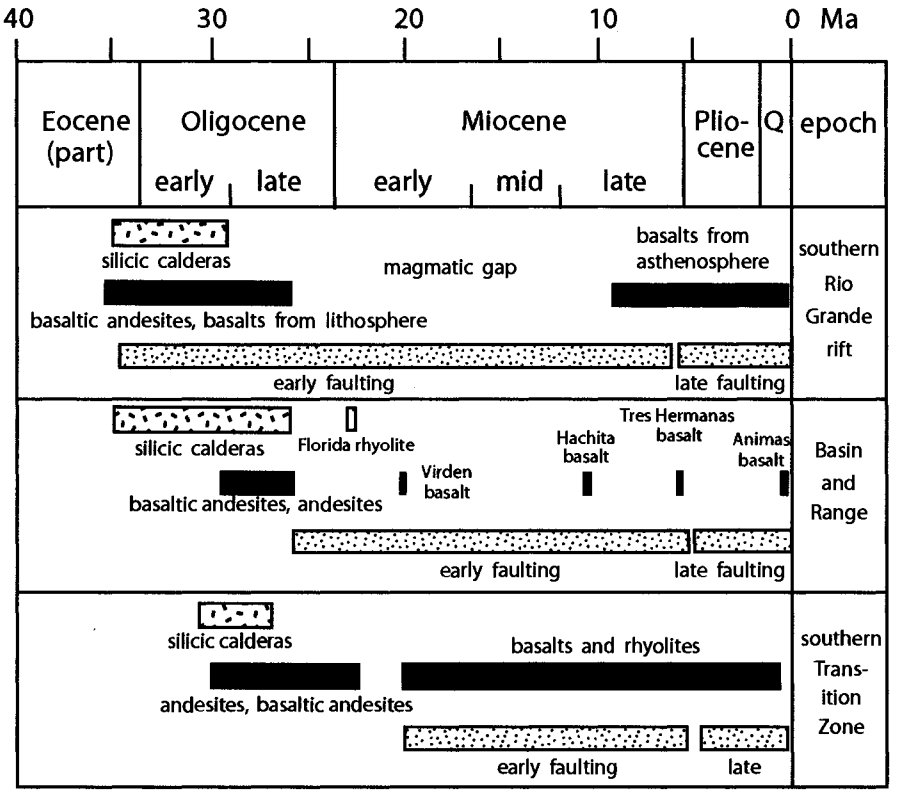

Figure 9. Summary of timing of middle and late Cenozoic volcanism and extensional faulting events in southwestern New Mexico. From Mack (2004).

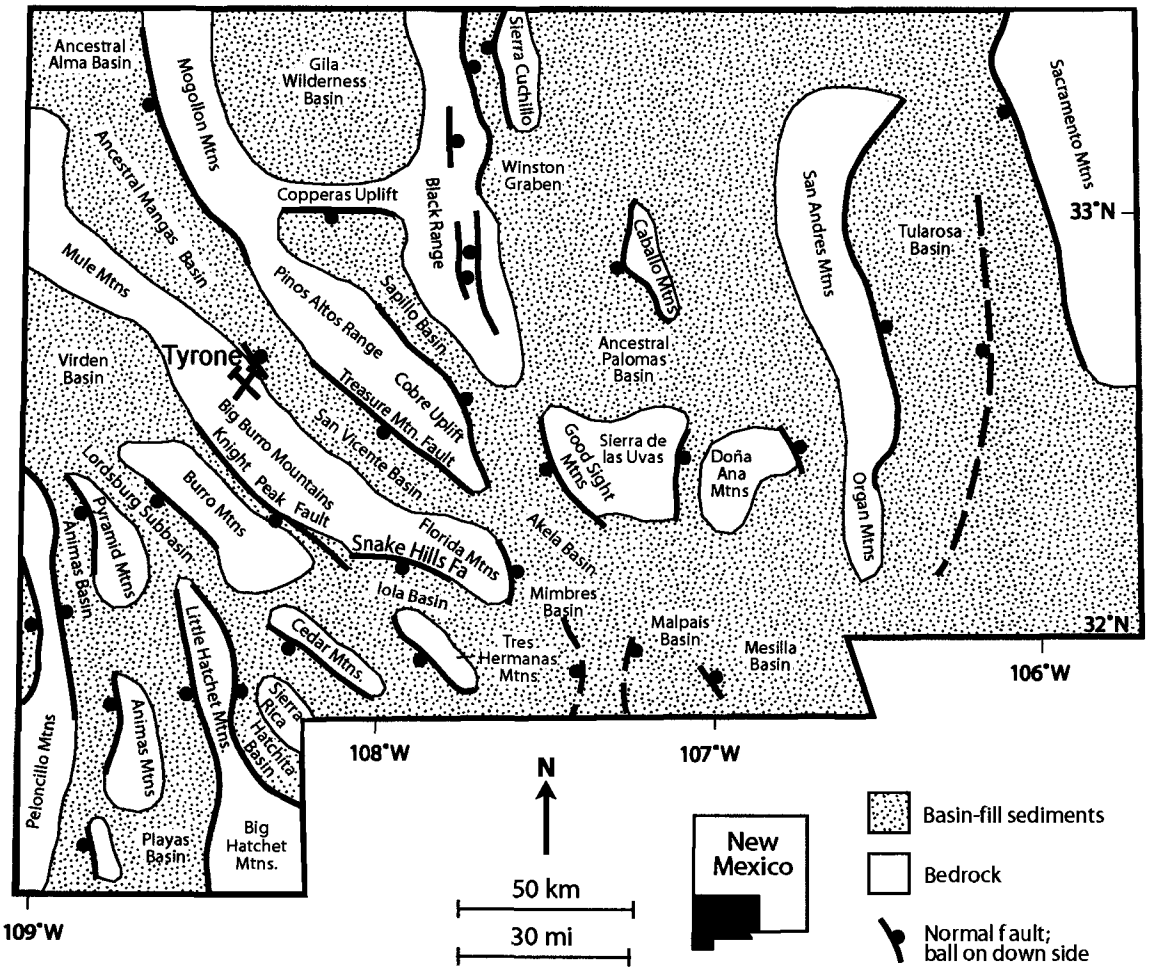

Figure 10. Miocene paleogeographic and paleotectonic map of southwestern New Mexico showing positions of the Big Burro Mountains uplift, Treasure Mountain and Knight Peak faults, and San Vicente basin. Modified from Mack (2004).

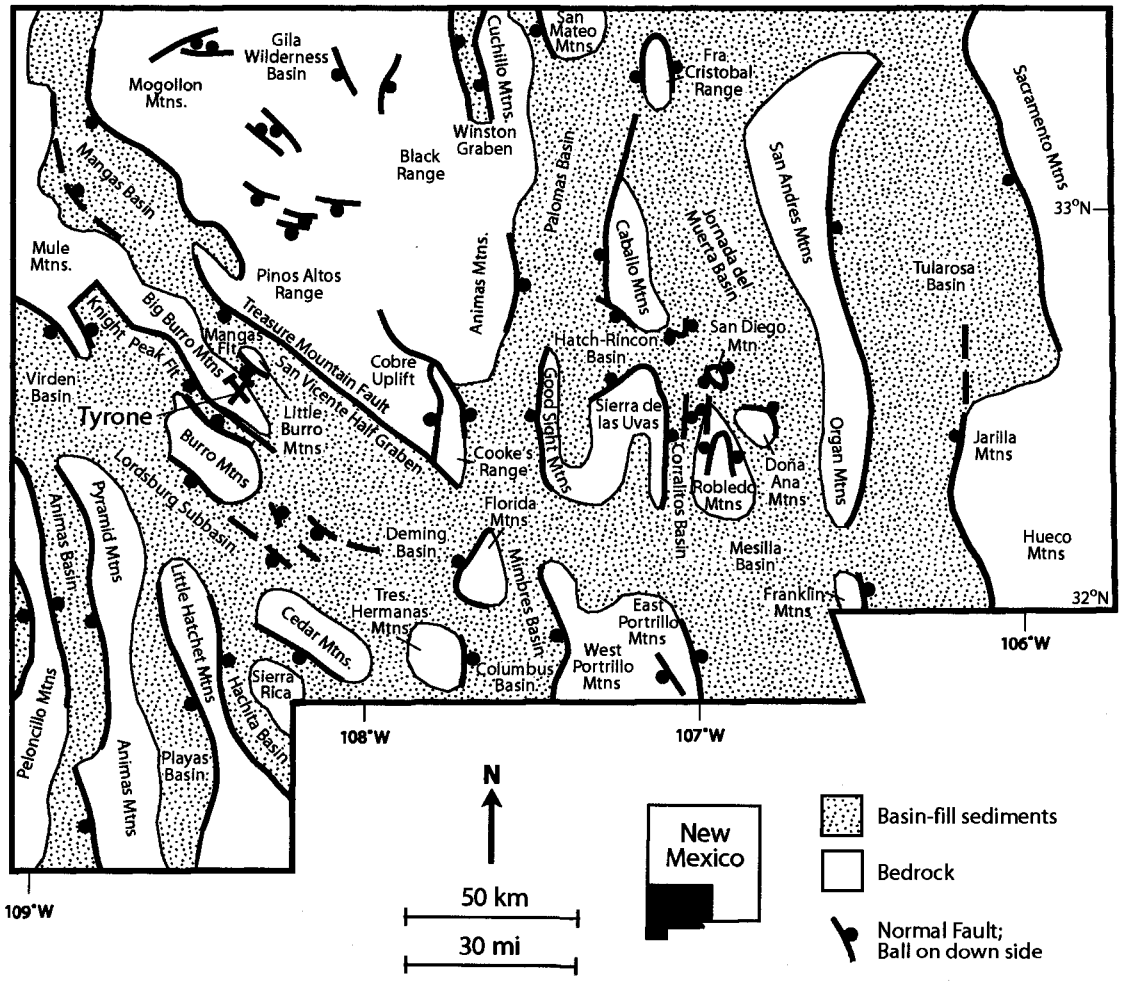

Figure 11. Latest Miocene-early Pleistocene paleogeographic and paleotectonic map of southwestern New Mexico showing the Little Burro Mountains uplift and the Mangas fault. Modified from Mack (2004) and Mack and Sout (2005).

CHAPTER 3: GEOLOGY OF THE SOUTHERN LITTLE BURRO MOUNTAINS

INTRODUCTION

Mapping for this project was conducted in the southern part of the Little Burro Mountains between Tyrone Peak and Indian Peak (Plates 1 and 2). Except where noted, the description of geology of the southern Little Burro Mountains is based on new data from the present study. In Chapter 5, the geology of the Tyrone district and surrounding area in the Big Burro Mountains is discussed, mostly from published data and information provided by the Tyrone mine geology group.

The Little Burro Mountains are a northwest-trending horst block tilted 10-33° to the northeast. The Little Burro Mountains are bounded on the southwest side by the Mangas fault, a major northwest-striking Basin and Range normal fault with as much as 430 m (1,400 ft) of displacement.

Basement rocks within the Little Burro Mountains include Proterozoic granite, gneiss, and schist and are overlain by Upper Cretaceous sedimentary rocks, Upper Cretaceous to Paleocene andesite and dacite, and a thick sequence (over 710 m (2,300 ft)) of upper Eocene to Oligocene volcanic rocks. In the southern part of the Little Burro Mountains, which was mapped for this research, the Proterozoic Burro Mountains granite is intruded by monzonite and quartz monzonite porphyry of the Eocene Tyrone stock.

Two unconformities exposed in the southern Little Burro Mountains record erosional unroofing events in the Tyrone deposit. The older unconformity occurs within tuffs of the Mogollon-Datil volcanic field, and is overlain by copper-bearing ferruginous sandstone and conglomerate. This unconformity surface is locally incised into Upper Cretaceous-Paleocene andesite. The younger unconformity surface is cut into the leached cap of the Tyrone copper deposit. Northeast-trending paleochannels in this unconformity surface are occupied by copper-

bearing ferricrete. The ferricrete and all older units are in turn unconformably overlain by alluvial fan gravel.

Ore deposits in the southern and central parts of the Little Burro Mountains consist of small gold, silver and base-metal veins along northeast-striking faults within the Proterozoic granite, Upper Cretaceous sedimentary rocks, and Upper Cretaceous-Paleocene andesite (Hedlund, 1985). No economic porphyry copper deposits have been found associated with the Tyrone stock in the southern Little Burro Mountains, although a number of small exotic copper deposits (up to 100,000 tons and >1% Cu) have been discovered in the younger ferricrete unit (DuHamel et al., 1995).

Petrographic descriptions of Mesozoic and Cenozoic igneous rocks in the Tyrone district and southern Little Burro Mountains are summarized in Table 1. The $^{40}Ar/^{39}Ar$ ages of Cenozoic igneous rocks in the southern Little Burro Mountains are summarized in Table 2. Stratigraphic relationships of Cenozoic rocks in the southern Little Burro Mountains are shown in Figure 12. Formation names used here are formal names except where otherwise noted.

LITHOLOGIC UNITS

Precambrian Rocks

Burro Mountain Granite

The dominant Precambrian rock type in the map area is the informally-named Mesoproterozoic Burro Mountain granite (p$\in$g). Burro Mountain granite crops out west of the Cedar Canyon and Contact faults in the northwestern part of the map area (Plt. 1) and has been intersected in deep drill holes NXBM-1 and NXBM-2 to the northwest and west of Tyrone Peak (Plt. 2). The Burro Mountain granite is light gray to brown, medium-grained, and consists of 30-50% oligoclase, 20-40% microcline, 30-38% quartz, and 2% biotite (Hedlund, 1985). The granite is argillized and silicified along faults, and some quartz veins occur west of the Contact fault (Plt.

1). Burro Mountain granite yielded a U-Pb zircon age of 1,445 Ma (Stacey and Hedlund, 1983; Hedlund, 1985).

Diabase Dikes

Mesoproterozoic diabase dikes (pЄdb) intrude The Burro Mountain granite along west-northwest- and northeast-striking Proterozoic faults (Plt. 1). The dikes are generally only a few meters thick but range up to 30 m (100 ft). Diabase exhibits a subophitic to intersertal texture, and consists of 64% andesine or labradorite, 30% clinopyroxene, 1% biotite, and 4% magnetite-ilmenite, with accessory apatite (Gillerman, 1964; Hedlund, 1985). The diabase is typically propylitized. These dikes have not been dated, but they are probably correlative with diabase dikes in east-central Arizona dated at 1,200 Ma (Drewes et al., 1985).

Upper Cretaceous Sedimentary Rocks

The Precambrian rocks are nonconformably overlain by Upper Cretaceous shallow marine sedimentary rocks (Mack et al., 1988; Lawton, 2004) including the Beartooth Quartzite and the overlying Colorado Formation (Plt. 1).

Beartooth Quartzite

The Beartooth Quartzite (Kb) is light gray to brown, medium-bedded to locally trough cross-bedded, well-sorted, fine- to medium-grained orthoquartzite to quartz sandstone. The quartzite is interbedded with thin beds of shale and fine conglomerate. The reported thickness for Beartooth Quartzite in the northern and central Little Burro Mountains ranges from 36 m (117 ft) (Edwards, 1960) to as much as 150 m (500 ft) (Hedlund, 1985). Only one small outcrop of the Beartooth quartzite occurs in the map area east of the Contact fault (Plt. 1). This exposure is about 20 x 40 m (70 x 130 ft) in dimension and <10 m (30 ft) thick. The Beartooth Quartzite in the Burro Mountains is probably Cenomanian in age (Mack et al, 1988).

Colorado Formation

The Beartooth Quartzite is conformably overlain by the Colorado Formation, a shale unit which is at least 90 m (300 ft) thick in the map area and as much as 150 m (500 ft) thick in the northern part of the Little Burro Mountains (Hedlund, 1985). The Colorado Formation crops out in an erosional window in Upper Cretaceous-Paleocene andesite immediately east of the Contact fault, and the base and top of the formation are not exposed (Plt. 1). The lower member of the Colorado Formation (Kcs) is ~50 m (170 ft) thick and consists of black, fissile shale with beds of tan, fine- to medium-grained, cross-bedded quartz sandstone up to ~2 m thick. The upper member of the Colorado Formation (Kc) is ~40 m (130 ft) thick and consists of gray to black platy shale and siltstone with thin nodular beds of gray fossiliferous limestone. The Colorado Formation is Cenomanian to Turonian in age (Mack et al., 1988).

Upper Cretaceous and (or) Paleocene Andesite

The Beartooth Quartzite, Colorado Formation, and Precambrian granite are intruded and unconformably overlain by a thick sequence of Upper Cretaceous and (or) Paleocene andesite and dacite hypabyssal intrusions, lava flows, flow breccias, lahar deposits, and volcaniclastic sandstone (TKa, Plt. 1). The andesite has not been dated, but Hedlund (1985) believed it may correlate with andesite flows of the Saddle Rock Canyon Formation exposed in the Mangas Springs quadrangle 20 km (12 mi) northwest of the Tyrone mine. The Saddle Rock Canyon Formation yielded a zircon fission-track date of 58.4 ± 4 Ma (Hedlund, 1985).

The andesite flows are dark greenish-gray to olive green and porphyritic, with phenocrysts of andesine (20-30%) and clinopyroxene ± hornblende (4-7%), and about 2% magnetite in an aphanitic, pilotaxitic to intergranular groundmass (Table 1). The upper ~60 m (200 ft) of the andesite has a platy fracture. Dacite is greenish-gray and has a similar content of plagioclase and hornblende phenocrysts, and up to 2% quartz phenocrysts. Massive lahar deposits are clast- to matrix-supported and contain andesite clasts up to 10 cm in diameter. Lahar

deposits are interbedded with thinly bedded volcaniclastic sandstone. The andesite and dacite are extensively altered to propylitic assemblages.

Phelps Dodge core hole IP-1 near Indian Peak encountered a thick sequence of propylitized and sericitized andesite and dacite, and terminated in propylitized andesite at a depth of 317 m (1,039 ft) (Plt. 2) (DuHamel and Cook, 1992). At Tyrone Peak, sericitized andesite lies beneath a sill of phyllically-altered Stage 3 quartz monzonite porphyry related to the Tyrone stock. The andesite occurs at depths of approximately 168 m (550 ft) and 174 m (570 ft), respectively, in drill holes TP-1 and TP-2 south and southeast of Tyrone Peak (Plts. 1 and 2). Andesite also underlies alluvial fan gravel in deep drill holes in the Mangas Valley (Plts. 1 and 2).

Upper Cretaceous and (or) Paleocene Latite Porphyry

Latite porphyry sills and dikes (TKl) intrude the Colorado Formation and andesite adjacent to the Contact fault (Plt. 1). The latite is light grayish-green to light reddish-brown and contains 25-35% phenocrysts of oligoclase, biotite, hornblende, and quartz in a microcrystalline, granular groundmass (Table 1). The latite is strongly propylitized and forms low, rounded outcrops. Maximum thickness is probably ~30 m (100 ft). The latite is probably Upper Cretaceous or Paleocene in age as it intrudes the andesite and Upper Cretaceous sedimentary rocks.

Eocene Intrusive Rocks of the Tyrone Stock

Of the five intrusive stages recognized in the Tyrone stock, intrusions from three stages crop out in an apophysis of the stock around Tyrone Peak. These intrusions occupy an area of about 6.5 km^2 (2.5 mi^2) and include numerous sills and dikes of Stage 2 monzonite porphyry and Stage 3 quartz monzonite porphyry, and a plug of late-stage (Stage 5) rhyodacite (Plts. 1 and 2). All were intruded into Proterozoic granite and Upper Cretaceous-Paleocene andesite.

The Stage 2 and Stage 3 porphyries in the southern Little Burro Mountains are in the pyritic, low-grade halo of the Tyrone deposit. Stage 3 quartz monzonite porphyry at Tyrone Peak

shows strong phyllic and argillic alteration and locally strong jarositic staining, but it does not contain a well-developed chalcocite blanket because of its low hypogene copper content (generally 0.04 to 0.05% Cu in drill holes).

Stage 2 Monzonite Porphyry

The Stage 2 monzonite porphyry (Tmp) is light greenish-gray to gray and contains up to 45% phenocrysts of oligoclase, biotite, and hornblende, and locally as much as 3% resorbed quartz phenocrysts in a microcrystalline to cryptocrystalline groundmass of orthoclase and quartz (Table 1). The high percentage (30-40%) of large (up to 10 mm) oligoclase phenocrysts gives a distinctive "crowded" porphyritic texture. The groundmass is flow-banded in places. Monzonite porphyry is typically altered to propylitic assemblages, although it is weakly argillized at Tyrone Peak and contains up to 1% pyrite.

Stage 3 Quartz Monzonite Porphyry

Stage 3 quartz monzonite porphyry (Tqmp) is tan to light gray and contains 30-35% phenocrysts of oligoclase, resorbed quartz, biotite, hornblende, and orthoclase in a microcrystalline to cryptocrystalline groundmass of orthoclase and quartz. Locally, the Stage 3 quartz monzonite porphyry also contains 3-4% orthoclase megacrysts to 12 mm in length. The Stage 3 quartz monzonite porphyry contains up to ~3% disseminated pyrite. Strong phyllic and argillic alteration typically results in destruction of groundmass and phenocrysts, and a vuggy texture. The Stage 3 quartz monzonite porphyry sill at Tyrone Peak is 150-180 m (500-600 ft) thick, and has a footwall of Upper Cretaceous-Paleocene andesite.

The Stage 3 quartz monzonite porphyry is distinguished from Stage 2 monzonite porphyry by differences in plagioclase phenocryst content (average 23% and 35% respectively), quartz phenocryst content (average 5% and 1% respectively), and locally orthoclase megacryst content of the Stage 3 quartz monzonite porphyry.

Stage 5 Rhyodacite Porphyry Plug

A plug of flow-banded rhyodacite porphyry (Trdp) forming two lobes roughly 370-490 m (1,200-1,600 ft) in diameter, crops out directly west of Tyrone Peak and intrudes Stage 2 monzonite porphyry (Plt. 1). The rhyodacite porphyry is light gray to pink and contains 25-35% phenocrysts of oligoclase, resorbed quartz, biotite, and orthoclase in a flow-banded, microcrystalline groundmass. Flow banding dips moderately to steeply inward and forms a concentric pattern around the margin of the plug. The rhyodacite porphyry plugs are unaltered and unmineralized, and represent late-stage intrusions related to the Tyrone stock. Fresh plagioclase from the eastern lobe of the plug was dated by $^{40}Ar/^{39}Ar$ for this study and returned an age of 54.10 ± 0.60 Ma (Table 2). This age is taken as a minimum age for the Tyrone stock.

Eocene and Oligocene Volcanic and Volcaniclastic Rocks of the Mogollon-Datil Volcanic Field

Upper Eocene and Oligocene volcanic and volcaniclastic rocks of the Mogollon-Datil volcanic field crop out throughout the southern part of the Little Burro Mountains and have an aggregate thickness of at least 710 m (2,300 ft). The rocks dip 10-33° to the northeast (Plts. 1 and 2) although dips average 20-25°. These rocks include: 1) rhyolite to latite ash-flow tuffs, air-fall tuffs, water-laid tuffs, and volcaniclastic deposits; 2) rhyodacite ash-flow tuffs, flows, and breccias; 3) basaltic andesite flows; and 4) ferruginous volcaniclastic sandstone and conglomerate (Fig. 12 and Plt. 1).

The upper Eocene-Oligocene volcanic rocks were areally extensive at the close of volcanism in the Mogollon-Datil volcanic field (Fig. 8). A thick section of the volcanic rocks is preserved in the Knight Peak half graben 16 km (10 miles) southwest of the Tyrone mine (Fig. 1) (Drewes et al., 1985). However, these rocks were removed by erosion from the Big Burro Mountains uplift (Fig. 1) at the onset of Basin and Range uplift in the early Miocene.

The complex volcanic stratigraphy of the Mogollon-Datil volcanic field was worked out by McIntosh et al. (1990, 1991, 1992) using detailed $^{40}Ar/^{39}Ar$ dating and paleomagnetic studies. This work allows volcanic units to be correlated based on $^{40}Ar/^{39}Ar$ ages, lithologic characteristics, and stratigraphic position (McIntosh et al., 1992). The upper Eocene-Oligocene volcanic rocks in the southern part of the Little Burro Mountains are herein correlated with the volcanic strata of the Mogollon-Datil volcanic field using new $^{40}Ar/^{39}Ar$ dates and petrography.

Rubio Peak Formation

At Tyrone Peak, intrusive rocks of the Tyrone stock are nonconformably overlain by a sequence of porphyritic rhyodacite ash-flow tuff, flows, and breccia herein correlated with the Rubio Peak Formation (Trp) of the Mogollon-Datil volcanic field. The Rubio Peak Formation at Tyrone Peak is as much as 120 m (400 ft) thick and overlies a northeast-sloping erosional surface developed upon pervasively argillized Stage 2 monzonite porphyry and Stage 3 quartz monzonite porphyry of the Tyrone stock (Plts. 1 and 2). The basal unit of the Rubio Peak Formation is a thin rhyodacite ash-flow tuff that reaches a maximum thickness of <30 m (100 ft). The basal ash-flow tuff unit is poorly exposed and is not mapped separately on Plates 1 and 2. The rhyodacite tuff is light gray, devitrified, and moderately to strongly welded. It exhibits well-developed eutaxitic texture and rarely, rheomorphic folds (Fig 13). The rhyodacite tuff typically contains 15-25% crystal fragments of oligoclase, quartz, biotite, and hornblende, and abundant lithic fragments and collapsed pumice fragments up to 6 cm in length (Table 1).

Rhyodacite flows and breccia overlie the basal ash-flow tuff unit. These rocks are light gray and contain up to 40% phenocrysts of plagioclase, biotite, hornblende, and quartz. The phenocryst mineralogy of the flows, breccia, and tuff is typically masked by argillic alteration and silicification. The rhyodacite weathers to distinctive red and purple hues with abundant manganese oxide staining.

Danley (1976) first tentatively identified the rhyodacite at Tyrone Peak as part of the Rubio Peak Formation. Rubio Peak Formation is the basal Eocene unit of the Mogollon-Datil volcanic field and it overlies the regional unconformity that marks the end of Laramide deformation in New Mexico (Elston, 1976; Seager, 2004). In the southern part of the Mogollon-Datil volcanic field, the lower part of the formation is dominated by andesite flows, and the upper part is dominated by latite flows; also common are ash-flow and air-fall tuff, volcanic breccia, and volcaniclastic rocks (Elston, 1976; McMillan, 2004). Danley (1976) also identified a 180 m-thick (600 ft-thick) section of rhyodacite tuff and flow breccia intercepted in drill hole NXBM-1 northwest of Tyrone Peak as Rubio Peak Formation (Plt. 2). In NXBM-1, the Rubio Peak Formation overlies Upper Cretaceous-Paleocene andesite (Danley, 1978) and underlies rhyolite ash-flow tuff herein correlated with Bell Top Formation.

The closest reported occurrence of Rubio Peak Formation in the published literature is approximately 19 km (12 mi) northeast of the Little Burro Mountains on the southwestern flank of the Pinos Altos Range (Fig. 1) (Jones et al, 1967; Jones et al. 1970). There, the Rubio Peak Formation is up to 265 m (870 ft) thick and consists of two rhyodacite ash-flow tuff sheets and basal volcaniclastic conglomerate (Jones et al. 1970; Elston, 1976).

The Rubio Peak Formation at Tyrone Peak is not overlain by other volcanic units in outcrop. However, on the north side of Tyrone Peak it lies in normal fault contact with younger ash-flow tuff and volcaniclastic units (herein identified as Bell Top Formation tuff member 3 and upper Sugarlump Tuff, respectively, see below) along the Tyrone Peak fault (Plt. 1). Because the Rubio Peak rhyodacite is in the footwall of the Tyrone Peak fault and Bell Top tuff member 3 and upper Sugarlump Tuff are in the hangingwall, the rhyodacite is older.

The Rubio Peak Formation in the southern Little Burro Mountains has not been dated by radiometric techniques. Published K-Ar and $^{40}Ar/^{39}Ar$ dates for the Rubio Peak Formation in the

southern part of the Mogollon-Datil volcanic field range from 46.3 ± 0.3 to 36.4 ± 2.3 Ma (McMillan, 2004) (Fig. 12).

Bell Top Formation

To the northwest of Tyrone Peak, the basal unit of the upper Eocene to Oligocene volcanic sequence is a poorly- to moderately-welded, crystal-poor, vitric ash-flow tuff, 0-70 m (0-230 ft) thick, that unconformably overlies Upper Cretaceous-Paleocene andesite and Stage 2 monzonite porphyry (Plts. 1 and 2). This unit was referred to as Sugarlump Tuff by Danley (1976), and as ash-flow tuff of Indian Peak by Hedlund (1978b). The unit is herein correlated with the Bell Top Formation tuff member 3 of the Mogollon-Datil volcanic field.

Tuff member 3 (Tbt) of the Bell Top Formation is light pink to orange and gray and contains 3-4% sanidine, quartz, and biotite crystal fragments, and pumice fragments as much as 4 cm in length (Table 1, Fig. 14). The tuff is devitrified in most places and has a characteristic pitted weathering surface. It is resistant to weathering and forms the cap rock of Indian Peak and other ridges in the southern Little Burro Mountains.

In this study, a sample of tuff member 3 of the Bell Top Formation was dated at 35.73 ± 0.09 Ma by $^{40}Ar/^{39}Ar$, using 12 single-crystal fusions of sanidine (Table 2). This age corresponds closely to the $^{40}Ar/^{39}Ar$ age of 35.69 ± 0.12 Ma on sanidine reported by McIntosh et al. (1991) for tuff member 3 of the Bell Top Formation from the Sierra de las Uvas, approximately 110 km (68 mi) east of the Little Burro Mountains (Fig 8). Seager (1995) described this unit in the Sierra de las Uvas as moderately- to poorly-welded, pinkish-gray, vitric ash-flow tuff, 0-107 m (0-350 ft) thick, a description very similar to that of the unit described here.

Ash-flow tuffs of similar lithology and in the same stratigraphic position on the southwestern flank of the Pinos Altos Range near the town of Bayard have been previously mapped as Sugarlump Tuff (Fig. 1) (Jones et al, 1967; Jones et al. 1970). However, Elston

(1976) and McIntosh et al. (1991) noted that rocks mapped as Sugarlump Tuff in some locations may correlate with the Bell Top Formation of Sierra de las Uvas. The only reported $^{40}Ar/^{39}Ar$ age for Sugarlump Tuff is 35.17 ± 0.12 Ma for the upper Sugarlump Tuff (McIntosh et al., 1991), which is about 0.5 Ma younger than the age of tuff member 3 of the Bell Top Formation.

Tuff member 3 of the Bell Top Formation was erupted during the first ignimbrite pulse in the Mogollon-Datil volcanic field, possibly from the Organ/Doña Ana caldera at Las Cruces, New Mexico (Fig. 8) (McIntosh et al., 1991; McIntosh et al., 1992; Chapin et al., 2004). Ash-flow tuffs erupted during the first ignimbrite pulse are predominantly low-silica rhyolites with a low aspect ratio (thickness:area) probably indicating a combination of subdued pre-eruptive topography and high energy or mobility of the ash flows (McIntosh et al., 1991).

Ferruginous Sandstone and Conglomerate

The Bell Top Formation is unconformably overlain by a thin, discontinuous unit (0-15 m (0-50 ft) thick, average ~1-3 m) of ferruginous, fine to coarse-grained, tuffaceous sandstone and pebble conglomerate (Tfs) (Fig. 15 and Plt. 1). The unit is medium to dark brownish-red, poorly-sorted, thin- to medium-bedded, and exhibits planar bedding and cross bedding (Fig. 15A). Clasts in the conglomerate are dominantly angular to rounded tuff and andesite, ranging from 4-15 mm in diameter. However, the conglomerate also contains rare small clasts (to ~10 mm) of porphyritic intrusive rocks with quartz veinlets, and these were probably derived from the Tyrone stock (Fig. 15B).

In the northern part of the map area, channels filled with ferruginous conglomerate cut through the Bell Top Formation and there, channel fill conglomerates lie directly on Upper Cretaceous-Paleocene andesite (Plt. 1). The ferruginous sandstone and conglomerate crops out discontinuously along a strike length of about 2,440 m (8,000 ft) from southeast of Indian Peak to south of Bald Mountain. Multi-element analyses on samples of the ferruginous sandstone and conglomerate confirmed that it contains exotic copper (up to 467 ppm; see Chapter 8). Quartz-

veined clasts and exotic copper content indicate that this unit represents detritus from an erosional unroofing event in the Tyrone deposit.

The ferruginous sandstone and conglomerate unit was not dated directly in this study, but its age is bracketed by $^{40}Ar/^{39}Ar$ dates on the underlying Bell Top Formation and the overlying Caballo Blanco Tuff (35.7 and 31.6 Ma, respectively) (Table 2).

Sugarlump Tuff, air-fall tuff member

The ferruginous sandstone and conglomerate unit is unconformably overlain by an air-fall tuff unit, 10 to 85 m (30-280 ft) thick, herein correlated with the lower member of the Sugarlump Tuff (Tsa) (Plt. 1). This unit was previously referred to as air-fall tuff of Indian Peak by Hedlund (1978b). The air-fall tuff is white to light pinkish-gray and pink, thin to medium planar-bedded and laminated, poorly indurated, and consists predominantly of devitrified, pumiceous rhyolite to latite ash to fine lapilli (Fig. 16A). The rock also contains 4-6% crystal fragments of sanidine, plagioclase, quartz, and biotite, and 8-10% lithic fragments consisting mostly of dense, gray, cryptocrystalline rhyolite up to 6 mm in diameter (Table 1). Locally the air-fall tuff contains thin interbeds of graded to cross-bedded, medium- to coarse-grained tuffaceous sandstone. Cross bedding indicates some tuff is reworked and water-laid. The air-fall tuff unit thins on paleotopographic highs around Indian Peak (Plt. 2).

Sugarlump Tuff, volcaniclastic member

The air-fall tuff unit is overlain by volcaniclastic rocks which consist of white to light gray, pink, and green, thick-bedded to massive, poorly-sorted volcaniclastic breccia, air-fall tuff, and conglomerate up to 250 m (820 ft) thick (Fig. 16B and Plt. 1). This unit was previously referred to as volcaniclastic rocks of Wind Mountain by Hedlund (1978b), but is herein correlated with the upper member of the Sugarlump Tuff (Tsv). The matrix of the volcaniclastic breccia is composed of devitrified, pumiceous rhyolite and quartz latite ash and lapilli. Interspersed in the matrix are abundant angular clasts of dense, cryptocrystalline, brownish-gray rhyolite exhibiting

strongly contorted flow banding. These clasts are dominantly granule to pebble size but range up to 50 cm in length and increase in abundance and size near the tops of many of the massive beds (Figure 16B). The sedimentary breccias are interpreted as debris flow deposits. The source of the flow-banded rhyolite clasts is not known, but Eocene rhyolite dikes and plugs have been reported in the Tyrone and Wind Mountain quadrangles by Hedlund (1978b, d). One such dike crops out south of drill hole NXBM-1 (Plt. 1). The volcaniclastic member is moderately to poorly indurated and forms rounded outcrops.

The air-fall tuff and overlying volcaniclastic rocks correlate with the Sugarlump Tuff based on their stratigraphic position, age, and lithology. Sugarlump Tuff is well-exposed in the Cobre Mountains and Mimbres Valley east of Silver City (Fig. 1), where it consists of white to green and pink rhyolite and quartz latite air-fall tuff, ash-flow tuff beds, water-laid tuffs, and epiclastic rocks (Elston, 1957; Elston, 1976). McIntosh et al. (1991, 1992) obtained a 35.17 ± 0.12 Ma $^{40}Ar/^{39}Ar$ age from the upper member of the Sugarlump Tuff on the southwestern flank of the Pinos Altos Range 18 km (11 mi) southeast of Silver City. Like the Rubio Peak and Bell Top formations, the Sugarlump Tuff was erupted during the first ignimbrite pulse in the Mogollon-Datil volcanic field, probably from the Organ/Doña Ana caldera (McIntosh et al., 1991; McIntosh et al., 1992; Chapin et al., 2004).

Rhyolite Dikes

Rhyolite dikes (Tir) are rare in the map area (Plt. 1). The rhyolite dikes are typically 3-4 m (9-12 ft) thick and consist of dense, brownish-gray, cryptocrystalline, finely flow-banded rhyolite with sparse phenocrysts of quartz, plagioclase, sanidine, and biotite. A rhyolite dike intrudes volcaniclastic rocks of the Sugarlump Tuff just north of the Southern Star fault (south of NXBM-1), but was not observed intruding units higher in the section.

Older basaltic Andesite

The Sugarlump Tuff is unconformably overlain by a thin (<10 m (30 ft) thick), discontinuous basaltic andesite flow (Tba) (Plt. 1). The basaltic andesite is dark reddish-brown, porphyritic, weakly vesicular, and contains ~2% hornblende and 1-2% olivine phenocrysts in a trachytic to intersertal groundmass (Table 1). Olivine phenocrysts are altered to iddingsite.

This basaltic andesite unit is lithologically similar to and in the same stratigraphic position as the Rustler Canyon Basalt of Elston (1957, 1976) in the Cobre Mountains and Santa Rita area, and may be time equivalent. The Rustler Canyon Basalt has not been dated, but it lies immediately below the Caballo Blanco Tuff (Elston, 1976).

Caballo Blanco Tuff

The basaltic andesite is unconformably overlain by light gray to pink, moderately- to densely-welded, crystal-vitric ash-flow tuff. This unit was previously referred to as ash-flow tuff of Wind Mountain by Hedlund (1978b), and is herein correlated with the Caballo Blanco Tuff (Tcb) (Plt.1). The Caballo Blanco Tuff in the map area contains abundant large crystal fragments (to ~5 mm) including 10-18% quartz, 7-9% oligoclase, 3-6% sanidine, and 0.5-2% biotite, and also as much as 10% compacted pumice and lithic fragments (Fig. 17, Table 1). The tuff exhibits eutaxitic texture, but the groundmass is devitrified. Hedlund (1978b) reported a thickness of up to 55 m (180 ft) in the Little Burro Mountains. The Caballo Blanco Tuff is absent in the northern part of the map area and is partly buried beneath alluvial fan gravel north of Tyrone Peak, where the exposed thickness is probably less than 15 m (45 ft).

The Caballo Blanco Tuff is characterized by abundant coarse phenocrysts (Elston, 1976), and according to McIntosh et al. (1992), is reliably distinguished from similar tuff units by its $^{40}Ar/^{39}Ar$ age of 31.65 ± 0.06 Ma. Plagioclase from the Caballo Blanco Tuff dated for this study yielded an $^{40}Ar/^{39}Ar$ age of 31.60 ± 0.36 Ma (Table 2).

The Caballo Blanco Tuff is distributed over an area of >10,000 km^2 of southwestern New Mexico (Fig. 8), and is well exposed in the Cobre Mountains, Mimbres Valley, and in the Knight Peak area of the Burro Mountains (Elston, 1976). The Caballo Blanco Tuff was erupted during the second pulse of ignimbrite volcanism in the Mogollon-Datil volcanic field (McIntosh et al., 1990, 1992); the source caldera is not known, but possible candidates are the Bursum, Twin Sisters, or Emery caldera northeast and northwest of Silver City (Fig. 8) (McIntosh et al., 1992).

Younger Basaltic Andesite

The Caballo Blanco Tuff is unconformably overlain by basaltic andesite flows with an aggregate thickness of ~40 m (130 ft) (Plt 1). The basaltic andesite (Tbu) is dark gray to brown, vesicular, and porphyritic, with 15-20% phenocrysts of andesine, 6-7% clinopyroxene, and 5-8% olivine in a pilotaxitic to intersertal groundmass (Table 1). Olivine phenocrysts are partly altered to iddingsite. In the northern part of the Little Burro Mountains, the unit consists of basaltic andesite and latite flows and has an aggregate thickness of 90 m (295 ft) (Hedlund, 1978d).

The basaltic andesite and latite flows are in the same stratigraphic position and are lithologically similar to the Razorback Formation in the Cobre Mountains and Mimbres Valley (Elston, 1976). The Razorback Formation has not been dated, but Elston (1976) estimates its age at between 29.7 and 29.3 Ma.

Miocene to Pleistocene Basin-Fill Sediments

The Proterozoic through Oligocene rocks in the map area are unconformably overlain by basin-fill gravels of Miocene to Pleistocene age. These sediments fill the Mangas half graben and partly conceal the Tyrone deposit (Fig. 1 and Plt. 2). The Mangas basin extends from the Mogollon Rim, where it is a full graben, southward into the area of the Little Burro Mountains where it is partitioned into a series of northeast-tilted half grabens by northwest-striking, southwest-dipping Basin and Range normal faults (Fig. 1).

Basin-fill gravels are up to 370 m (1,200 ft) thick in the vicinity of the Tyrone mine (Fig. 18), and include a discontinuous, well-indurated basal ferricrete unit (Tf) and two overlying, semiconsolidated alluvial fan units (QTg) (Griffin, 2001). The three basin-fill units are separated by unconformities that record at least three major Basin and Range faulting and erosion events: 1) before deposition of the ferricrete; 2) after deposition of the ferricrete and before deposition of the lower alluvial fan gravel; 3) after deposition of the lower alluvial fan gravel and before deposition of the upper alluvial fan gravel (this study). Although the alluvial fan gravels are poorly indurated, they are somewhat resistant to erosion and hold up open cuts such as the 100 m-tall highwall in gravel in the north wall of the Main pit (Fig 18A). The gravel units are not differentiated on Plate 1.

Figure 19 is a structure contour map, prepared for this study, of the unconformity surface at the base of the basin-fill deposits in the Mangas half graben. The map is based on 202 Phelps Dodge exploratory drill holes that penetrated the gravel in Mangas Valley. Structure contours indicate the unconformity surface has an average northeast dip of 10-12°, from an elevation of about 1,900 m (6,250 ft) at the mine to an elevation of 1,460-1,490 m (4,800-4,900 ft) near the Mangas fault in the deepest part of the basin. The unconformity surface is highly irregular, and steeper northeast dips are common locally, especially within paleochannels and along late-stage faults such as the Burro Chief and Town Fault zones (Fig 19).

The description of the ferricrete that follows is from this study. Descriptions of the alluvial fan gravel units are from Griffin (2001) and Mack and Stout (2005).

Ferricrete

The ferricrete unit at the base of the basin-fill gravels is 0-55 m (0-180 ft) thick, and consists of conglomerate and sedimentary breccia. The thickest preserved sections of ferricrete occupy northeast-trending paleochannels cut into the Tyrone stock, Proterozoic granite, and Oligocene tuffs (Figs. 18, 20-22). Paleochannels are controlled by northeast-striking faults and

lithologic contacts in the mine area (Fig. 19). Erosion of the ferricrete prior to deposition of the overlying alluvial fan gravel removed most of the ferricrete except for the thicker, more resistant deposits in the paleochannels (Fig. 20). Surface exposures of the ferricrete extend 3.2 km (2 mi) northeast of the mine into the southern Little Burro Mountains (Figs. 21 and 22, Plt. 1).

Ferricrete in the paleochannels consists of dark red to brownish-red, poorly-sorted, massive to thick-bedded, clast-supported, coarse angular conglomerate and breccia with some medium- to coarse-grained, planar- and cross-bedded lithic sandstone beds and lenses that show graded bedding (Figs. 21 and 22). Clasts are mostly <20 cm in length but range up to 120 cm. The clasts consist dominantly of porphyry from the Tyrone stock, many eroded from the leached cap and containing limonitic boxworks, but they also include granite and andesite. The ferricrete is cemented by hematite, chalcedony, and K-Mn oxides. A peculiar feature of the ferricrete is sieve texture in which clast-supported conglomerate contains no matrix. This texture formed either by dissolution of the matrix by acidic solutions after deposition, or nondeposition/ flushing of matrix during deposition. Cross bedding and graded bedding in the sandstone beds indicate a fluvial origin for the ferricrete. The ferricrete accumulated along the eastern margin of the Big Burro Mountains uplift (western margin of the San Vicente basin) during Miocene erosion of the Tyrone deposit.

The unconformity at the top of the ferricrete is exposed in the north walls of the Main, Savanna, and Gettysburg pits, where semiconsolidated alluvial fan gravel fills channels cut into the ferricrete (Figs. 18A and 20). Where alluvial fan gravel overlies the ferricrete, the basal part of the alluvial fan gravel is commonly stained by a dispersion halo of goethite (Fig. 20). The goethitic halo is probably due to dissolution and remobilization of iron in the ferricrete by groundwater, and transport of iron into the overlying alluvial fan gravel by capillary action (W. Seibert, pers. comm., 2006).

The structure contour map of the base of the basin-fill deposits (Fig. 19) shows a number of northeast-trending paleochannels. One of the largest paleochannels is exposed in the north wall of the Main Pit (Fig. 18A). Remnants of this paleochannel also occur at the crest of the southern Little Burro Mountains 1,500-2,400 m (5,000-8,000 ft) northeast of the Main pit (Plt. 1) where the ferricrete is about 15 m (50 ft) thick. The same paleochannel was intersected under 90 m (295 ft) of alluvial fan gravel in AMAX drill hole NXBM-6 north of Tyrone Peak, where the ferricrete is 11 m (35 ft) thick (see Fig. 42 for the location of drill hole NXBM-6).

X-ray diffraction analysis conducted for this study of ferricrete cement from a paleochannel deposit in the southern Little Burro Mountains revealed the mineral cryptomelane ($K(Mn^{2+},Mn^{4+})_8O_{16}$). This material yielded a $^{40}Ar/^{39}Ar$ age of 12.06 ± 0.14 Ma (Table 2), which is a minimum age for the ferricrete, but probably is a close approximation to the time of deposition of the ferricrete. As shown on Plates 1 and 2, the Mangas fault offsets the ferricrete-filled paleochannels. The ferricrete thus predates displacement on the Mangas fault, which probably began in the latest Miocene-early Pliocene (Fig. 9). However, the northeast trends of the paleochannels show that they were formed after the beginning of uplift and northeast tilting of the Big Burro Mountains uplift on Basin and Range normal faults in the Miocene.

Lower Alluvial Fan Gravel Unit

Griffin (2001) divided the semiconsolidated alluvial fan gravel into upper and lower units based on color, paleocurrent directions, and source areas of detritus. The lower gravel unit was deposited at the western margin of the San Vicente basin, a wide, shallow, northwest-trending, northeast-tilted half graben that borders the Big Burro Mountains uplift (Fig. 1). The San Vicente Basin extends as far eastward as the Silver City Range and is bounded on the east by the Treasure Mountain fault (Fig. 10) (Mack, 2004). The Big Burro Mountains uplift and the San Vicente half graben were formed by displacement on the Treasure Mountain and Knight Peak faults in the Miocene (Fig. 10) (Mack, 2004).

In the Tyrone area, the lower gravel unit is late Miocene-early Pliocene in age (this study), and contains clasts derived mostly from the Big Burro Mountains (Griffin, 2001). The lower gravel unit is light tan to pink and consists dominantly of matrix-supported, poorly-sorted coarse gravel with a coarse-grained sandy matrix (Griffin, 2001). Clasts are dominated by quartz monzonite, granite, and diorite derived from the Big Burro Mountains to the west, and the unit fines eastward from the Big Burro Mountains (Griffin, 2001). Dips in the lower unit within the Mangas half graben are typically 10-15° to the northeast (Plt. 1). The lower unit attains a thickness of 640 m (2,100 ft) in a drill hole approximately 4 km (2.5 mi) northeast of the Little Burro Mountains (Griffin, 2001). The Mangas basin narrows to the north of Tyrone, and in the vicinity of the Silver City Range the lower unit contains clasts derived from both the Big Burro Mountains and the Silver City/Pinos Altos Range (Fig. 1) (Mack and Stout, 2005). The lower gravel unit was truncated by uplift of the Little Burro Mountains on the Mangas fault in the latest Miocene-early Pliocene.

Upper Alluvial Fan Gravel Unit

The upper alluvial fan gravel unit unconformably overlies the lower alluvial fan gravel unit and was deposited in the Pliocene-Pleistocene during and following uplift of the Little Burro Mountains along the Mangas fault (Figs. 1 and 11). The upper gravel is a local unit in the Mangas half graben, and extends only as far southwestward as the axis of the Mangas Valley (Griffin, 2001). The unit is reddish-orange to reddish-brown and consists of very poorly sorted, matrix-supported coarse gravel in a matrix ranging from coarse sand to clay. Clasts include granite, andesite, shale, limestone, rhyolite, basalt, and quartz monzonite, all derived from the Little Burro Mountains (Griffin, 2001).

Both the lower and upper alluvial fan gravel units contain calcic paleosols that indicate hiatuses and a climate prone to long, dry periods (Griffin, 2001). Rare, thin (1-2 m (3-6 ft) thick) tuff beds occur in the lower gravel unit in the vicinity of the Tyrone mine. Basalt flows of

probable Pliocene age cap alluvial fan gravel in Mangas Valley, 10 km (6 mi) northwest of the Tyrone mine (Hedlund, 1985). These flows may represent fissure eruptions along the Mangas fault (Hedlund, 1985). Attempts to date the tuff horizon and the overlying basalt by $^{40}Ar/^{39}Ar$ proved unsuccessful (DuHamel et al., 1995; Griffin, 2001).

Diabase Dikes

Diabase dikes (Tdb) intrude Eocene and Oligocene rocks throughout the map area (Plt. 1). The age of the diabase dikes is uncertain; however, some dikes were emplaced along faults that cut the alluvial fan gravel. The diabase dikes are typically only a few meters thick but range up to ~25 m (~80 ft). Diabase is dark green to greenish-gray and brown, porphyritic, and slightly vesicular, with a subophitic texture. Phenocrysts consist of plagioclase (~2%), clinopyroxene (6-10%), and hornblende (1-2%), with accessory magnetite (Table 1). The diabase is typically altered to propylitic assemblages.

STRUCTURAL GEOLOGY

The southern part of the Little Burro Mountains and the Tyrone district are characterized by several generations of crosscutting, northwest- and northeast-striking, high-angle faults. Dominantly northwest-striking fractures and faults of Precambrian age, as reflected by orientations of Proterozoic diabase dikes, are offset by Laramide-aged northeast- and east-northeast-striking faults (Gillerman, 1970; Hedlund, 1985). These are in turn offset by northwest-striking Basin and Range normal faults, many of which have large displacements. Northeast- and east-northeast-striking Laramide faults underwent recurrent displacements that pre-date and post-date intrusion of the Tyrone stock (Gillerman, 1970; Hedlund, 1985).

Precambrian Faults

Several northwest-striking faults occupied by Proterozoic diabase dikes occur in Burro Mountain granite in the footwall of the Cedar Canyon fault (Plt. 1). These faults strike ~N70°W

and dip 45 to 70° to the northeast. A few faults filled with Proterozoic diabase dikes strike northeast (N20-25°E), and dip southeast to northwest at ~60-70°. Many of the northeast-striking faults are silicified and have quartz veins along them.

Laramide Faults

Numerous northeast- and east-northeast-striking Laramide faults occur in the southern part of the Little Burro Mountains. Prominent among these are the Southern Star, Cedar Canyon, and Contact faults which have normal displacements of 100 m (330 ft) or more based on offset of stratigraphic units (Plts 1 and 2) . The northeast- and east-northeast-striking faults typically have normal displacements of 60 m (200 ft) or less (Plts. 1 and 2).

Several of the northeast-striking faults host silver, gold, and base-metal vein deposits associated with the Tyrone stock (Hedlund, 1985). Faults hosting veins include the Contact fault and faults immediately east of the Cedar Canyon fault, such as those at the Silver King-Mystery and Afternoon mines. The host rocks for vein deposits are Proterozoic granite, shale and sandstone of the Colorado Formation, and Upper Cretaceous-Paleocene andesite.

Some of the northeast-striking Laramide faults offset upper Eocene-Oligocene volcanic rocks, indicating they were reactivated in the Miocene (?). Only a few of the faults, such as the Southern Star and Indian Peak faults in the southern Little Burro Mountains and the Burro Chief fault in the Big Burro Mountains, cut alluvial fan gravel (Fig. 4).

Southern Star Fault

Mapping and drill hole data indicate that a major east-northeast striking normal fault occurs 1,100 m (3,600 ft) southeast of Indian Peak (Plts. 1 and 2, Fig. 4) and is partly buried beneath alluvial fan gravel and landslide deposits. The fault juxtaposes 480 m (1,570 ft) of upper Eocene-Oligocene tuff in the hangingwall (Amax drill hole NXBM-1; see Plate 2) against Stage 2 monzonite porphyry in the footwall. This fault lies along the eastern projection of the Southern Star fault in the Big Burro Mountains (Fig. 4), a major east-northeast-striking normal fault that

juxtaposes Proterozoic granite against the lower alluvial fan gravel (Figs. 4 and 5). The Southern Star fault in the Big Burro Mountains dips 57° north and exhibits 306 m (1,005 ft) or more of displacement based on thickness of gravel in drill holes in the hangingwall of the fault (Hedlund, 1985). The Mangas Valley widens from 2 km (1.2 mi) south of the Southern Star fault to over 5 km (3 mi) north of the fault (Fig. 4). However, there is no discernible offset of the Mangas fault across the projection of the Southern Star fault.

Preservation of the thick section of upper Eocene-Oligocene tuffs in the hangingwall of the Southern Star fault in the Little Burro Mountains and the straight trace of the Mangas fault indicate that major displacement on the Southern Star fault occurred prior to movement on the Mangas fault and uplift and erosion of the Big Burro Mountains. However, tuff units have not been encountered in deep drill holes in Mangas Valley in the projected hangingwall of the Southern Star fault. The first bedrock units encountered in Mangas Valley are Upper Cretaceous-Paleocene andesite, intrusive rocks of the Tyrone stock, and Proterozoic granite (Plts. 1 and 2). Upper Eocene-Oligocene tuff units do occur as fault slivers along the Mangas fault southwest of Indian Peak (Plt. 1). Therefore, tuff units extended at least as far westward as the position of the Mangas fault before displacement on the Mangas fault in the latest Miocene-early Pliocene. A pinchout of the tuff units probably occurs in the Mangas half graben to the northeast of the Mangas Creek Road (Plts. 1 and 2).

The intersection of the Mangas and Southern Star faults is concealed by alluvial fan gravel so it is unclear whether or not the Southern Star fault offsets the Mangas fault. Furthermore, the interaction of the Southern Star and Burro Chief faults is unknown (Fig. 4). If the Southern Star fault extends across Mangas Valley from the Big Burro Mountains, it shows very little post-alluvial fan gravel displacement. Structure contours at the base of the gravel on Figure 19 are not strongly deflected across the projection of the fault. Furthermore, only minor post-alluvial fan gravel displacement is seen in cross section A-A' (Plts. 1 and 2) constructed

across the projection of the fault. Drill hole T-62 on cross section A-A' intersects a fault along the projection of the Southern Star fault, and this fault shows only 60 m (200 ft) or less of post-alluvial fan gravel displacement.

The contrast of a large amount of post-alluvial fan gravel displacement on the western portion of the Southern Star fault in the Big Burro Mountains and little or no post-alluvial fan gravel displacement on the projected eastern part of the fault may be explained by linking of normal faults in the Mangas half graben during the Pliocene-Pleistocene. The Southern Star fault may have been linked with the Burro Chief and Town faults as these faults form the western margin of a graben within the Mangas half graben (Fig. 4; cross section A-A', Plt. 2). It is possible that the Southern Star fault is a Laramide structure that facilitated intrusion of the Tyrone stock, and was then reactivated during Basin and Range extension.

Contact Fault

The Contact fault hosts silver and base-metal vein deposits in the Contact and Virtue mines (Plt. 1) (Hedlund, 1985). The fault strikes N17-18°E, dips 76-80° east, and is characterized by quartz veins and a zone of mineralized breccia and gouge, 3-9 m (10-30 ft) wide. The Contact fault has 100-120 m (330-400 ft) of normal displacement based on juxtaposition of Upper Cretaceous formations and Proterozoic granite along the fault. Gillerman (1964) and Paige (1911) did not note post-mineral brecciation in their descriptions of base metal vein deposits in the Contact mine by, so the latest movement was probably during the Laramide orogeny.

Cedar Canyon Fault

The Cedar Canyon fault is parallel to and ~180 m (600 ft) east of the Contact fault (Plt. 1). The Cedar Canyon fault strikes N04-20°E, dips 77-85° east, and has at least 320 m (1040 ft) of normal displacement based on the thickness of Upper Cretaceous-Paleocene andesite encountered in drill hole IP-1 (Plt. 2, cross section B-B'). The fault surface is well exposed at the

mouth of Cedar Canyon and exhibits vertical striations and ~4 m (12 ft) wide zone of silicified breccia and gouge in Upper Cretaceous-Paleocene andesite.

Indian Peak Fault

The Indian Peak fault is the only northeast-striking fault in the southern part of the Little Burro Mountains that clearly offsets the Mangas fault (Plt. 1). The Indian Peak fault strikes N52°E, dips 86° southeast, and exhibits about 80 m (250 ft) of normal displacement based on offset of the Bell Top Formation. The Indian Peak fault is along the projected strike of the Burro Chief fault in the Big Burro Mountains and may be a continuation of Burro Chief fault (Fig. 4). The Burro Chief fault is discussed below in the chapter on the geology of the Tyrone mine.

Basin and Range Faults

Northwest-striking Basin and Range normal faults offset basin-fill alluvial fan gravel units, and, except for the Indian Peak and Burro Chief faults, are the youngest faults in the southern part of the Little Burro Mountains. Basin and Range faults include the Mangas fault, Town fault, and a prominent fault north of Tyrone Peak, herein named the Tyrone Peak fault (Plt. 1).

Mangas Fault

Displacement on the Mangas fault resulted in uplift of the Little Burro Mountains and formed the Mangas half graben. The Mangas fault forms the southwest-facing scarp of the Little Burro Mountains and extends at least 38 km (24 mi) along strike (Fig. 1) (Drewes et al., 1985). In the map area, the fault strikes N40°W and dips 63-80° southwest (Fig 4, Plt 1). At least 460 m (1,400 ft) of dip-slip displacement on the fault is indicated by dips of volcanic rocks in the upthrown block, and the thickness of alluvial fan gravel (370 m (1200 ft)) penetrated by drilling in Mangas Valley (Plt. 2). Tilting of the Tyrone copper deposit along the Mangas fault is illustrated by the 7-9° northeast tilt of the chalcocite blanket in the Main pit (Fig. 23, sec. H-H'),

and the 10-12° northeast tilt of the Mangas half graben indicated by structure contours on the unconformity surface at the base of the basin-fill deposits (Fig. 19).

The Mangas fault offsets all basin-fill gravel units including the upper alluvial fan gravel. Mack (2004) placed the age of the Mangas fault as early Pliocene, associated with the second phase of normal faulting that began at ~6-5 Ma in the Basin and Range province (Figs. 9 and 11). The fault has probably experienced repeated movements since the Pliocene, as evidenced by pulses of sedimentation in the upper alluvial fan gravel (this study; Griffin, 2001).

Tyrone Peak Fault

The Tyrone Peak fault occurs on the northeast side of Tyrone Peak and juxtaposes volcaniclastic rocks of the Sugarlump Tuff against the Rubio Peak Formation (Plt. 1). It has at least 150 m (500 ft) of normal displacement. The Tyrone Peak fault must have experienced early Miocene displacement like the Southern Star fault because it preserves a thick sequence of upper Eocene-Oligocene volcanic rocks in its hangingwall. AMAX hole NXBM-6, drilled in the hangingwall of the fault approximately 550 m (1,800 ft) from the fault trace (see Fig. 42 for location), terminated in tuff at a depth of 405 m (1,328 ft).

Bedding Orientations

One of the goals of mapping in the southern part of the Little Burro Mountains was to identify angular unconformities or dip fanning in the upper Eocene-Oligocene section that would provide evidence for extensional faulting and uplift events prior to the onset of Basin and Range faulting in the early Miocene. However, no evidence was found in the upper Eocene-Oligocene section in the map area for dip fanning or angular unconformities. The only sedimentary unit that marks a clear erosional event between volcanic units is the ferruginous sandstone and conglomerate. Tuffs underlying and overlying this unconformity (Bell Top Formation, Sugarlump Tuff, respectively) show no discernible change in dip across the unconformity surface (Plt.1). Furthermore, Hedlund (1978b, d) noted no angular unconformities or discordances in the

upper Eocene-Oligocene section in the northern part of the Little Burro Mountains. The upper Eocene-Oligocene section in the southern part of the Little Burro Mountains dips 10-33° to the northeast (average 20-25°) with no consistent variations up or down section. The Upper Cretaceous Colorado Formation has similar dips of 10-30° to the northeast (Plt. 1).

The Miocene-Pleistocene basin-fill deposits in Mangas Valley typically dip10-15° to the northeast, somewhat less than the dip of the upper Eocene-Oligocene rocks in the southern Little Burro Mountains. Thus, an angular unconformity separates the upper Eocene-Oligocene rocks from the younger basin-fill sediments.

Table 1. Mesozoic and Cenozoic igneous rocks in the southern Little Burro Mountains and Tyrone district.

Formation	Symbol	Rock Type/Description	Phenocrysts, Crystals, and Clasts	Groundmass/Texture	Accessory Minerals	Reference
—	Tdb	Dk green to greenish-gray and brown porphyritic diabase dikes, slightly vesicular	Phenos: 2% plag (0.1-2 mm), 6-10% cpx (0.2-4 mm), 1-2% hbl (0.1-2 mm)	Pilotaxitic to trachytic, subophitic	1-3% mt (0.01-2 mm)	
—	Tbu	Dk gray to brown porphyritic basaltic andesite, vesicular and amygdaloidal	Phenos: 15-20% and (0.2-2 mm), 6-7% cpx (0.1-8 mm), 5-8% ol (0.1-2 mm) altered to iddingsite	Pilotaxitic to intersertal	2-3% mt (0.05-0.5 mm)	
Caballo Blanco Tuff	Tcb	Lt gray to pink, moderaly-welded, crystal-vitric rhyolite ash-flow tuff	Crystals: 10-18% qtz (0.1-5mm), 7-9% olig (0.1-2 mm), 3-6% san (0.1-4 mm), 0.5-2% bio (0.1-2mm); also as much as 10% pumice and lithic fragments	Eutaxitic, devitrified glass shards, axiolitic	<1% mt (0.1-3 mm)	
—	Tba	Dk reddish-brown porphyritic basaltic andesite, vesicular	Phenos: 2% hornblende (0.2-2 mm) and 1-2% olivine (0.1-1 mm) altered to iddingsite	Trachytic, intersertal	1% mt (0.05-0.3 mm)	
—	Tir	Grayish-brown, dense, flow-banded rhyolite dikes, sparse phenocrysts	Phenos: 0.5-1% plag (0.3-3 mm), 0.5-1% qtz (0.5-2 mm), tr san (0.1-2 mm), tr bio (0.1-2 mm)	Finely banded/laminated, devitrified, cryptocrystalline	Tr mt (0.05-0.2 mm), tr zr (0.05-0.1 mm)	
Sugarlump Tuff	Tsv	White, pink and green volcaniclastic rocks consisting of massive to thick-bedded, poorly-sorted tuffaceous debris flow deposits, air-fall tuff, and tuffaceous sandstone and conglomerate	80-85% devitrified tuff lapilli and ash, 10-15% lithic clasts up to 50 cm (mostly 2-10 mm), <5% crystals (san, plag, qtz, bio) to ~3 mm	Matrix of devitrified ash and tuff lapilli		
Sugarlump Tuff	Tsa	White to pink, poorly indurated, thin planar-bedded rhyolite to latite air-fall tuff and cross-bedded tuffaceous sandstone	70-80% devitrified tuff lapilli (2-20 mm), 8-10% accessory lithic clasts to ~6 mm, 4-6% crystals (san, olig, qtz, bio) to ~3 mm	Devitrified ash and tuff lapilli		
Bell Top Formation tuff member 3	Tbt	Pink, orange, and gray, poorly to moderately-welded, vitric rhyolite ash-flow	Crystals: 2-3% san (0.2-3 mm), 0.5-1% qtz (0.1-2 mm), 1-2% bio (0.1-2 mm); ~5-10% pumice fragments	Devitrified glass shards, locally eutaxitic, axiolitic	Tr mt (0.05-0.6 mm), tr zr	
Rubio Peak Formation	Trp	Lt gray, pink and purple, porphyritic rhyodacite ash-flow tuff, flows, and breccia	Crystals: Tuff- 6-20% plg (0.1-4 mm), 5-7% qtz (0.2-3 mm), 2-3% bio (0.2-2 mm), <1% hbl (0.3-2 mm), 5-20% pumice and lithic fragments; Phenos: Flows- 20-35% plag (0.1-10 mm), 1-4% qtz (0.1-3 mm), 2-4% bio+hbl (0.2-4 mm)	Microcrystalline to crypto-crystalline, devitrified glass, eutaxitic, rheomorphic	Tr ap (0.1-0.4 mm), 0.5-1% mt (0.01-0.2 mm), tr zr	
Tyrone stock - Stage 5	Trdp	Lt gray to pink, flow-banded rhyodacite porphyry plugs	Phenos: 15-25% olig (0.1-12 mm), 4-8% qtz (0.1-8 mm), 3-5% bio (0.1-3 mm); 2-4% ortho (1-9 mm)	Flow banded, glassy to microcrystalline	<1% mt (0.05-0.5 mm), tr ap, tr sph	
Tyrone stock - Stage 4	Tlqmp	Light gray qtz monzonite porphyry	Phenos: 20-40% plag (1-4 mm), 10-15% ortho (1-4 mm), 5-10% qtz (2-10 mm), 4-8% bio + hbl, 5% ortho megacrysts to 40 mm	Granophyric		Phelps Dodge, 2002
Tyrone stock - Stage 3	Tqmp	Tan to lt gray qtz monzonite porphyry	Phenos: 20-25% olig (0.1-9 mm), 3-6% qtz, (0.1-4 mm), 3-5% bio (0.1-4 mm), 1-3% ortho (0.5-2 mm), 1-2% hbl (0.4-5 mm), locally 3-4% ortho megacrysts to 12 mm	Microcrystalline to crypto-crystalline	0.5-1% ap (0.05-0.4 mm), tr mt (0.05-0.3 mm), tr zr (0.01-0.2 mm)	
Tyrone stock - Stage 2	Tmp	Lt greenish-gray monzonite porphyry	Phenos: 30-40% olig (0.1-10 mm), <1-3% qtz (0.1-3 mm), 1-3% bio (0.2-3 mm), 1-2% hbl (0.2-1 mm)	Microcrystalline to crypto-crystalline, locally flow-banded	1-2% mt (0.01-1.4 mm), <1% ap (0.1-0.7 mm)	
Tyrone stock - Stage 1		Light gray, equigranular to porphyritic granodiorite and qtz diorite	Phenos: 25-45% plag (1-4 mm), 5-10% ortho (1-5 mm), 3-5% bio, 1-2% qtz (1-3 mm)	Aphanitic to granophyric		Phelps Dodge, 2002
—	TKl	Lt greenish-gray to tan latite porphyry sills and dikes	Phenos: 15-25% olig (0.2-11 mm), 4-6% bio (0.1-5 mm), 2-3% hbl (0.1-2 mm), 0.5-3% qtz (0.5-3mm)	Microcrystalline	<1% mt (0.01-6 mm), <1% ap (0.01-0.7 mm)	
—	Tka	Dk greenish-gray porphyritic andesite and dacite flows and breccia, lahar deposits	Phenos: 20-30% and (0.3-3 mm), 4-7% cpx + hbl (0.1-3 mm); also 1-2% qtz (0.5-2 mm) in dacite	Pilotaxitic to intergranular	2% mt (0.02-0.8 mm), <1% ap (0.02-0.4 mm)	

Abbreviations: and - andesine, ap - apatite, bio - biotite, cpx - clinopyroxene, hbl - hornblende, mt - magnetite, ol - olivine, olig - oligoclase, ortho - orthoclase, phenos - phenocrysts, plag - plagioclase, qtz - quartz, san - sanidine, sph - sphene, tr - trace, zr - zircon

Table 2. Summary of $^{40}Ar/^{39}Ar$ dates for igneous rocks and ferricrete in the southern Little Burro Mountains, analytical error one sigma

Sample No.	Total Gas Age, Ma	Plateau Age, Ma	Isochron Age, Ma	Mineral	Location	Description
61-7			35.73 ± 0.09	Sanidine	T19S, R15W, SW¼ NE¼ Sec 11	Bell Top Formation tuff member 3 (Tbt)
89-5	54.61 ± 0.81	54.43 ± 0.81	54.1 ± 0.6	Plagioclase	T19S, R14W, SW¼ SW¼ Sec 7	Rhyodacite porphyry plug (Trdp)
89-8	31.54 ± 0.38	31.55 ± 0.39	31.6 ± 0.36	Plagioclase	T19S, R14W, NE¼ SE¼ Sec 7	Caballo Blanco Tuff (Tcb)
817-1	12.06 ± 0.14			Cryptomelane	T19S, R15W, NW¼ NE¼ Sec 13	Ferricrete (Tf)

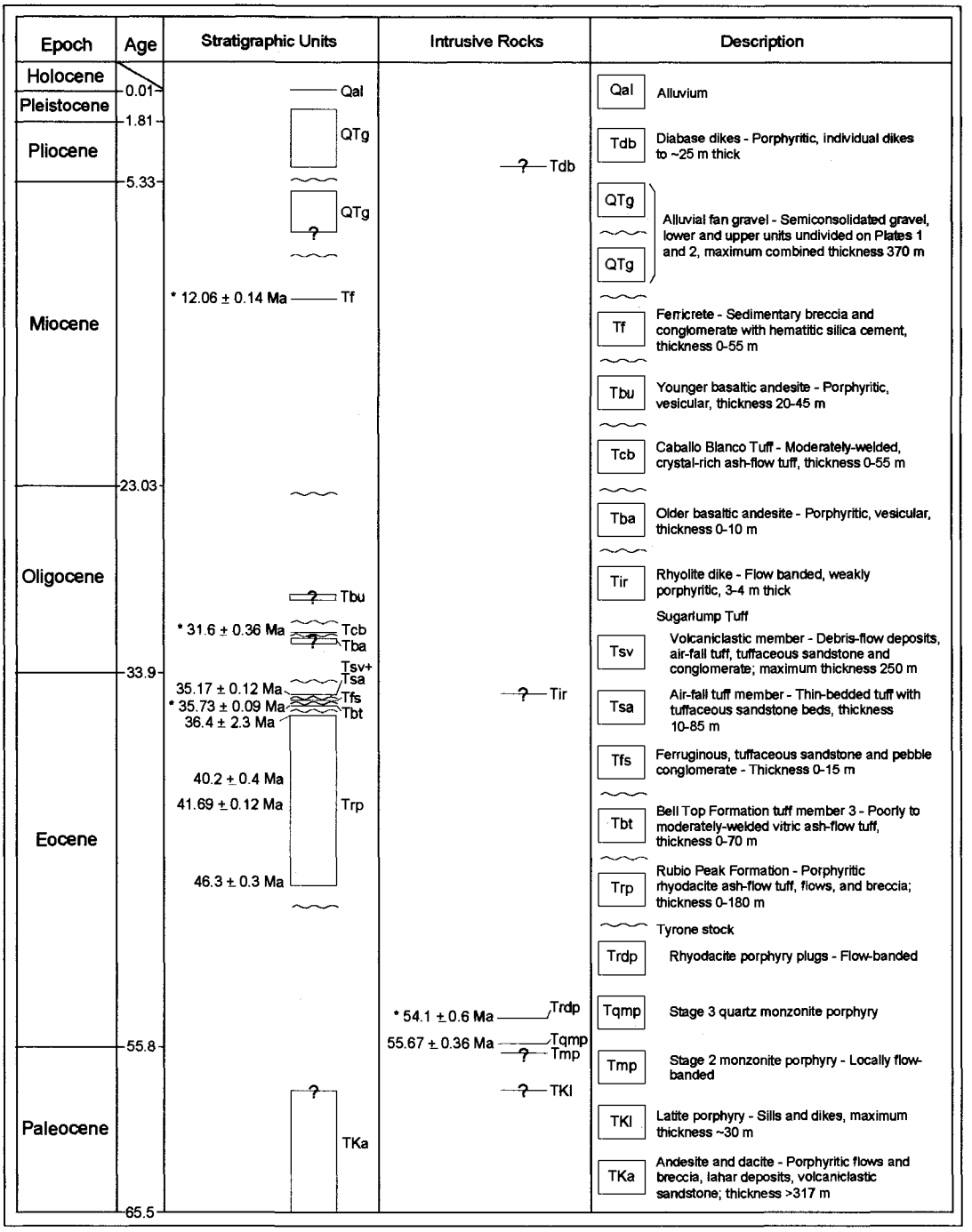

Figure 12. Chronostratigraphic and lithostratigraphic diagram for Cenozoic units in the southern part of the Little Burro Mountains, showing $^{40}Ar/^{39}Ar$ ages. Symbols are the same as those used on Plates 1 and 2. $^{40}Ar/^{39}Ar$ ages from this study are designated by an asterisk. The published $^{40}Ar/^{39}Ar$ age for the upper Sugarlump Tuff (Tsv) is from McIntosh et al. (1990) for exposures in the Black Hill area 18 km (11 mi) southeast of Silver City. Published $^{40}Ar/^{39}Ar$ ages for Rubio Peak Formation (Trp) are from MacMillan (2004) for exposures in the Good Sight Mountains and Cookes Range. The age for Stage 3 monzonite porphyry (Tqmp) was provided by R. Stegen (pers. comm., 2003). Time scale from International Commission on Stratigraphy (2008).

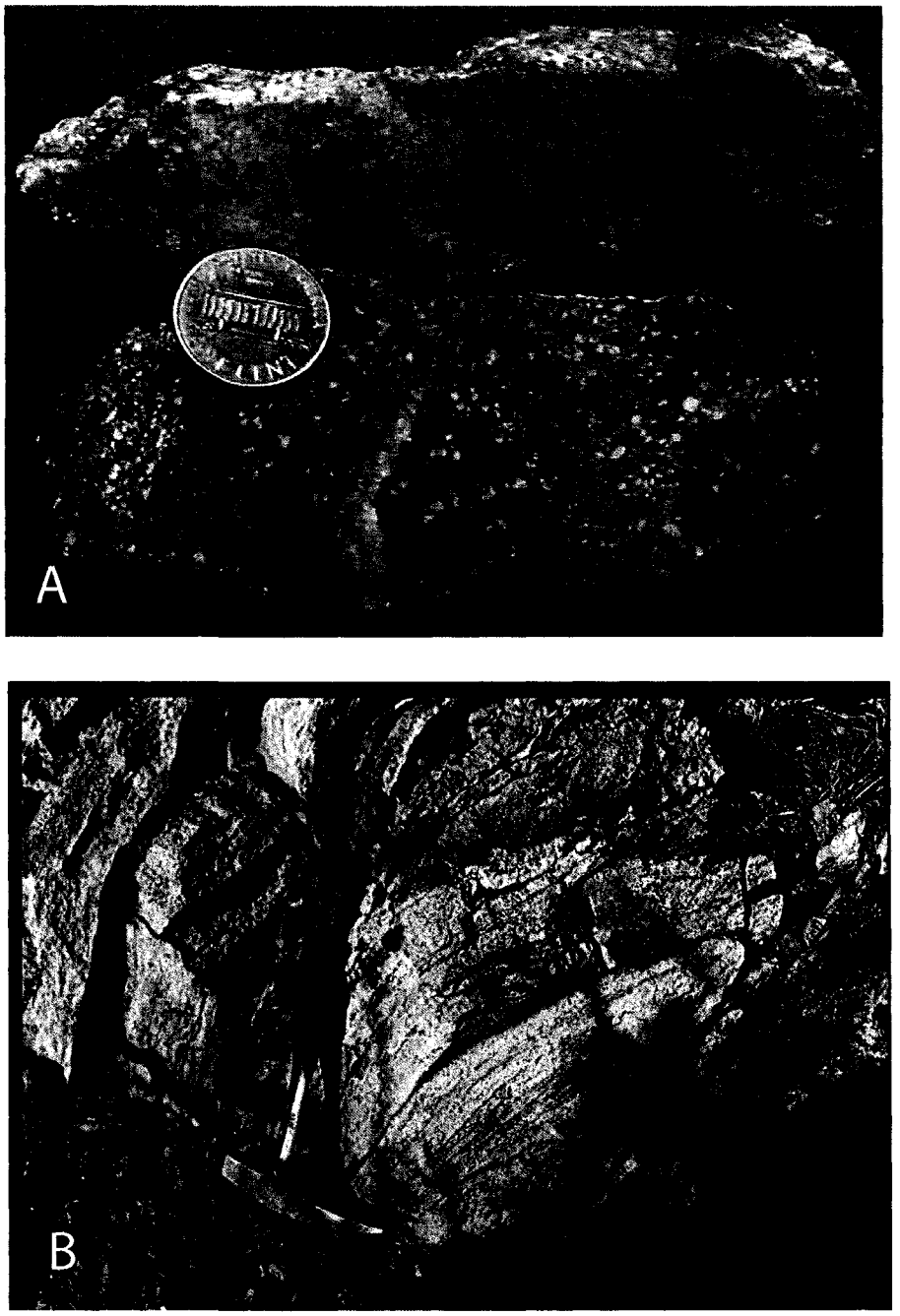

Figure 13. Rubio Peak Formation, Tyrone Peak. A. Rhyodacite ash-flow tuff contains abundant pumice fragments and crystal fragments of plagioclase, biotite, and quartz. The tuff is argillized and weakly silicified. B. Rheomorphically-folded ash-flow tuff.

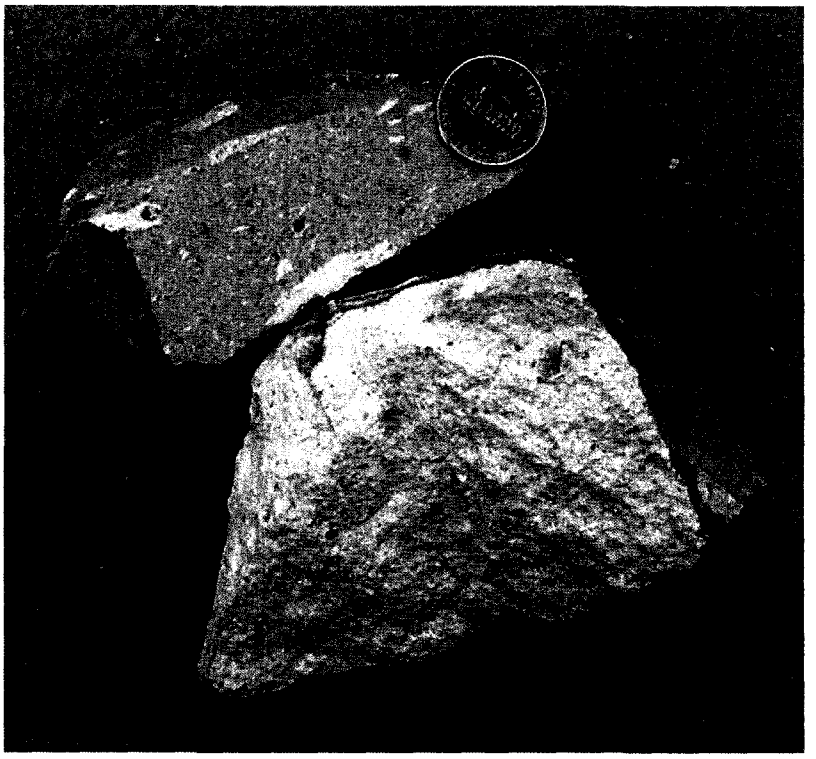

Figure 14. Tuff member 3 of the Bell Top Formation; poorly- to moderately-welded vitric ash-flow tuff contains 4% sanidine and trace quartz crystal fragments, and locally ~8% flattened pumice fragments.

A

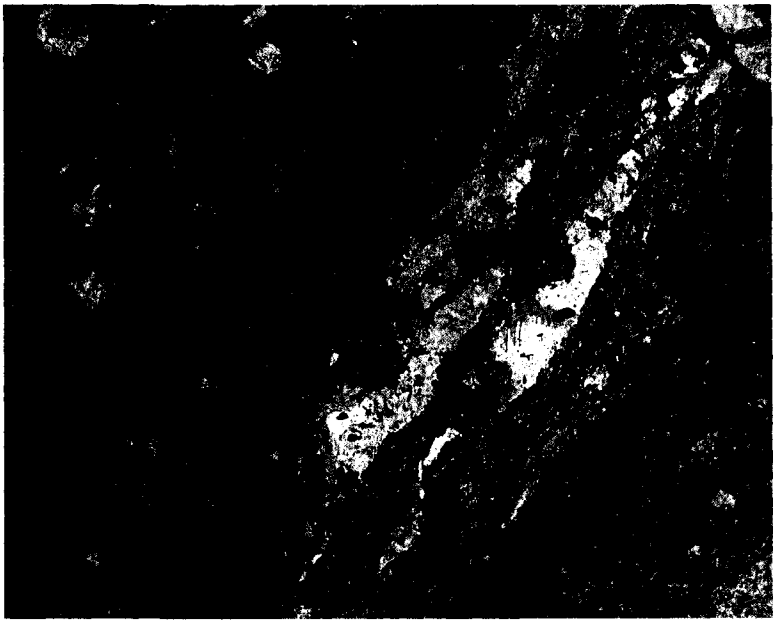

B

Figure 15. A. Upper Eocene ferruginous sandstone and conglomerate in the southern part of the Little Burro Mountains. At this location, the conglomerate fills a channel cut into Upper Cretaceous-Paleocene andesite. B. Photomicrograph of clast of altered, quartz-veined porphyry from ferruginous conglomerate. Field of view = 0.85 mm.

A

B

Figure 16. Sugarlump Tuff in the southern Little Burro Mountains. A. Thin-bedded air-fall tuff, locally contains cross-bedded tuffaceous sandstone. B. Volcaniclastic rocks consisting mostly of mudflow deposits containing large, angular clasts of flow-banded rhyolite in a matrix of rhyolite lapilli tuff.

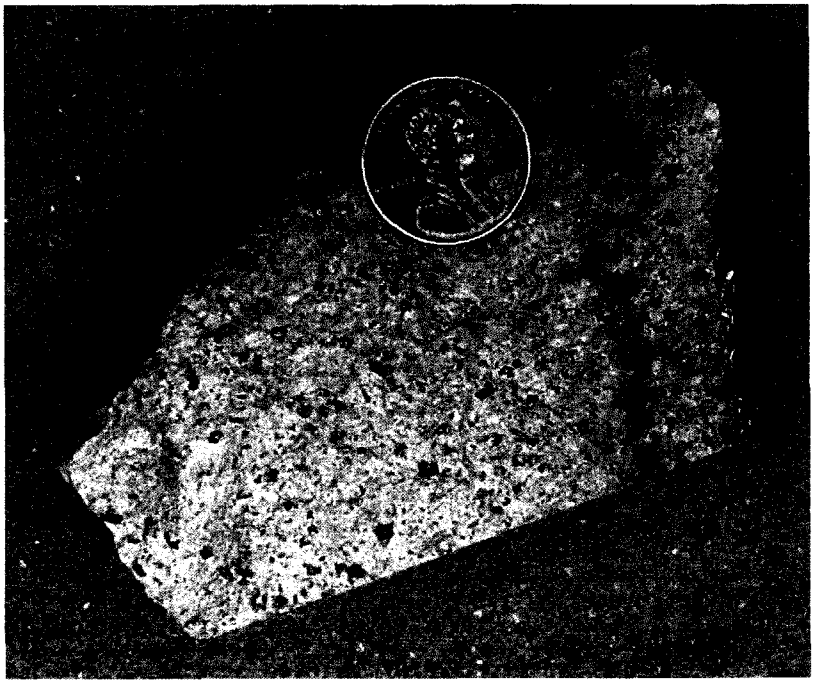

Figure 17. Caballo Blanco Tuff; moderately-welded, crystal-rich ash-flow tuff with ~35% phenocrysts of quartz, plagioclase, sanidine, and biotite.

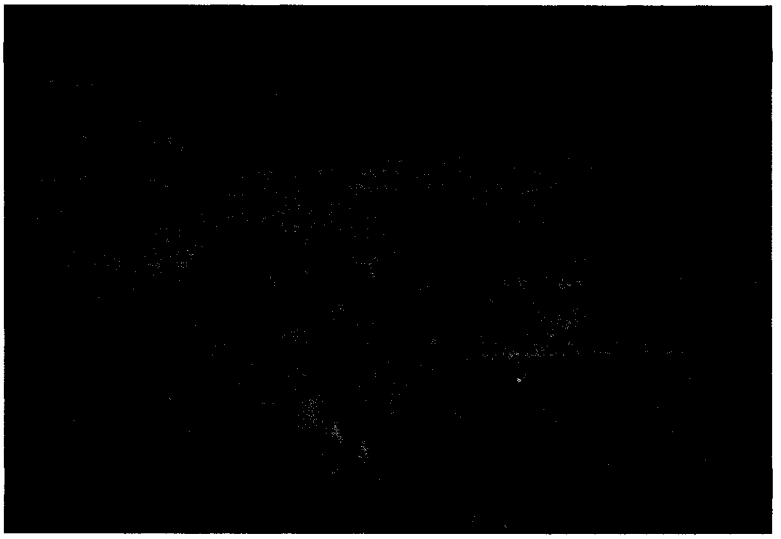

A

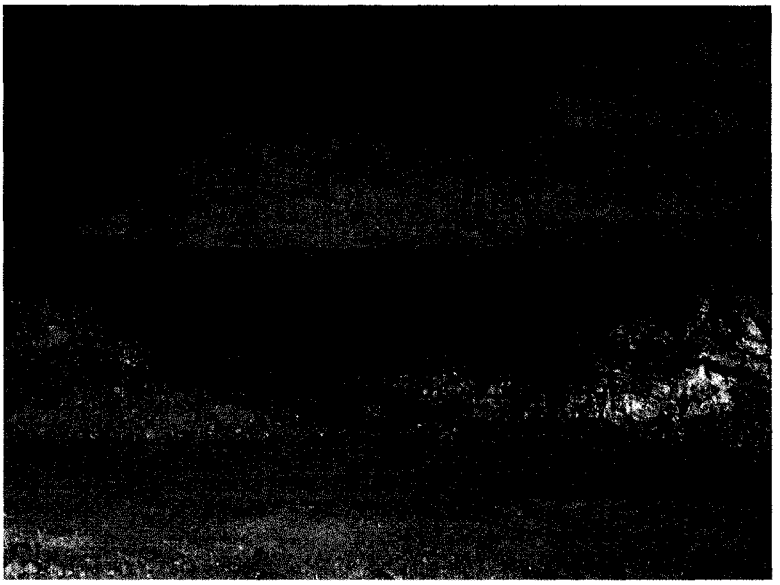

B

Figure 18. Miocene ferricrete paleochannel deposits in the Tyrone mine. A. Main pit looking northeast, bench height 15 m (50 ft). Paleochannel deposit (red) about 24 m (80 ft) thick lies on an erosion surface cut into sericitized and argillized Stage 3 quartz monzonite porphyry. The ferricrete is overlain along an erosional contact by the lower semiconsolidated alluvial fan gravel unit (tan), about 98 m (320 ft) thick. Brown material above the gravel is mine dump. A thin remnant of ferricrete can also be seen at the bedrock surface to the right of the paleochannel. B. Savanna pit looking northeast. Close-up of ferricrete deposit about 9 m (30 ft) thick filling paleochannel cut into argillized Stage 3 quartz monzonite porphyry. Note dispersion halo of yellow goethite in the porphyry bedrock. Photo by Bill Seibert.

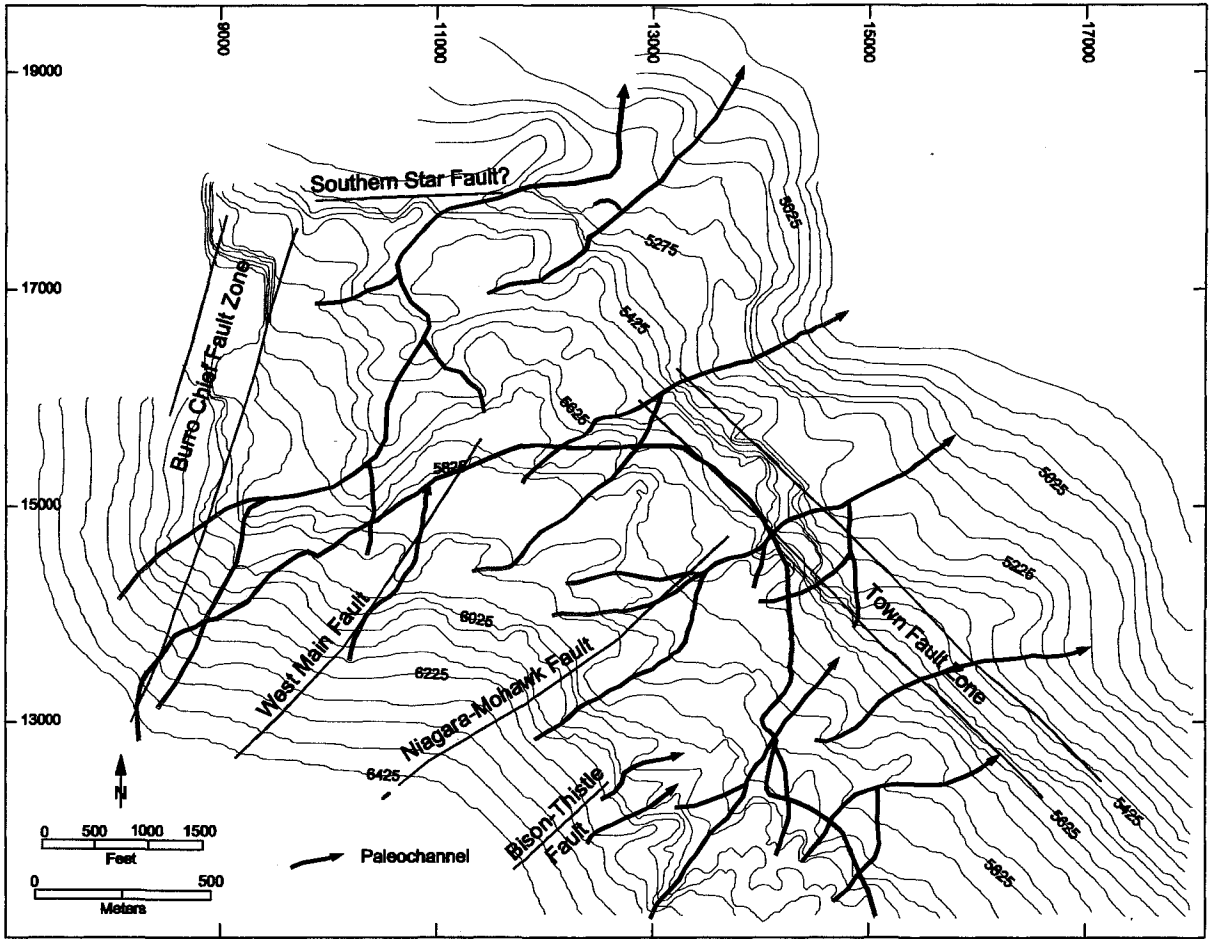

Figure 19. Structure contour map of the base of basin-fill deposits in Mangas Valley, constructed using data from 202 drill holes. Paleochannels are marked by blue lines with arrows. Northeast fault control is apparent for most of the larger paleochannels. The large paleochannel between the Main and Savanna pits is possibly controlled by the contact between Stage 2 and Stage 3 porphyry. Contour interval 50 feet (15 m). Modified from Phelps Dodge Tyrone Geological Services, 2003.

Figure 20. Photomosaic looking northeast at a ferricrete-filled paleochannel in the Savanna pit; bench height is 15 m (50 ft). The erosional surface at the top of the ferricrete is clearly visible as is the yellow goethite dispersion halo extending from the ferricrete upward into alluvial fan gravel on the right side of the mosaic. Photos by Bill Seibert.

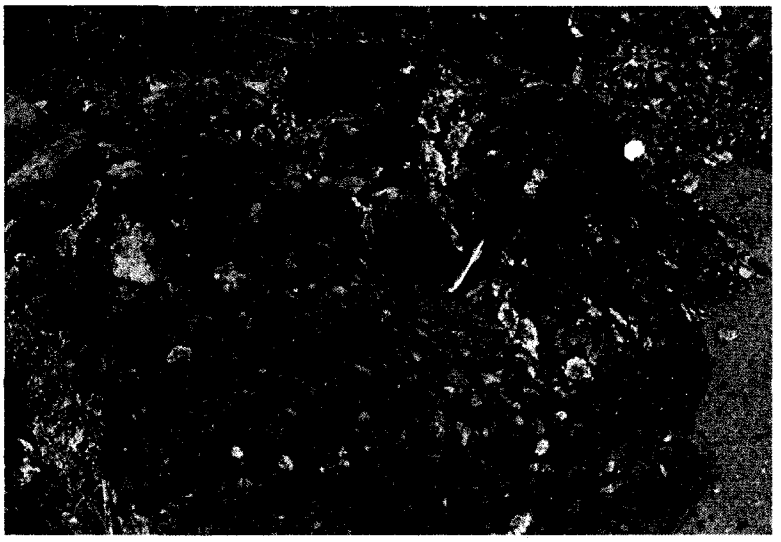

A

B

Figure 21. Miocene ferricrete paleochannel deposits in the southern Little Burro Mountains. A. Poorly-sorted, massive conglomerate containing angular to subrounded clasts of altered porphyry from the Tyrone stock and Proterozoic granite in a sand/granule matrix. B. Medium to thick beds of poorly-sorted conglomerate containing beds and lenses of planar- and cross-bedded, fine- to coarse-grained lithic sand. The paleochannel deposits are cemented by hematite, K-Mn oxides, and chalcedony.

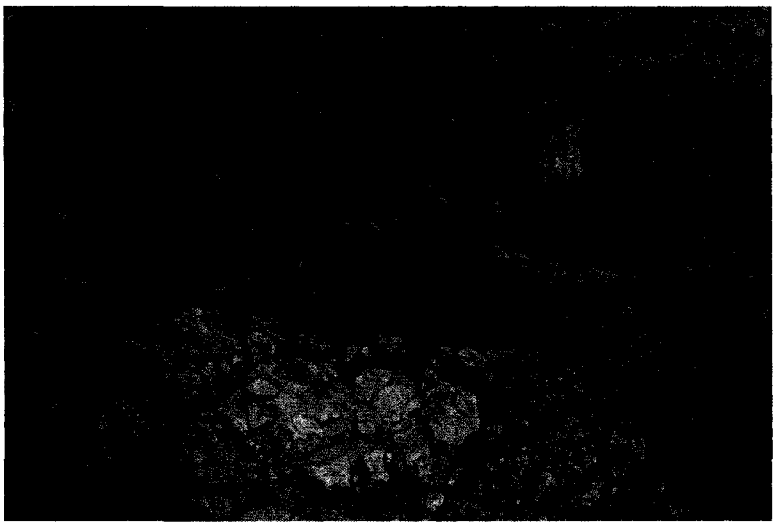

A

B

Figure 22. Miocene ferricrete in the southern Little Burro Mountains. A. Paleochannel deposits overlying Bell Top Formation tuff member 3. B. Distal ferricrete on the southeast flank of Tyrone Peak cemented with black Mn-Cu-Fe oxides. Clasts consist of locally-derived, argillized porphyry.

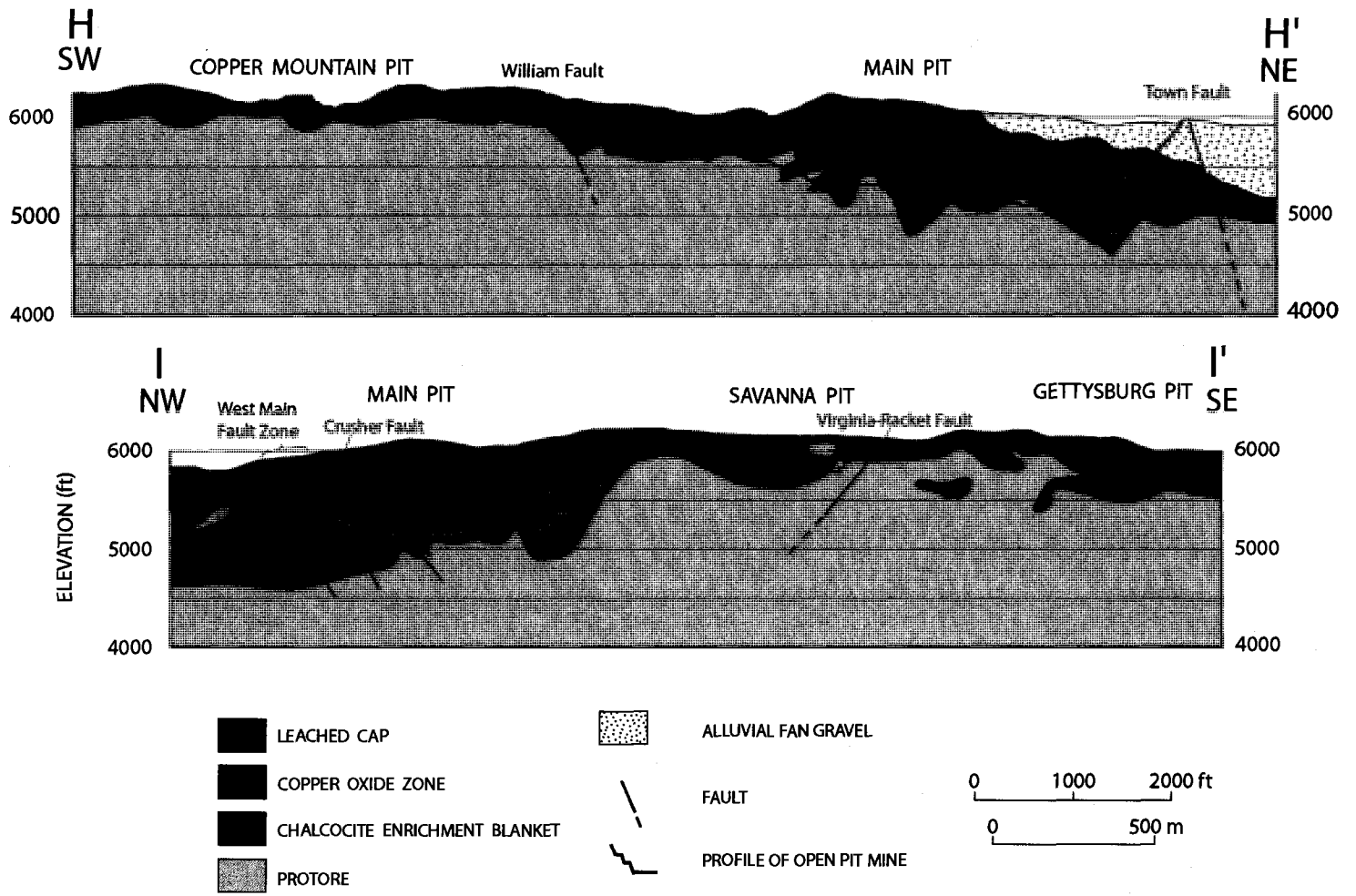

Figure 23. Generalized northeast and northwest cross sections of the Tyrone supergene system. Modified from Smith (1998). No vertical exaggeration. Cross section locations are shown on Figure 5.

CHAPTER 4: $^{40}Ar/^{39}Ar$ GEOCHRONOLOGY OF IGNEOUS ROCKS AND FERRICRETE IN THE SOUTHERN LITTLE BURRO MOUNTAINS

INTRODUCTION

$^{40}Ar/^{39}Ar$ dating of samples from the southern part of the Little Burro Mountains for this study was designed to determine the timing of the end of igneous activity in the Tyrone stock, and to constrain the timing of erosional unroofing and supergene enrichment events. Four samples were dated, including: 1) plagioclase from the Stage 5 rhyodacite porphyry plug (Trdp, sample 89-5) associated with the Tyrone stock; 2) sanidine from tuff member 3 of the Bell Top Formation (Tbt, sample 61-7); 3) plagioclase from Caballo Blanco Tuff (Tcb, sample 89-8); and 4) cryptomelane cement from the ferricrete (Tf, sample 817-1). Sample locations are shown on Plate 1 and $^{40}Ar/^{39}Ar$ ages are summarized in Table 2. The stratigraphy and $^{40}Ar/^{39}Ar$ ages of Cenozoic units in the southern Little Burro Mountains are shown on Figure 12. The $^{40}Ar/^{39}Ar$ step-heating data are included in Appendix A.

$^{40}Ar/^{39}Ar$ RESULTS FOR IGNEOUS ROCKS

Stage 5 Rhyodacite Porphyry Plug

The rhyodacite porphyry plug is an unmineralized, late-stage intrusion related to the Tyrone stock. The $^{40}Ar/^{39}Ar$ age on plagioclase from this unit thus represents a minimum age for the end of the hypogene mineralizing event. Sample 89-5 was taken from the eastern lobe of the plug, 670 m (2,200 ft) northwest of Tyrone Peak (Plt. 1). The sample is light gray, flow-banded rhyodacite porphyry. Plagioclase from the sample yielded a plateau age of 54.43 ± 0.81 Ma (steps 3 through 11 with 97% of total ^{39}Ar released, Fig. 24A), and an isochron age of 54.1 ± 0.6 Ma (steps 4 through 10 out of 11, Fig. 24B). A plateau age is identified by a series of adjacent

steps within an age spectrum in which more than 50% of the total ^{39}Ar is released, and each step yields an age within two standard deviations of the mean.

Tuff member 3 of the Bell Top Formation

Tuff member 3 of the Bell Top Formation lies near the base of the 710 m (2,300 ft) thick section of upper Eocene-Oligocene volcanic and volcaniclastic rocks in the southern part of the Little Burro Mountains, and it is unconformably underlain by the ferruginous conglomerate and sandstone unit (Plts. 1 and 2).

Sample 61-7, collected 180 m (600 ft) south of Indian Peak (Plt. 1), consists of gray, crystal-poor, moderately-welded ash-flow tuff. Sanidine in the sample was dated by 12 single-crystal fusions using a CO_2 laser (Fig. 25A, B). Single sanidine crystals can be easily dated by $^{40}Ar/^{39}Ar$ because of the high potassium content of the mineral, and dating single crystals gives the advantage of identifying any older xenocrysts. The analyses defined a coherent population yielding a weighted mean age of 35.7 ± 0.3Ma (n=11), with one younger outlier (Fig. 25A) (T. Spell, pers. comm., 2004). Five of the 12 sanidine crystals define an isochron age of 35.73 ± 0.09 Ma, and show no evidence of excess argon (Fig 25B).

As noted above, this unit is herein correlated with tuff member 3 of the Bell Top Formation. The age of 35.7 Ma provides a maximum age on the ferruginous conglomerate and sandstone unit.

Caballo Blanco Tuff

The Caballo Blanco Tuff is approximately 340 m (1,120 ft) stratigraphically above the ferruginous conglomerate and sandstone unit. Sample 89-8 of the Caballo Blanco Tuff, which was collected 970 m (3,200 ft) northeast of Tyrone Peak (Plt. 1), consists of gray, moderately-welded, crystal-rich ash-flow tuff. Plagioclase from the sample yielded a plateau age of 31.55 ± 0.39 Ma (steps 4 through 12, with 98% of total ^{39}Ar released, Fig. 25C), and an isochron age of 31.6 ± 0.36 Ma (steps 1 through 10 out of 12, Fig. 25D).

The age of the copper-bearing ferruginous sandstone and conglomerate unit in the southern Little Burro Mountains is bracketed between the ages of the Bell Top Formation (35.7 Ma) and the Caballo Blanco Tuff (31.6 Ma). The age of the ferruginous sandstone and conglomerate is further constrained by the Sugarlump Tuff which underlies the Caballo Blanco Tuff and unconformably overlies the ferruginous sandstone and conglomerate unit. The upper member of the Sugarlump Tuff has been dated at 35.17 ± 0.12 Ma by McIntosh et al. (1991, 1992). These data indicate the ferruginous sandstone and conglomerate unit is about 35.5 Ma, confirming an Eocene erosional and enrichment event at Tyrone.

$^{40}Ar/^{39}Ar$ RESULTS FOR FERRICRETE

A sample of ferricrete was collected from a paleochannel deposit 1,400 m (4,600 ft) west-southwest of Tyrone Peak (Plt. 1). Cryptomelane cement in the ferricrete was dated by $^{40}Ar/^{39}Ar$. The cryptomelane is black, massive, and finely crystalline with a botryoidal rind. It occurs as cement filling open space in the ferricrete. Cryptomelane was identified by XRD analysis and the identification later confirmed by Scanning Electron Microscopy at the University of Nevada, Reno. The finely crystalline material in the core of the sample was dated. The analysis yielded a fairly concordant age spectrum with ages between ~9 Ma and ~13 Ma, but no plateau or isochron age was defined (Fig. 26) (T. Spell, pers. comm.., 2004). The best estimate for this sample is the total gas age of 12.06 ± 0.14 Ma (T. Spell, pers. comm., 2004). This age is important because the ferricrete formed during active supergene enrichment, and predates the Mangas fault.

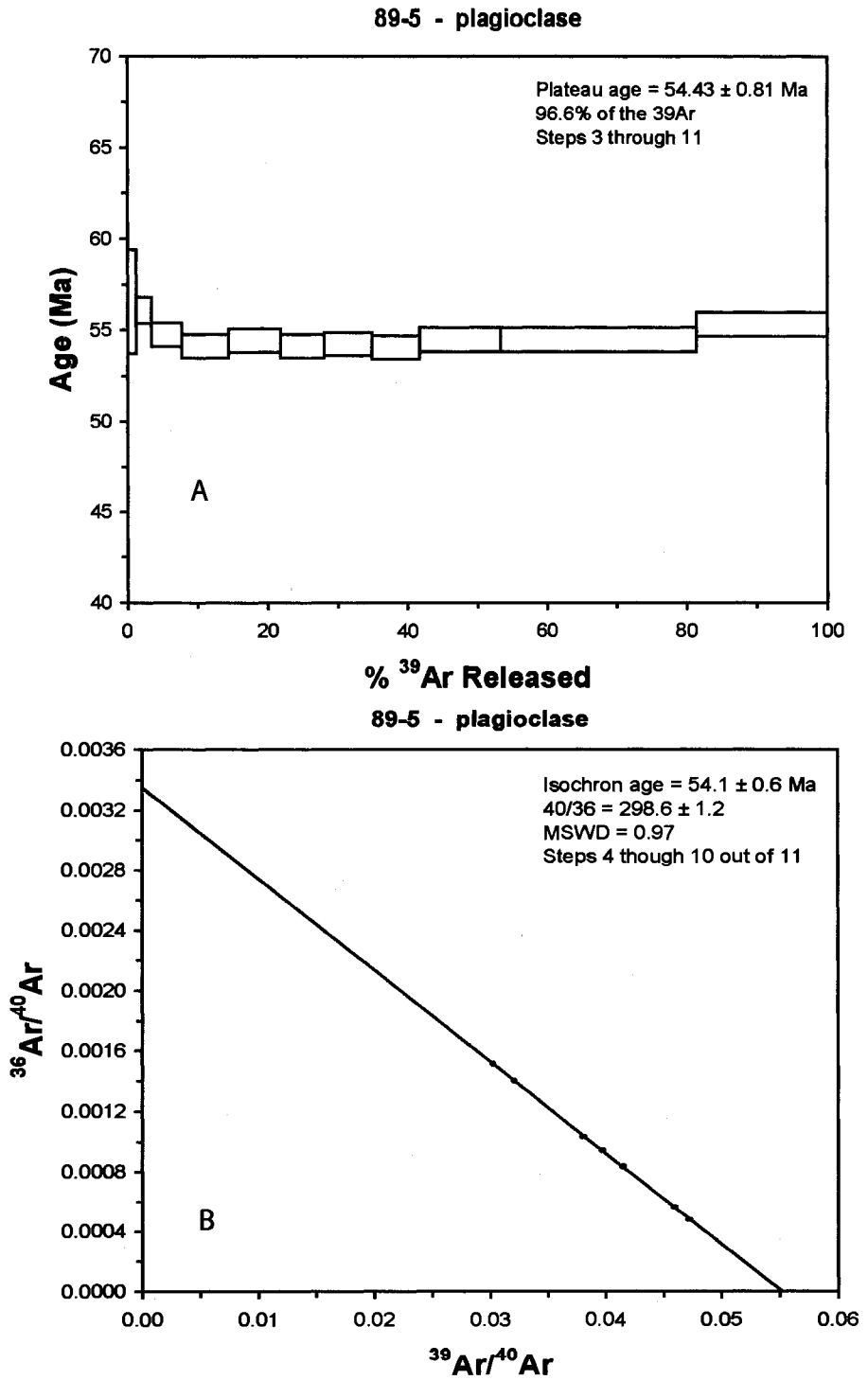

Figure 24. $^{40}Ar/^{39}Ar$ age spectrum (A) and isochron plot (B) for plagioclase from the rhyodacite porphyry plug (Trdp) in the southern Little Burro Mountains, sample 89-5. The rhyodacite plug is a late-stage, unmineralized intrusion associated with the Tyrone stock. Sample location is shown on Plate 1.

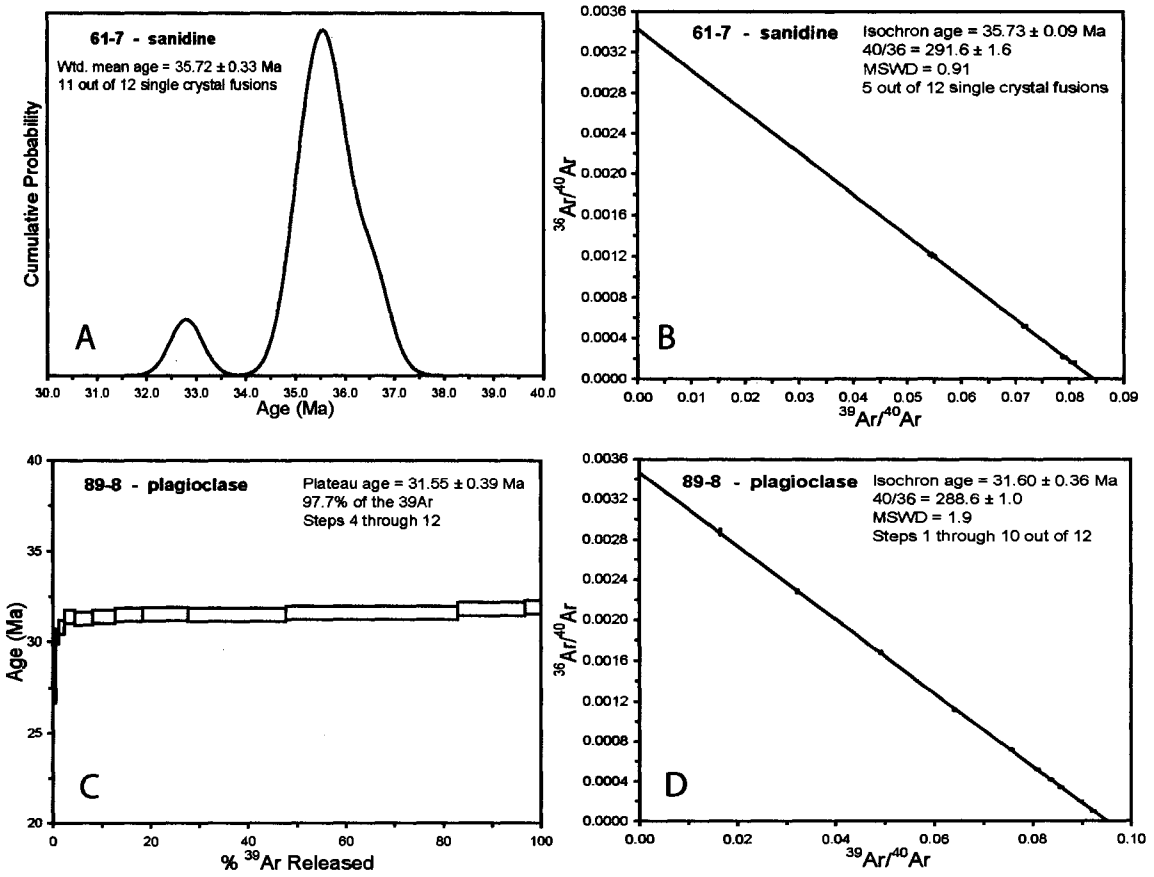

Figure 25. $^{40}Ar/^{39}Ar$ dating results for ash-flow tuff units in the southern Little Burro Mountains. (A) and (B) are cumulative probability and isochron plots for 12 single-crystal fusions of sanidine from the Bell Top Formation tuff member 3, sample 61-7; (C) and (D) are an age spectrum and isochron plot for plagioclase from the Caballo Blanco Tuff, sample 89-8.

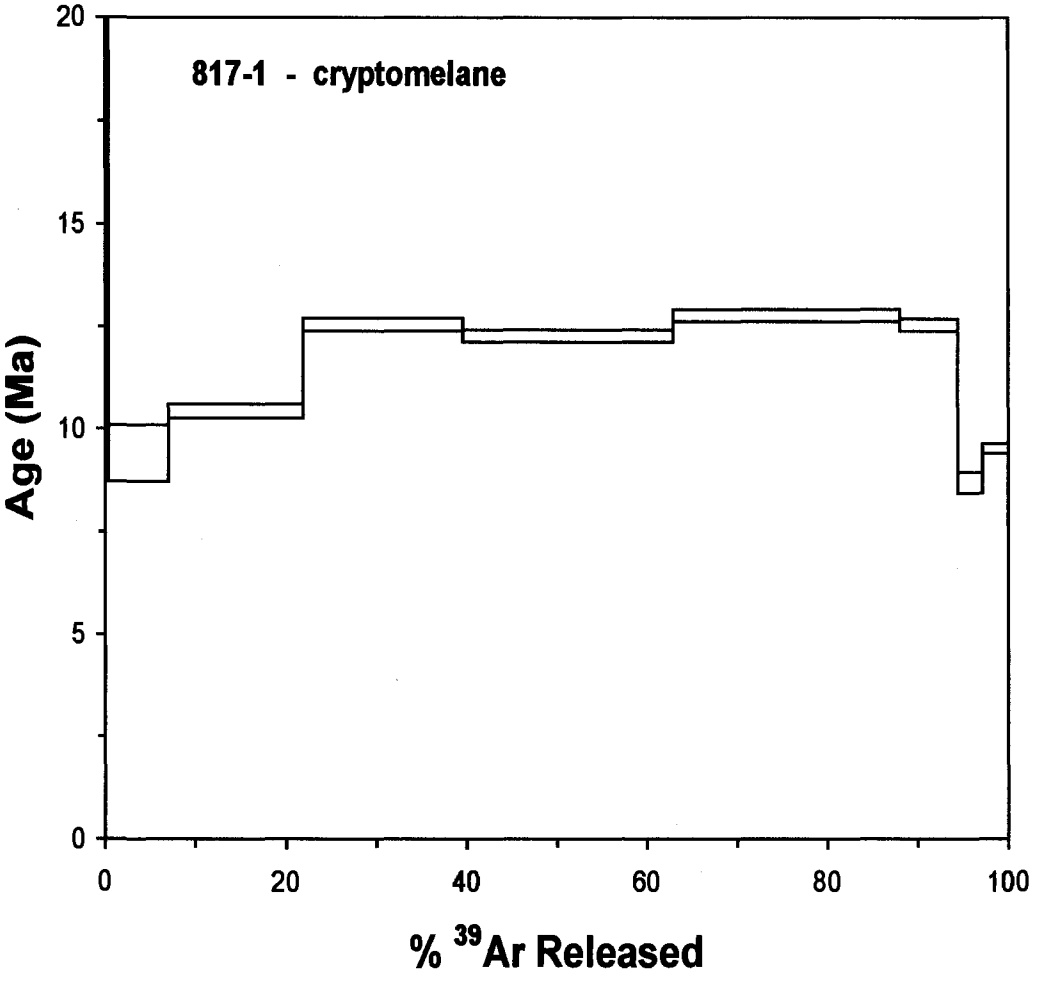

Figure 26. Age spectrum for cryptomelane cement from ferricrete in the southern Little Burro Mountains, sample 817-1. No plateau or isochron age was defined for the sample, and the total gas age of 12.06 + 0.14 Ma is the best estimate for the age (T. Spell, pers. comm., 2004). Sample location shown on Plate 1.

CHAPTER 5: GEOLOGY OF THE TYRONE MINE AREA IN THE BIG BURRO MOUNTAINS

INTRODUCTION

The geology of the Tyrone mine area presented below is summarized mostly from DuHamel et al. (1995), Hedlund (1985), and Gillerman (1970). The reports by Hedlund (1985) and Gillerman (1970) were based on surface geologic work that was completed before extensive open-pit mining at Tyrone, while the report by DuHamel et al. (1995) was based on geology of open-pit exposures of the deposit. Note that the grid used on Figure 5 and subsequent figures is the Tyrone mine grid.

Rocks in the vicinity of the Tyrone mine consist dominantly of Proterozoic Burro Mountain granite which has been intruded by the Tyrone stock (Fig. 3). The Tyrone stock was intruded in five stages, but only units from Stages 1 to 4 are exposed in the Big Burro Mountains (Table 1). The stock occupies an area about 8 km (5mi) long by 6 km (4 mi) wide (Fig. 4), and consists of irregular plugs, dikes, sills, and intrusive breccia of granodiorite to quartz diorite (Stage 1), monzonite porphyry (Stage 2), and quartz monzonite porphyry (Stages 3 and 4). Dikes associated with the stock generally strike northeast to east in the mine area (Fig. 5). A rhyolite dike swarm was intruded along preexisting northeast-striking faults in the areas to the northwest and southeast of the stock following intrusion of the stock and associated quartz monzonite dikes (Hedlund, 1985). Upper Cretaceous-Paleocene andesite locally occurs along the northern margin of the stock in the mine area (Fig. 5) (DuHamel et al., 1995). As discussed above, an apophysis of the Tyrone stock 6.5 km^2 (2.5 mi^2) in area and comprising intrusions of Stages 2, 3, and 5 also occurs in the southern Little Burro Mountains (Figs. 1 and 4, Plt. 1).

The porphyry copper deposit is confined to an area about 17 km^2 (6.5 mi^2) in the northeast portion of the stock in the Big Burro Mountains. In this area, the cupola of the stock consists of porphyritic rocks of Stages 2 to 4 (DuHamel et al., 1995). Stage 2 monzonite

porphyry and Stage 3 quartz monzonite porphyry are altered and mineralized, but Stage 4 quartz monzonite porphyry is unaltered and unmineralized and interpreted as post-mineral (DuHamel et al., 1995). Extensive exposures of Stage 1 granodiorite and quartz diorite to the southwest of the orebody have equigranular to porphyritic textures, and exhibit far less hydrothermal alteration than the Stage 2 monzonite porphyry and Stage 3 quartz monzonite porphyry. These exposures of Stage 1 porphyry represent deeper level portions of the intrusion (Fig. 5) (DuHamel, 1986). The mineralized top of the stock is thus in the northeastern part of the district, preserved by 10-20° northeast tilt of the range, whereas the deeper levels of the stock are exposed to the southwest (Hedlund, 1985).

Magmatic biotite and orthoclase in Stage 1 quartz diorite and Stage 3 quartz monzonite porphyry yielded $^{40}Ar/^{39}Ar$ total gas ages ranging from 55.76 ± 0.53 Ma to 51.04 ± 0.35 Ma (R. Stegen, pers. comm., 2004). The dates show considerable geological discordance due to the long-lived hypogene system. Five K-Ar dates on hypogene sericite and illite from the Tyrone deposit yielded ages of 56.6±1.6 Ma to 52.8±1.2 Ma (DuHamel et al., 1995).

LITHOLOGIC UNITS

Precambrian Rocks

Burro Mountain Granite

Precambrian rocks consist dominantly of the informally-named Mesoproterozoic Burro Mountain granite (1,445 Ma, Stacey and Hedlund, 1983). In contrast to the medium-grained granite in the southern Little Burro Mountains, the granite within the Tyrone district is inhomogeneous, medium- to coarse-grained, and equigranular to locally porphyritic. The granite consists of orthoclase and/or microcline, plagioclase, quartz, and biotite ± hornblende. Mafic minerals comprise up to 10% of the rock, and biotite dominates over hornblende. In some varieties of the granite, mafic minerals are scarce, and comprise a few percent or less of the rock.

Porphyritic varieties contain microcline phenocrysts to 5 cm in length (Gillerman, 1970; DuHamel et al., 1995). The Burro Mountain granite is pegmatitic in places, locally foliated, and contains dikes of pegmatite and aplite (Paige, 1922; DuHamel et al., 1995). Within and adjacent to the copper deposit, the granite is typically sericitized and silicified.

Diabase Dikes

Mesoproterozoic diabase dikes (~1,200 Ma, Drewes et al., 1985) intrude the Burro Mountain granite along northwest-striking faults, and less commonly, along east-west-striking faults (Gillerman, 1970; Hedlund, 1985). The diabase dikes exhibit subophitic texture and consist of labradorite, clinopyroxene, and magnetite-ilmenite (Hedlund, 1985), and are strongly biotitized in the area of the copper deposit (DuHamel et al., 1995). The Proterozoic diabase dikes and granites host some of the higher hypogene copper grades at Tyrone, up to ~0.4% Cu (DuHamel et al., 1995; Smith, 1998).

Upper Cretaceous Sedimentary Rocks

A small (170 x 120 m (570 x 380 ft)) outcrop of Beartooth Quartzite nonconformably overlying Burro Mountain granite occurs ~1,890 m (6,200 ft) south of the Gettysburg pit (not shown on Fig. 4) (Phelps Dodge Tyrone Geological Services, 2003). A sliver of Beartooth quartzite also occurs along the Virginia-Racket fault zone within the mine (DuHamel et al., 1995).

Upper Cretaceous and (or) Paleocene Andesite

Upper Cretaceous and (or) Paleocene andesite flows and breccias similar to those described earlier in the southern part of the Little Burro Mountains are exposed in the Main, Savanna, and Gettysburg pits, but most notably in the north wall of the Main pit (Fig. 5). Core holes adjacent to the north wall of the Main pit intercepted 150 m (500 ft) of propylitized andesite porphyry and another 76 m (250 ft) of andesite and dacite porphyry breccia (DuHamel et al., 1995). Where exposed in the pit, the primary textures of these rocks have been destroyed by

pervasive quartz-sericite alteration and supergene argillic alteration (DuHamel et al., 1995; Phelps Dodge Tyrone Geological Services, 2003).

Eocene Intrusive Rocks of the Tyrone Stock

The descriptions of the Tyrone stock given below are summarized from Phelps Dodge Tyrone Geological Services (2002), Smith (1998), DuHamel et al. (1995), and the author.

Stage 1 Granodiorite to Quartz Diorite

Stage 1 granodiorite to quartz diorite makes up the bulk of the Tyrone stock and is exposed almost as far southwest as Burro Peak (Figs. 4 and 5). This rock is light gray, medium to coarse-grained, with an equigranular to porphyritic texture. Porphyritic varieties contain up to 60% phenocrysts of plagioclase, orthoclase, and biotite, and locally 1-2% quartz phenocrysts, in an aphanitic to granophyric groundmass.

Stage 2 Monzonite Porphyry

Stage 2 monzonite porphyry occurs mainly in the Savanna and Gettysburg pits, although small bodies also occur in the Main pit (Fig. 5). Stage 2 porphyry generally has a crowded porphyritic texture, with up to 45% phenocrysts mostly of oligoclase with sparse phenocrysts of quartz, biotite and hornblende in an aphanitic groundmass (this study). The Stage 1 and 2 porphyries locally contain up to 10% by volume of stockwork sulfide veinlets with broad alteration halos (DuHamel et al., 1995).

Stage 3 Quartz Monzonite Porphyry and Intrusive Breccia

Stage 3 quartz monzonite porphyry is the dominant ore host in the Tyrone district (DuHamel et al., 1995). Large, irregular bodies of Stage 3 porphyry occur in the Main pit and extend southwest toward the Copper Mountain pit, and smaller bodies occur throughout the mine area (Fig. 5). Stage 3 quartz monzonite porphyry is light gray and contains up to 35% phenocrysts of oligoclase, quartz, biotite, and hornblende in an aphanitic groundmass (this study). Within the mine area, the Stage 3 quartz monzonite porphyry also locally contains as much as 5%

orthoclase megacrysts up to 15 mm in length (Phelps Dodge Tyrone Geological Services, 2002). In comparison, only sparse megacrysts (locally up to 3% and 12 mm maximum size) were observed in the Stage 3 porphyry in the southern part of the Little Burro Mountains (this study). The rock at Tyrone and in the southern Little Burro Mountains is typically altered to phyllic and argillic assemblages (this study). In comparison to the Stage 1 and 2 porphyries, the Stage 3 quartz monzonite porphyry contains less veinlet sulfide (vein densities rarely exceed 5% by volume) but more disseminated sulfide (up to 5%) (DuHamel et al. 1995).

Dikes of the Stage 3 quartz monzonite porphyry strike north and northeast through the district and are closely associated with bodies of intrusive breccia in the Main, Savanna, and Gettysburg pits (DuHamel et al., 1995) (Fig. 5). The Stage 3 intrusive breccias are heterolithic and dominantly clast-supported, and consist of rounded to angular clasts of Proterozoic granite, porphyry of Stages 1 and 2, Cretaceous andesite, and Proterozoic diabase in a matrix of siliceous rock flour (DuHamel et al., 1995; Smith, 1998). Clasts of Stage 3 porphyry are also present in the breccias, but other lithologies are far more abundant (DuHamel et al., 1995). In some breccias in the Main pit, the matrix material is indistinguishable from Stage 3 porphyry. The matrix locally contains fragments of coarse vein quartz. The breccias contain the most abundant hypogene sulfides in the deposit, typically 3-10% by volume of disseminated, fine-grained hypogene pyrite $\pm$ chalcopyrite $\pm$ sphalerite. Many breccia clasts contain hypogene sulfide veins, but these veins are rare in the matrix (DuHamel et al., 1995; Smith, 1998). The breccias form elliptical bodies 60-120 m (200-400 ft) in diameter . Most intrusive breccia bodies are too small to be shown on Figure 5, the pit geologic map. The largest intrusive breccia body is an elongate body in the southwestern part of the Gettysburg pit.

The intrusive breccias are excellent hosts for supergene mineralization (DuHamel et al., 1995). The area between the Mohawk and Crusher faults in the Main Pit held a cluster of

intrusive breccias that contained some of the highest grade supergene ores (2-3% Cu) in the mine (DuHamel et al., 1995).

Stage 4 Quartz Monzonite Porphyry

Stage 4 quartz monzonite porphyry was intruded as dikes and small irregular plugs after emplacement of intrusive breccia in Stage 3 (DuHamel et al., 1995). Stage 4 porphyry intrusions occur throughout the Tyrone district (Fig. 5), but do not occur in the southern part of Little Burro Mountains (this study). The Stage 4 porphyry is light gray and contains up to 70% phenocrysts of plagioclase, orthoclase, quartz, and biotite or hornblende in a granophyric groundmass (Phelps Dodge Tyrone Geological Services, 2002). The unit is characterized by its content of up to 5% orthoclase megacrysts up to 4 cm in length, and its lack of alteration (Phelps Dodge Tyrone Geological Services, 2002). The Stage 4 porphyry is interpreted to be post-mineral due to its lack of alteration and copper mineralization (DuHamel et al., 1995). Stage 4 porphyry contains no stockwork sulfide veins and less than 0.5% disseminated sulfide, but locally it contains disseminated molybdenite (DuHamel et al., 1995).

STRUCTURAL GEOLOGY

Structural relationships in the Big Burro Mountains are similar to those in the southern Little Burro Mountains, and are characterized by several generations of crosscutting, northwest- and east- to northeast-striking, dominantly high-angle faults. Northwest-striking faults and fractures occupied by Proterozoic diabase dikes are cut by east- to northeast-striking Laramide faults, some of which host quartz monzonite dikes associated with the Tyrone stock. These older faults are cut by northwest-striking Basin and Range normal faults.

The dominant faults in the Tyrone district shown on the figures and plates were taken from an interpretive geologic map of the Tyrone mine area by Phelps Dodge Tyrone Geological Services (2003), which is presented in simplified form on Figure 5. Structural data on the mine

maps are limited to strikes and dips of faults, fractures, veins, and dikes. Mapping and detailed structural interpretations in the deposit are hampered by the lack of marker units, apparent reactivation of faults, and especially the strong wallrock alteration. Hypogene phyllic alteration overprinted by supergene argillic alteration has reduced most of the wallrocks along faults to mixtures of sericite and clay.

Precambrian Faults

Northwest-striking faults and fracture zones in the Burro Mountains granite commonly host Proterozoic diabase dikes in the Big Burro Mountains. Many of the faults exhibit silicified wall rocks (Gillerman, 1970). These faults probably played an important role in the emplacement of the Tyrone stock; however, with few exceptions, the faults do not show evidence of recurrent movement (Gillerman, 1970).

Laramide Faults

Austin-Amazon and Sprouse-Copeland Faults

Northeast- and east-northeast-striking Laramide faults (most strike N40-80°E) are associated with the Santa Rita lineament (Chapin et al., 2004; Hedlund, 1985; McLemore et al., 2000) (Fig. 1). Two major northeast-striking normal faults, the Austin-Amazon and Sprouse-Copeland faults (Fig. 4), bound the Tyrone stock and probably made room for its emplacement by facilitating doming or upward displacement of the horst between the faults (Gillerman, 1970; Hedlund, 1985). This horst, named the Tyrone horst (Fig. 4), is bounded on the southeast by the Sprouse-Copeland fault, which dips 70° southeast and has as at least 150 m (500 ft) of dip-slip displacement. The Austin-Amazon fault zone on the northwest edge of the horst dips 70° northwest and has 210-300 m (700-1,000 ft) of displacement (Gillerman, 1970; Hedlund, 1985; DuHamel, 1991). The Sprouse-Copeland and Austin-Amazon faults show evidence for several episodes of displacement. In places, they are intruded by quartz monzonite porphyry dikes and rhyolite dikes that were brecciated by recurrent fault displacements (Hedlund, 1985). The Tyrone

horst may have had some subdued topographic relief during the late Eocene due to displacements on the Sprouse-Copeland and Austin-Amazon faults.

Burro Chief-West Main Fault Zone

The Burro Chief-West Main fault zone is the dominant northeast-striking fault in the Tyrone deposit and forms the western limit of the main chalcocite orebody (Figs. 5 and 27). The West Main fault strikes N40-55°E and dips 45° to the southeast. The Burro Chief fault strikes N15°E and dips 70° east. The Burro Chief-West Main fault zone displaces the southeast side of the Tyrone stock down (Fig. 5), with displacement decreasing to the southwest (Hedlund, 1985). According to Kolessar (1970), the Tyrone deposit has been tilted 5-8° northwest along the Burro Chief fault, and the zone of maximum displacement on the Burro Chief fault occurs at its intersection with the Mangas fault. However, northwest tilt of the chalcocite blanket is not apparent on east-west ore mineral type cross sections (Plt. 6, cross sections E-E' and F-F').

The Burro Chief fault is locally marked by strongly brecciated and silicified rocks, and it hosts late-stage (post-sulfide) fluorite deposits (Gillerman, 1970). Repeated slip on the Burro Chief fault resulted in at least 3 stages of brecciation in the fluorite deposits, and the latest displacement occurred after deposition of the lower alluvial fan gravel unit (Gillerman, 1970). The fault shows approximately 100 m (330 ft) of post-alluvial fan gravel normal displacement north of the Main pit, where it juxtaposed the gravel against Proterozoic granite (Figs. 4 and 5) (Kolessar, 1982; DuHamel et al., 1995; Griffin, 2001). Splays of the Burro Chief fault continue along strike into the Mangas Valley, as indicated by minor offsets of up to 1.2 m (4 ft) in lower alluvial fan gravel in road cuts on the Mangas Valley Road (Fig. 4) (Griffin, 2001).

Other Northeast-Striking Faults

Numerous northeast-striking faults occur in the area southeast of the Burro Chief-West Main fault (Fig. 5), and most of these faults dip steeply to the southeast. Two of the prominent northeast-striking faults are the Mohawk (N50°E, 70-90°SE) and Crusher (N25-40°E, 70°SE)

faults. DuHamel and Cook (1992) reported that the Crusher fault offsets the lower alluvial fan gravel by 15 m (50 ft). However, this offset cannot be detected on the structure contour map at the base of basin-fill gravel (Fig. 19). The Virginia-Racket fault zone is a prominent east-northeast-striking fault that dips to the north (N80°E, 50°NW). The Mohawk fault and Virginia-Racket fault zone do not cut the alluvial fan gravel.

Fracture studies by Paige (1911, 1922) and Gillerman (1964) prior to open-pit mining showed abundant northeast-striking fractures in the deposit, independent of rock type, in the area between the West Main-Burro Chief fault zone and the projection of the Sprouse-Copeland fault (South Rim fault area) (Fig. 4). Fracture density is greatest immediately southeast of the Burro Chief-West Main fault zone and diminishes gradually to the southeast (Gillerman, 1964). The zone of abundant fractures extends southwestward from Mangas Valley to about 3.2 km (2 mi) southwest of the old townsite of Leopold (Figs. 4 and 28). As a whole, these fractures are highly irregular, but near the Burro Chief-West Main fault zone, the dominant strike is northeasterly with dips to the southeast. Further to the southeast, the dominant fractures strike east with steep north dips (Paige, 1922).

The northeast-striking faults and associated fracture zones, and the intrusive breccias were major conduits for downward movement of meteoric water and facilitated supergene leaching and enrichment. These structures allowed groundwater to flow deep into the deposit, resulting in deep oxidation and producing the irregular geometries of the leached cap, copper oxide zone, and chalcocite enrichment blanket (Fig. 23, Plt. 6). Northeast-striking faults also allowed lateral transport of copper in the supergene system as they were conduits for metal-laden acidic solutions that exited the deposit into paleochannels (see Chapter 10).

High-grade supergene chalcocite orebodies (average 2-3% copper) exploited in early underground mining operations occur within five trends, the Sampson, Bison-Thistle, Niagara-Mohawk, Copper Gulf-Virginia-Racket-Klondike, and Gettysburg-Oquaque-Boone (Fig. 28).

These trends were controlled by zones of closely-spaced fractures along the larger northeast-striking faults (Paige, 1922; Gillerman, 1964). The majority of supergene ore at Tyrone is localized in a graben roughly triangular in shape and bounded by the Burro Chief-West Main system on the north and the Virginia-Racket fault on the south (Figs. 23 and 27) (DuHamel et al., 1995). This graben formed a structural sink for the deposition of supergene copper in the chalcocite blanket. The Crusher and Mohawk faults lie within this graben and both are host to veins of steel-glance chalcocite in the open pit (DuHamel et al., 1995). No significant supergene ore occurs north of the Burro Chief-West Main fault or south of the east-northeast-striking South Rim fault (N70°E, 40-60°N) (Fig. 5) (R. Stegen, pers. comm., 2002).

Southern Star Fault

The Southern Star fault is a major east-northeast-striking normal fault that occurs 1 km (3,300 ft) north of the mine site and juxtaposes Proterozoic granite against lower alluvial fan gravel (Figs. 4 and 5). It strikes nearly east-west, dips 57° north, and exhibits 306 m (1,005 ft) or more of displacement, based on the thickness of gravel intercepted by drill holes in the hangingwall of the fault (Gillerman, 1970; Trauger, 1972; Hedlund, 1985). The Mangas Valley widens from 2 km (1.2 mi) south of the Southern Star fault to over 5 km (3.1 mi) north of the fault (Fig. 4). The lower alluvial fan gravel is tilted 50° to the north along the fault (Hedlund, 1985). Copper-bearing ferricrete is exposed at the Southern Star mine in the hangingwall of the fault (Fig. 4). Evidence from mapping in the southern Little Burro Mountains (Chapter 3) suggests that the Southern Star fault extends into the Little Burro Mountains (Plts. 1 and 2).

Basin and Range Faults

Town Fault

The Town Fault is a Basin and Range normal fault in Mangas Valley immediately northeast of the Main pit (Fig. 4). It strikes northwest along the trend of Mangas Valley and dips steeply northeast. Where intersected in drill holes, this fault offsets the lower alluvial fan gravel

by as much as 60 m (200 ft) (cross section A-A', Plt. 2). The fault partly bounds the west side of a graben within the Mangas half graben.

William Fault

The William fault is a northwest-striking normal fault that occurs within the Main pit and dips 75° northeast (Fig. 5). Pit mapping by Phelps Dodge shows that the William fault offsets some northeast-striking faults. The William fault is possibly related to subsidence of the graben between the Burro Chief-West Main fault zone and Virginia-Racket fault zone. The fault marks the transition where the northeast tilt on the enrichment blanket steepens, from a few degrees or less southwest of the fault to an average of ~9° northeast of the fault (Fig. 23).

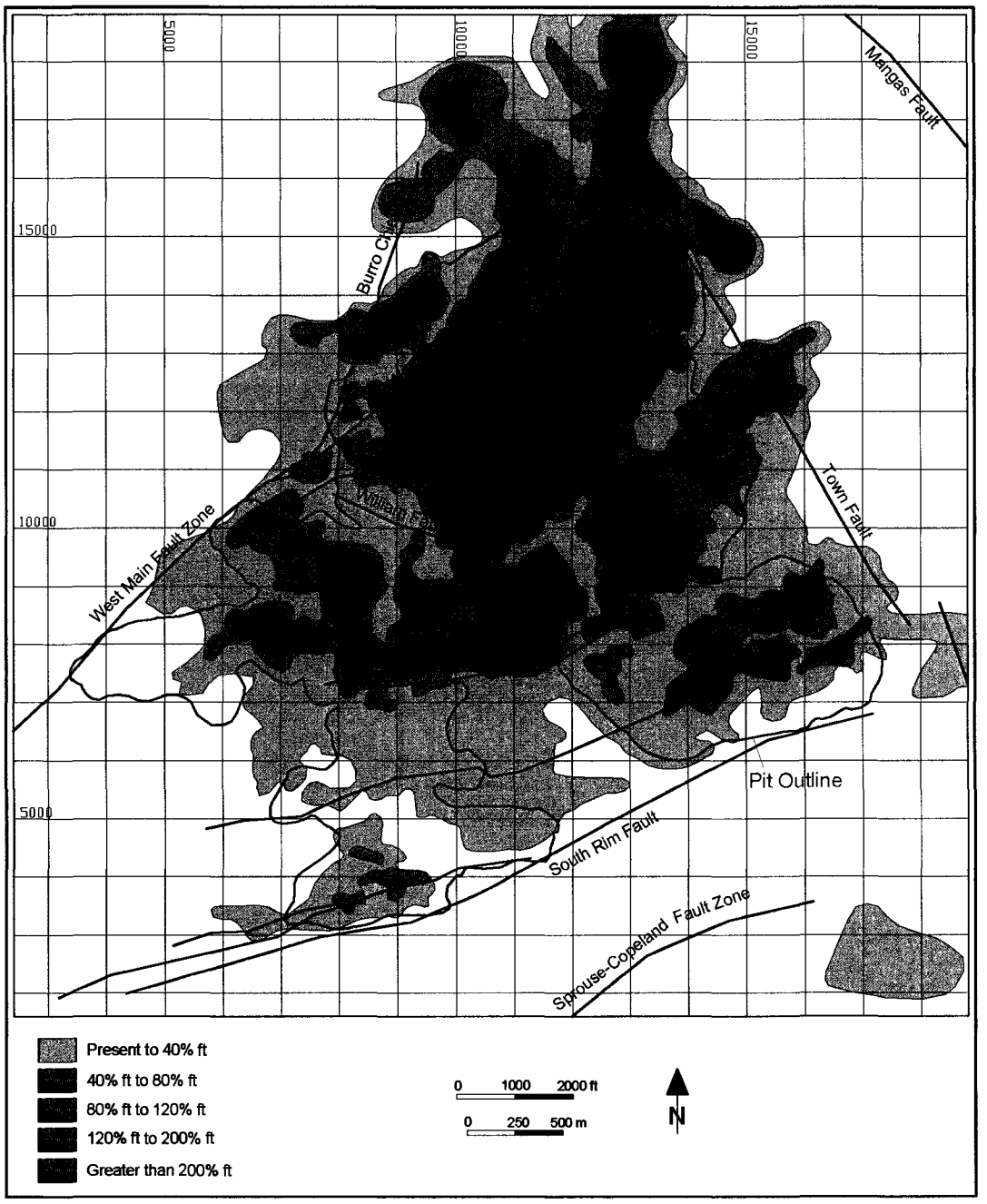

Figure 27. Generalized copper grade x thickness map in percent feet for chalcocite blanket, ore mineral types 3 (mixed oxide-chalcocite), 4 (chalcocite-pyrite), and 5 (chalcocite>chalcopyrite-pyrite). Modified from Phelps Dodge Tyrone Geological Services, 2004.

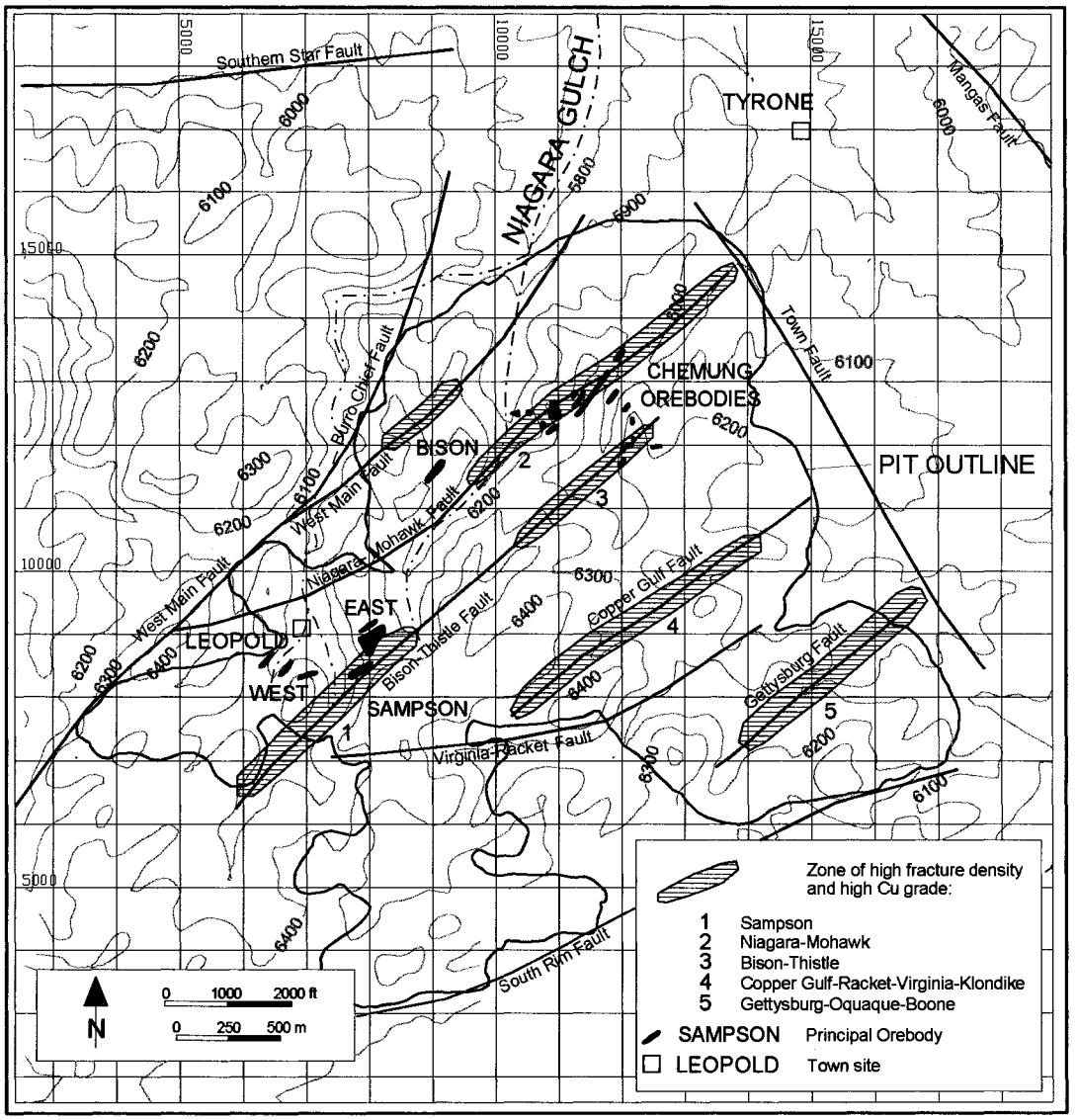

Figure 28. Map showing zones of high fracture density and high supergene copper grades along northeast-striking faults. Also shown are principal chalcocite orebodies mined underground and pre open-pit topography. Elevations are in feet. Contour interval = 100 feet (30 m). Modified from Paige (1922), Gillerman (1964), and Hedlund (1985).

CHAPTER 6: ORE DEPOSITS-THE TYRONE HYPOGENE SYSTEM

INTRODUCTION

The description of the Tyrone hypogene system that follows is summarized mostly from Hedlund (1985), Gillerman (1970), DuHamel et al. (1995), and Smith (1998). The Tyrone porphyry copper deposit is restricted to the northeast part of the Tyrone stock in the Big Burro Mountains (Fig. 4). As discussed above, the stock has been tilted approximately 10-20° to the northeast preserving the mineralized porphyritic cupola zone of the intrusion downdip (Hedlund, 1985).

The Tyrone stock and copper deposit occurs within the Tyrone horst. Northwest and southeast of the Tyrone horst, Proterozoic granites host northeast-striking precious- and base-metal veins probably related to the Tyrone stock (Gillerman, 1970; Hedlund, 1985). Northeast-striking silver-bearing base-metal veins also occur in the southern and central Little Burro Mountains where they are hosted by Proterozoic granite, Upper Cretaceous-Paleocene andesite, and Upper Cretaceous sedimentary rocks (e.g., Contact, Afternoon, and Silver King-Mystery mines, Plt. 1). These precious- and base-metal veins provide evidence for lateral and vertical hypogene mineral zoning (Gillerman, 1967, 1970). Precious- and base-metal veins that may have existed above the porphyry copper deposit have been removed by uplift and erosion of the Tyrone stock (Gillerman, 1967; Hedlund, 1985).

The Tyrone deposit consists of an extensive supergene copper deposit developed over a very low grade hypogene copper deposit. Phelps Dodge reports an average grade of 0.09% copper in hypogene pyrite-chalcopyrite 'protore' for Tyrone (W. Seibert, pers. comm., 2005). Smith (1998) calculated an average hypogene grade of 0.08% copper from nearly 5,900, 15-m (50-foot) composite assays containing at least 10 m (30 ft) of protore, and a slightly higher average copper grade of 0.1% for Proterozoic granites and diabase dikes. Hypogene copper

grades of greater than 0.1% Cu are mostly restricted to the northern and northeastern portion of the deposit and at elevations below 1,680 m (5,500 ft) (Fig. 29) (Smith, 1998). Hypogene copper grade distribution is discussed further in a following section.

The hypogene sulfide minerals consist of pyrite and chalcopyrite with minor amounts of sphalerite, galena, molybdenite and bornite (Kolessar, 1982). Hypogene sulfides occur as veins/veinlets and disseminations. Chalcopyrite and sphalerite are typically very fine grained. The sulfide content of the protore is <6% by weight (Kolessar, 1982). Hedlund (1985) reported an overall pyrite:chalcopyrite ratio of 6:1 for the district.

Based on drill hole logging by the author (86 holes in a 370 x 370 m (1200 x 1200 ft) grid) and logs by Phelps Dodge geologists, the total hypogene sulfide content (pyrite and chalcopyrite) of protore in the southwestern part of the district ranges from about 0.5 to 2.5 volume percent. The pyrite content averages about 1.5 volume percent and chalcopyrite about 0.2 volume percent (range 0.1 to 0.3 volume percent). Pyrite:chalcopyrite thus averages ~7:1.

In the northeastern part of the district, the hypogene sulfide content is 2 to 5 volume percent (locally 6 volume percent or more), including an average of about 2.3 volume percent pyrite (this study). Chalcopyrite ranges from 0.1 to 0.5 volume percent and averages ~0.2 volume percent. The pyrite:chalcopyrite ratio is ~11:1. Individual drill holes in the northeastern part of the district show decreasing copper concentrations below the transition from phyllic alteration at shallower levels to potassic alteration at deeper levels (Smith, 1998). The higher overall pyrite content and higher pyrite:chalcopyrite ratio in the northeastern part of the district reflects strong phyllic alteration.

The dominant hypogene ore hosts in the district are the porphyries of Stages 2 and 3, Proterozoic granite, and Upper Cretaceous-Paleocene andesite (Hedlund, 1985; DuHamel et al., 1995). The Stage 1 granodiorite and quartz diorite porphyries are generally poorer ore hosts. Early silicification is concentrated in the contact zone between the porphyry stock and the

Proterozoic granite (Kolessar, 1970). DuHamel et al. (1995) noted that hypogene copper mineralization is best developed in Stage 3 quartz monzonite porphyry intrusions and associated intrusive breccias that invaded chilled and fractured Stage 1 and 2 porphyries to form salients in the Upper Cretaceous-Paleocene andesite and Proterozoic granite country rocks. These salients of ore-stage porphyry formed in the hood zone or cupola of the larger stock, as noted by Hedlund (1985). The Stage 3 porphyry salients are located in the Main, Savanna, and Gettysburg pits (Fig. 5) (DuHamel et al., 1995). Most copper was introduced with Stage 3 quartz monzonite porphyry as indicated by associated mineralized intrusive breccias, and the dominance of disseminated sulfides versus veinlet sulfides in the Stage 3 porphyry (DuHamel et al., 1995).

Stockwork chalcopyrite-molybdenite mineralization occurs in potassically-altered rocks just below the transition from phyllic to potassic alteration at a depth of 300-460 m (1,000-1,500 ft) below the bottom of the Main pit and continues to a depth of at least 900 m (3,000 ft) (DuHamel et al., 1995). In contrast, weak potassic and propylitic alteration are exposed at or near the surface (depths of <100 m (<330 ft)) in the southwestern part of the district around the South Rim and Copper Mountain pits, and are overprinted by a thin phyllic zone (Smith, 1998; this study). The potassic zone in the southwestern part of the district contains chalcopyrite plus minor molybdenite mineralization (this study). Shallow potassic alteration in the southwestern part of the district reflects, in part, the northeast tilt of the system.

Geologic mapping (this study) and drill data from the southern Little Burro Mountains show that the Stage 3 quartz monzonite porphyry sill at Tyrone Peak is probably within the low-grade pyritic halo of the deposit. The Stage 3 quartz monzonite porphyry at Tyrone Peak exhibits strong phyllic and argillic alteration and a locally strong jarositic cap. Drill holes indicate poor supergene chalcocite enrichment and low hypogene copper grades generally averaging 0.04-0.05% Cu.

HYPOGENE ALTERATION ZONING

Using drill core, Smith (1998) investigated the relationship between hypogene alteration zoning and copper grade distribution at Tyrone. Her conclusions are described below.

Five hypogene alteration stages are recognized related to main-stage hydrothermal activity. These stages are defined by vein-controlled alteration assemblages that show distinct mineralogical and textural characteristics. Crosscutting vein relationships indicate that early propylitic and potassic alteration stages were overprinted by middle phyllic and late argillic alteration stages. All were overprinted by later (supergene) argillic alteration. The potassic and phyllic alteration assemblages are associated with hypogene pyrite and chalcopyrite, but phyllic assemblages have higher copper values. Propylitic assemblages show low concentrations of hypogene sulfides and low copper values.

The early potassic stage at Tyrone is characterized by veinlets of biotite ± quartz ± K-feldspar ± magnetite ± pyrite ± chalcopyrite. Pervasive K-feldspar alteration is associated with quartz ± K-feldspar veins, whereas pervasive quartz + sericite ± chlorite alteration is associated with magnetite veins.

The phyllic stage is characterized by veinlets of quartz ± pyrite ± chalcopyrite ± sphalerite. Pervasive vein-controlled alteration consists of quartz + sericite ± chlorite. Phyllic and argillic alteration affected all of the porphyries older than Stage 4, and also the Proterozoic granite and Upper Cretaceous-Paleocene andesite. The higher concentrations of chalcopyrite are associated with pyrite in phyllic alteration assemblages along faults and within intrusive breccias.

In the Main pit area, potassic alteration has been overprinted by texturally-destructive phyllic and deep supergene argillic alteration. In the Copper Mountain pit, phyllic and supergene argillic alteration are less developed than in the Main pit. Smith (1998) noted that the phyllic-potassic transition surface slopes to the northeast in the district from an average elevation of

1,710 m (5,600 ft) in the Copper Mountain pit to an average elevation of ~1,280 m (4,200 ft) in the Main pit.

DISTRIBUTION OF HYPOGENE COPPER GRADES

Figure 29 illustrates the distribution of high hypogene copper grades (≥ 0.1% Cu) relative to depth in the Tyrone district compiled by Smith (1998). The copper grades are based on 15 m (50 ft) composite assays taken from ≤ 50 ft above the 6,000, 5,500, 5,000, and 4,500-ft elevation levels, and the contour interval is 0.1% Cu. At the 1,830 m (6,000 ft) elevation, the highest copper grades (≥ 0.1% Cu) occur within the West Racket and Gettysburg areas. At 1,680 m (5,500 ft) elevation, localized high hypogene copper grades of over 0.2% Cu occur within the Main, Savanna, and Gettysburg pits.

A comparison of Figure 29 with Figure 5, the district geologic map, reveals that the highest grades in the Main and Savanna pits (up to 0.4% Cu), are at the contact of Stage 3 quartz monzonite porphyry with Proterozoic granite. The highest grades in the Gettysburg pit appear to be related to the contact of Stage 2 monzonite porphyry with Proterozoic granite and Upper Cretaceous-Paleocene andesite. At 1,520 m (5,000 ft) elevation, isolated zones of 0.1% Cu occur at the Proterozoic granite contact in the Main pit. At 1,370 m (4,500 ft) elevation, numerous high-grade copper zones of up to 0.4% Cu occur around the Proterozoic granite.

Smith (1998) noted that the distribution of high grades may be, in part, an artifact of the lack of consistent deep drill hole assay data in the district. Fewer deep holes have been drilled in the Gettysburg, Copper Mountain, West Racket and San Salvador areas than in the Main pit and the Mohawk area north of the Main pit (Smith, 1998).

Copper grade x thickness for hypogene ore mineral types is shown on Figure 30. The highest grade x thickness values for hypogene ore are in the northeastern part of the district within the Main, Savanna, and Gettysburg pits, and to the north and northeast of the pits under

basin-fill gravels in Mangas Valley. When Figures 5 and 30 are compared, it is apparent that the highest grade x thickness values are associated with Proterozoic granite and to a lesser degree the Upper Cretaceous-Paleocene andesite where they are in contact with Stage 3 quartz monzonite porphyry. The highest grade x thickness values form an irregular elliptical zone around the margin of the Proterozoic granite in the Main pit, and a barren zone occurs in the center of the granite mass.

The distribution of hypogene copper grades has implications for the distribution of supergene copper grades if all copper transport was in a vertical direction in the supergene environment. With vertical transport, the distribution of supergene copper grades will reflect the distribution of hypogene grades. However, mass balance calculations show that at Tyrone extensive lateral transport of copper has occurred and the distribution of supergene copper grades is structurally controlled (Chapter 10).

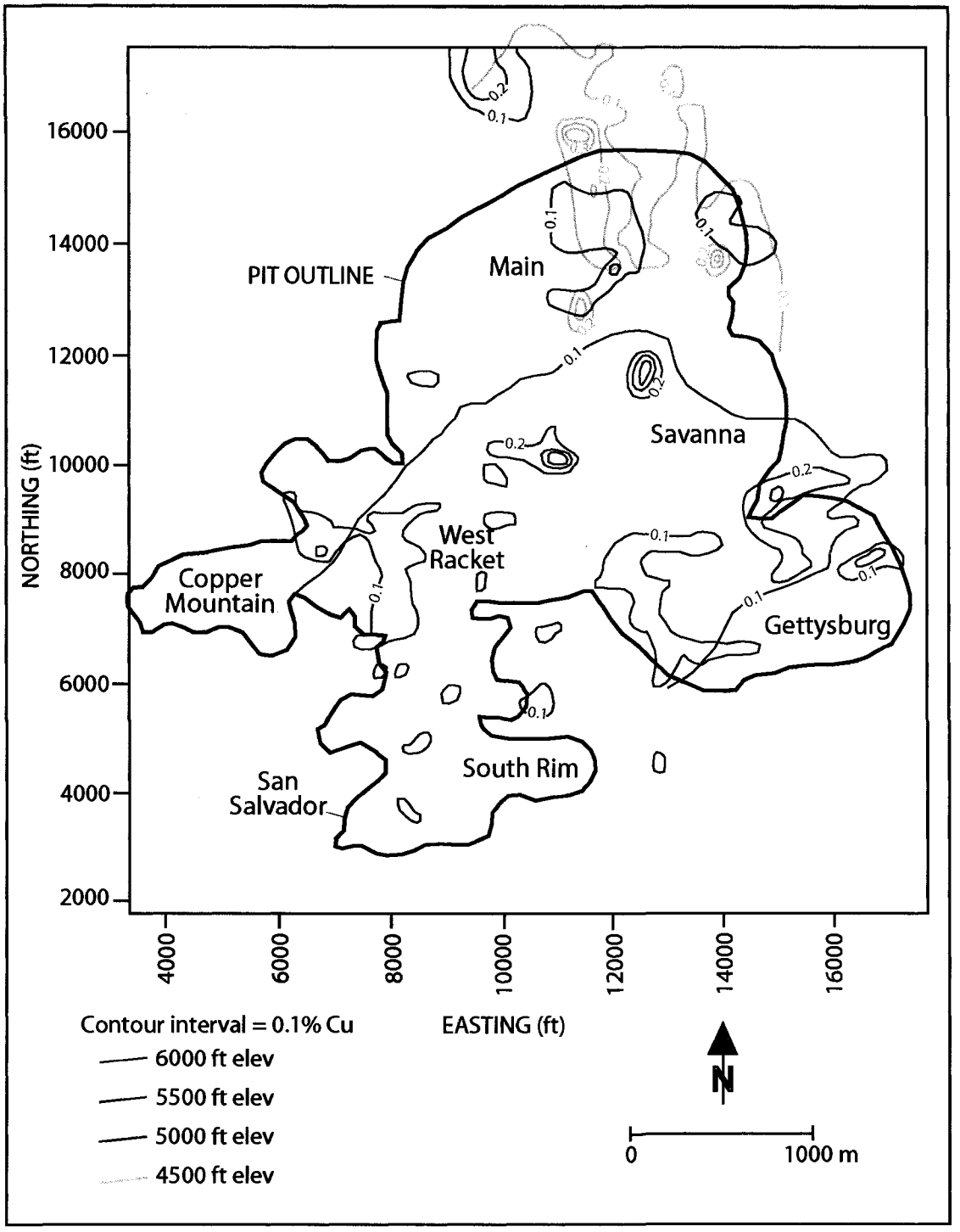

Figure 29. Contoured hypogene copper grades at 0.1% contour interval using 50-foot (15 m) composited drill assays. Contoured data are ≤50 ft above each of the four elevations shown. Areas outside of 0.1% copper contours are <0.1 percent Cu. Modified from Smith (1998).

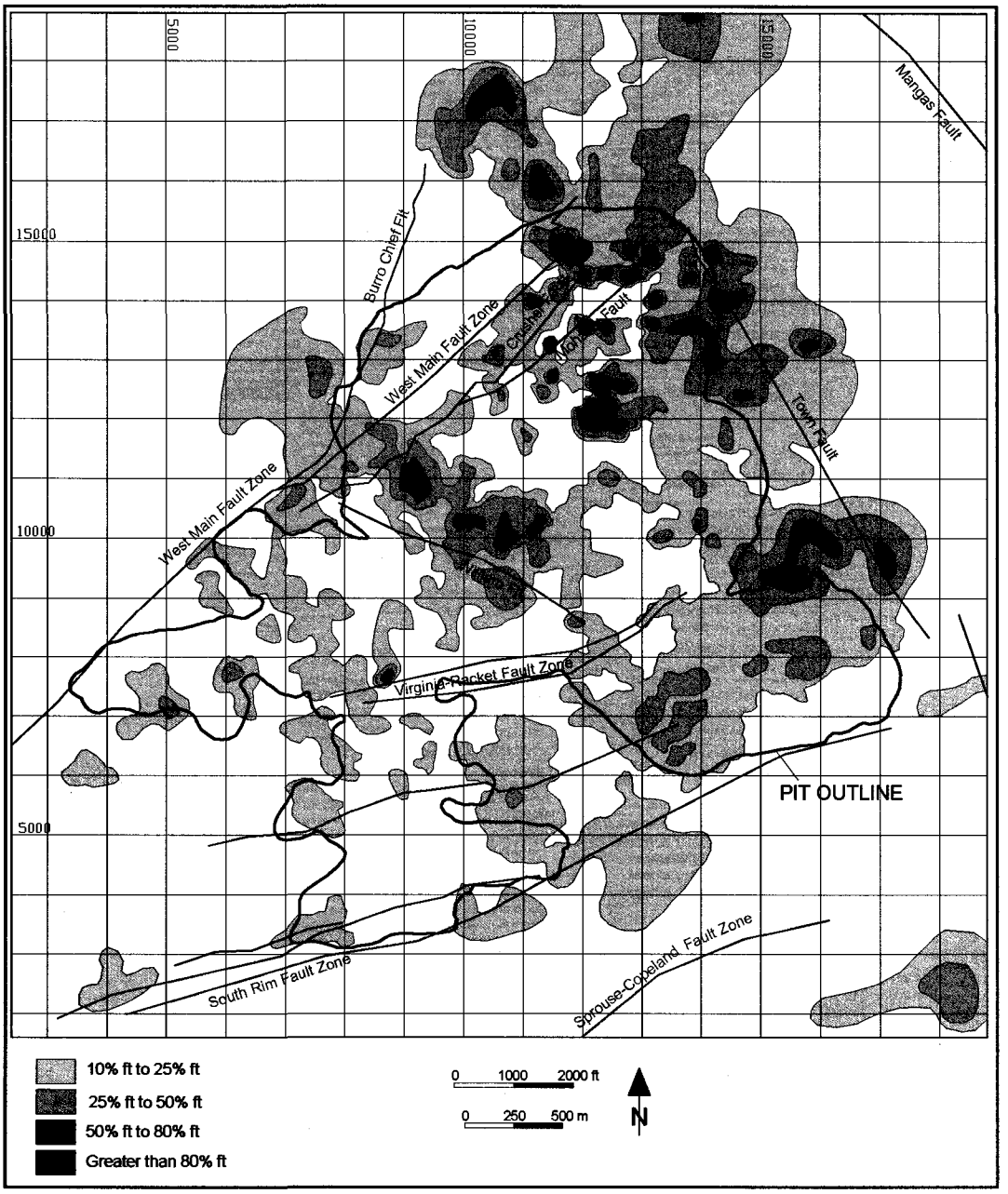

Figure 30. Generalized copper grade x thickness map in percent feet for hypogene copper, ore mineral types 51 (chalcopyrite-pyrite>chalcocite) and 6 (chalcopyrite-pyrite). Modified from Phelps Dodge Tyrone Geological Services, 2004.

CHAPTER 7: SUPERGENE PROCESSES

ENVIRONMENT OF SUPERGENE SULFIDE ENRICHMENT

During supergene sulfide enrichment, hypogene copper sulfide minerals (dominantly chalcopyrite and bornite) are oxidized and dissolved above the groundwater table. Copper is transported down in acidic sulfate solutions and redeposited in secondary copper sulfide minerals (dominantly chalcocite and covellite) in reducing conditions below the groundwater table. Deposition of copper is by replacement of hypogene chalcopyrite and pyrite through cation exchange reactions. A supergene chalcocite enrichment blanket is formed, often with grades significantly above protore grades (Titley, 1982b).

The processes of supergene oxidation, leaching, and enrichment are most efficient in rocks with a low acid neutralizing potential and a high pyrite content favorable for acid generation. Rocks with phyllic alteration assemblages are thus favorable for deep oxidation and mature chalcocite enrichment blankets. Intense acid leaching results in a supergene argillic overprint of the phyllic alteration assemblage in the leached cap. Unaltered rocks or rocks altered to potassic and propylitic assemblages have more buffering capacity and result in diminished leaching.

A semi-arid climate and seasonal precipitation are most favorable for developing mature supergene enrichment blankets because temperatures are high enough to promote oxidation, and water is available in sufficient quantities for the oxidizing reactions and to transport copper released into solution (Anderson, 1982; Sillitoe, 2005). Most downward transport of copper probably occurs during seasonal precipitation/recharge. Fracture zones, stockwork veinlets and steep, through-going faults provide permeability for descent of oxidized solutions (Sillitoe, 1985).

Figure 31 shows the development of a supergene enrichment profile over two cycles of weathering and enrichment. The diagram is predicated on sufficient pyrite relative to

chalcopyrite to maintain acidic conditions (pyrite:chalcopyrite = 5:1 to 10:1; Fig. 31, column A). The oxide zone is uppermost in columns B and C and consists of residual minerals such as insoluble iron oxides, hydroxides, and clays left from the leaching of sulfides and destruction of primary silicates. The zone of leaching underlies and overlaps the zone of oxidation. In the zone of leaching, the sulfide minerals undergo oxidation resulting in the production of acid and release of copper into solution. The zones of oxidation and leaching are, therefore, depleted in copper. The zone of enrichment underlies the zone of leaching and is the site of copper deposition (supergene sulfide enrichment blanket in Figure 31, columns B and C).

Inorganic geochemical processes in the zones of oxidation, leaching, and enrichment will be briefly reviewed here as will numerical geochemical modeling of supergene copper oxide systems. This information will be used to assess the role of of hypogene sulfide content and alteration zoning in formation of the laterally-zoned (copper sulfide/copper oxide) supergene system at Tyrone. The chapter will end with a discussion of leached cap classifications. Some possible reactions in the supergene environment are presented in Table 3.

GEOCHEMICAL PROCESSES IN THE ZONE OF OXIDATION AND LEACHING

Pyrite has a higher sulfur content than chalcopyrite and bornite, and when pyrite is oxidized it produces abundant sulfuric acid (Table 3, reaction 1) which is required to dissolve and mobilize copper as cupric sulfate (Blanchard, 1968; Titley and Marozas, 1995). The oxidation of chalcopyrite (and pyrite) also produces abundant ferric sulfate (Table 3, reaction 2), which acts as an additional oxidant for hypogene pyrite and chalcopyrite, and also for supergene chalcocite (Table 3, reactions 3, 4, and 5). Pyrite:chalcopyrite ratios of greater than 2:1 and total sulfide content of >3 weight percent are most favorable for complete oxidation and leaching of copper sulfides (Titley and Marozas, 1995).

Copper is more soluble than iron in acidic solutions, and is leached preferentially over iron (Anderson, 1982). Destruction of primary silicate minerals in acidic solutions produces a mixture of residual limonite minerals (hematite, goethite, and jarosite, Table 3, reactions 6 through 8) along with clay minerals (Table 3, reactions 10 through 12) in the leached cap.

Repeated cycles of leaching and enrichment (i.e., during recurrent tectonic uplift and falling groundwater table) involve oxidation of any previously-formed supergene chalcocite blanket (Table 3, reaction 5). In reaction 5, hematite precipitates in the leached cap as a result of the destruction of chalcocite. Hematite-rich leached caps are characteristic of supergene systems having well-developed chalcocite blankets, and strongly hematitic horizons with boxwork relief texture known as "live limonites" mark the locations of former chalcocite blankets (Loghry, 1972; Titley and Marozas, 1995).

Supergene alunite precipitates in leached caps from low-pH sulfate solutions by destruction of sericite or K-feldspar (Table 3, reaction 9) (Sillitoe, 2005; Bladh, 1982). Kaolinite is abundant through the leached cap but may give way to smectite with depth due to progressive neutralization of acid (Fig. 31) (Titley and Marozas, 1995).

GEOCHEMICAL PROCESSES IN THE ENRICHMENT ZONE

Redeposition of copper in secondary sulfide minerals generally takes place below the groundwater table as the decrease in the partial pressure of oxygen marks the transition between oxidizing and reducing conditions (Fig. 33). Local oxidizing conditions may prevail along faults that conduct oxygenated meteoric water below the groundwater table, and oxidation of hypogene sulfides along faults is the dominant process in some porphyry systems (Anderson, 1982; Sillitoe, 2005).

Replacement of hypogene minerals by chalcocite occurs by reactions similar to those shown in Table 3, reactions 13 and 14. Pyrite is typically the only hypogene sulfide remaining in

the enrichment blanket and it occurs as cores rimmed by secondary chalcocite and covellite (Fig. 34). Pyrite is first replaced by covellite, then covellite is replaced by digenite and chalcocite (Table 3, reaction 15). Djurleite is also an abundant supergene copper sulfide in many copper deposits, including Tyrone (DuHamel et al., 1995; Chávez, 2000). The enrichment process results in the highest copper grades at the top of the blanket (chalcocite and digenite) with weaker enrichment at deeper levels (covellite) due to progressive depletion of copper in descending solutions (Alpers and Brimhall, 1989). Massive or steel glance chalcocite commonly makes up the higher-grade upper part of the enrichment blanket.

GEOCHEMICAL PROCESSES IN THE COPPER OXIDE ZONE

At Tyrone and many other porphyry copper deposits, a copper oxide zone occurs between the leached cap and the chalcocite enrichment blanket (Plt. 6, Figs. 23, 35, 36). Copper oxide zones form through two mechanisms: 1) by addition of copper to a volume of rock being oxidized, and 2) through in-situ oxidation of a copper deposit (Chávez, 2000). In the first mechanism, a source area must supply copper through oxidation and leaching, and the pyrite content of the source rock must be sufficient to maintain a low pH. In this case, significant enrichment of copper can occur.

In the second mechanism, the pyrite content of the source rock is insufficient to generate enough acid to mobilize copper, and little copper is transported away in solution. During in-situ oxidation of hypogene sulfide minerals there is no extensive development of a copper-deficient leached cap; supergene enrichment is suppressed and supergene copper grades will not be significantly enriched over hypogene copper grades (Kwong et al., 1982; Chávez, 2000). In this case, the copper oxide zone may span the entire interval from the top of bedrock to the top of hypogene sulfides (Sillitoe, 2005).

Copper sulfates such as water soluble chalcanthite form in the upper, low-pH parts of an oxidizing system in rocks with a high pyrite content (Fig. 33). Chalcanthite is rarely encountered in leached caps because it is water soluble and easily dissolved by dilute recharge waters (Anderson, 1982). Rarely, chalcanthite occurs in the upper part of the leached cap at Tyrone. Other copper sulfate minerals such as brochantite and antlerite are stable in near-neutral conditions in the lower parts of the system and form by the oxidation of chalcocite (Table 3, reaction 16, Fig. 33) (Chávez, 2000). The copper sulfates are commonly replaced by chrysocolla (Chávez, 2000). Only minor brochantite is reported in the copper oxide zone at Tyrone, but chrysocolla is an important copper oxide ore mineral (Kolesssar, 1982).

Cuprite and native copper replace chalcocite in the upper part of the enrichment blanket by in-situ oxidation in near-neutral or alkaline conditions (Table 3, reaction 17; Fig. 33) (Anderson, 1982; Chávez, 2000). Native copper usually occurs with cuprite, but at greater depths (Chávez, 2000). Cuprite and native copper are common but not abundant in the oxide zone at Tyrone (Kolessar, 1982; DuHamel et al., 1995).

The black copper oxides tenorite and paramelaconite occur above cuprite and native copper in the upper parts of copper oxide zones (Table 3, reaction 18, Fig. 33) in which near-neutral to alkaline pH is maintained, reflecting the decreasing copper oxidation state with depth (Chávez, 2000). Residual copper in the leached cap is hidden or "camouflaged" in co-precipitating limonite minerals, pitch limonite (cupriferous goethite) and neotocite (Anderson, 1982).

Malachite and azurite are common constituents of copper oxide zones where carbonate is available. The copper carbonates and chrysocolla are generally paragenetically late, replacing earlier oxides and sulfides and occupying previously unmineralized fractures (Chávez, 2000). Copper carbonates and chrysocolla are typically the most abundant copper oxide minerals (with volumetrically minor black copper oxides) in geochemically mature copper oxide zones formed

under near-neutral to alkaline pH conditions (Chávez, 2000). Possible reactions for the formation of malachite and chrysocolla are given in Table 3, reactions 19 and 20.

Lichtner and Biino (1992) conducted numerical geochemical modeling of supergene enrichment of a porphyry system assuming a water table at a fixed depth of 50 m, protore containing 2% chalcopyrite, 4% pyrite, 2% magnetite, and inert gangue mineralogy. These parameters approximate supergene enrichment of the central or northern part of the Tyrone district in the Miocene. The modeling showed that supergene enrichment takes place in two stages. During the initial stage of oxidation, dissolution of pyrite in the oxidizing column of rock maintained low pH, and a chalcocite blanket formed below the water table. The second stage began after an elapsed time of about 100,000 years, when pyrite was completely consumed in the oxide zone and top of the chalcocite blanket allowing the pH to rise at the top of the chalcocite blanket. The destruction of pyrite and rise in pH allowed copper oxide minerals including tenorite, brochantite, cuprite and native copper to form overlapping "ghost zones" immediately above the chalcocite blanket. These ghost zones then migrated downward with the chalcocite blanket through time. Both the copper oxide zone and the chalcocite enrichment blanket formed below the groundwater table (Lichtner and Biino, 1992).

LEACHED CAP CLASSIFICATION

Leached caps in porphyry copper deposits are classified by their dominant limonite mineralogy (hematite, jarosite, and goethite) (Anderson, 1982; Sillitoe, 2005). The limonite mineralogy of the leached cap reflects the total sulfide content and the pyrite:chalcopyrite ratio of the protore which, along with host rock alteration mineralogy, control the acidity of fluids produced during oxidation. Goethite is stable over a wide range of pH in oxidizing conditions, whereas jarosite is stable only at low pH (Fig. 32).

Along with mineralogical type, a distinction is made between "indigenous" and transported limonite. Indigenous limonites are formed by in-situ oxidation of sulfide minerals and occupy the pores that had been the sites of precursor sulfide minerals (including veinlets and boxworks) (Gilmour, 1995). Indigenous limonites generally signify low pyrite content (low pyrite:chalcopyrite), near-neutral pH conditions, and limited metal transport. Transported or exotic limonites precipitate away from the site of the parent sulfide minerals and signify higher initial pyrite content (high pyrite:chalcopyrite). The distance traveled depends on pyrite content of the sulfide source, gangue mineralogy, and permeability (Loghry, 1972; Chávez, 2005).

Goethitic leached caps overlie hypogene ore where copper leaching and enrichment are limited, and indicate a low pyrite:chalcopyrite ratio and reactive host rock/alteration assemblage. Goethitic leached caps typically contain camouflage copper and black copper oxide minerals.

Jarositic leached caps reflect pyrite-rich mineralization and are typically associated with phyllic alteration overprinted by supergene kaolinite alteration (Gilmour, 1995). Jarositic leached caps form over the copper-poor pyrite halo of the porphyry system and surround the hematitic and goethitic cappings. Jarosite is typically transported rather than indigenous. Two types of jarositic cappings are recognized. Original (upper) jarositic cappings form by oxidation of the pyrite-chalcopyrite protore and occur above first-cycle enrichment blankets (Fig. 31, profile B). Original jarositic capping occurs in argillized pyritic but copper-poor Stage 2 and 3 porphyry in the Tyrone Peak area. Lower jarosite cappings form by oxidation of pyrite-chalcopyrite protore beneath a former enrichment blanket during rapid lowering of the groundwater table (Fig. 31, profile C) (Anderson, 1982; Titley and Marozas, 1995). Lower jarosite cappings thus occupy the intervals between successive chalcocite enrichment blankets formed during multi-cycle enrichment, and result in layered hematite and jarosite leached caps. In contrast, a gradual lowering of the groundwater table produces hematitic leached caps without distinct layering.

Hematite-rich leached caps containing live limonite overlie mature supergene chalcocite enrichment blankets (pyrite:chalcocite = ~ 5:1) as noted above, and indicate thorough leaching over more than one cycle (Anderson, 1982; Sillitoe, 2005). Interlayered hematite and jarosite horizons occur in the leached cap in some drill holes at Tyrone (e.g., core hole B-36, Plts. 3 and 5) indicating multiple enrichment cycles.

FORMATION OF EXOTIC COPPER DEPOSITS

Exotic copper deposits are formed during active oxidation and enrichment of porphyry copper deposits when portions of the acidic, copper-bearing solutions migrate laterally along conduits such as faults and exit the deposit through zones of enhanced permeability, commonly alluvium-filled stream channels cut into bedrock (Münchmeyer, 1996; Hayes, 2004). Copper deposition is believed to be contemporaneous with deposition of the host alluvial gravel sequence, which is typically kaolinized (Münchmeyer, 1996; Sillitoe, 2005; Hayes, 2004). Gravels are cemented by hematite and copper oxide minerals. A semi-arid climate is ideal for formation of exotic copper deposits, and the hydraulic gradient must be low to increase residence time of solutions; <3° is ideal (Sillitoe, 2005).

Exotic deposits are dominated by chrysocolla, with minor atacamite (very arid climates only), tenorite and neotocite (Münchmeyer, 1996). Copper and alteration minerals are zoned downgradient reflecting an increase in pH of the solutions in space; copper precipitation does not begin until solution pH exceeds ~5.5 (Sillitoe, 2005; Anderson, 1982). Three zones are common (Münchmeyer, 1996; Hayes, 2004). The proximal zone extends from 0 to 2 km (0-1.2 mi) from the source and consists of hematite in unaltered gravel. Proximal gravels are typically unaltered because they are late stage in the aggradational channel fill and exposed only to higher pH solutions (Münchmeyer, 1996). An intermediate or transition zone, 2 to 4 km (1.2-2.5 mi) from the source, consists of copper wad in clay-altered gravel (kaolinite ± montmorillonite), or

chrysocolla in unaltered gravel. The distal zone 4 to 6 km (2.5-3.7 mi) from the source consists of chrysocolla in unaltered gravel.

A crude mineral zoning is observed in the Miocene ferricrete/exotic copper deposits at Tyrone. The proximal zone is hematite rich and occurs in kaolinized gravel. The distal and peripheral zone contains less iron (no hematite) and abundant black, Mn-rich chrysocolla (Emma and Tyrone Peak occurrences; Chapter 8).

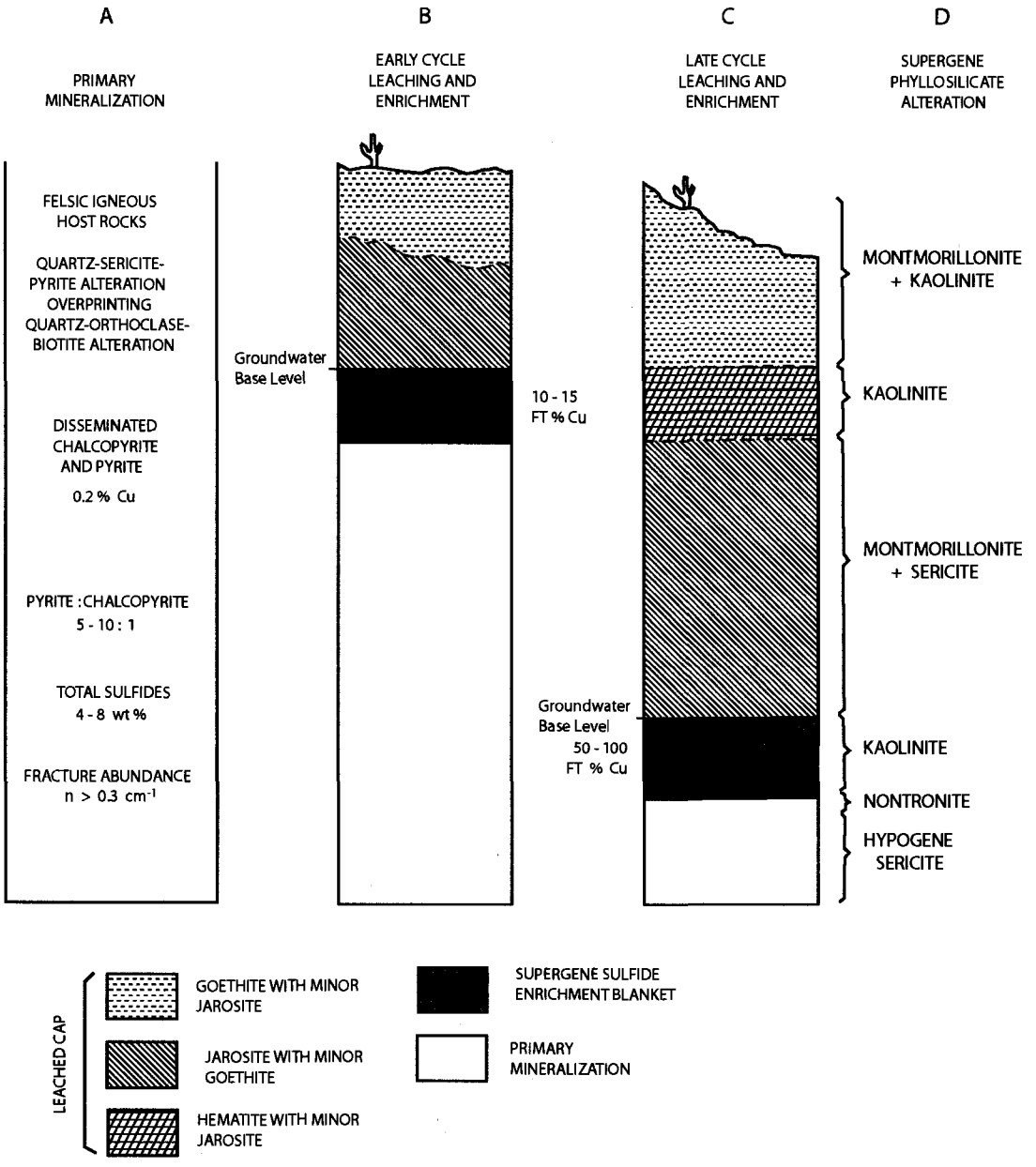

Figure 31. Generalized vertical profiles showing: A. characteristics of a hypogene porphyry copper system in quartz-sericite-pyrite altered felsic igneous rocks; B. early cycle weathering and enrichment with development of a goethitic to jarositic leached cap and supergene sulfide enrichment blanket; C. late cycle weathering and enrichment driven by tectonic uplift/lowering of groundwater base level resulting in downward migration of the sulfide enrichment blanket, lower jarosite zone, and hematitic zone occupying position of the former sulfide enrichment blanket; D. locations of phyllosilicate alteration phases across the profiles. No vertical scale implied; profile may range from 50 m to several hundred meters in thickness. From Titley and Marozas (1995).

Table 3. Some possible reactions in the supergene environment from Titley and Marozas, 1995; Guilbert and Park, 1998; Blanchard, 1968; Enders, 2000.

Reactions in the zone of oxidation and leaching
Oxidation of pyrite (1) and chalcopyrite (2) by oxygen:
1. $FeS_2 + 7/2\ O_2 + H_2O = Fe^{2+} + 2\ SO_4^{2-} + 2\ H^+$
2. $12\ CuFeS_2 + 51\ O_2 = 2\ Fe_2O_3 + 12\ Cu^{2+} + 8\ Fe^{3+} + 24\ SO_4^{2-}$
Oxidation of pyrite (3) and chalcopyrite (4) by ferric iron:
3. $FeS_2 + 8\ H_2O + 14\ Fe^{3+} = 15\ Fe^{2+} + 2\ SO_4^{2-} + 16\ H^+$
4. $2\ CuFeS_2 + 8\ Fe^{3+} + 12\ SO_4^{2-} = 2\ Cu^{2+} + 10\ Fe^{2+} + 12\ SO_4^{2-} + 4\ S$
Oxidation of chalcocite:
5. $Cu_2S + 2\ Fe^{3+} + 3\ SO_4^{2-} + 2\ H_2O + 2.5\ O_2 = Fe_2O_3 + 2\ Cu^{2+} + 4\ H^+ + 4\ SO_4^{2-}$
Formation of hematite (6), goethite (7), and jarosite (8):
6. $2\ Fe^{3+} + 3\ SO_4^{2-} + 3\ H_2O = Fe_2O_3 + 6\ H^+ + 3\ SO_4^{2-}$
7. $2\ Fe^{3+} + 3\ SO_4^{2-} + 6\ H_2O = 2\ Fe(OH)_3 + 6\ H^+ + 3\ SO_4^{2-}$
8. $4\ KAl_3Si_3O_{10}(OH)_2 + 12\ Fe^{2+} + 12\ SO_4^{2-} + 25\ H_2O + 2.5\ O_2 = 4\ KFe_3(SO_4)_2(OH)_6 + 6\ Al_2Si_2O_5(OH)_4 + 8\ H^+ + 4\ SO_4^{2-}$
Formation of alunite by destruction of sericite:
9. $2\ KAl_3Si_3O_{10}(OH)_2 + 4\ H^+ + 2\ SO_4^{2-} + 2\ H_2O + 3\ O_2 = 2\ KAl_3(SO_4)_2(OH)_6 + 6\ SiO_2$
Hydrolysis of orthoclase to sericite (10); biotite to sericite (11); sericite to kaolinite (12):
10. $3\ KAlSi_3O_8 + 2\ H^+ = KAl_3Si_3O_{10}(OH)_2 + 6\ SiO_2 + 2\ K^+$
11. $3\ KAlMgSi_4O_{10}(OH)_2 + 8\ H^+ = KAl_3Si_3O_{10}(OH)_2 + 9\ SiO_2 + 3\ Mg^{2+} + 2\ K^+ + 6\ H_2O$
12. $2\ KAl_3Si_3O_{10}(OH)_2 + 2\ H^+ + 3\ H_2O = 3\ Al_2Si_2O_5(OH)_4 + 2\ K^+$
Reactions in the sulfide enrichment zone
Replacement of chalcopyrite by covellite (13) and pyrite by chalcocite(14):
13. $CuFeS_2 + Cu^{2+} + SO_4^{2-} = 2\ CuS + Fe^{2+} + SO_4^{2-}$
14. $5\ FeS_2 + 14\ Cu^{2+} + 14\ SO_4^{2-} + 12\ H_2O = 7\ Cu_2S + 5\ Fe^{2+} + 24\ H^+ + 17\ SO_4^{2-}$
Reduction of covellite to chalcocite:
15. $CuS + Cu^{2+} + SO_4^{2-} + H_2O = Cu_2S + 2\ H^+ + SO_4^{2-} + 0.5\ O_2$
Reactions in the copper oxide zone
Formation of brochantite from oxidation of chalcocite:
16. $2\ Cu_2S + 4\ H_2O + 5\ O_2 = Cu_4SO_4(OH)_6 + 2\ H^+ + SO_4^{2-}$
Formation of native copper and cuprite from oxidation of chalcocite:
17. $2\ Cu_2S + 8\ Fe^{3+} + 12\ SO_4^{2-} + 1.5\ O_2 + 6\ H_2O = 2\ Cu^0 + Cu_2O + 8\ Fe^{2+} + 12\ H^+ + 14\ SO_4^{2-}$
Formation of tenorite by oxidation of native copper and cuprite:
18. $Cu^0 + Cu_2O + O_2 = 3\ CuO$
Formation of malachite from tenorite:
19. $2\ CuO + CO_2 + H_2O = Cu_2(OH)_2CO_3$
Formation of chrysocolla:
20. $Cu^{2+} + SiO_2 + 2\ H_2O = CuSiO_3 \cdot H_2O + 2\ H^+$

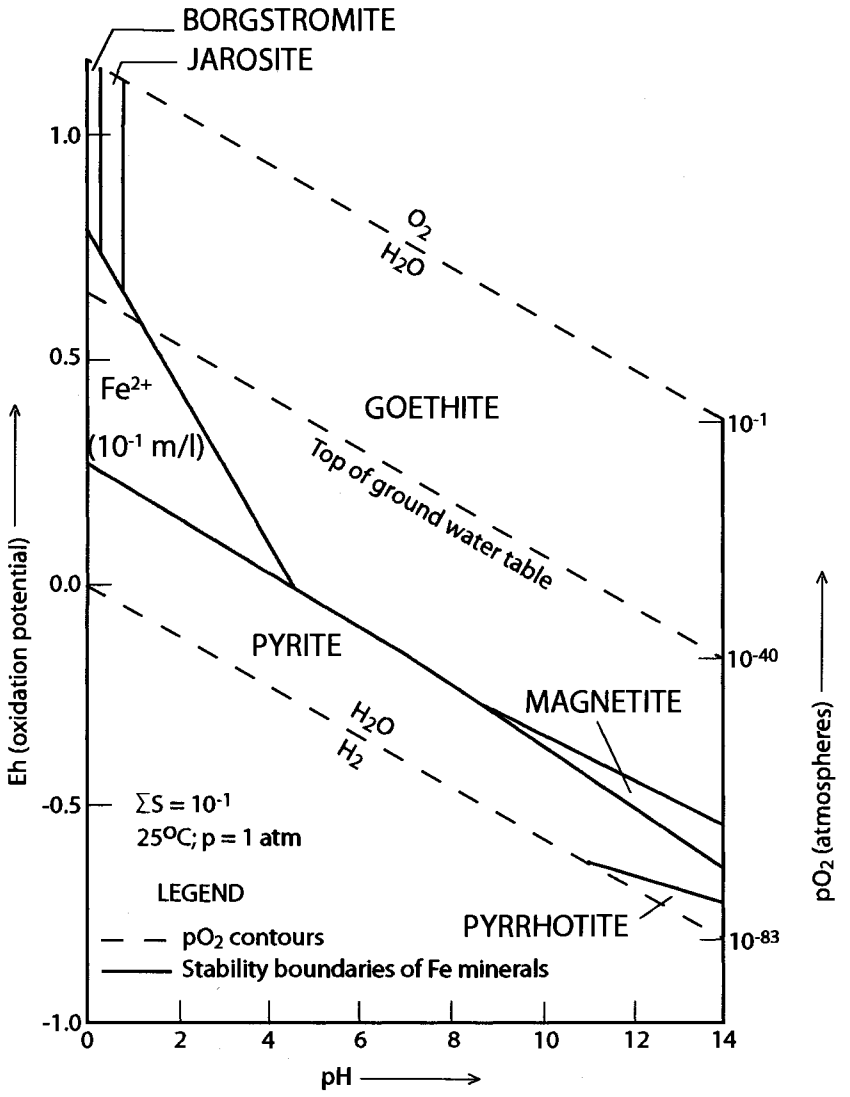

Figure 32. Eh-pH diagram showing the stability fields of iron minerals in the system Fe-S-H_2O at 25°C and 1 atmosphere total pressure. Modified from Anderson (1982).

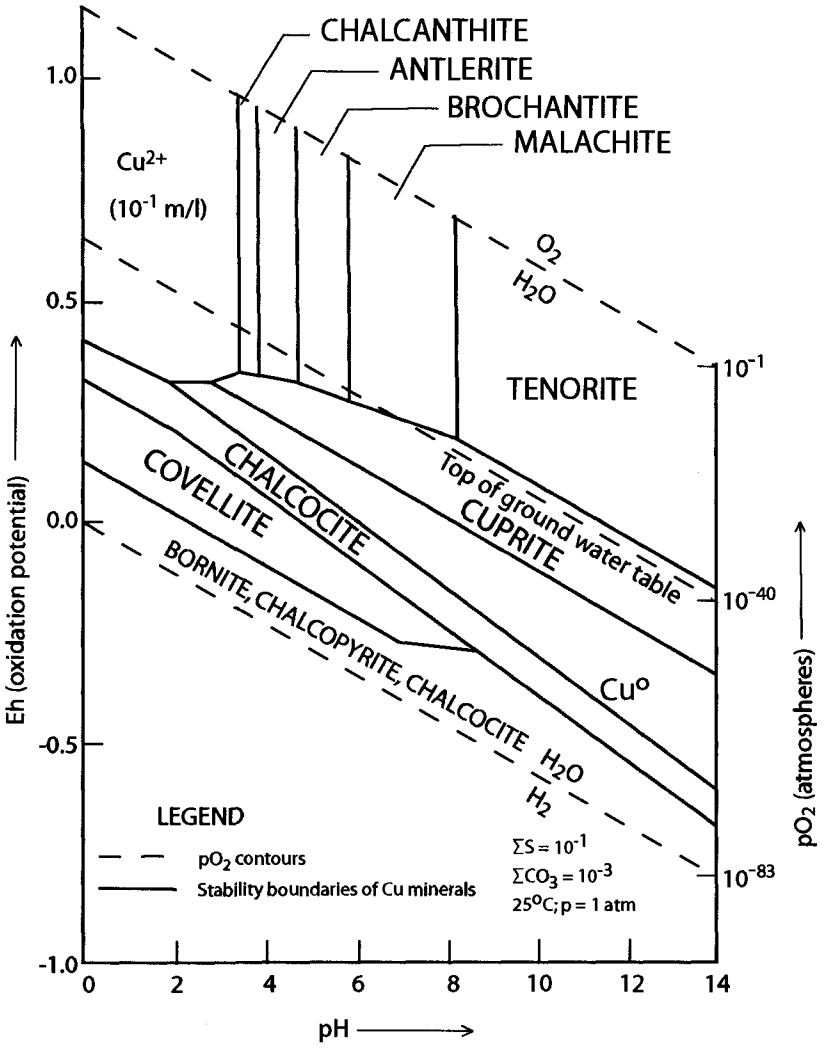

Figure 33. Eh-pH diagram showing the stability fields of copper minerals in the system Cu-S-H_2O at 25°C and 1 atmosphere total pressure. Modified from Anderson (1982).

A

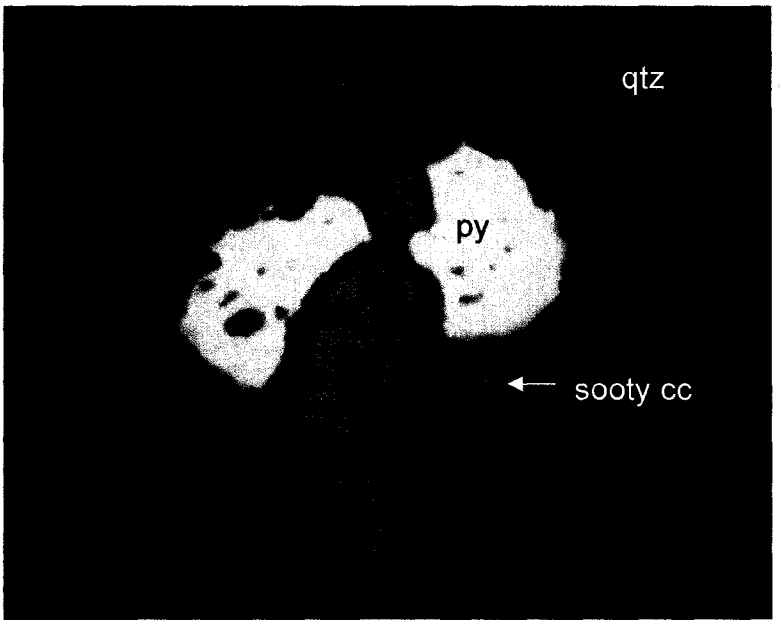

B

Figure 34. Photomicrographs of Tyrone supergene chalcocite ore. A. Steel glance chalcocite (cc) veining and replacing chalcopyrite (cpy) and pyrite (py). Note that chalcopyrite is replaced before pyrite. Field of view = 0.85 mm. B. Steel glance chalcocite with some remnant sooty chalcocite forming rims around pyrite grains. Most of material in view is quartz (qtz) and clays. Field of view = 0.43 mm.

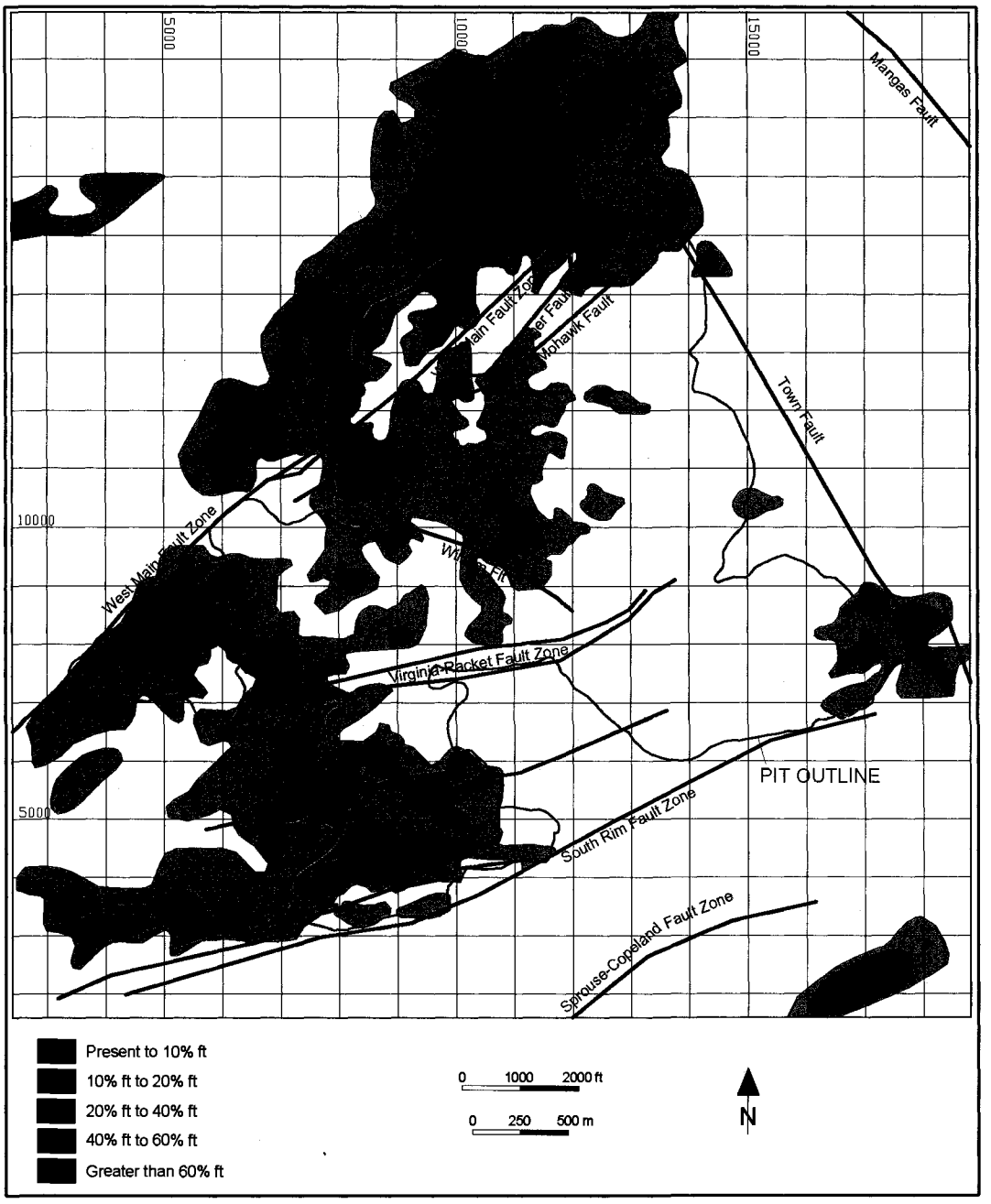

Figure 35. Generalized copper grade x thickness map in percent feet for ore mineral type 21, acid-soluble black copper oxides (copper wad, copper pitch, tenorite, and neotocite), and ore-mineral type 8, insoluble copper oxides (native copper, cuprite, and turquoise). Modified from Phelps Dodge Tyrone Geological Services, 2004.

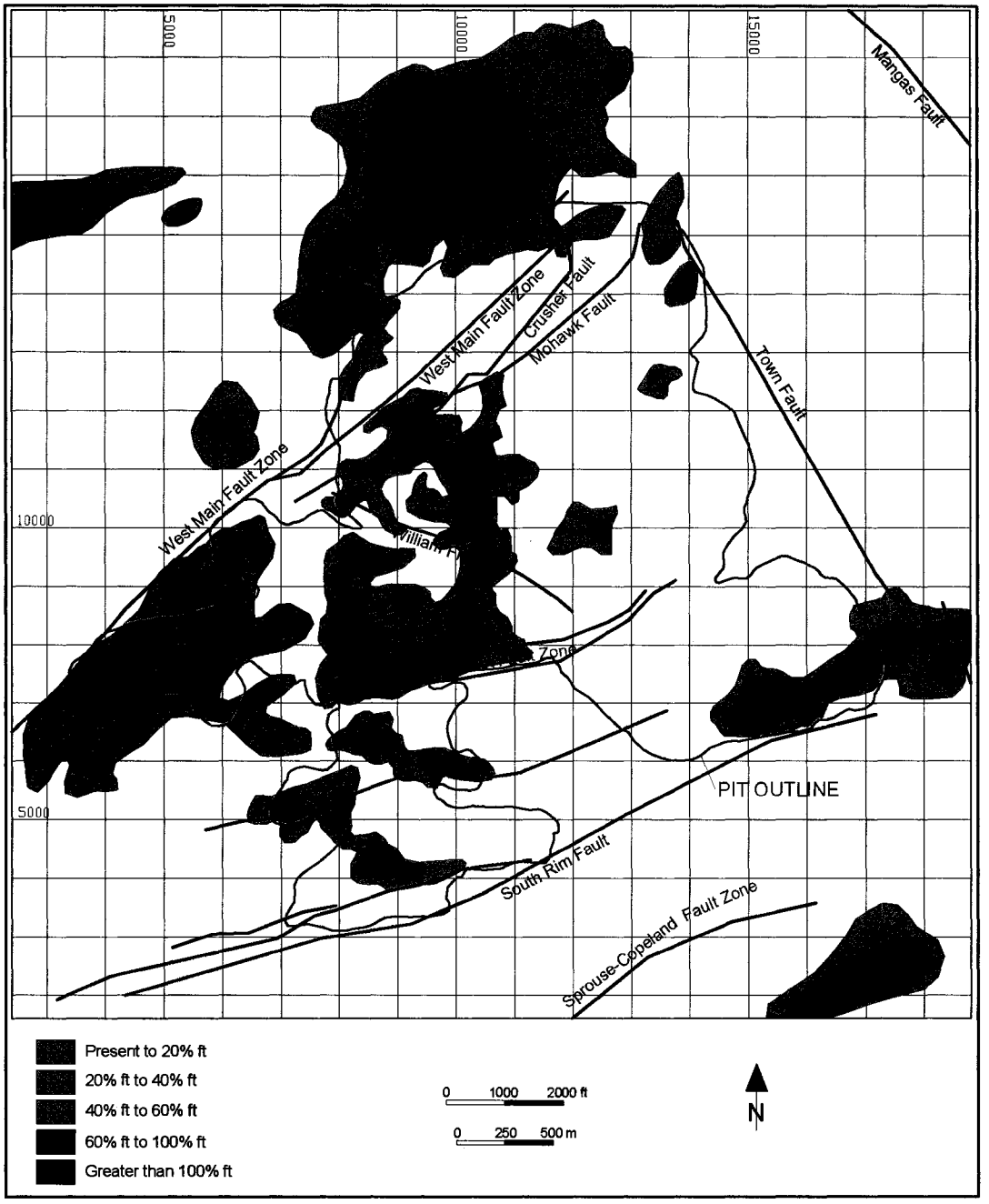

Figure 36. Generalized copper grade x thickness map in percent feet for ore mineral type 2, green, acid-soluble copper oxides (chrysocolla, malachite, and azurite). Modified from Phelps Dodge Tyrone Geological Services, 2004.

CHAPTER 8: ORE DEPOSITS–THE TYRONE SUPERGENE SYSTEM

INTRODUCTION

The description of the Tyrone supergene system that follows is from observations in this study, except where otherwise noted, and is based primarily on three types of data: 1) new drill hole logs and leached cap maps from this study (Plts. 3, 4, and 5); 2) grade x thickness maps of the various supergene ore types (Figs. 27, 35, and 36) provided by Phelps Dodge Tyrone Geological Services; and 3) ore mineral-type cross sections (Plt. 6) provided by Phelps Dodge Tyrone Geological Services.

For ease in comparison, the district geologic map (Fig. 5), map of the principal orebodies mined underground (Fig. 28), grade x thickness maps for ore mineral types (Figs. 27, 30, 35, and 36), isospach maps of hematite- and goethite-dominant leached cap (Figs. 39 and 40), and mass balance contour maps (Figs. 48, 49, and 50) were all prepared for this study to cover the same area, and are plotted at the same scale of 1:36,000 (1in = 3000 ft).

The supergene system at Tyrone consists of an oxidized and leached zone (leached cap), a discontinuous copper oxide zone, and a sulfide enrichment zone (chalcocite blanket) developed over the hypogene protore. The supergene system is characterized by its irregular nature (Fig. 23, Plt. 6). The boundaries between the various zones are controlled by downward projections of oxidized and enriched material along steep, through-going faults, fracture zones, and breccia zones (Fig. 37). Leached oxide zones plunging along faults and fracture zones bound all ore types (Plt. 6), and in many places, leached zones also lie between lenses of copper oxide material and the chalcocite enrichment blanket. Chalcocite zones extend into the protore along structures, and perched or isolated zones of hypogene sulfide material are also common within the leached cap, especially in the footwall zones of faults that acted as aquicludes for downward-moving, oxidizing solutions (Fig. 38).

The leached cap and copper oxide zones also show lateral variations in mineralogy across the district reflecting the variations in the hypogene alteration assemblage, pyrite:chalcopyrite ratio and hypogene sulfide content. In the northeastern part of the district where the copper deposit is characterized by high pyrite:chalcopyrite (~11:1), high total hypogene sulfide content (2-5 vol. %), and deep phyllic alteration, the chalcocite enrichment blanket is well-developed, hematite and jarosite are abundant in the leached cap, and the copper oxide zone is absent or poorly developed (Plt. 6). In contrast, in the southwestern part of the district where the copper deposit is characterized by lower pyrite:chalcopyrite (~7:1), lower total hypogene sulfide content (0.5-2.5 vol. %), and potassic alteration, goethite and pitch limonite are dominant in the leached cap, there is a thick, enriched copper oxide zone, and the chalcocite blanket is thin and poorly developed (Plt. 6).

The highly irregular nature of the supergene system and complex distribution of supergene ore types is the result of a number of factors including: 1) lateral variations in the sulfide content and alteration assemblage in the hypogene system, 2) structural control of groundwater movement, 3) differential uplift and depression of the hypogene system during faulting, 4) development of the supergene system in stages during episodic tectonic uplift and lowering of the local groundwater table, 5) lateral flux of copper and formation of exotic deposits, 6) local transition to more alkaline conditions during enrichment cycles as pyrite was consumed in the oxidizing column and top of the chalcocite enrichment blanket resulting in formation of copper oxide zones at the top of the enrichment blanket, 7) late-stage in-situ oxidation of sulfides in the enrichment blanket and copper oxide zone(s), and 8) faulting and tilting of the already-formed enrichment blanket and supergene system.

Figure 23 shows highly generalized southwest-northeast and northwest-southeast cross sections (H-H' and I-I', respectively), of the supergene system in the Tyrone district using the pre-mine topography. The cross sections were presented by Smith (1998) and illustrate the

lateral and vertical variability of the supergene system. Cross section H-H' shows 7-9° of northeast tilt of the chalcocite enrichment blanket beginning in the area of the William fault, and the northeast thickening of the leached cap and chalcocite enrichment blanket. Section H-H' is nearly parallel to the northeast-striking faults, so these faults are not shown on the section. The northeastern part of the deposit is covered by alluvial fan gravel (Figs. 5 and 23). The irregular nature of the leached cap, copper oxide zone, and chalcocite enrichment blanket are apparent. The base of the chalcocite enrichment blanket is characterized by "prongs" of chalcocite plunging deep into the protore along steeply-dipping, northeast-striking faults. The copper oxide zone is discontinuous and, while strongly developed in the central and southwestern parts of the district, it is absent in the northeastern part of the district around the Main pit. Late-stage erosion occurred after active supergene enrichment ceased, and has nearly cut into the chalcocite enrichment blanket in the southern part of the Main pit and in the Copper Mountain pit.

Cross section I-I' shows the thick chalcocite blanket in the area of the Main pit and lack of a well-developed copper oxide zone. Strong structural control of the chalcocite blanket is also apparent; the chalcocite blanket is thickened in the graben bounded by the Burro Chief-West Main fault zone on the northwest and the Virginia-Racket fault zone on the southeast. The chalcocite enrichment blanket and leached cap are thin and poorly-developed in the area of the Savanna and Gettysburg pits. An apparent 5-8° northwest tilt of the chalcocite blanket can be seen in the Main pit. Kolessar (1970) attributed the tilt to post-supergene displacements on the Burro Chief fault. However, this tilt is not evident on the ore mineral type sections (Plt. 6), nor on the structure contour map at the base of the alluvial fan gravel (Fig. 19). Since the post-alluvial fan gravel displacement on the Burro Chief fault is only 100 m (330 ft) in the vicinity of the Main pit, the apparent tilt is probably due to deep oxidation on the Burro Chief-West Main fault zone rather than to northwest tilt of the blanket.

ORE MINERAL TYPES

Table 4 summarizes the ore mineral types used by Phelps Dodge for modeling and ore control at the Tyrone mine (W. Seibert, pers. comm., 2005). Ore mineral type sections presented in Plate 6 are based on exploration and blast-hole drill data, and show the vertical and lateral relationships of the ore mineral types. The sections also show drill holes logged for this study. The order of ore mineral types on Table 4 reflect the typical downward transition or vertical zoning from leached cap (ore mineral type 1) consisting of limonite minerals, through black copper oxides (ore mineral type 21) consisting of acid soluble copper oxides such as copper wad, copper pitch, tenorite, and neotocite, into green copper oxides (ore mineral type 2) consisting of acid-soluble copper oxides such as chrysocolla and malachite, and finally into the enrichment blanket (ore mineral types 3, 4, and 5). Ore mineral type 8, insoluble copper oxides, is not abundant in the district and consists of native copper, cuprite, and turquoise. It typically occurs in the upper part of the copper oxide zone within black copper oxides, and above ore mineral types 2 and 3.

It should be noted that all of the copper oxide ore mineral types are enriched, having copper grades at least twice that of the protore (Table 4). For example, the green copper oxides (ore mineral type 2) have an average grade of 0.34% copper, or nearly a four-fold enrichment over the average hypogene ore grade of 0.09% copper; these high copper grades probably reflect in-situ oxidation of the chalcocite blanket. The black copper oxides (ore mineral type 21) and insoluble copper oxides (ore mineral type 8) have average grades of 0.18% copper, only twice that of the protore. These lower grades are typical of first-cycle oxidation and enrichment. The copper oxide ores are less enriched overall than ore types within the chalcocite blanket, which average 0.48% copper. The various ore mineral types are discussed in the following sections on the leached cap, copper oxide zone, and enrichment blanket.

LEACHED CAP

The leached cap at Tyrone is extremely variable in its thickness (Fig. 23), limonite mineralogy, and degree of leaching. The leached cap contains 200 to 700 ppm copper (0.02-0.07%) and averages 500 ppm copper (0.05%) due to incomplete leaching (Chávez, 2000). This residual copper is included in limonite and copper-iron mineraloids (black copper oxides).

In the northeastern part of the district around the Main pit, the leached cap and chalcocite enrichment blanket are developed within phyllically-altered, sulfidic (2-5 vol. % total hypogene sulfide) rocks that produced abundant acid. The leached cap in that area is hematitic as it is derived from the oxidation of previous chalcocite blankets, and it overlies a mature chalcocite blanket. For the most part, copper leaching has been thorough and black copper oxide zones are absent or weakly developed because pH of recharge waters remained acidic (pyrite was not completely consumed). The phyllic alteration zone is overprinted by deep supergene argillic alteration consisting of kaolinite and montmorillonite, along with limonite minerals. Some lower jarosite zones occur in the leached cap, marking positions of pyrite-rich protore between successive enrichment blankets. However, jarosite-dominant zones are not common as both upper and lower jarosite zones were probably converted to mixtures of goethite and jarosite during later-stage oxidation and leaching (Titley and Marozas, 1995). Chalcanthite occurs in places in the leached cap overprinting the remaining perched sulfide zones.

In the southwestern part of the district around the Copper Mountain and South Rim pits, the leached cap is developed within a thin phyllic alteration zone that overprints propylitic and weak potassic assemblages. The total hypogene sulfide content is lower (0.5-2.5 vol. %). Goethite and black copper oxide minerals dominate in the leached cap and kaolinite is less abundant. Copper leaching and enrichment were less thorough due to the low sulfide content and reactive host rocks. The copper oxide zone is well-developed and it overlies a chalcocite blanket

that is thinner and of lower grade than the blanket in the northeastern part of the district (see grade x thickness maps, Figs. 27, 35, and 36).

Focused movement of oxidized solutions along faults and fracture zones resulted in deep oxidation and leaching along these structures. In many places, oxidized material extending along faults has truncated the enrichment blanket or formed perched sulfide zones. Figure 37A is a photo in the San Salvador pit looking southwest at a strand of the South Rim fault. A goethitic oxidized zone is present along the trace of the fault, with unoxidized chalcocite preserved in the hangingwall. In Figure 37B, clay gouge along the Crusher fault formed a permeability barrier to downward-moving copper-bearing solutions leading to deep chalcocite enrichment along the hangingwall side of the fault. Subsequent leaching and oxidation of the chalcocite produced live limonite.

The intrusive apophysis of Stage 2 monzonite porphyry and Stage 3 quartz monzonite porphyry at Tyrone Peak in the southern Little Burro Mountains is characterized by phyllic alteration overprinted by supergene argillic alteration with locally strong jarosite staining. Drilling at Tyrone Peak indicates lack of a well-developed chalcocite enrichment blanket. Based on the original jarosite zone in the leached cap and low hypogene copper values (0.04-0.05% Cu), Tyrone Peak is interpreted to be in the copper-poor pyritic halo at the margin of the porphyry copper system.

COPPER OXIDE ZONE

The copper oxide zone is discontinuous, highly irregular, and structurally-controlled (Plt. 6). It averages 60-90 m (200-300 ft) thick where present in the mine and ranges up to 240 m (800 ft) in thickness. It is up to 460 m (1,500 ft) thick in the Burro Chief-West Main fault zone outside of the mine area (Plt. 6). The most abundant minerals in the copper oxide zone are chrysocolla, black copper oxides such as tenorite, melaconite and delafossite, and black copper silicates such

as neotocite (Kolessar, 1982; DuHamel et al., 1995). Malachite, cuprite, and native copper are common but not abundant, and are typically found mixed with limonite in areas where older supergene mineralization has been re-weathered (DuHamel et al., 1995). Tenorite, malachite, and azurite, together with rare cuprite, native copper, brochantite, and chalcanthite were present in the leached capping and in the Burro Chief fault zone (Kolessar, 1982). Azurite and turquoise were also commonly found in the early years of mining (DuHamel et al., 1995). The typical vertical sequence in the copper oxide zone is, from top to bottom, black copper oxides including pitch limonite and tenorite (ore mineral type 21), grading into green copper oxides chrysocolla and malachite (ore mineral type 2), mixed oxide-chalcocite (ore mineral type 3), and finally chalcocite (ore mineral type 4). The insoluble copper oxides cuprite and native copper (ore mineral type 8) typically occur as relict lenses within black copper oxides (ore mineral type 21), between the black copper oxides and green copper oxides (mineral type 2), and overlying the partially oxidized chalcocite blanket (ore mineral type 3).

In the southwestern part of the district, a thick, enriched copper oxide zone typically overlies a thin, low-grade chalcocite blanket, and in places, the grade of the oxide zone is actually higher than the grade of the underlying chalcocite enrichment blanket. This is reflected in copper grades of oxide ore mineral types shown in Table 4. Ore mineral type 2 (green copper oxides) has an average grade of 0.34% Cu, which is near the average grade of ore mineral type 4, the chalcocite blanket, at 0.48% Cu. Such a relationship (i.e., higher copper grade in the oxide zone than in the enrichment blanket) suggests that either, 1) enrichment occurred in the copper oxide zone above the blanket during active enrichment as described by Lichtner and Biino (1992), and copper oxide was preferentially enriched over the chalcocite blanket, or 2) copper in the higher grade portion at the top of the chalcocite blanket was fixed by in-situ oxidation of chalcocite, with only minor leaching of copper (Chávez, 2000).

The copper oxide zone is not as well developed in the northeastern part of the district. Most commonly, the supergene system in the northeastern part of the district consists of a leached cap overlying the chalcocite enrichment blanket, with no intervening copper oxide zone, or late-stage oxidation has resulted in ore mineral type 3 (mixed oxide-chalcocite) at the top of the chalcocite blanket (Fig. 23, Plt. 6).

The copper oxide ore mineral types and copper oxide zones formed through several related processes described in Chapter 7. In the southwestern part of the district where the host rocks are altered to potassic assemblages and the hypogene sulfide content is low, acidic conditions were not maintained during oxidation. The black copper oxides pitch limonite and tenorite (ore mineral type 21) may have formed within goethitic leached cap by essentially in-situ oxidation of chalcopyrite protore during first-cycle leaching. Cuprite and native copper probably also formed in a near-neutral environment in the deeper parts of the oxidizing column above the chalcocite blanket, the downward progression from tenorite through cuprite, native copper, and finally chalcocite reflect a decrease in oxygen fugacity with depth (Kwong et al., 1982).

In the northeastern part of the district, copper oxide minerals did not begin to form until pH increased as pyrite was consumed from the column of oxidizing rock. With the increase in pH, copper oxide minerals could have been deposited during active enrichment in ghost zones above the chalcocite blanket in a downward progression from tenorite through brochantite, cuprite, native copper, and finally chalcocite (Lichtner and Biino, 1992). This process could have been repeated during numerous cycles of enrichment. Cuprite and native copper zones (ore mineral type 8) that occur as relict lenses within the leached cap may be remnants of copper oxide ghost zones that were incompletely leached during renewed uplift and supergene enrichment. Finally, the chalcocite blanket was partially oxidized and earlier-formed copper sulfates destroyed by late-stage in-situ "weathering" oxidation. Late-stage in-situ oxidation occurred in arid conditions after active leaching and enrichment had essentially ended, the groundwater table was

rapidly lowered below the top of the chalcocite blanket, and pyrite was completely consumed in the oxidized zone. The latter mode of copper oxide formation may have been most important in the northeastern part of the district as there is evidence for strongly acidic conditions through the Miocene and into the Pliocene including the ferricrete deposits (~12.1 Ma) which required strongly acidic conditions for transport of copper and iron, and alunite as young as 4.6 Ma (Chapter 9). Copper oxide zones could also have formed locally during active enrichment in the northeastern part of the district where strong groundwater recharge along faults allowed solutions to become dilute.

The common occurrence of chrysocolla, which is paragenetically late and occupies "clean", late-stage fractures (Somers, 1915) immediately above the chalcocite enrichment blanket indicates that late-stage in-situ oxidation is characteristic of the Tyrone supergene ore. Chalcocite and any copper sulfates formed during active leaching and enrichment would all have been subject to late stage oxidation and replacement by chrysocolla. Cuprite and native copper (ore mineral type 8) may also have formed by in-situ oxidation of chalcocite (Anderson, 1982) as these commonly occur at the top of the partially oxidized chalcocite blanket (ore mineral type 3). Somers (1915) noted that small flakes of native copper occur in fractures with red powdery hematite, an oxidation product of chalcocite. Where pre-mine drainages such as Niagara Gulch (Fig. 28) were incised into the top of the chalcocite blanket, the chalcocite blanket was oxidized to copper oxide minerals (DuHamel et al., 1995).

The enriched copper oxide zone at Tyrone is important in supergene copper mass balance calculations. The enriched copper oxides must be included in the chalcocite blanket for meaningful results, as discussed in Chapter 10.

CHALCOCITE ENRICHMENT BLANKET

The chalcocite blanket is generally 60-90 m (200-300 ft) thick in the northeastern part of the district, but ranges up to ~150 m (~500 ft) thick (Plt. 4). It thins to the southwest and is generally less than 60 m (200 ft) thick in the southwestern part of the district. The chalcocite blanket is very irregular in form, with uneven upper and lower surfaces, and it is locally cut by leached, oxidized zones that plunge along high-angle faults, fracture zones and intrusive breccias (Figs. 37 and 38, Plt. 6). Leached, oxidized zones along structures are especially common in the northeastern part of the district where descending groundwater solutions were much more acidic. The chalcocite blanket extends from the Copper Mountain mine down-dip to the northeast and is offset by the Town fault beneath alluvial fan gravel in the Mangas Valley (Fig. 23).

Ore mineral type cross sections through the district (Plt. 6) show that the chalcocite blanket has a variable northeast tilt. In the southwest part of the district, the chalcocite blanket is nearly horizontal and the top of the blanket is a gently undulating surface that maintains an elevation of approximately 1,890 m (6,200 ft) (Plt. 6). In the northeastern part of the district, the chalcocite blanket is tilted 7-9° to the northeast. The change in tilt is fairly abrupt with an apparent hinge line in the vicinity of the William fault and the Virginia-Racket fault zone (Fig. 23; Plt. 6, section 10800E). The irregular nature of the chalcocite blanket and northeast grain due to northeast-striking faults and fracture zones are also evident on the structure contour map on the top of the chalcocite blanket (Plt. 7).

The chalcocite blanket consists of fissure fillings, disseminations, and breccia ore in which chalcocite has replaced pyrite, chalcopyrite, and sphalerite (Somers, 1915; Gillerman, 1964; DuHamel et al., 1995). Prior to 1921, underground mining concentrated on rich chalcocite orebodies along northeast-striking fracture zones associated with the Niagara-Mohawk, Bison-Thistle, Copper Gulf, and Gettysburg faults (Fig. 28) (Somers, 1915; Gillerman, 1964). These ores contained both open-space fillings and replacements of hypogene veins (DuHamel et al.,

1995). The highest-grade chalcocite orebodies in the Main pit occur in fracture zones and breccia bodies in a graben between the northeast-striking Burro Chief-West Main fault on the northwest and the east-northeast-striking Racket Virginia fault on the south. The graben is clearly visible on ore mineral-type cross sections (Plt. 6; Fig. 23) and on the chalcocite grade x thickness map (Fig. 27).

Both sooty and steel glance or massive chalcocite occur at Tyrone (DuHamel et al., 1995). Sooty chalcocite is most common and is composed mostly of djurleite ($Cu_{1.9}S$) and anilite ($Cu_{1.7}S$) with true chalcocite being less abundant (DuHamel et al., 1995). Disseminated ore consists of sooty chalcocite rimming and replacing hypogene chalcopyrite and pyrite. Chalcocite replaces chalcopyrite before pyrite, and where there is strong development of chalcocite, usually little chalcopyrite remains. Steel glance chalcocite is more characteristic of complete replacements in veinlet and breccia ore (Fig. 34) and is found mainly in the area between the Burro Chief-West Main and Mohawk-Crusher fault zones (DuHamel et al., 1995).

DISTRIBUTION OF SUPERGENE COPPER GRADES AND GRADE X THICKNESS

As noted above, the chalcocite grade x thickness map (ore mineral types 3, 4, and 5, Fig. 27) shows that most of the chalcocite ore is restricted to the graben between the Burro Chief-West Main and Virginia-Racket fault zones. The highest grade x thickness values in chalcocite ore (>200% feet) are at the margins of the Proterozoic granite in contact with Stage 3 quartz monzonite porphyry in the Main pit, and within Stage 2 monzonite porphyry and Stage 3 quartz monzonite porphyry in contact with Upper Cretaceous-Paleocene andesite in the Savanna pit. Strong chalcocite mineralization of >200% feet is also found around Stage 3 intrusion breccias and Proterozoic granite in the Gettysburg pit. Grade x thickness values of >200% feet also occur beneath alluvial fan gravel in the Mangas Valley north of the Main pit. Northeast and northwest

fabric are visible in the chalcocite grade x thickness corresponding to northeast and northwest faults that served as conduits for movement of copper-bearing fluids.

Grade x thickness maps for copper oxide ore mineral types 21 and 8 (Fig. 35) and ore mineral type 2 (Fig. 36) reveal a similar distribution for the copper oxide ore mineral types. Ore mineral types 21 and 8 (Fig. 35) are more widely distributed than ore mineral type 2 but are characterized by lower grade x thickness values than ore mineral type 2 (Fig. 36). The copper oxides are concentrated in four areas: 1) in Stage 1 granodiorite porphyry in the southwestern parts of the district in the Copper Mountain, San Salvador, and South Rim pits; 2) in Proterozoic granite to the northwest of the Burro Chief-West Main fault zone; 3) to the north of the South Rim fault in the Gettysburg pit; and 4) north of the Main pit under alluvial fan gravel in Mangas Valley. The copper oxide ore minerals are most strongly developed in the area north of the Main pit between the Burro Chief and West Main faults, but strong grade x thickness values (>60% ft for ore types 21 and 8 and >100% ft for ore type 2) are also found throughout the southwestern part of the district. A wide north-trending zone devoid of copper oxide mineralization occurs in the eastern part of the district between the Main and Gettysburg pits.

The distribution of high grade x thickness values for ore mineral type 2 (Fig. 36) more closely mimic the distribution of the chalcocite grade x thickness values (Fig. 27) than do the grade x thickness values for ore mineral types 21 and 8 (Fig. 35), indicating that ore mineral type 2 is most strongly developed over the chalcocite blanket. This is especially evident in the central part of the district north of the Virginia-Racket fault zone and around the William fault (Fig. 36). The chalcocite blanket has been oxidized in the central part of the district where erosion has removed much of the leached cap along Niagara Gulch and other drainages (Fig. 28).

As mentioned above, ore mineral types 21 and 8 are low grade and probably formed by essentially in-situ oxidation of a reactive protolith capable of buffering acid and suppressing

leaching of copper. Ore mineral type 2 is higher grade possibly because it was derived dominantly from late stage in-situ oxidation of chalcocite.

DRILL HOLE LOGGING AND LEACHED CAP LIMONITE MAPPING

As part of this study, the leached cap, copper oxide zone (if present), and top of the chalcocite blanket were logged in 86 drill holes in a 370 m x 370 m (1,200 ft x 1,200 ft) grid over the district (Plt. 4) for a total of 9,035 m (29,643 feet). The drill holes used included older (1950s vintage) churn rotary holes from the pre-mine development drilling, and newer reverse circulation and core holes. Logging was done to determine: 1) the distribution of limonite minerals in the leached cap and the relationship of leached cap limonite mineralogy to the underlying supergene copper mineralogy (i.e., oxide vs. sulfide); 2) the lateral continuity of limonite mineral zones (e.g., strong hematite intervals representing relict chalcocite blankets) to document, if possible, the number of enrichment events; 3) the dip of the supergene blanket(s) and the possibility of discernible dip fanning in limonite zones in the leached cap to distinguish separate uplift and tilting events during active enrichment; and 4) hypogene alteration assemblage and hypogene sulfide content.

Drill holes that best represent the entire leached cap (i.e., pre-mining) were selected for logging. Older churn holes and reverse circulation holes that penetrated the entire leached cap were used wherever possible. The holes were logged for lithology, structure, limonite and copper oxide mineralogy, hypogene alteration type, and supergene alteration type. Logging in each hole was stopped below the transition from oxide to sulfide, and an estimate of the hypogene sulfide content was made in the chalcocite blanket. Transitions in the limonite mineralogy and alteration type were easier to distinguish in reverse circulation cuttings and core than in churn cuttings because churn cuttings were more mixed by the drilling process.

The dominant limonite minerals were identified by comparing the streak color of the powdered limonite with standard Munsell Soil Color chips. Limonite minerals and corresponding Munsell colors are given by Loghry (1972). The limonite minerals were logged as indigenous or transported based on their textures. The only copper oxide minerals observed in the logging were black copper oxides recorded as pitch limonite, and chrysocolla. Pitch limonite plates copper with HCl when powdered with a steel knife blade, and probably contains some tenorite and neotocite.

The leached cap data were recorded using the Kennecott coding scheme. Coded features on the drill hole logs in Plate 3 and Appendix C are: 1) dominant indigenous limonite mineralogy, 2) percentage of indigenous limonite divided by ten, 3) texture of limonite boxworks, 4) percentage of indigenous limonite that occurs in veins as opposed to limonite replacing disseminated sulfide grains, and 5) original percentage of sulfides.

Representative logs of core hole B-36 and reverse circulation hole H-012 are shown on Plate 3; drill hole locations are shown on Plate 4. Drill holes B-36 and H-012 illustrate the differences in hypogene alteration and sulfide mineral content from the northeastern part of the district (B-36) to the southwestern parts of the district (H-012). These holes are dicscussed below.

Core hole B-36 is located within the West Main fault zone in the Main pit (Plt. 4). The dominant lithologies in B-36 are Stage 2 monzonite porphyry, Stage 3 quartz monzonite porphyry, and Proterozoic granite. Alteration consists of moderate to strong hypogene phyllic alteration overprinted by weak to moderate supergene argillic alteration. B-36 clearly shows characteristics of a leached cap overlying a chalcocite blanket. A thick hematitic interval occurs from the collar to a depth of 122 m (400 ft) and is underlain by a lower jarosite interval from 122 m to 155 m (510 ft). These zones lie above the current top of the chalcocite blanket which is at a depth of 155 m. Limonite minerals in the hematite and jarosite intervals are mixtures of

transported and indigenous varieties, with transported varieties being dominant. Alunite veins occur in numerous intervals in the leached cap from 11 to 119 m (36 to 392 ft). Individual alunite veins are up to 12 cm thick but average 1 cm or less. The alunite veins were sampled for $^{40}Ar/^{39}Ar$ dating and sulfur and oxygen stable isotope work; results of $^{40}Ar/^{39}Ar$ and stable isotope analyses are discussed in Chapters 8 and 9, respectively. Within the logged sulfide interval, hypogene pyrite plus chalcopyrite (and or chalcocite) average 2-4 volume percent.

Drill hole H-012 is a reverse-circulation hole drilled immediately south of the South Rim pit (Plt 4). The lithology in hole H-012 is Stage 1 granodiorite that has been altered to propylitic and potassic assemblages. A phyllic overprint occurs from 0 to 70 m (0 to 230 ft). These assemblages contain 1-2.5 volume percent hypogene pyrite plus chalcocite. A thin zone of ~1% molybdenite mineralization occurs from 104 to 113 m (340 to 370 ft). The goethitic leached cap extends from the surface to 61 m (200 ft), and a thin (21 m (70 ft)), low-grade chalcocite enrichment blanket occurs from 61 to 82 m (200 to 270 ft). A copper oxide zone consisting of an upper pitch limonite zone and a lower chrysocolla zone occurs from 43 to 67 m (140 to 220 ft), with the chrysocolla zone overlapping the enrichment blanket. This is a good example of late-stage oxidation producing chrysocolla that partially replaced the chalcocite enrichment blanket.

East-west and north-south cross sections were constructed through the district with the drill hole logs hung by elevation (Plt. 5, cross sections C-C' and D-D'). In general, the cross sections show that limonite mineral zones are not laterally continuous, and very few limonite mineral zones in the leached cap can be correlated between holes. This is probably due to both the wide spacing of the logged holes (370 m (1200 ft)) and the highly irregular, structurally-controlled supergene system as described above. The ore mineral type sections (Plt. 6) clearly illustrate the strong structural control on the supergene system.

On east-west drill hole cross section C-C' in the northern part of the district (Plt. 5), the leached cap is up to 183 m (600 ft) thick and consists of hematite and lower jarosite horizons.

Some possible correlations of strong hematite and lower jarosite horizons are shown between drill holes BD-35 and B-36 on the section. BD-35 and B-36 are located within the Burro Chief/West Main fault zone. East-west ore mineral type section E-E' (13,600 N, Plt. 6) is on the same northing as section C-C' (13,600 N, Plt. 5), and it reveals that the supergene profile between the Burro Chief and West Main faults is strongly structurally controlled, with irregular unoxidized remnants of mixed oxide-chalcocite, chalcocite, and protore extending upward into the leached cap. Therefore, the correlations shown on cross section C-C' (Plt. 5) are doubtful.

North-south cross section D-D' (Plt. 5) shows a clear transition from thin (30-60 m (100-200 ft) thick), goethite-dominant leached cap containing copper oxides in the southern part of the district to thick, hematite-dominant leached cap in the northern part of the district. The base of the leached cap/top of the chalcocite blanket on section D-D' is at a fairly consistent elevation of 1,890 m (6,200 ft) from south to north to the vicinity of drill hole N-12; the leached cap then thickens dramatically to the north, and the top of the chalcocite blanket slopes to the north at 7-9°. Cross section D-D' demonstrates both the thickening and northeast tilt of the leached cap in the northern part of the district. Again, few definite correlations of limonite mineral horizons can be made in the leached cap, and no dip fanning of hematite horizons is visible. A strong hematite horizon can possibly be correlated between drill holes M-35 and M-41 on the north end of the section.

Plate 4 summarizes the distribution of limonite minerals and alteration types in the leached cap based on the drill hole logs. For each drill hole, the total thickness of hematite-, goethite-, jarosite-, and pitch limonite-dominant intervals is given. It should be noted that these are aggregate thicknesses. Limonite intervals were logged as weak, moderate, and strong, but these distinctions were not broken out in the aggregate thickness. In addition, many intervals have mixed limonite mineralogy with nearly equal amounts of more than one limonite mineral. In these cases, the limonite mineral considered to be more abundant was used. Alteration logged

in the leached cap in most of the holes is hypogene phyllic alteration with a supergene argillic overprint, although propylitic and potassic alteration was logged in some holes in the southern and southwestern parts of the district as noted above.

The limonite distribution map (Plt. 4) clearly shows goethite-dominant leached cap in the southwestern part of the district and hematite-dominant (and locally interlayered hematite-jarositic) leached cap in the northeastern part of the district. Pitch limonite is rarely the dominant limonite type and it occurs mostly in the southwestern part of the district. The transition from goethite- to hematite-dominant leached cap is somewhat irregular and trends in a northwest direction through the Gettysburg and Main pits. This break appears to correspond roughly with the William fault, a northwest-striking normal fault that cuts some northeast-striking faults.

Hematite and Goethite Isopach Maps

Figures 39 and 40 are isospach maps of hematite- and goethite-dominant leached cap thickness, respectively, from data presented on Plate 4. The hematite-dominant leached cap ranges from 0-305 m (0-1,000 ft) thick (Fig. 39), and with many exceptions, broadly reflects the grade x thickness values for chalcocite (Fig. 27). The thickest hematite-dominant leached cap and highest chalcocite grade x thickness values occur in the graben between the Burro Chief and Virginia-Racket faults. This graben formed a sink for laterally-transported copper in the supergene environment.

The goethite-dominant leached cap (Fig. 40) ranges from 0 to 180 m (0-590 ft) thick, and is best developed in the central and southern parts of the district. Of the two copper oxide grade x thickness maps (Figs. 35 and 36), the goethite leached cap thickness corresponds most closely to the grade x thickness distribution for ore mineral types 21 and 8 (black copper oxides, cuprite, native copper) (Fig. 35). These copper oxide minerals and the goethitic leached cap probably formed dominantly by in-situ oxidation of hypogene sulfides during active supergene enrichment in areas with a low pyrite content and reactive host rocks.

The leached cap has been extensively eroded and illustrates the effects of lateral copper flux. Many areas of post-enrichment erosion of the leached cap are visible on the ore mineral type cross sections on Plate 6. In these areas, a thin leached cap overlies a thick chalcocite blanket. The hematitic leached cap is dramatically thinned to the south of the William fault because goethite becomes dominant to the south of the fault, but also because of post-enrichment erosion of the leached cap along Niagara Gulch (Fig. 39).

Examples of lateral copper flux can be seen in drill holes C-42 and AL-0, both of which contain thick hematitic leached caps (305 m (1000 ft) and 155 m (510 ft), respectively) (Plt. 4) but no chalcocite blanket. The leached cap in these holes is dominated by weak to moderate hematite, with only short intervals of strong hematite (15 m (50 ft) in C-42 and 6 m (20 ft) in AL-0). These holes fall within zones of negative copper flux (Chapter 10, Plt. 10), indicating that copper was transported away laterally during supergene enrichment.

The laterally-zoned supergene system at Tyrone, from a chalcocite-dominant supergene deposit in the northeast part of the district to a copper oxide-dominant deposit in the southwest part of the district, is thus clearly reflected in the limonite mineralogy of the leached cap. However, the thickness of hematite-dominant leached cap cannot always be used to predict the thickness (or presence) of an underlying chalcocite enrichment blanket. Post-enrichment erosion of the leached cap and lateral copper flux are factors that must be kept in mind when using leached cap limonite data as a predictive tool in exploration for chalcocite ore.

Alunite Veins

Supergene alunite veins are abundant in the leached cap in the northern part of the Tyrone district and they also occur in argillized monzonite porphyry at Tyrone Peak. Alunite veins were logged in several core holes in the Main pit. The alunite veins are massive, cryptocrystalline, porcelaneous, and occur in phyllically-altered Proterozoic granite or porphyry of the Tyrone stock that is overprinted by supergene kaolinite. Most veins are a few mm to a few

cm thick, but they range up to 20 cm (8 inches) in thickness (Kolessar, 1970). Figure 41 shows typical alunite veins from the Tyrone deposit.

The alunite veins are dominantly east-northeast-striking (N69-85°E) with steep southeast dips, or west-northwest-striking (N20-90°W) with northeast and southwest dips. Less commonly the veins strike to the north-northeast (N18-39°E) with northwest dips. The various vein orientations show no consistent relative ages, and many crosscutting relationships are equivocal. Supergene alunite is also found as disseminated masses within the argillized wall rock but disseminated alunite was not sampled for this study. A supergene origin for the alunite is indicated by Miocene-Pliocene ages (4.55 ± 0.13 to 22.15 ± 0.23 Ma) determined by Ar^{40}/Ar^{39} dating (Chapter 9), and by sulfur isotopes ($\delta^{34}S$ = -0.6 to 2.4‰) which show that alunite contains sulfur derived from destruction of hypogene sulfides (Chapter 11).

MULTI-ELEMENT GEOCHEMISTRY OF EXOTIC DEPOSITS

Two Tertiary sedimentary units in the Tyrone area contain exotic copper derived from weathering and erosion of the porphyry copper deposit. These include the upper Eocene ferruginous sandstone and conglomerate unit that lies between the Bell Top Formation and the Sugarlump Tuff in the southern part of the Little Burro Mountains, and the ferricrete unit at the base of late Miocene-Pleistocene alluvial fan gravel. Both copper-bearing units are fluvial channel-fill deposits. Copper, iron and manganese minerals in these units were deposited from groundwater that flowed laterally away from the oxidizing copper deposit into paleochannels.

Multi-element analyses were completed on 14 samples of ferricrete and six samples of ferruginous sandstone and conglomerate. The ferricrete samples include four samples of distal copper- and manganese-rich conglomerate and sedimentary breccia from the Emma prospect and Tyrone Peak. Sample locations are shown on Figure 42 along with values for Cu, Mn, and Fe.

The location of the Emma samples south of the Gettysburg pit are shown on Figure 4. Analyses for the samples are included in Appendix B.

Eocene Ferruginous Sandstone and Conglomerate

The upper Eocene ferruginous sandstone and conglomerate unit occurs in the southern Little Burro Mountains where it fills paleochannels cut into the Bell Top Formation and Cretaceous-Paleocene andesite (Fig. 15). The geometry of the channel fill deposits is not known as the unit is thin (average 1-3 m (3-10 ft)) and occurs in discontinuous outcrops. The unit is red to reddish-brown, strongly hematitic, planar to cross-bedded and contains pebbles of tuff, andesite, and rarely, altered intrusive rocks from the Tyrone stock.

Samples of the ferruginous sandstone and conglomerate were collected along a strike length of 2,440 m (8,000 ft). Multi-element analyses confirmed the presence of exotic copper in the unit. Copper values are fairly low, ranging from 23 to 467 ppm. The copper values are highest (222-467 ppm) near the Tyrone mine, and they decrease with distance from the mine (Fig. 42). Copper probably resides in hematite or copper wad, although no black copper oxide minerals were noted. Manganese (243 to 1110 ppm) and iron (2.3-11.0%) values are high, and they show no consistent variation with distance from the mine. Some of the highest manganese and iron values (1110 ppm and 11.0%, respectively), are from a paleochannel 3.7 km (12,000 ft) north of the Main pit (Fig. 42). The ferruginous sandstone and conglomerate unit appears to be proximal facies in the Münchmeyer (1996) classification, consisting of hematite-cemented conglomerates. The ferruginous sandstone and conglomerate unit provides strong evidence for weathering and erosion of the upper parts of the Tyrone deposit during the Eocene erosional event that followed the Laramide orogeny.

Miocene Ferricrete

The ferricrete occupies northeast-trending paleochannels at the base of the basin-fill gravels, and attains a maximum thickness of about 55 m (180 ft.). The paleochannel deposits

overlie the Tyrone stock in the Big Burro Mountains, and they extend northeast into the southern Little Burro Mountains where they overlie porphyritic units of the Tyrone stock and late Eocene-Oligocene tuff (Plt. 1, Fig. 22A). The ferricrete consists of coarse, poorly-sorted conglomerate and planar- and cross-bedded, medium- to coarse-grained lithic sandstone. Clasts consist predominantly of altered, gossanous rocks from the leached cap of the Tyrone deposit including porphyry units of the Tyrone stock and Proterozoic granite. The ferricrete is mineralogically zoned from a hematite-rich proximal zone extending at least 3.2 km (2 mi) into the Little Burro Mountains, to a chrysocolla-rich distal or peripheral zone beyond the hematite zone.

Copper values in the hematite-rich proximal zone range from 237 to 2290 ppm, and copper is very persistent laterally. Paleochannel material sampled north of Tyrone Peak contains 1710 to 2290 ppm copper, and the same paleochannel intersected in drill hole NXBM-6, 3.2 km (2 mi) northeast of the Main pit contains as much as 2700 ppm copper (Fig. 42). The iron content of ferricrete in the proximal zone ranges from 2.3 to 18.6%. Iron is also laterally persistent and strongest in the paleochannel deposits, ranging from 12 to 18.6%. Manganese content of ferricrete in the proximal zone ranges from 158 to 1940 ppm. The distribution of copper in northeast-trending paleochannels demonstrates the role of northeast tilting in lateral movement of copper away from the deposit during Miocene oxidation and erosion.

Isolated, distal outcrops of breccia and conglomerate cemented with copper wad and manganese-rich chrysocolla occur at the Emma prospect south of the Gettysburg pit (Fig. 4), and on the southeast slopes of Tyrone Peak (Fig. 42). The distal ferricretes are extremely rich in copper and manganese but lower in iron than many of the paleochannel samples. Hematite is conspicuously absent. The Emma samples contain up to 4.7% Cu, 6760-9730 ppm Mn, and 1.8-2.6% Fe. Chrysocolla occurs as a cement in the Emma samples, making up about 6-8% of the rock. The Tyrone Peak samples (Fig. 22B) contain 3570-6040 ppm Cu, >10,000 ppm Mn, mostly as black copper wad, and 2.3-2.9% Fe. The Emma and Tyrone Peak ferricretes are similar in that

they both contain only locally-derived clasts. The Emma breccia lies on Proterozoic granite and the rock consists of disaggregated granite. The Tyrone Peak breccia lies on Stage 3 quartz monzonite porphyry, and the rock consists of angular clasts of quartz monzonite porphyry, monzonite porphyry, and rhyodacite. Similar exotic copper deposits at the Southern Star mine were probably derived from the Little Rock copper deposit (Fig. 4).

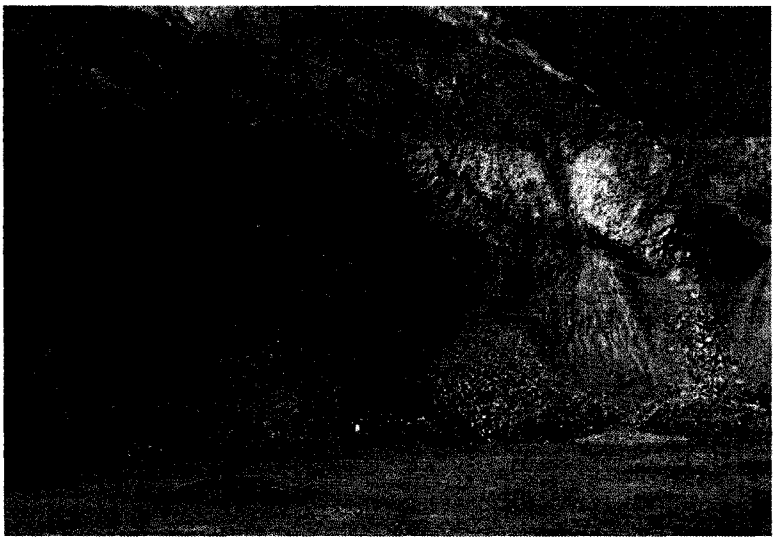

A

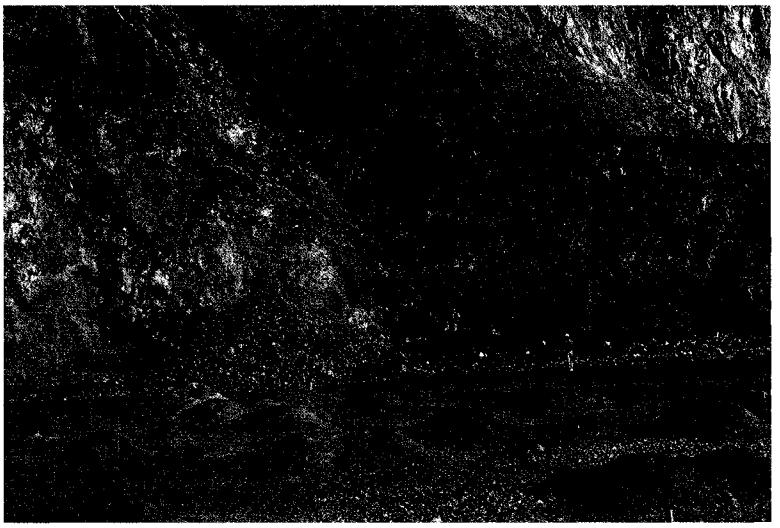

B

Figure 37. A. South Rim fault zone in the San Salvador pit, looking southwest. Bench height 15 m (50 ft). The South Rim fault zone strikes northeast and dips northwest; it is the southern boundary of supergene chalcocite mineralization in the district. Hematitic (reddish-brown) and goethitic (yellowish-brown) oxide of the leached cap are visible plunging along the fault, and a perched chalcocite zone (gray) is preserved in the hangingwall. B. Crusher fault in the Main pit, looking north. The Crusher fault is a major northeast-striking, southeast-dipping structure. Deep chalcocite enrichment on the hangingwall side of the fault is indicated by strong hematite (live limonite) replacing chalcocite.

A

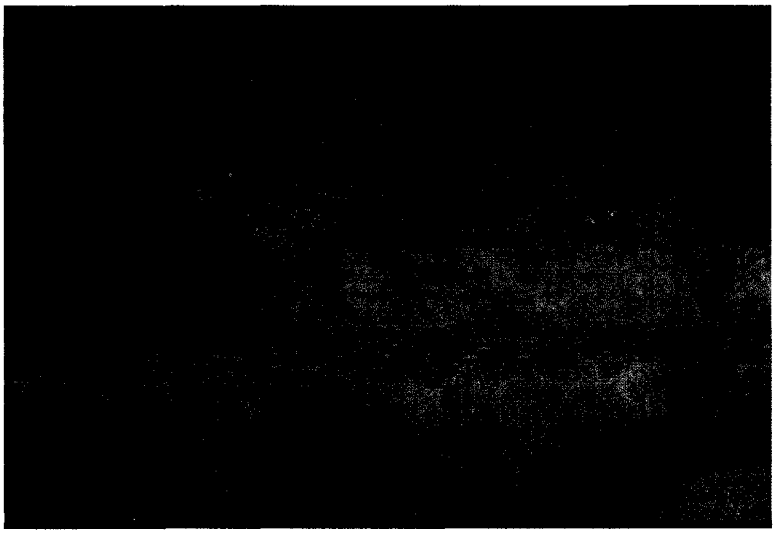

B

Figure 38. A. Main pit looking north. Hammer for scale at center of photo. The chalcocite enrichment blanket (gray) is partially leached and oxidized to "live limonite" consisting of dark red hematite with boxwork texture. Hypogene phyllic alteration assemblage is overprinted by a supergene argillic alteration assemblage. B. South Rim pit looking north, bench height = 15 m (50 ft). The chalcocite enrichment blanket is thin in this location, reaching a thickness of about 30 m (100 ft); material below the floor of the pit is protore. The hypogene potassic alteration assemblage is overprinted by weak argillic alteration and goethite is the dominant limonite mineral. A strong northeast structural control of the supergene blanket is visible, with oxidation plunging along structures.

Table 4. Tyrone ore mineral types (W. Seibert, pers. comm., 2005).

	Ore Mineral Type	Description	Mean Grade % Cu	Mean Density (g/cm^3)
	1	Leached cap (limonite minerals with included copper)	0.05	2.54
Copper Oxide Zone	21	Black copper oxides, acid-soluble (copper wad, copper pitch, tenorite, and neotocite)	0.18	2.48
Copper Oxide Zone	8	Insoluble copper oxides (native copper, cuprite, turquoise, local)	0.18	2.48
Copper Oxide Zone	2	Green oxide copper, acid-soluble (chrysocolla; may include malachite, accessory azurite	0.34	2.53
Sulfide Enrichment Blanket	3	Mixed oxide-chalcocite (copper oxides with chalcocite and pyrite)	0.48	2.63
Sulfide Enrichment Blanket	4	Chalcocite-pyrite	0.48	2.63
Sulfide Enrichment Blanket	5	Chalcocite>chalcopyrite-pyrite	0.48	2.63
Protore	51	Chalcopyrite-pyrite>chalcocite	0.09	2.67
Protore	6	Chalcopyrite-pyrite protore	0.09	2.67

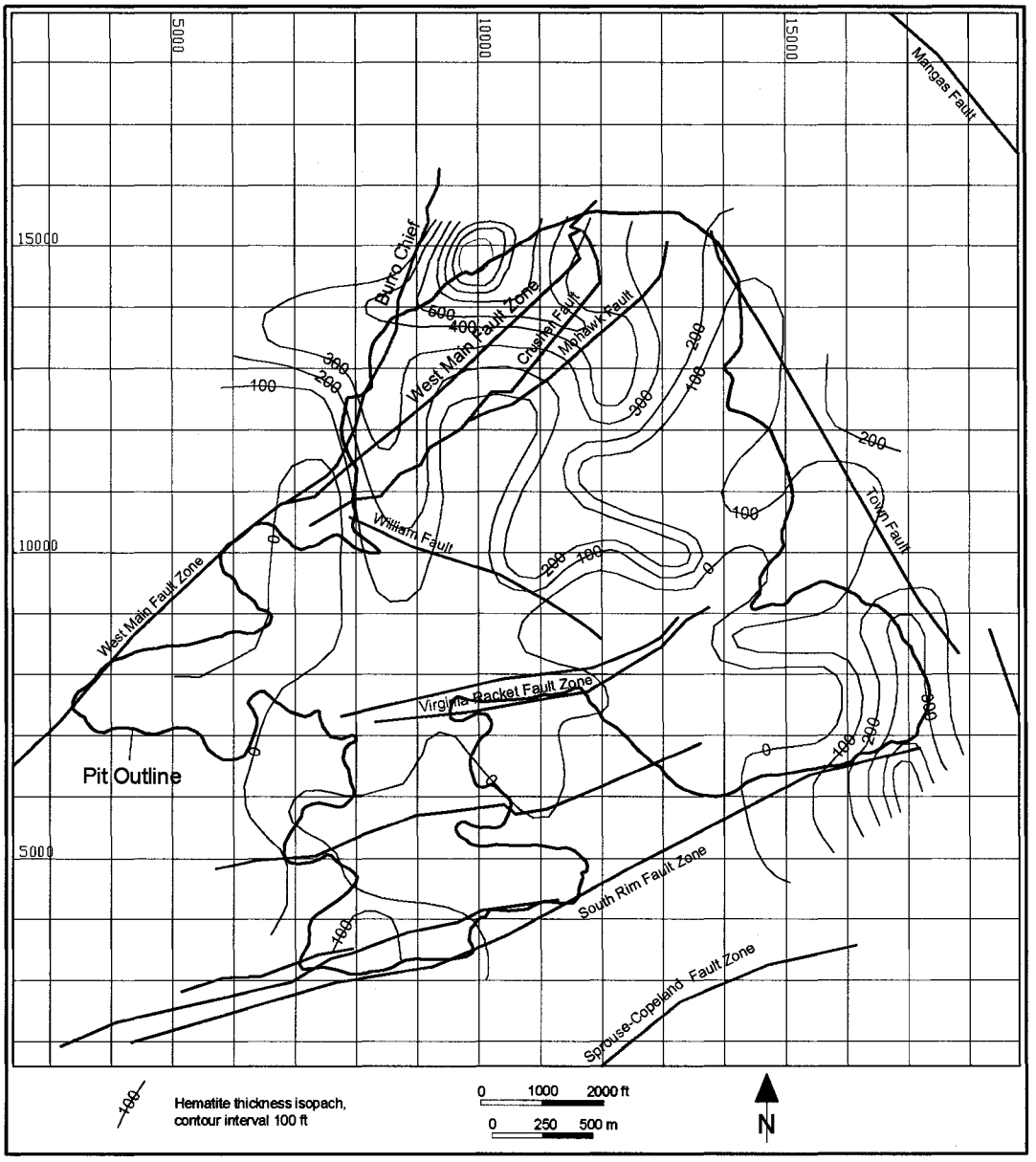

Figure 39. Isopach map of hematite-dominant leached cap from drill hole logs. Drill hole locations and hematite thickness data are shown on Plate 4. Contour interval = 100 ft (30 m).

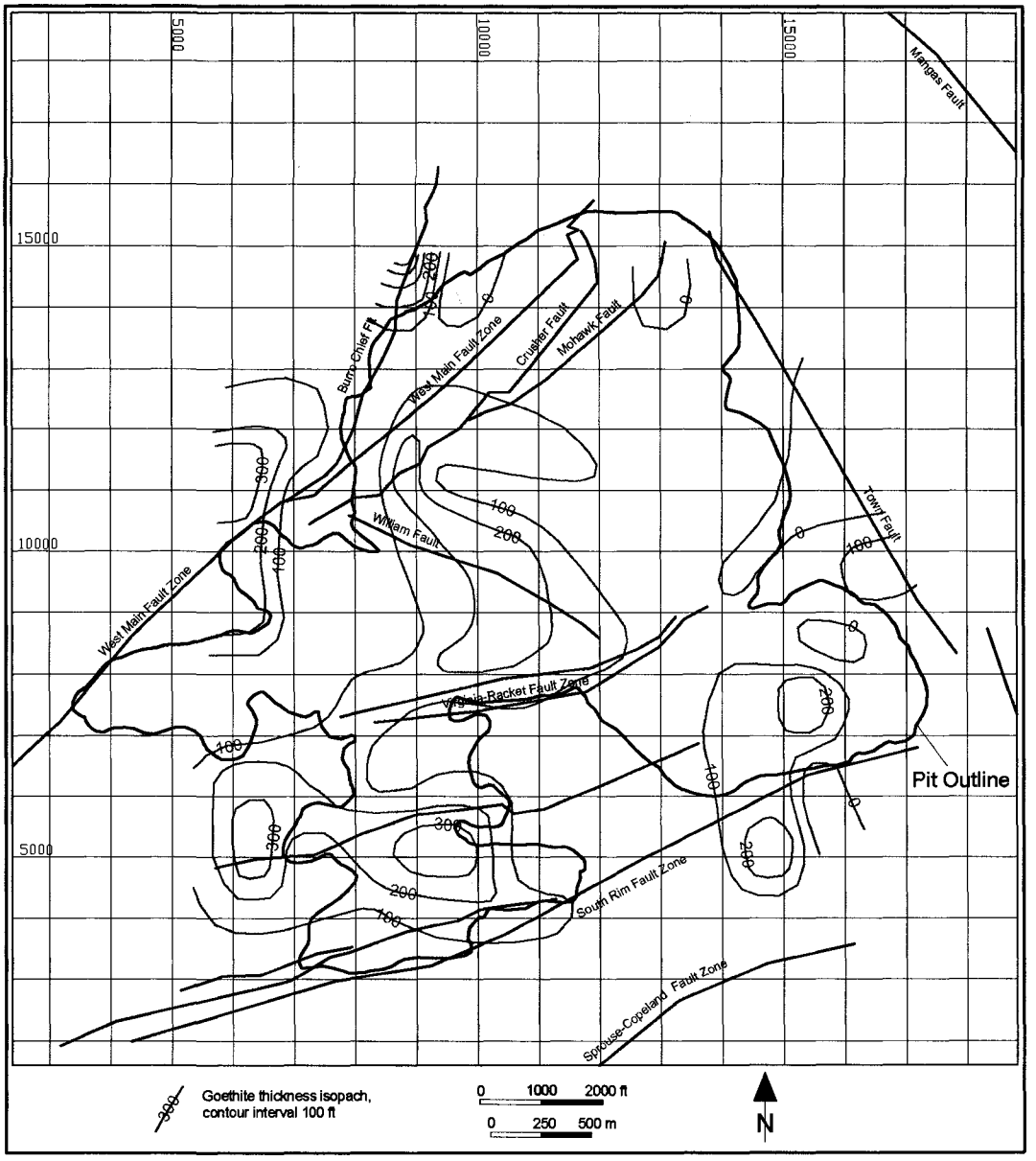

Figure 40. Isopach map of goethite-dominant leached cap from drill hole logs. Drill hole locations and goethite thickness data are shown on Plate 4. Contour interval = 100 ft (30 m).

A

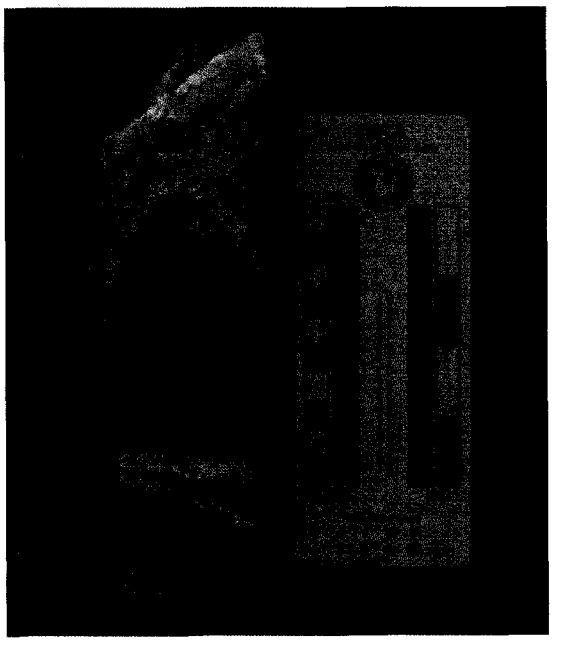

B

Figure 41. Alunite vein samples from core hole B-36 in the Main pit. A. Fine-grained, white alunite vein ~10 cm thick from a depth of 12 m (40 ft), elevation 1823 m (5982 ft). Sample 1-15-03-1. B. Alunite veins to ~2 cm thick in sericitized and argillized Proterozoic granite from a depth of 14 m (45 ft), elevation 1822 m (5977 ft). Sample 1-15-03-5.

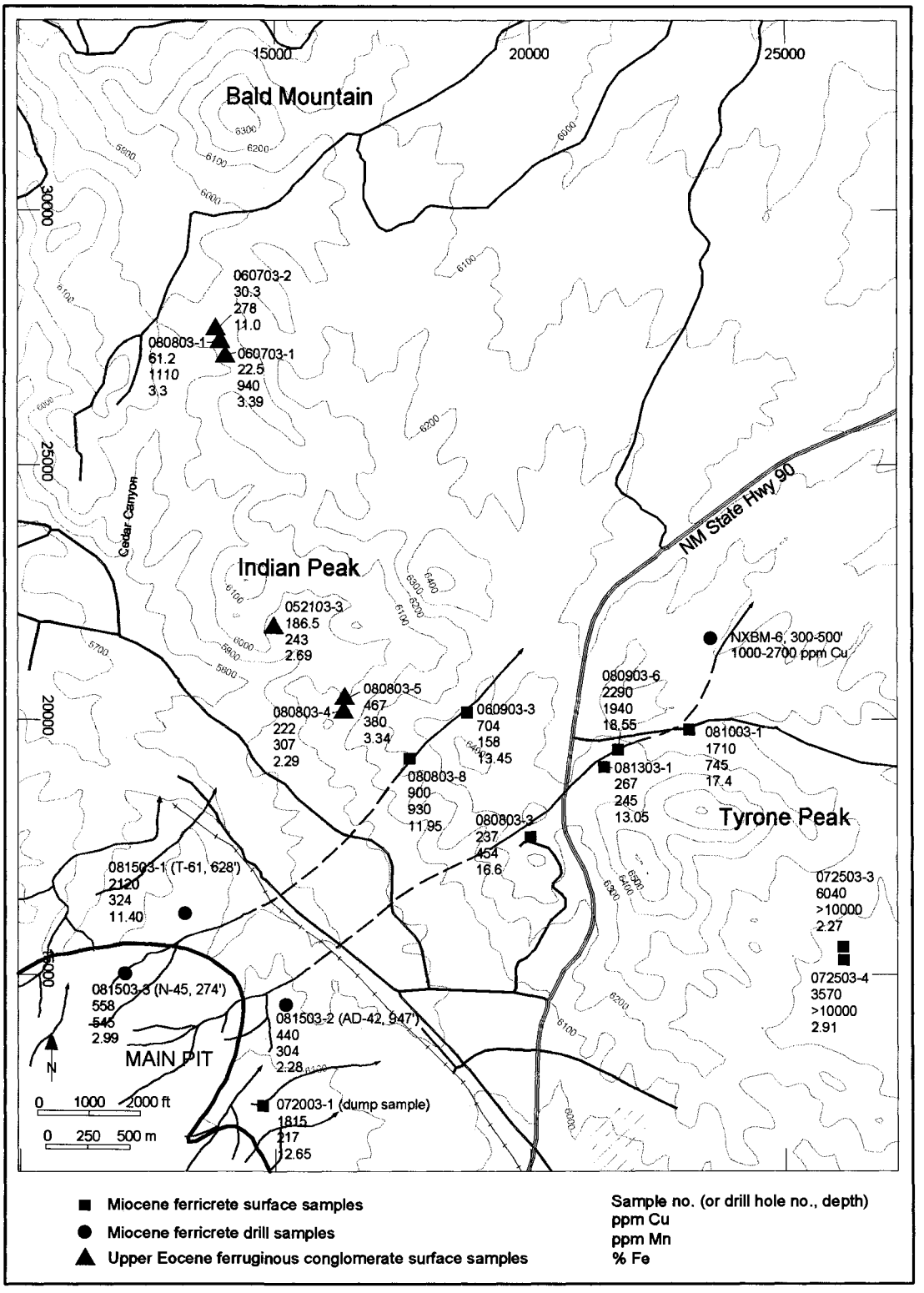

Figure 42. Sample map of the Miocene ferricrete and upper Eocene ferruginous conglomerate showing values for ppm Cu, ppm Mn, and % Fe, and Miocene paleochannels.

CHAPTER 9: ALUNITE $^{40}Ar/^{39}Ar$ GEOCHRONOLOGY

INTRODUCTION

$^{40}Ar/^{39}Ar$ dates of supergene alunite obtained for this study constrain the timing of erosional unroofing and supergene enrichment events in the Tyrone deposit. Ten samples of alunite were dated by the Nevada Isotope Geochronology Laboratory at the University of Nevada, Las Vegas, including nine samples from the Tyrone mine and one from the southern Little Burro Mountains. Sample locations are shown on Figure 43. The alunite $^{40}Ar/^{39}Ar$ dates are summarized in Table 5 together with three alunite $^{40}Ar/^{39}Ar$ dates previously obtained by Phelps Dodge (unpublished). The $^{40}Ar/^{39}Ar$ data, step-heating spectra and isochron plots are included in Appendix A.

Alunite samples were collected from drill core, mine exposures, and outcrops. The alunite occurs as veins (fracture fillings) in the leached cap in Proterozoic granite and intrusive rocks of the Tyrone stock that exhibit a supergene kaolinite overprint of hypogene phyllic assemblages. Individual dated veins are from 5 mm to 8 cm thick. The alunite material is massive, fine-grained, porcelaneous, and white to cream in color. Soft, powdery, and obviously impure veins were avoided.

Alunite samples were collected from locations as widely-separated and with as much elevation difference as possible to identify changes in age with depth. The hypothesis was that alunite from higher elevations in the deposit would yield older dates, and alunite ages would decrease with depth reflecting the downward progression of supergene enrichment. Many benches in the mine are not accessible, and although several benches were examined in the Main, Savanna, and Gettysburg pits, most useable alunite veins were found on the 5700 and 5800 benches in the northwest wall of the Main pit (Table 5 and Fig. 43). A single sample (3-20-03-1) is from the 5350 bench in the Main pit. Three pairs of crosscutting veins were also sampled on

the 5700 and 5800 benches in the Main pit (samples 712-3A,B; 728-5A,B; and 728-6A,B) in an attempt to date overprinted supergene enrichment events (Table 5).

Thirty veins were sampled in all. X-ray diffraction (XRD) analyses were completed on alunite samples before $^{40}Ar/^{39}Ar$ dating and stable isotope work. Samples were discarded if contaminating phases such as clays were identified in XRD analyses. XRD analyses were done on a Phillips 3100 Diffractometer and mineral identifications made with JADE software. Of the 30 alunite samples analyzed by XRD, 19 were selected for stable isotope work, and 10 of these for $^{40}Ar/^{39}Ar$ dating. All of the alunite samples selected consist of pure alunite with no natroalunite component.

$^{40}Ar/^{39}Ar$ RESULTS FOR ALUNITE

For most of the alunite samples, the total gas ages are reliable (no evidence for excess argon, argon loss, or ^{39}Ar recoil) (Table 5; T. Spell, pers. comm., 2005). Samples 1-12-03-2 and 1-15-03-4 may have contained excess argon or experienced argon recoil (T. Spell, pers. comm.., 2005) and were not used (Fig. 44A, B). Sample 1-16-03-1 contained excess argon, but an isochron age (19.25 ± 0.13 Ma) was obtained for that sample (T. Spell, pers. comm., 2005) (Fig. 44C, D). The alunite samples did not give good step-heating age spectra in general and only one sample, 728-5A, yielded a plateau age of 22.15 ± 0.23 Ma (Fig. 45B). Sample 728-6A yielded a "pseudo plateau" age of 21.8 ± 0.4 Ma based on 69% of ^{39}Ar released in steps 3 to 6 (Fig. 45D) (T. Spell, pers. comm., 2004).

The alunite veins in crosscutting pairs from the Main pit did not give ages sufficiently different to distinguish separate supergene events. In the 712-3A/B pair, the younger, crosscutting vein yielded an older total gas age (Table 5); however, these are total gas ages. All crosscutting vein ages are between 22.15 ± 0.23 Ma and 16.96 ± 0.34 Ma.

In general, the alunite $^{40}Ar/^{39}Ar$ ages in the Main pit decrease with decrease in elevation, but the relationship is not consistent. The ages of alunite samples from the Main pit are tabulated by elevation in Table 6. Samples T-3 and 1-16-03-1 are separated by an elevation difference of 79 m (258 ft) (Table 6), but have nearly indistinguishable ages of 19.4 Ma and 19.25 Ma, respectively. In contrast, sample 3-20-03-1 from the 5350 bench in the Main pit yielded a total gas age (14.37 Ma) that is 5.5 to 7.8 m.y. younger than samples on the 5800 bench (19.87 to 22.15 Ma). These samples are separated by a vertical distance of 137 m (450 ft). Sample 3-20-03-1 is also 910 m (3,000 ft) east of the samples on the 5800 bench. If the 9° northeast tilt of the deposit (much of which post-dates alunite formation) is taken into account, sample 3-20-03-1 is separated from samples on the 5800 bench by a vertical distance of about 77 m (250 ft). The conflicting age relationships of alunite support the assertion by Sillitoe (2005) that supergene alunites which formed over large vertical intervals in porphyry copper deposits may be nearly synchronous in their time of formation.

Alunite $^{40}Ar/^{39}Ar$ dates previously obtained by Phelps Dodge (Table 5, samples T-3, T-8, T-15) range from 19.4 Ma to 4.55 Ma. Alunite and cryptomelane dates obtained for this study range from 22.15 to 12.06 Ma (Tbls. 2 and 5). These dates shows that the supergene system was active from about 22.2 Ma to 4.6 Ma (Fig. 46). The main supergene enrichment event at Tyrone spanned the Miocene from 22.2 to 8.7 Ma (Fig. 46). This event began with uplift of the Big Burro Mountains and erosional unroofing of the deposit in the early Miocene, and probably involved a number of supergene enrichment cycles related to episodic uplift that extended into the late Miocene. Supergene enrichment was rejuvenated in the early Pliocene with uplift of the Little Burro Mountains on the Mangas fault and renewed uplift of the Big Burro Mountains. The Pliocene event is represented by a single alunite date of 4.6 Ma (Fig. 46) from the southern Little Burro Mountains.

The alunite age data indicate that in the Tyrone area, Basin and Range faulting must have begun some time before 22.2 Ma in order to erode volcanic rocks from the deposit and initiate supergene enrichment. This is in agreement with Mack's (2004) reported age of ~26 Ma for the beginning of Basin and Range deformation in the Basin and Range province of southwestern New Mexico (Fig. 9).

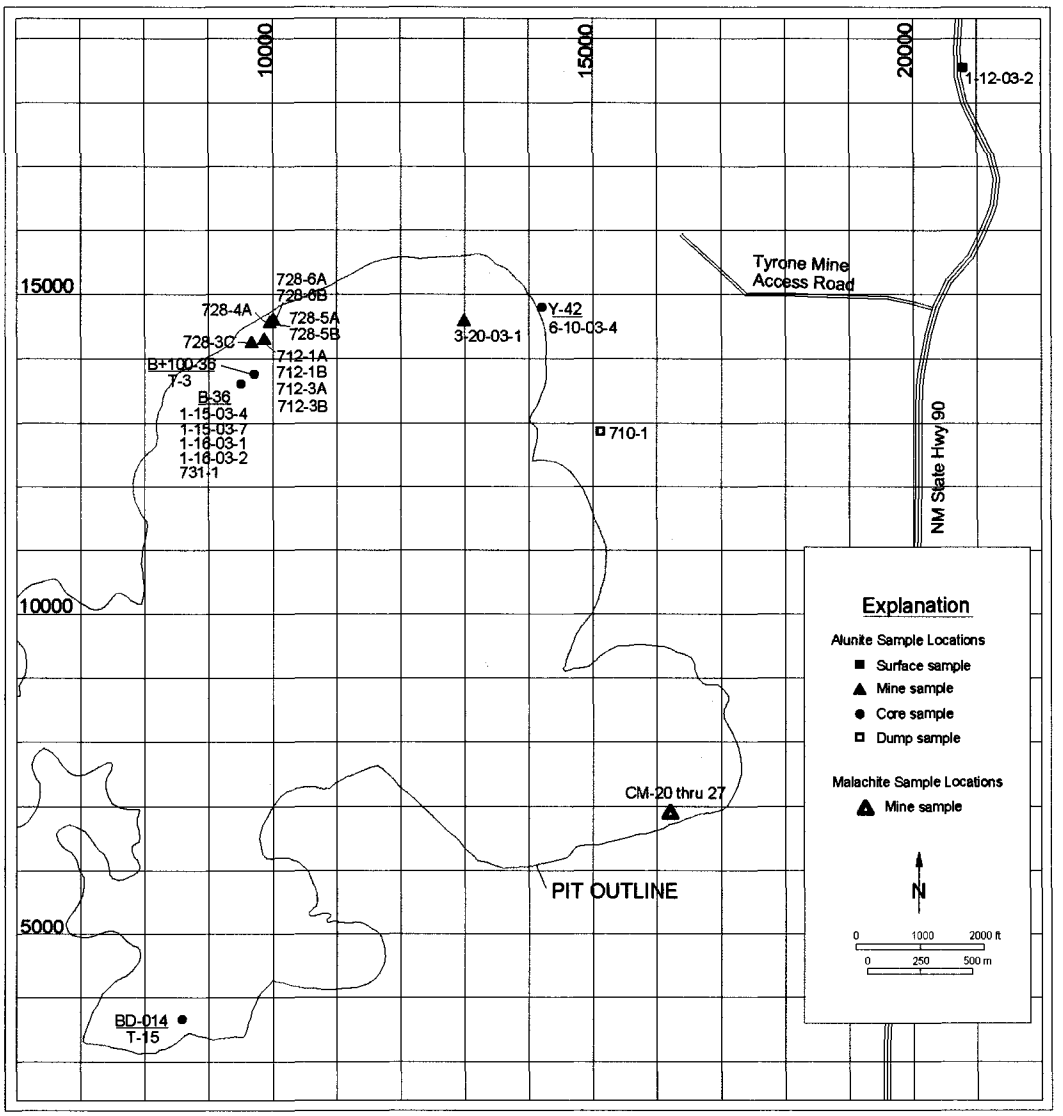

Figure 43. Alunite and malachite sample location map.

Table 5. Summary of $^{40}Ar/^{39}Ar$ dates for alunite, analytical error one sigma

Sample No.	Total Gas Age, Ma	Plateau Age, Ma	Isochron Age, Ma	Location	Description	Comments
1-12-03-2	16.35 ± 0.19			Roadcut on NM State Hwy 90 T19S, R15W, NE¼ NE¼ Sec 13	8 cm-thick vein in argillized T qtz monz por	Excess argon or ^{39}Ar recoil
1-15-03-4	32.57 ± 0.15			Core hole B-36, 78' depth 13610N, 9500E, 5944 Elev	2 cm-thick vein in argillized T qtz monz por	Excess argon or ^{39}Ar recoil
1-16-03-1	32.86 ± 0.20		19.25 ± 0.13	Core hole B-36, 380' depth 13610N, 9500E, 5642 Elev	2 cm-thick vein in argillized pC granite	Excess argon; use isochron age
3-20-03-1	14.37 ± 0.09			Main Pit 14577N, 12993E, 5350 Elev	1 cm-thick vein	
712-3A	16.96 ± 0.34			Main Pit 14290N, 9865E, 5700 Elev	Crosscutting vein pair in sericitized T qtz monz por.	
712-3B	17.29 ± 0.31				Vein 3B (8 mm) offsets vein 3A (5 mm) by 30 mm	
728-5A	21.07 ± 0.21	22.15 ± 0.23		Main Pit 14595N, 10,000E, 5800 Elev	Crosscutting vein pair in sericitized pC granite.	Use plateau age for 728-5A
728-5B	21.53 ± 0.20				Vein 5B (15 mm) offsets vein 5A (8 mm) by 35 mm	
728-6A	19.58 ± 0.21	21.8 ± 0.4		Main Pit 14600N, 10,010E, 5800 Elev	Crosscutting vein pair in sericitized pC granite.	Use pseudo plateau age for 728-6A
728-6B	19.87 ± 0.23				Vein 6B (6 mm) offsets vein 6A (9 mm) by 10 mm	
T-3	19.1 ± 0.23	19.4 ± 0.71		Core hole B+100-36 13750N, 9710E, 5900 Elev	Vein in pC granite	R. Stegen, pers. comm., 2003
T-8	4.6 ± 0.23	4.55 ± 0.13		T19S, R15W, SE¼ SE¼ Sec 12	Vein in T monzonite por	R. Stegen, pers. comm., 2003
T-15	9.05 ± 0.24	8.71 ± 0.32		Core hole BD-014 3660N, 8590E, 6450 Elev	Vein in T qtz diorite por	R. Stegen, pers. comm., 2003

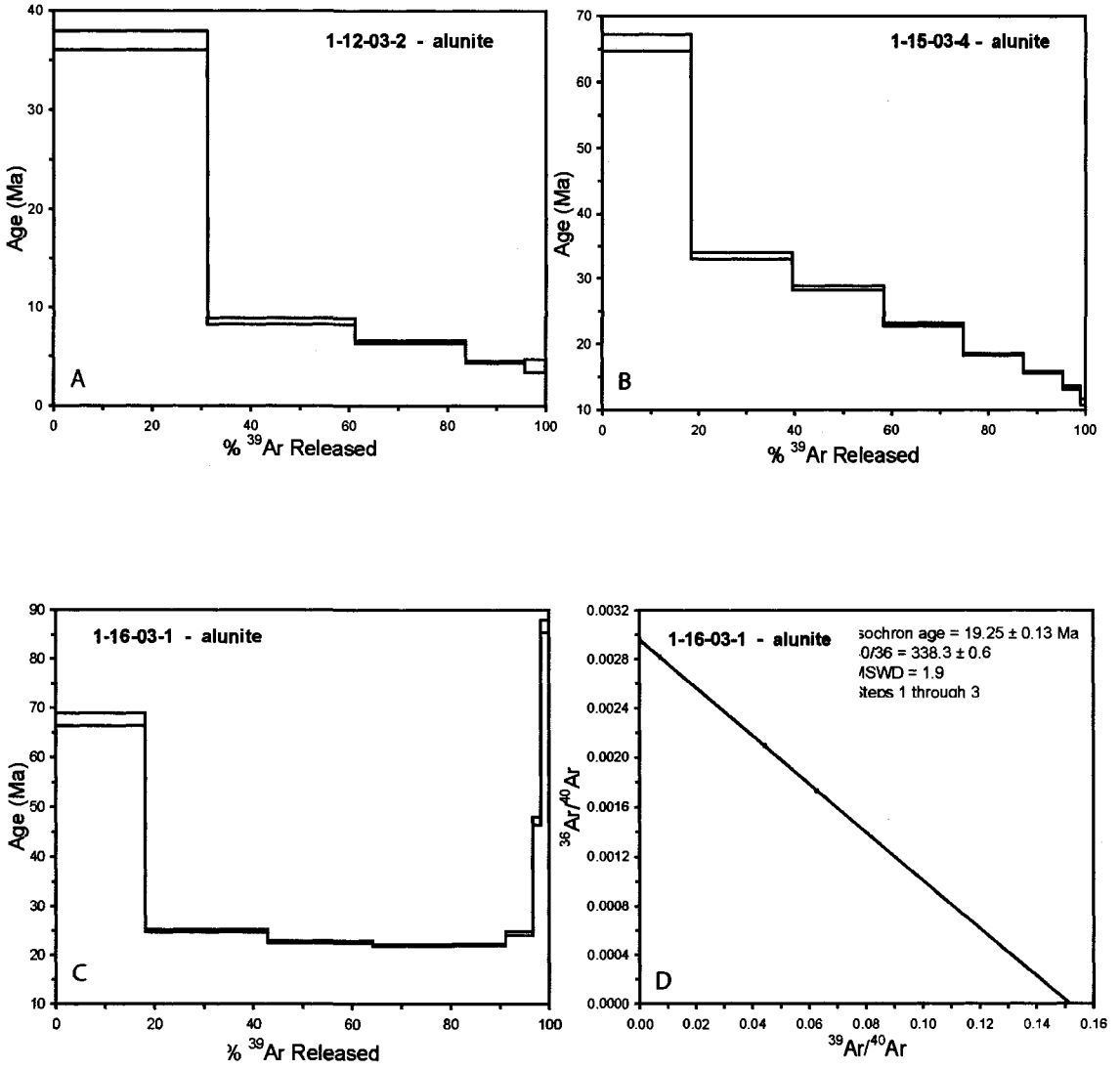

Figure 44. $^{40}Ar/^{39}Ar$ age spectra for alunite samples 1-12-03-2 (A) and 1-15-03-4 (B), and age spectrum and isochron plot for alunite sample 1-16-03-1 (C and D, respectively). The age spectra for samples 1-12-03-2 (A) and 1-15-03-4 (B) are similar, with older initial ages that fall at higher temperatures through the step-heating run. These age spectra indicate excess argon or ^{39}Ar recoil during irradiation. ^{39}Ar recoil is common in fine-grained minerals of less than 50-100 μm (T. Spell pers. comm., 2005). The total gas ages for the two samples may be too old and were not used. The age spectrum for sample 1-16-03-1 (C) is saddle-shaped indicating excess argon in the sample. Excess argon is confirmed by the isochron (D) which shows the initial $^{40}Ar/^{36}Ar$ in the sample is >295.5 ($^{36}Ar/^{40}Ar$ <0.0034) (atmospheric argon). Non-radiogenic argon was present in the sample on crystallization. The isochron age is valid, but based on only three points (T. Spell, pers. comm., 2005). Sample locations are shown on Figure 43.

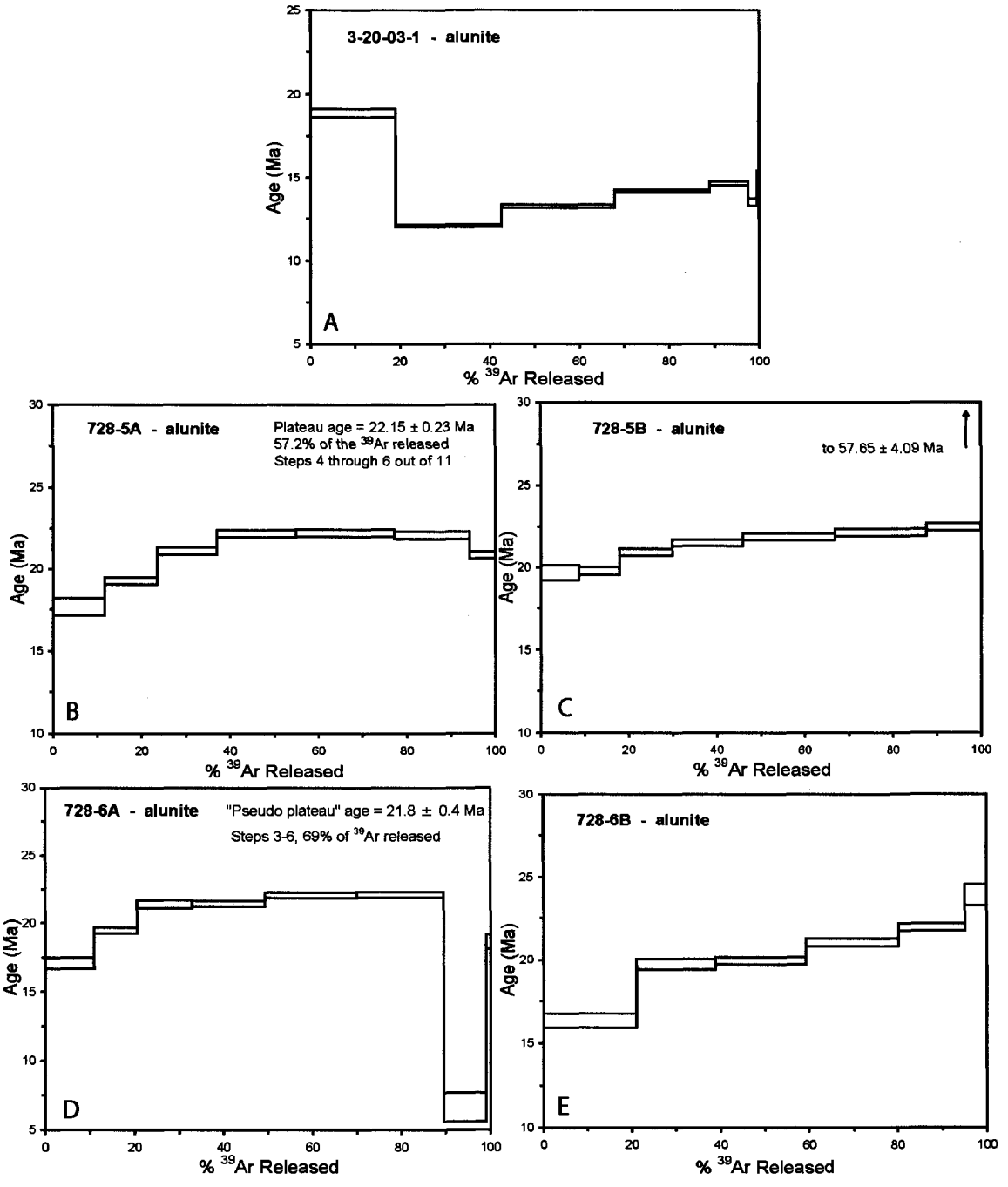

Figure 45. $^{40}Ar/^{39}Ar$ age spectra for alunite samples. Age spectra for samples 3-20-03-1 (A), 728-5B (C) and 7-28-6B (E) are discordant and only total gas ages are useable (Table 5). A plateau age was obtained for sample 728-5A (B) and a useable "pseudo plateau" age for sample 728-6A (D) based on steps 3-6, with 69% of ^{39}Ar released (T. Spell, pers. comm., 2004). Sample locations are shown on Figure 43.

Table 6. Alunite $^{40}Ar/^{39}Ar$ age vs. elevation in Main pit.

Sample No.	Elevation, ft	$^{40}Ar/^{39}Ar$ age (Ma)
T-3	5900	19.4 ± 0.71
728-5A	5800	22.15 ± 0.23
728-5B	5800	21.53 ± 0.20
728-6A	5800	21.8 ± 0.4
728-6B	5800	19.87 ± 0.23
712-3A	5700	16.96 ± 0.34
712-3B	5700	17.29 ± 0.31
1-16-03-1	5642	19.25 ± 0.13
3-20-03-1	5350	14.37 ± 0.09

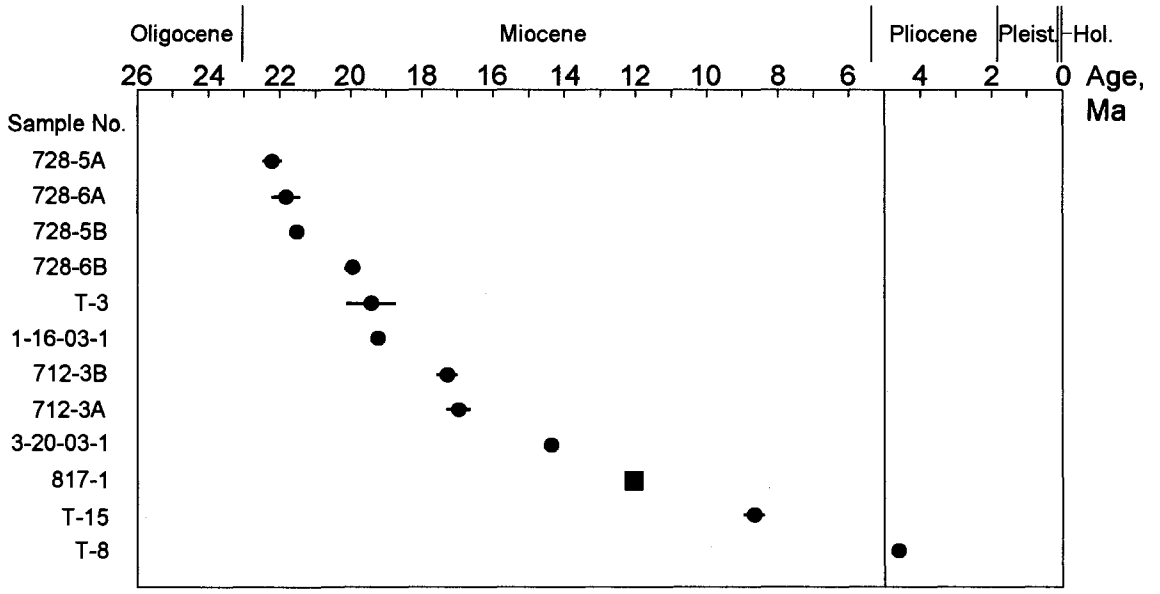

Fig 46. Distribution of $^{40}Ar/^{39}Ar$ dates for supergene alunite (circles) and cryptomelane (square) from Tyrone. Error bars are shown. Two main supergene stages are indicated. The first stage began before ~23 Ma in the early Miocene with the onset of Basin and Range normal faulting and erosion of upper Eocene-Oligocene volcanic rocks from the deposit. The first stage involved episodic faulting and uplift that persisted into the late Miocene, and formation of ferricrete which is represented by the cryptomelane age. The second stage occurred with renewed uplift in the Pliocene that involved displacement on the Mangas fault and uplift of the Little Burro Mountains. Alunite sample T-8 is from argillized Stage 2 monzonite porphyry in the southern part of the Little Burro Mountains. The two main supergene enrichment events are separated by a 4 Ma gap in the $^{40}Ar/^{39}Ar$ dates.

CHAPTER 10: SUPERGENE COPPER MASS BALANCE

INTRODUCTION

Copper mass-balance calculations were completed as part of this study to determine the approximate elevation of the top of the protore (upper extent of hypogene copper-bearing sulfides) prior to leaching, erosion, and supergene enrichment. Lateral flux calculations were used to determine the extent and direction of lateral flux of copper from the supergene system. The calculations were performed using composited copper grades in 180 drill holes shown on north-south and east-west ore mineral type cross sections produced by Phelps Dodge Tyrone Geological Services. The cross sections are spaced at 370 m x 370 m (1,200 ft x 1,200 ft), and are on the same northings and eastings as the holes logged for the leached cap mapping. Calculations are included as an Excel spreadsheet in Appendix D on the CD. Three contour maps were produced from the mass balance calculations depicting: 1) the thickness of the leached zone prior to erosion assuming no lateral flux of copper (Fig. 48, Plt. 8), 2) the elevation of the top of the hypogene copper system prior to erosion and corrected for northeast tilt (Fig. 49, Plt. 9), and 3) lateral flux of copper (Fig. 50, Plt. 10). Figures are at a scale of 1 in = 3,000 ft. The plates (scale 1 in = 600 ft) are identical to the figures, but include mass balance data for individual drill holes.

Mass-balance analysis is applied to supergene copper systems to quantitatively evaluate redistribution of copper from the leached zone into the enrichment blanket (Brimhall et al., 1985; Ague and Brimhall; 1989). The method uses copper grades (in weight percent copper), bulk-rock density (in grams/cm^3), and thickness of the leached zone and enrichment blanket (in meters or feet). Calculation of copper flux is used to determine source areas, transport pathways and depositional sinks (Brimhall et al., 1985; Mote et al., 2001).

Brimhall et al. (1985) developed a method for copper mass balance calculations using individual drill holes as stand-alone vertical geochemical profiles. Polygonal volumes may be used for mass balance analysis rather than individual drill holes in well-constrained orebodies that are modeled in three dimensions.

The individual drill hole method was used for the mass-balance analysis in this study. Average bulk densities for the various ore mineral types reported by Phelps Dodge (Table 4) were used in the calculations. Copper grades were taken from 15-m (50-ft) composited grades for the drill holes shown on the ore mineral-type cross sections. In many places on the ore mineral-type sections, the boundaries of the 15-m (50-ft) composited intervals fell on or near transitions between ore zones (i.e., between the leached cap and enrichment blanket or between the enrichment blanket and protore), making assigning grades to the ore zones very straightforward. In other places on the cross sections, the boundaries of the composited intervals did not fall on ore zone transitions, and weighted averages were used to distribute the copper grades from the composited intervals into the overlying and underlying ore zones. Drill holes in which the composited copper grades could not be satisfactorily separated into the ore zones (e.g., making the leached cap or protore grades too high) were not used.

The characteristics of the initial hypogene system, including vertical and lateral copper grade variations and bulk rock density of the protore, must be known for mass balance calculations. However, the characteristics of the protore within what is now the leached cap and enrichment blanket are obscured by leaching and erosion in the former and by enrichment in the latter. Most drill holes penetrated the chalcocite enrichment blanket and were terminated a short distance into protore; these are not useable for mass balance calculations unless sufficient protore was penetrated to estimate the grade. Deep drill holes are thus desirable because they give protore grades below the enrichment blanket. Some older, shallow drill holes were twinned with

deeper drill holes. The shallow holes and their corresponding deep twins were considered as single drill holes in cases where the twin holes gave a better estimate of the protore grade.

Likewise, holes that cut little of the leached cap (whether the leached cap was removed by erosion or mining) cannot be used because the grade of the leached cap cannot be accurately estimated. Drill holes used in the mass balance analysis penetrated the leached cap, enrichment blanket, and enough of the protore to determine the grade of all three zones. Calculations were also restricted to those holes that contain a chalcocite enrichment blanket, i.e., drill holes that penetrated a copper oxide zone but no chalcocite blanket were not used.

For mass balance calculations, assumptions must be made as to the original hypogene copper grades in the leached zone and enrichment blanket. It is necessary to assume the vertical protore grades in vertical rock columns such as a drill holes were homogeneous before the onset of oxidation, erosion, and supergene enrichment. The copper grades in the protore below the leached cap are "projected" upward through the enriched and leached zones. Vertical homogeneous copper grades appear to be a valid first assumption in modeled copper deposits studied by Brimhall et al. (1985) and Mote et al. (2001). Lateral copper grades are more variable and related to hypogene alteration zoning. Lateral variations in protore grade are accounted for by using individual drill holes as stand-alone vertical rock columns.

The first step in a simple mass balance analysis is to determine the original vertical height of the copper-bearing hypogene system (protore) in each hole before erosion. This is known as the total leached zone column height (L_T^0) (Brimhall et al., 1985). In the symbol L_T^0, the superscript zero denotes an assumption of no lateral flux of copper, i.e., all of the copper removed from the leached cap was added to the subjacent enrichment blanket, fixed by secondary sulfides precipitating below the water table (Brimhall et al., 1985). Geochemical modeling of supergene systems in existing porphyry copper deposits by Ague and Brimhall (1989) shows that very little

copper exits the system through vertical flux. The assumption of no lateral flux is tested in the mass balance calculations.

The simple model in which it is assumed that hypogene copper grades are homogeneous within each vertical column from the base of the enrichment blanket through the entire leached cap, and that there is no lateral flux of copper, is referred to as a first-order model by Brimhall et al. (1985). The first-order model is an accurate approximation in most cases but can be improved if vertical copper protore grade variations can be modeled, and if bulk-rock density variations are modeled through the deposit (Brimhall et al., 1985; Ague and Brimhall, 1989; Mote et al., 2001). As the drill data considered here were limited to data presented on cross sections, a first-order model was used.

The equation for total leached zone column height given by Brimhall et al. (1985) is:

(21) $L_T^0(p\rho_p - l\rho_l) = B(b\rho_b - p\rho_p)$ (lateral flux = 0),

where p, b, and l are copper grades for protore, blanket, and leached zone, respectively; ρ_p, ρ_b, and ρ_l are bulk rock densities for these zones, respectively, and B is the enrichment blanket thickness. Equation (21) is represented graphically in Figure 47. The leached zone column height (L_T^0) is the only unknown. The mass of copper added to the blanket is given by the right side of equation (21), while the mass of copper removed from the leached zone is given by the left side of equation (21). The validity of the above expression has been borne out in studies of copper grade data in drill holes by Brimhall et al. (1985). Enrichment blanket metal grades evolve from protore grades (p) with a fairly constant ratio of L_T^0:B to a final value of b, determined by the extent of metal leaching in the zone of oxidation and leaching (Brimhall et al., 1985). The constancy of the ratio L_T^0:B indicates simultaneous deepening of the zone of oxidation and thickening of the enrichment blanket under conditions of a descending ground water table (Brimhall et al., 1985). Solving for L_T^0, the equation is written:

(22) $L_T^0 = B(b\rho_b - p\rho_p)/(p\rho_p - l\rho_l)$.

Equation (22) gives L_T^0, the total leached zone column height or the column height of protore leached to yield the same mass of copper fixed in the enrichment blanket of thickness B (Mote et al., 2001). The total leached zone column height includes the portion of the leached cap removed by erosion.

Slightly enriched protore (e.g., ore type 51 at Tyrone) beneath the enrichment blanket can result in minimum values for L_T^0 (Brimhall et al., 1985). Calculations for L_T^0 can also be flawed by any enriched copper zones, sulfide or oxide, remaining in the leached cap due to incomplete leaching. These enriched zones will result in an overall higher average grade for the leached cap and will give erroneous low or negative values for L_T^0 in the mass balance calculations. Perched sulfide zones occur locally at Tyrone, especially in the footwall zones of faults that acted as aquicludes for descending oxidizing solutions (ore mineral types 3, 4, and 5, Plt. 6). More commonly at Tyrone, an enriched copper oxide zone (ore mineral types 21, 2, and 8) overlies the chalcocite enrichment blanket or occurs within the leached cap. To eliminate the problem of erroneously high grades in the leached cap, any oxide copper zones or perched sulfide zones with copper grades greater than protore grades were included in the enrichment blanket in the calculations.

Once the calculations for L_T^0 are complete, the elevation of the top of the enrichment blanket (ETB) in each hole is added to the value of L_T^0 to give an elevation surface referred to as SL_T^0, or the topographic protore surface:

(23) $$SL_T^0 = L_T^0 + ETB.$$

The elevation of the top of the enrichment blanket (ETB) for each drill hole was taken from ore mineral type cross sections. The contoured SL_T^0 values depict the elevation of the top of the copper-bearing hypogene system prior to leaching and erosion assuming no lateral flux of copper, i.e., all copper is fixed in the enrichment blanket.

According to Brimhall et al. (1985), there are three possible interpretations for the topography observed on contour maps of calculated L_T^0 and SL_T^0 values: 1) the assumptions used (i.e., vertical protore grade homogeneity and zero lateral flux) are correct and the topography is real, 2) the assumption of no lateral flux is incorrect and the contoured topography represents source (topographic lows) and sink (topographic highs) regions for copper, or 3) the assumption of vertical protore grade homogeneity is invalid, resulting in spurious topography. The high and low topographic anomalies observed on the L_T^0 contour map could be due to any combination of these factors (Brimhall et al., 1985). However, the average value of SL_T^0 for the deposit is assumed to represent the average elevation of the topographic protore surface (Brimhall et al., 1985).

TOTAL LEACHED ZONE COLUMN HEIGHT, L_T^0

Figure 48 and Plate 8 are contour maps of total leached zone column height (L_T^0) for Tyrone at a contour interval of 300 m (980 ft). Several aspects of the L_T^0 data are apparent from the contour maps. Anomalous high L_T^0 values are concentrated in the northeast part of the district in the Main and Savanna pits (up to 3,551 m (11,650 ft) and 2,694 m (8,840 ft), respectively, Plt. 8). The anomalous high L_T^0 values do not necessarily follow larger northeast-striking faults/fracture zones which are host to high-grade chalcocite ores as might be expected, but they do have general northeast trends reflecting the structural fabric in the district. The anomalously high L_T^0 values occur in the graben between the West Main-Crusher and Virginia-Racket fault zones, and to the northeast of the William fault. This area has the most strongly developed chalcocite enrichment blanket in the district as illustrated by the chalcocite grade x thickness map (Fig. 27). The hole with the highest L_T^0 value in the Main pit, B-28/B-28A (3,551 m, 11,650 ft, Plt. 8), has a chalcocite enrichment blanket 200 m (650 ft) thick with a grade of 0.322% Cu, and leached cap and protore grades of 0.038 and 0.051% Cu, respectively. Since the

protore grade is only 34% higher than the leached cap grade, the thick, strongly enriched blanket would require a leached zone 3,551 m (11,650 ft) thick if all of the assumptions are correct. This is not a reasonable thickness for protore, so some other mechanism such as addition of copper through lateral transport must be considered.

The highest L_T^0 value in the Savanna pit is 2,694 m (8,840 ft) in drill hole V-24 (Plt. 8). This hole has a chalcocite enrichment blanket 180 m (590 ft) thick at a grade of 0.476% Cu. The leached cap and protore grades are 0.047 and 0.053% Cu, respectively. In this hole, the protore grade is only 12% higher than the leached cap grade, so once again, the leached zone would have been very thick if the assumptions are correct.

A northeast-trending anomalous low in the L_T^0 values lies in the area between the Main and Savanna pits (Fig. 48, Plt. 8) and may represent a source area for copper or an area where lateral flux has removed copper from the supergene system. This low appears to lie along the northeast-trending contact between Stage 3 quartz monzonite porphyry and Proterozoic granite (Fig. 5), but no large structures are mapped at the contact. This is also the location of a major northeast-trending ferricrete-filled paleochannel (Fig. 19). Anomalous low L_T^0 values within the pit occur mostly to the southwest of the William fault and to the south of the Virginia-Racket fault zone. However, the only negative value, L_T^0 = -58 m (-190 ft), is in drill hole N-42 in the Main pit (Plt. 8). The negative value in this hole is due to the high average protore copper grade (0.202% Cu), and low enrichment blanket copper grade (0.186% Cu); the leached cap copper grade (0.12% Cu) is also higher than average. A negative value for leached zone column height is not possible in the case for zero lateral flux, and it indicates that much copper has exited the rock column laterally. The hole suggests that the assumption of constant vertical copper grade is incorrect, at least at this location.

As would be expected, most of the low L_T^0 values occur outside of the pit (Fig. 48, Plt. 8). These occur to the northwest of the Burro Chief-West Main fault zone, southeast of the South

Rim fault zone, and in the unmined area between the South Rim and Gettysburg pits. The L_T^0 values in these areas indicate that complete leaching of as little as 5-15 m (16-50 ft) of protore would be sufficient to provide the copper contained in the thin, low-grade enrichment blanket. For example, the chalcocite blanket between the Gettysburg and South Rim pits is only 6 to 34 m (20-110 ft) thick and has grades of 0.13 to 0.25% Cu, while the leached cap has grades ranging from 0.033 to 0.047% Cu and the protore has grades of 0.07 to 0.16% Cu. In some cases, the blanket grade is only weakly enriched over the protore grade. An example of this is drill hole E-0 in which the blanket (0.184% Cu) is slightly enriched compared to the protore (0.16% Cu). Another example is hole J-0, in which the blanket grade (0.13% Cu) is a little less than twice the protore grade (0.071% Cu).

In the area of the Copper Mountain pit, incomplete leaching of copper, a strong copper oxide zone and poorly developed chalcocite enrichment blanket made mass balance calculations impossible. As noted above, any enriched copper oxide or sulfide zones occurring in the leached cap affect the mass balance calculations since they generally give the leached cap an unrealistically higher grade overall, commonly higher than the protore. Inefficient leaching that results in copper being fixed in the leached zone as copper oxides or in a discrete enriched copper oxide zone is the result of alkaline conditions due to low pyrite:chalcopyrite and highly reactive wall rocks that are able to buffer pH to higher values.

Alternatives to the apparent thick leached zone required to account for the copper contained in the enrichment blanket in the northeastern part of the district are: 1) the assumption of consistent vertical copper grades is incorrect, and protore grades were actually much higher in the eroded upper part of the leached cap, or 2) large quantities of copper were introduced to some parts of the enrichment blanket through lateral flux. Smith (1998) noted higher hypogene copper grades in deep drill holes in the northeastern part of the district (Fig. 29), and the possibility that grades are not consistent with depth. However, Smith (1998) also noted that the distribution of

higher hypogene grades may be a function of the available deep drill data, since drill holes were usually terminated a short distance into protore once the supergene enrichment blanket was penetrated. The southwestern part of the district has less deep drilling because the supergene enrichment blanket is shallow.

Addition of copper to the supergene blanket through lateral flux is likely in the northeastern part of the district. Stegen (2002, pers. comm.) considers the area between the Burro Chief-West Main and Virginia-Racket fault zones to be a geochemical sink for supergene copper in the enrichment blanket. The exotic copper deposits in the district are also strong evidence for lateral copper flux. Lateral copper flux calculations will be covered below.

TOPOGRAPHIC PROTORE SURFACE, SL_T^0

The topographic protore surface in each drill hole is calculated by adding the elevation of the top of the supergene enrichment blanket (ETB) to the calculated value of L_T^0. The topographic protore surface is important because it represents the top of the hypogene copper deposit before leaching and erosion began. As was discussed in Chapter 6, the enrichment blanket at Tyrone is tilted 7-9° northeast in the area to the northeast of the William fault. Although northeast tilting of the Tyrone deposit began in the late Oligocene-early Miocene (26-20 Ma), most of the northeast tilting observed in the chalcocite enrichment blanket today post-dates the formation of the blanket (Kolessar, 1982; Duhamel et al., 1995), and is related to latest Miocene-Pleistocene (6-5 Ma) faulting on the Mangas fault. The northeast tilting has an obvious affect on the elevation of the top of the enrichment blanket (ETB) since it displaces the topographic protore surface progressively downward to the northeast, and the tilt requires a correction for determining the elevation of SL_T^0.

Figure 49 and Plate 9 show the topographic protore surface corrected for the northeast tilt ($SL_T^0{}_{untilted}$). On Figure 49 and Plate 9, the elevations of the top of the enrichment blanket

northeast of the William fault (~9600 N) and east of the West Main fault are corrected for 9° northeast tilt. This was done by solving for a right triangle using an angle (tilt) of 9° and the approximate distance of the drill hole from the William fault (adjacent side of the triangle) to find the difference in elevation due to tilting. The resulting values were added to SL_T^0 in each hole to give an untilted surface:

(24) $SL_T^0{}_{untilted} = SL_T^0 + a$

where "a" is the difference in elevation. Note that the values for "a" are assumed to be due solely to tilting (not deeper oxidation and enrichment), and this is a valid assumption since the Mangas half graben is tilted 10-12° to the northeast. The $SL_T^0{}_{untilted}$ surface is thus the topographic protore surface before leaching, erosion, and tilting. To the north of the William fault, $SL_T^0{}_{untilted}$ elevations are slightly higher than SL_T^0 elevations, but the elevation correction is larger with greater distance from the fault. The same assumptions are made for the topographic surface ($SL_T^0{}_{untilted}$) on Figure 49 as those made for the leached zone column height (L_T^0) on Figure 48, namely, no lateral copper flux and vertically constant protore copper grade. Holes showing SL_T^0 values lower than the pre-mine topography are geologically impossible and indicate lateral flux of copper.

The $SL_T^0{}_{untilted}$ topography (Fig. 49, Plt. 9) mimics contoured L_T^0 values shown on Figure 48 and Plate 8. Anomalous high elevation areas occur over the thickest and highest-grade enrichment blanket in the Main and Savanna pits. Of the 180-hole data set used, 20 have $SL_T^0{}_{untilted}$ elevations of over 3,000 m (9,840 ft) (Plt. 9); nine of these holes are in the Main pit, five in the Savanna pit, three in the West Racket area, two at Copper Mountain and one in the Gettysburg pit. The $SL_T^0{}_{untilted}$ topography exhibits high relief, with steep, narrow lows and highs ranging from 1,949 to 5,532 m (6,390-18,150 ft) for an elevation difference of 3,583 m (11,760 ft) (Fig. 49, Plt. 9). Again, this elevation difference is probably too large for topography of the protore suface, and indicates lateral copper flux. The highest $SL_T^0{}_{untilted}$ elevation on Plate 9 is

5,532 m (18,150 ft), in drill hole B-28/B-28A in the Main pit. The corrected, "untilted" elevation in drill hole B-28/B-28A is about 115 m (380 ft) higher than the uncorrected elevation (SL_T^0) of 5,417 m (17,770 ft) for the same hole (Appendix D). The corrections resulted in an average elevation increase of ~220 m in the northern part of the district (i.e., between the SL_T^0 values and $SL_T^0{}_{untilted}$ values) (Appendix D).

The SL_T^0 topography in the southern part of the district has more moderate relief (Fig. 49, Plt. 9), with broad lows and subdued highs ranging from 1,915 to 3,704 m (6,280 to 12,150 ft) for an elevation difference of 1,789 m (5,870 ft), and an average elevation of 2,100 m (6,890 ft). The $SL_T^0{}_{untilted}$ data indicate an average topographic protore surface for the district of 2,100-2,200 m (6,890-7,218 ft) (Fig. 49, Plt. 9). This surface is ~250 m (820 ft) above the pre-mine topography which was at an average elevation of about 1,900 m (6,200 ft) (Fig. 28), indicating that on average 250 m (820 ft) of leached material has been removed by erosion. An average elevation of 2150 m (7050 ft) was used as the topographic protore surface for the copper flux calculations below.

LATERAL FLUX OF COPPER

The anomalous $SL_T^0{}_{untilted}$ topography observed especially in the northeast part of the district, with highs and lows much greater than the average topographic protore surface, can be most readily explained by lateral flux of copper in the supergene environment. Copper flux (in g/cm^2) refers to lateral flux either into or out of the volume of rock represented by the vertical drill hole or geochemical profile (Alpers and Brimhall, 1989). The equation for lateral flux of copper given by Brimhall et al. (1985) is:

(25) $$\text{flux} = B(b\rho_b - p\rho_p) - L_T(p\rho_p - l\rho_l)$$

where L_T is the original height of the protore (copper-bearing hypogene material) above the enrichment blanket in an open system. Note that L_T is not the same as L_T^0, which assumed no

lateral flux (Brimhall et al., 1985). To evaluate the lateral flux, a value must be assumed for L_T. The leached zone at Tyrone has undergone erosion from an original topographic protore surface at an elevation of ~2,150 m (~7,050 ft). The value for L_T is calculated using the estimated pre-erosion elevation for the protore surface ($SL_T^0{}_{untilted}$ = ~2,150 m (~7,050 ft), and the elevation of the untilted enrichment blanket ($ETB_{untilted}$):

(26) $$L_T = 2150 - ETB_{untilted}.$$

The calculated lateral flux values in g/cm^2 (Equation 25) are contoured on Figure 50 and Plate 10. Negative lateral flux corresponds to possible source regions of copper (i.e., copper was not quantitatively fixed) whereas positive lateral flux corresponds to possible supergene copper sinks (Brimhall et al., 1985). For a quantitatively closed system, the contour for zero lateral flux on Figure 50 and Plate 10 coincides with the contour for $SL_T^0{}_{untilted}$ = ~2,150 m (~7,050 ft) on Figure 49.

The possible directions and magnitudes of lateral flux are shown by arrows on Figure 50 and Plate 10. Prominent source areas occur between the Burro Chief and West Main faults, and dominant sink areas in the graben between the Burro Chief-West Main and Virginia-Racket fault zones to the north of the William fault. The graben shows strong "internal drainage" with numerous source areas providing copper to sinks within the graben. Northeast fault control on source and sink areas within the graben is not as clearly evident. However, the strongest copper sink near the trace of the Mohawk fault was penetrated by drill hole N-35, which shows positive flux of 348 g/cm^2.

The northern part of the district shows several source areas that may have provided copper for exotic deposits. Three source areas occur in the northern and western parts of the Main pit and the northern part of the Savanna pit (Fig. 50, Plt. 10). A very rough estimate of the copper flux from these areas was made by multiplying the average negative copper flux in drill holes in each area by the surface area. It should be noted that the negative flux of copper from

these source areas is based on only 17 drill holes. This rough estimate indicates that as much as 370,000 metric tons of copper has been transported out of the source areas. Most of this copper was probably deposited in the sink between the Burro Chief-West Main and Virginia-Racket fault zones, or in chalcocite deposits to the north of the Main pit (Fig. 27). However, some of the copper exited the deposit in groundwater flowing into northeast-trending paleochannels (northward flux of copper designated by arrows on Figure 50 and Plate 10), and now resides in the exotic deposits.

Evidence that lateral flux of copper accompanied northeast tilting of the deposit during Miocene Basin and Range extensional faulting includes: 1) copper-bearing ferricrete in northeast-trending paleochannels, 2) northeast grain of the SL_T^0 topography, and 3) the concentration of copper in the graben between the Burro Chief-West Main and Virginia-Racket fault zones in the northern part of the district. The lateral flux was partly controlled by the northeast sloping groundwater surface and northeast-striking faults which fed groundwater flow into the paleochannels.

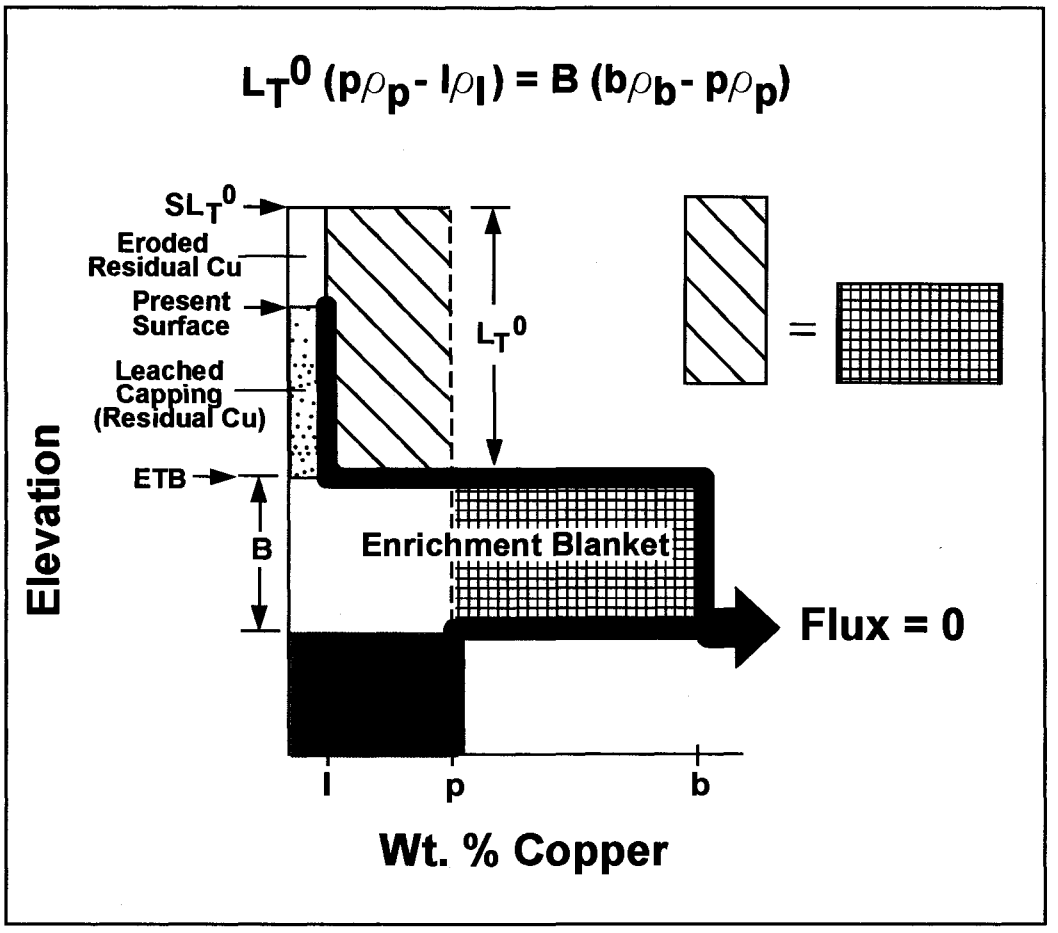

Figure 47. Graphic representation of mass balance calculation for the case of zero lateral flux of copper signified by zero superscript. The diagram and equation assume complete fixation of copper in the enrichment blanket, so the copper removed from the leached zone (diagonal striped pattern) must equal the copper added to the enrichment blanket (square ruled pattern) above the initial protore grade, p. Once the leached zone column height (L_T^0) is calculated, the elevation of the upper protore surface (SL_T^0) is found by adding the elevation of the top of the enrichment blanket (ETB) to L_T^0. Symbols: B = thickness of enrichment blanket; copper grades: l = leached zone, p = protore, b = blanket; densities: ρ_l = leached zone, ρ_p = protore, ρ_b = blanket. Modified from Brimhall et al. (1985) and Mote et al. (2001).

Figure 48. Contour map of leached zone column height assuming no lateral flux of copper (L_T^0). Data are included in Appendix D and Plate 8.

Figure 49. Contour map of upper protore surface (SL_T^0), untilted blanket. Elevation in meters. Data are included in Appendix D and Plate 9.

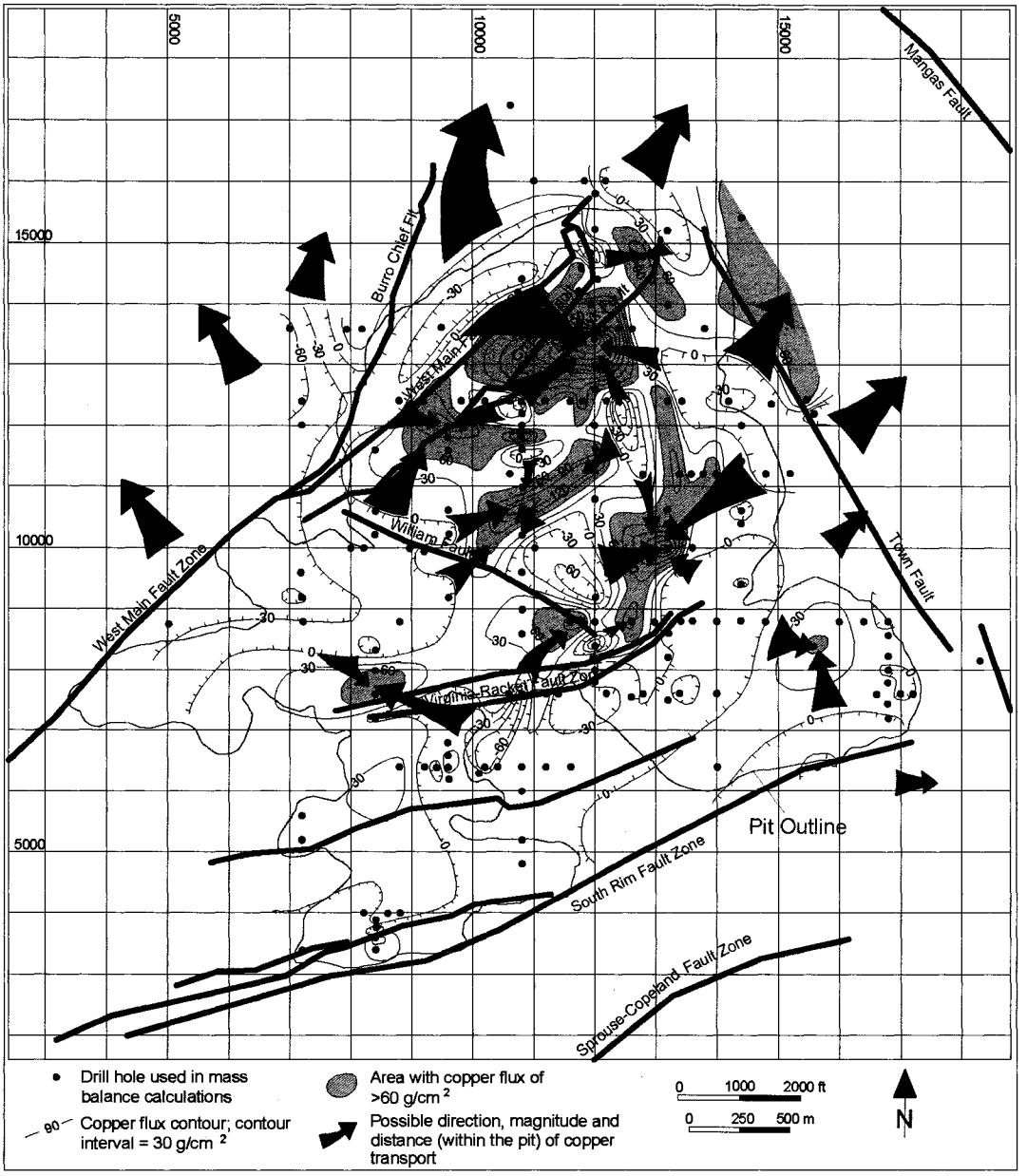

Figure 50. Contour map of calculated lateral flux of copper in g/cm². Data are included in Appendix D and Plate 10.

CHAPTER 11: STABLE ISOTOPE GEOCHEMISTRY OF ALUNITE AND MALACHITE

INTRODUCTION

Stable isotope analyses (sulfate O, H, and S) were completed on 19 samples of alunite to determine the groundwater conditions during supergene enrichment (i.e. fully saturated vs. a groundwater table at depth) and the source of sulfur. The groundwater conditions have implications for paleoclimate, as a deep groundwater table would likely be associated with arid conditions believed to be prevalent in the Miocene (Nations et al., 1985; Sillitoe and McKee, 1996).

Stable isotope analyses (C, O) were also completed on eight samples of malachite to determine the conditions of formation of copper carbonate minerals and the source of carbonate. Malachite and azurite are not abundant in the district and are much less common than chrysocolla due to the lack of carbonate host rocks. The paucity of copper carbonate minerals made it difficult to locate malachite in-place at the mine. All of the malachite samples analyzed are from fractures exposed in the 6050 bench of the Gettysburg pit.

The stable isotope analyses were performed by Dr. Simon Poulson at the Nevada Stable Isotope Laboratory at the University of Nevada, Reno. Sample locations are shown on Figure 43. Stable isotope analyses are summarized in Tables 7 and 8.

STABLE ISOTOPE GEOCHEMISTRY OF ALUNITE

Alunite samples were taken from the leached cap where they occur as veins (fracture fillings) in Proterozoic granites and intrusive rocks of the Tyrone stock that are altered to hypogene phyllic assemblages and overprinted with supergene kaolinite. Alunite veins occur mostly in the Main pit area in the northern part of the district and were collected from pit

exposures, core, and outcrop. Alunite samples were not used for isotopic analyses if XRD analyses indicated contained clays or other impurities. Alunites were analyzed for S, H, and sulfate O isotopes. Sulfate oxygen analyses were completed on barite precipitates prepared from alunite dissolved in NaOH following the method of Wasserman et al. (1992). Alunite hydroxyl oxygen was not analyzed.

Sulfur Isotopes of Alunite

The $\delta^{34}S$ values of the Tyrone alunites range from -0.6 to +2.4‰ (VCDT), and average 0.9‰ (Table 7). These values are within the range of sulfur isotope values for most hypogene sulfide minerals in porphyry copper deposits in the southwestern U.S. (generally between -5 and +5‰ and averaging 0‰ (Ohmoto and Goldhaber, 1997)). During the oxidation of hypogene sulfide minerals and formation of supergene sulfate, the sulfur contained in the hypogene sulfides undergoes quantitative, unidirectional oxidation (i.e. not associated with equilibrium) (Field, 1966). The resulting sulfate has sulfur isotopic compositions nearly identical to the precursor hypogene sulfide minerals (Field, 1966). In contrast, equilibrium fractionation of sulfur isotopes in the hypogene environment results in sulfate minerals with appreciable ^{34}S enrichment relative to associated sulfide minerals. Therefore, the criterion for distinguishing hypogene and supergene sulfates using sulfur isotopes is that hypogene sulfates are enriched in ^{34}S relative to sulfides, whereas supergene sulfate is isotopically very similar to the precursor sulfides (Field, 1966; Rye et al., 1992). Sulfur isotope data were not available for the hypogene sulfide minerals at Tyrone when this study was completed. A sulfur isotope study of the Tyrone hypogene sulfide minerals is currently being conducted by T. Thompson (pers. comm., 2008). The alunite sulfur isotope ratios at about 0‰ indicate the sulfur was derived from oxidation of hypogene sulfides (Rye et al., 1992). The $^{40}Ar/^{39}Ar$ ages (22.2-4.6 Ma) and sulfur isotope ratios of the Tyrone alunites confirm they are supergene in origin.

Hydrogen Isotopes of Alunite

The H isotopes of the alunites range from -85 to -46‰ (VSMOW) (Table 7). Stoffregen et al. (1990) suggested that fine-grained alunite may undergo complete H exchange with ground water in less than 10,000 years at 25°C. However, Rye et al. (1992) noted that the fractionation of H between alunite and water is very small. Low-temperature exchange will not result in significant changes in the δD of alunite unless groundwater of a different δD is involved than the groundwater present during supergene enrichment, such as water from standing pools that have undergone repeated exchange (Rye et al., 1992). Rye et al. (1992) found no examples of low-temperature hydrogen isotope exchange in their study of supergene alunite, and believe that nearly all supergene alunites retain their primary hydrogen isotope composition. This was confirmed by Arehart and O'Neil (1993) who found that Tertiary supergene alunites in Nevada retained their original δD values, which are considerably different from modern meteoric waters. Arehart and O'Neil (1993) point out that Stoffregen's (1990) suggestion was based on experiments with disaggregated alunite at high water:mineral ratios, conditions not representative of natural conditions in the late Tertiary and Quaternary in the Great Basin (Arehart and O'Neil, 1993). The δD and $\delta^{18}O$ values of the Tyrone alunites are considered below.

Sulfate Oxygen Isotopes of Alunite

Sulfate from the Tyrone alunites yielded $\delta^{18}O$ values ranging from 7.4 to 9.7‰ (VSMOW) (Table 7). In supergene alunite formed from the oxidation of pyrite, the $\delta^{18}O_{SO4}$ values are determined by two kinetically-controlled reactions, given as reactions 1 and 3 in Table 3. In reaction 1, pyrite is oxidized by oxygen, and 87.5% of sulfate oxygen is contributed from atmospheric oxygen and 12.5% from meteoric water. In reaction 3, pyrite is oxidized by ferric iron and sulfate oxygen is contributed from meteoric water alone (Rye et al., 1992). Since atmospheric oxygen ($\delta^{18}O \approx +23$‰ constant) and surface water have large difference in isotopic ratios at all latitudes, a wide range of $\delta^{18}O_{SO4}$ values can result depending on which of the two

processes (reaction 1 or 3) is dominant (Rye et al., 1992). The range in sulfate oxygen compositions is indicated by the supergene alunite sulfate field (SASF) shown on Figure 51. For meteoric water with any value of δD, a range of $\delta^{18}O_{SO4}$ values are possible depending on the dominant pyrite oxidation reaction (Rye et al., 1992).

The supergene alunite SO_4 field is defined by the minimum kinetic fractionation (4‰) of oxygen between sulfate and water observed for reaction 3, the maximum value for the combined kinetic fractionations between sulfate and atmospheric oxygen and sulfate and water resulting from reaction 1, and the small low-temperature fractionation of hydrogen between alunite and water (Rye et al., 1992). The maximum fractionations occur when reactions 1 and 3 are catalyzed by bacteria at low temperature (Rye et al., 1992). Supergene alunite will not have δD or $\delta^{18}O_{SO4}$ compositions to the right of the supergene alunite SO_4 field unless the sulfate is derived from redox recycling in the presence of sulfate-reducing bacteria (i.e., in standing pools of water) or it undergoes exchange with water in low pH solutions (Rye et al., 1992). The largest fractionations observed in $\delta^{18}O_{SO4}$ are expected in oxygenated conditions during alternating wet and dry cycles rather than in saturated, anaerobic conditions (Fig. 51) (Rye et al., 1992).

The δD and $\delta^{18}O_{SO4}$ values of alunite are plotted on Figure 51. All samples lie within the supergene alunite SO_4 field. From the figure it is apparent that reactions due to atmospheric oxygen dominated during oxidation of sulfides and the formation of alunite at Tyrone. These results indicate that oxidation of hypogene sulfides occurred in alternating wet and dry, well-oxygenated conditions rather than in saturated conditions (Rye et al., 1992), reflecting the semi-arid Miocene climate (Nations et al., 1985; Sillitoe and McKee, 1996) and a water table at depth. Seasonal flushing with meteoric water was probably very important in dissolution of soluble copper sulfates in the leached zone, and transport of copper below the groundwater table.

STABLE ISOTOPE GEOCHEMISTRY OF MALACHITE

Malachite samples were collected from the copper oxide zone on the 6050 bench in the southern part of the Gettysburg pit (Fig. 43). The copper oxide zone in this area is dominated by ore mineral type 2 (green copper oxides, Fig. 36) in connection with near-surface oxidation of chalcocite mineralization (Fig. 27). The malachite occurs as thin crusts of radiating crystals on goethite-stained fractures in weakly argillized Stage 2 monzonite porphyry. Mineral separates were prepared by hand-picking malachite crystals under a binocular microscope. Carbon and oxygen isotope analyses were made on CO_2 gas prepared by reaction with H_3PO_4 (McCrea, 1950).

The $\delta^{13}C$ values for the Tyrone malachites range from -13.5 to -11.4‰ (VPDB) (Table 8). The $\delta^{13}C$ values of malachite are controlled by the source of carbon. Carbon isotope compositions of 0 to -21‰ (PDB) are typical for malachite, and reflect a combination of carbonate-rock derived carbon (-4 to +10‰, average ~0‰ (Ohmoto and Goldhaber, 1997)) with a significant contribution from vegetation-respired soil CO_2 (~-10 to -12‰ in coexisting soil carbonate (Cerling, 1984)) or bacteria ((Melchiorre et al., 1999; Melchiorre and Enders, 2003). The 6050 bench in the Gettysburg pit is near the pre-mine surface and it is reasonable to assume the CO_2 was derived at least in part from near-surface organic processes.

The $\delta^{18}O$ values are +22.6 to +25.8‰ (VSMOW). However, all but one sample (CM-24, $\delta^{18}O$ = 25.8‰), yielded $\delta^{18}O$ values ranging from +22.6 to +23.3‰, with an average of +23‰. The $\delta^{18}O$ values of malachite are controlled by the oxygen isotope composition of the local meteoric water and the temperature of formation (Melchiorre et al., 1999).

The stable isotope geochemistry of natural and synthetic malachite was investigated by Melchiorre et al. (1999). They determined that natural malachites have $\delta^{18}O$ values ranging from +18.1 to +30.5‰ and $\delta^{13}C$ values ranging from -19.9 to +1.8‰. Figure 52 shows the isotopic ratios of 61 natural malachites analyzed by Melchiorre et al. (1999), and the eight Tyrone

samples. The isotopic values fall within the fields for caliche and speleothem carbonates, suggesting that the conditions of malachite formation are similar to caliche and speleothems (Melchiorre et al., 1999). The carbon compositions of these near-surface minerals are affected by organic carbon, either by CO_2 respired by roots or oxidation of bacteria, with some inorganic carbon being contributed by dissolution of primary or secondary carbonate minerals in carbonic acid solutions (Melchiorre et al., 1999; Melchiorre and Enders, 2003).

The malachite carbon and oxygen stable isotope compositions indicate that malachite formed in the near-surface environment with carbon probably supplied from plant-respired carbon. These data support the conclusion of Chávez (2000) that malachite commonly forms as late-stage fracture fillings by destruction of previously-formed copper oxide and supergene copper sulfide minerals. It must be kept in mind that these samples are from one area in the mine and may not be representative of all malachite at Tyrone. However, malachite (and chrysocolla) are evidence of widespread, late-stage oxidation of the deposit.

Table 7. Summary of alunite stable isotope data.

Sample No.	$\delta^{34}S$ (‰, VCDT)	δD (‰, VSMOW)	Sulfate $\delta^{18}O$ (‰, VSMOW)	Northing	Easting	Elevation	Comments
1-12-03-2	-0.6	-57	7.9	18560	20780	6325	NM Hwy 90
1-15-03-4	2.0	-76	7.5	13610	9500	5944	Core hole B-36
1-15-03-7	2.4	-56	9.0	13610	9500	5825	Core hole B-36
1-16-03-1	1.0	-85	7.4	13610	9500	5642	Core hole B-36
1-16-03-2	2.3	-70	8.8	13610	9500	5635	Core hole B-36
3-20-03-1	2.0	-55	9.0	14577	12993	5350	Main Pit
610-4	0.3	-54	8.3	14800	14200	5345	Core hole Y-42
710-1	-0.4	-46	7.8	12900	15100		Savanna Dump
712-1A	0.6	-53	7.6	14290	9865	5700	Main Pit
712-1B	1.8	-68	8.7	14290	9865	5700	Main Pit
712-3A	-0.1	-53	8.5	14290	9865	5700	Main Pit
712-3B	0.9	-60	9.7	14290	9865	5700	Main Pit
728-3C	1.1	-52	8.6	14240	9665	5800	Main Pit
728-4A	1.2	-52	9.6	14550	9955	5800	Main Pit
728-5A	0.6	-56	7.9	14595	10000	5800	Main Pit
728-5B	0.3	-49	8.1	14595	10000	5800	Main Pit
728-6A	0.3	-52	8.1	14600	10010	5800	Main Pit
728-6B	0.7	-60	8.2	14600	10010	5800	Main Pit
731-1	1.6	-66	7.6	13610	9500	5970	Core hole B-36

Table 8. Summary of malachite stable isotope data.

Sample No.	Carbonate $\delta^{13}C$ (‰, VPDB)	Carbonate $\delta^{18}O$ (‰, VPDB)	Carbonate $\delta^{18}O$ (‰, VSMOW)
CM-20	-11.6	-7.8	22.8
CM-21	-12.4	-7.6	23.1
CM-22	-12.5	-7.4	23.3
CM-23	-12.3	-7.9	22.8
CM-24	-11.4	-4.9	25.8
CM-25	-12.4	-7.7	23.0
CM-26	-13.5	-8.0	22.6
CM-27	-12.0	-7.4	23.3

All samples are from the Gettysburg pit, 6050 bench, 6900N, 16190E to 6910N, 16210E.

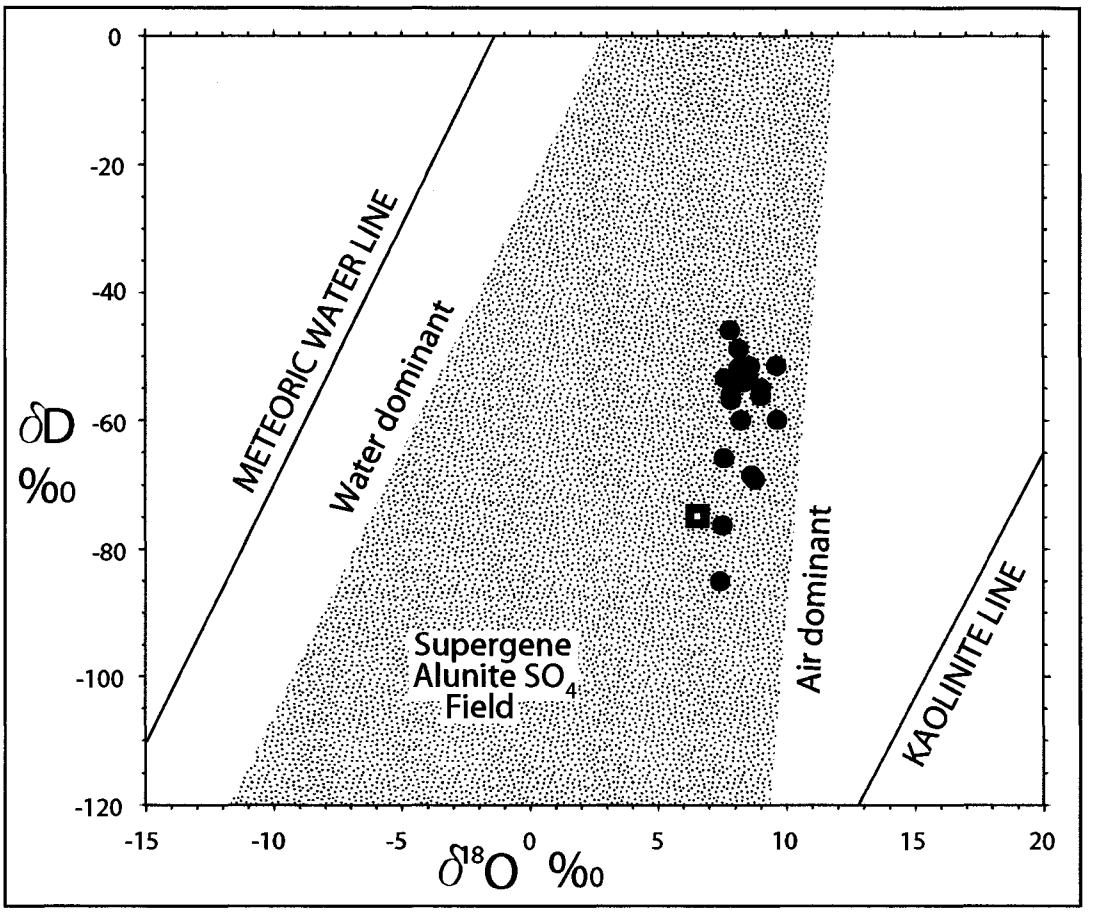

Figure 51. δD vs δ^{18}O plot showing the supergene alunite SO_4 field (SASF, stipple pattern), modified from Rye et al., 1992. Tyrone alunite samples are plotted as filled circles. A data point for alunite from the Chino mine from Field (1966, sample C-6) is shown as an open square. The Tyrone alunite compositions fall in the air-dominant side of the SASF indicating a well-oxygenated supergene profile and only intermittently saturated conditions due to the semi arid Miocene climate.

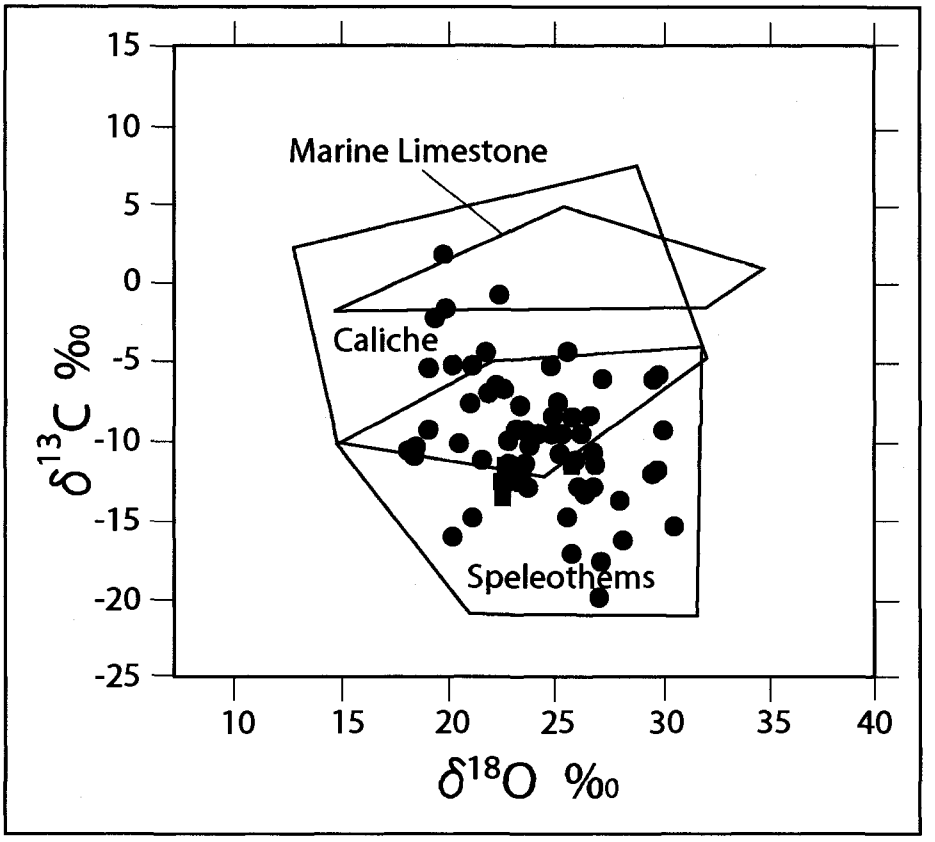

Figure 52. $\delta^{13}C$ and $\delta^{18}O$ diagram showing the overlapping fields for caliche, speleothems, and marine limestone. Also shown are the ratios of 61 natural malachites analyzed by Melchiorre et al. (1999) in black circles and eight Tyrone malachite samples from this study in red squares. The Tyrone malachite samples fall within the speleothem field indicating a probable plant-respired source for CO_2. The isotopic ratios as well as the occurrence of malachite coating limonite minerals in fractures in the leached cap indicate the mineral is late stage. Diagram modified from Melchiorre et al. (1999).

CHAPTER 12: TIMING AND TECTONIC CONTROLS OF SUPERGENE ENRICHMENT

INTRODUCTION

The timing and tectonic controls of supergene enrichment events at Tyrone can be placed into the context of Cenozoic tectonics of southwestern New Mexico using new information from this study including $^{40}Ar/^{39}Ar$ dates on alunite and cryptomelane, and the recognition and dating of the copper-bearing ferruginous conglomerate in the southern Little Burro Mountains. Three stages of supergene enrichment occurred at Tyrone: 1) during the late Eocene after the close of the Laramide orogeny and with erosional unroofing of the Tyrone stock; 2) during the Miocene as episodic uplift on major Basin and Range normal faults resulted in erosion of upper Eocene-Oligocene ash-flow tuffs from the deposit and depression of the local groundwater table (Fig. 46); and 3) during the Pliocene-Pleistocene after deposition of ferricrete and lower alluvial fan gravel, and with renewed uplift of the Big Burro Mountains and uplift of the Little Burro Mountains on the Mangas fault. The Miocene was the principal stage of enrichment at Tyrone as evidenced by the cluster of early to late Miocene dates on alunite and cryptomelane in ferricrete. These stages will be considered individually below in light of $^{40}Ar/^{39}Ar$ dates from this study, and studies of late Cenozoic tectonism in the southern Transition Zone and Basin and Range province in southwestern New Mexico summarized by Mack (2004) and Seager et al. (1984).

Figure 53 is a sequence of six schematic cross sections, prepared by the author, that depict Cenozoic tectonic development of the Tyrone mine area from 54 to 1.5 Ma. The cross sections extend from the Big Burro Mountains northeast through Tyrone Peak in the southern Little Burro Mountains. Figure 53A, 54 Ma, represents the Tyrone deposit near the end of Laramide volcanism but before deep erosion and supergene enrichment.

LATE EOCENE SUPERGENE ENRICHMENT

The first stage of supergene enrichment occurred in the late Eocene (between about 45 and 35 Ma) as erosion removed Laramide andesitic volcanic flows and tuffs, that possibly formed the volcanic carapace of the Tyrone system, and Late Cretaceous sedimentary rocks from the deposit (Fig. 53B, 35 Ma). Where erosion reached the level of the Tyrone stock, mineralized portions of the stock were exposed to oxygenated groundwater. A supergene enrichment blanket probably formed before the close of the Eocene. As erosion progressed, a landscape of subdued topography was formed (Nations et al., 1985; McIntosh et al., 1992).

The copper-bearing ferruginous sandstone and conglomerate unit in the southern part of the Little Burro Mountains was deposited during the late Eocene erosional event. This early stage of erosion and enrichment ended when the Tyrone deposit was covered by as much as 710 m (2,300 ft) of volcanic and volcaniclastic rocks associated with the Mogollon-Datil volcanic field beginning in the latest Eocene (Fig. 53C, 30 Ma). Deep burial cut off groundwater recharge and arrested supergene enrichment through the Oligocene. No supergene alunite was identified from this event, and it is likely that any alunite that may have existed was removed by subsequent erosion.

The late Eocene erosional and supergene enrichment event was not accompanied by extensional faulting. Upper Cretaceous sedimentary rocks and upper Eocene-Oligocene volcanic rocks in the southern Little Burro Mountains all have similar dips, which indicates that tilting occurred after the volcanism ceased. Tilting began with the first phase of Basin and Range normal faulting (Figs. 9 and 10).

MIOCENE SUPERGENE ENRICHMENT

The second stage of supergene enrichment began during the early Miocene with uplift of the Big Burro Mountains on major northwest-striking normal faults related to Basin and Range extension. The Big Burro Mountains horst block and corresponding San Vicente half graben formed by normal displacements on the Treasure Mountain fault on the northeast and Knight Peak fault on the southwest (Mack, 2004) (Fig. 10). The San Vicente basin contains a nearly continuous sedimentary record of Miocene and younger basin fill deposits (up to 1,288 m (4,226 ft)) that thicken toward the basin-bounding Treasure Mountain fault (Mack, 2004). Miocene faults that bound half grabens, including the Treasure Mountain and Knight Peak faults, are characterized by the preservation of upper Eocene-Oligocene volcanic rocks of the Mogollon-Datil volcanic field in their hangingwall side (Fig. 1). The amount of northeast tilt of the Big Burro Mountains block and San Vicente half graben was probably only a few degrees initially as this amount of tilt provides sufficient room to account for thick basin fill deposits.

At the beginning of the Miocene stage of supergene enrichment (before ~22 Ma, Fig. 10), upper Eocene-Oligocene volcanic and sedimentary rocks were stripped from the Big Burro Mountains uplift and redeposited as sediments in the western part of the San Vicente basin. Local grabens (i.e., along the Southern Star fault) formed within the Big Burro Mountains uplift preserving upper Eocene-Oligocene volcanic rocks from erosion. Proterozoic granites and intrusive rocks of the Tyrone stock were exposed and eroded, and the Eocene chalcocite enrichment blanket was also leached and eroded. Mass balance calculations show that about 250 m (800 ft) of mineralized material must have been present above the pre-mine surface to provide sufficient copper to produce the current chalcocite enrichment blanket. The leached cap is much less than 250 m (800 ft) thick in most parts of the district except in the far northeast.

A strongly enriched chalcocite blanket formed in the early Miocene (Fig. 53D, 12 Ma). Alunite and cryptomelane $^{40}Ar/^{39}Ar$ dates (Fig. 46) show that supergene enrichment was active in

the Miocene from 22.2 to 8.7 Ma, and probably included a number of enrichment cycles controlled by episodic uplift of the Big Burro Mountains and descending groundwater levels. These enrichment cycles are evidenced by alternating hematite and lower jarosite horizons in the leached cap (Plate 5), and possibly by 2-3.5 million year gaps in the alunite dates particularly in the later Miocene (16-6 Ma). Individual supergene enrichment cycles may have been of short duration, with complete oxidation of pyrite in the oxide zone occurring in as little as 500,000 years for each cycle (Lichtner and Biino, 1992).

Some groundwater carrying dissolved iron and copper exited the supergene system by lateral flux to form exotic copper deposits in northeast-trending paleochannels (ferricrete) that drained the oxidizing porphyry copper deposit. Renewed uplift after ~12 Ma (age of the ferricrete), lowered the groundwater table and exposed the ferricrete to erosion. The single late Miocene alunite date of 8.7 Ma (Fig. 46) may represent the last cycle of Miocene enrichment when groundwater levels fell and the ferricrete was eroded. Supergene enrichment had largely diminished after ~10 Ma as the late Miocene climate became more arid (Sillitoe and McKee, 1996). Local, late-stage, in-situ oxidation of parts of the chalcocite blanket may have begun at this time.

The lower alluvial fan gravel partially buried the porphyry copper deposit before ~6 Ma (Fig. 53E, 6 Ma). These sediments were deposited at the western margin of the San Vicente basin as the Mangas basin had not yet formed. Deposition of thick gravel indicates that uplift had waned in the late Miocene in agreement with Mack (2004) (Fig.9).

PLIOCENE-PLEISTOCENE SUPERGENE ENRICHMENT

The third stage of supergene enrichment occurred with rejuvinated Basin and Range faulting in the latest Miocene-Pleistocene (Figs. 9 and 11). This later phase of Basin and Range faulting began at ~5 Ma in the southern Transition Zone (Fig. 11) (Mack, 2004), and in the

Tyrone area it involved displacement on the Mangas fault, uplift of the Little Burro Mountains, and formation of the Mangas half graben (Fig. 11; Fig. 53F, 1.5 Ma). The initial displacements on the Mangas fault occurred after deposition of the ferricrete (12.1 Ma) and the lower alluvial fan gravel. Uplift of the Little Burro Mountains exposed previously buried upper Eocene-Oligocene volcanic rocks. Renewed displacement on the Knight Peak fault also resulted in further uplift and tilting of the Big Burro Mountains.

Most of the tilting at Tyrone is due to displacements on the Mangas fault as evidenced by the tilt of the Mangas half-graben (at least 10-12°). The cumulative tilt of the Big Burro Mountains block resulting from all Basin and Range extensional faulting is probably less than 20° based on the tilt of the Mangas half graben and the chalcocite enrichment blanket (7-9°). Volcanic rocks in the Little Burro Mountains dip at an average of 20-25° to the northeast.

The resumption of extensional faulting at ~5 Ma corresponds well with the youngest alunite date of 4.6 Ma (Fig. 46). The sample that yielded this age is from the pyrite-rich but copper-poor halo of the porphyry deposit in the southern Little Burro Mountains. Strong supergene kaolinite alteration and jarosite staining in Stage 3 quartz monzonite porphyry in the southern Little Burro Mountains indicate this part of the system produced abundant acid upon uplift and oxidation.

Pliocene-Pleistocene uplift and tilting of the Miocene chalcocite enrichment blanket and lowering of the groundwater table probably caused only local leaching of the chalcocite blanket due to the arid climate that began in the late Miocene at about 10 Ma (Sillitoe and McKee, 1996), and (nearly) complete consumption of pyrite in the oxidized zone. Active supergene enrichment ended. The chalcocite blanket underwent in-situ oxidation to chrysocolla and malachite throughout the district, and especially where erosion exposed the blanket (DuHamel et al., 1995).

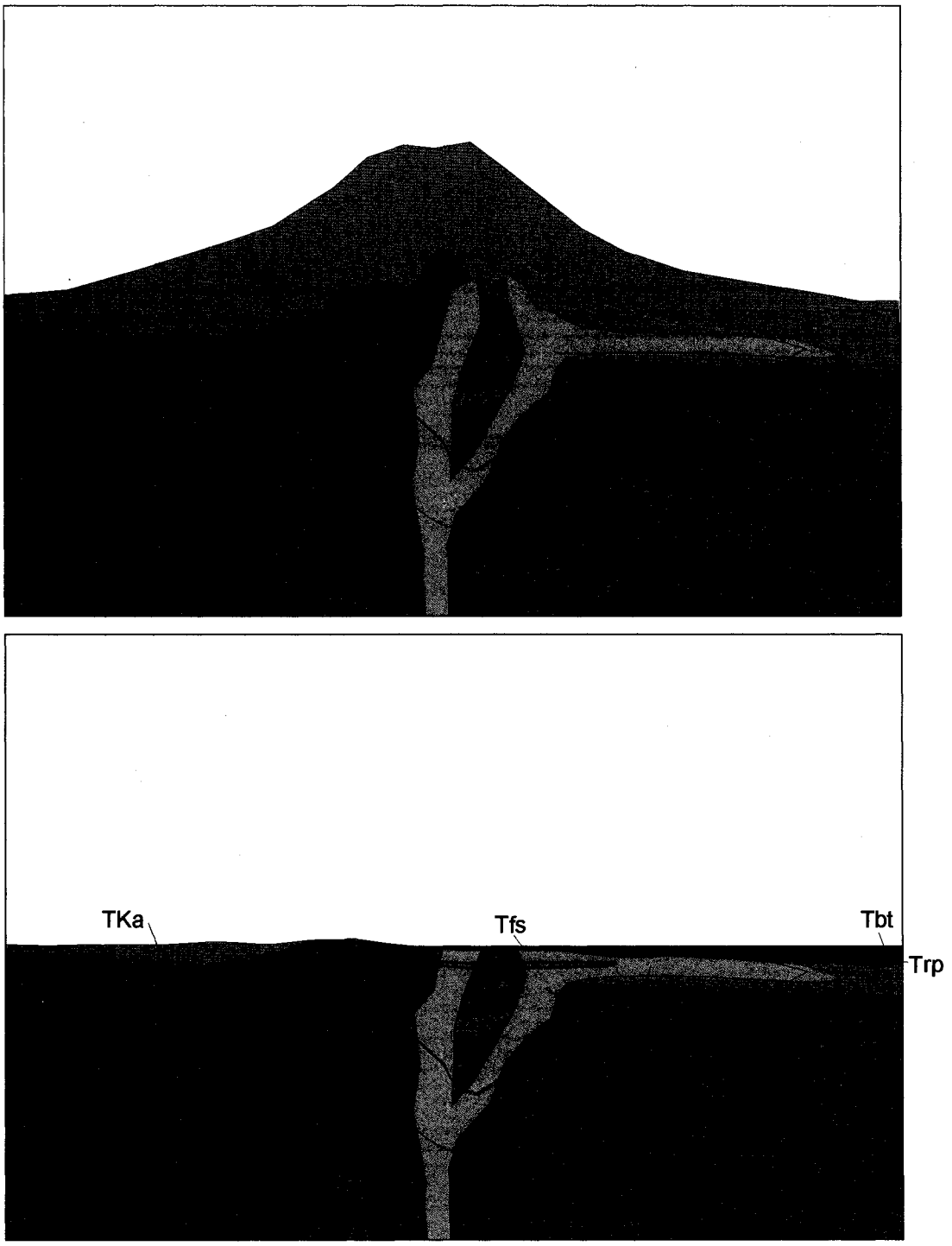

Figure 53. Schematic tectonic development of the Tyrone supergene system in a line of section from Burro Peak to Tyrone Peak. Not to scale. Lithologic symbols are the same as those used on Figure 12 and Plate 1. Intrusive stages of porphyry units associated with the Tyrone stock are designated as Stage 1 and Stages 2-3. Green line is boundary of potassic alteration zone; red line is boundary of overprinting phyllic alteration zone. Chalcocite blanket designated by diagonal hatch pattern. See text for discussion.

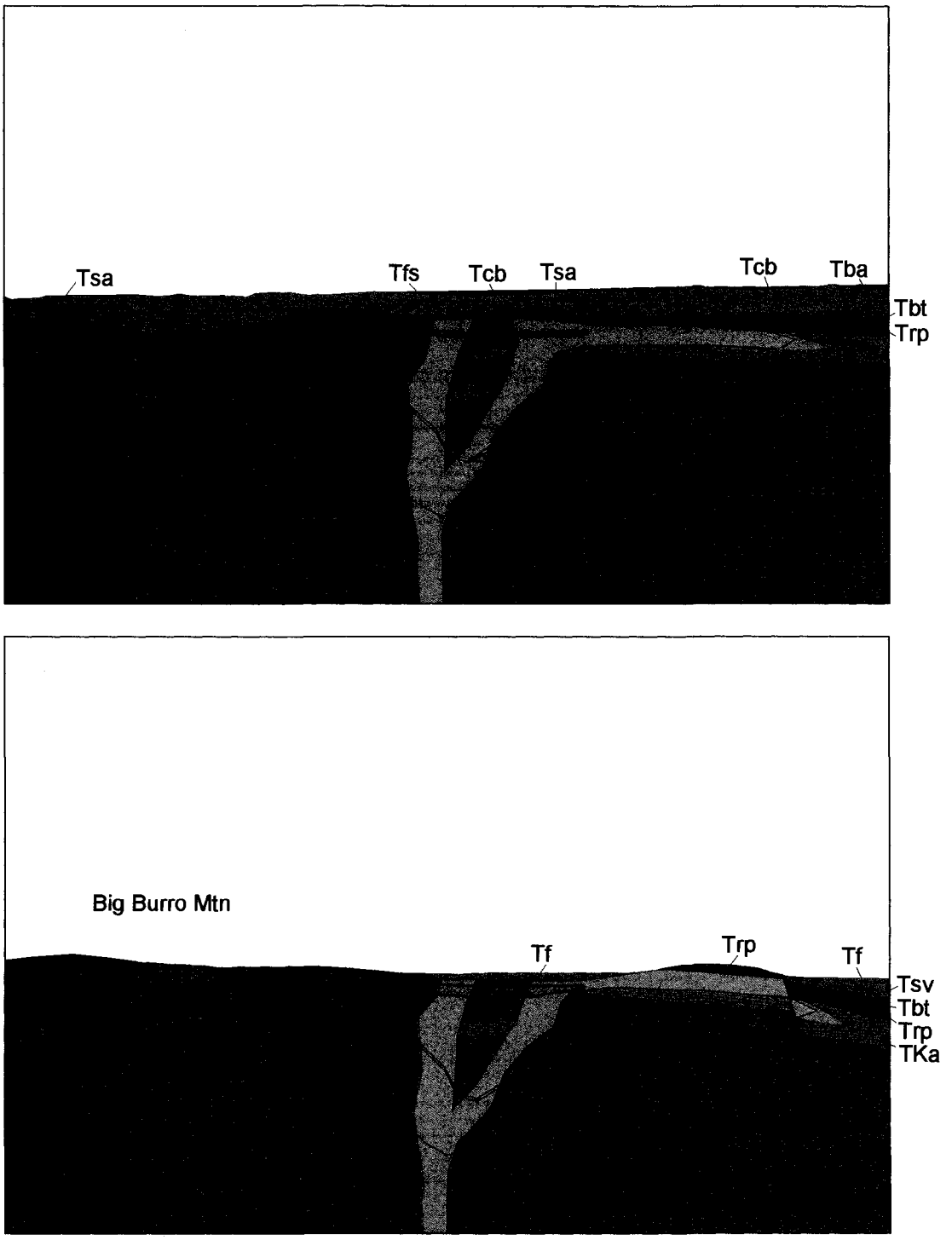

Figure 53, continued. Tectonic development of the Tyrone supergene system.

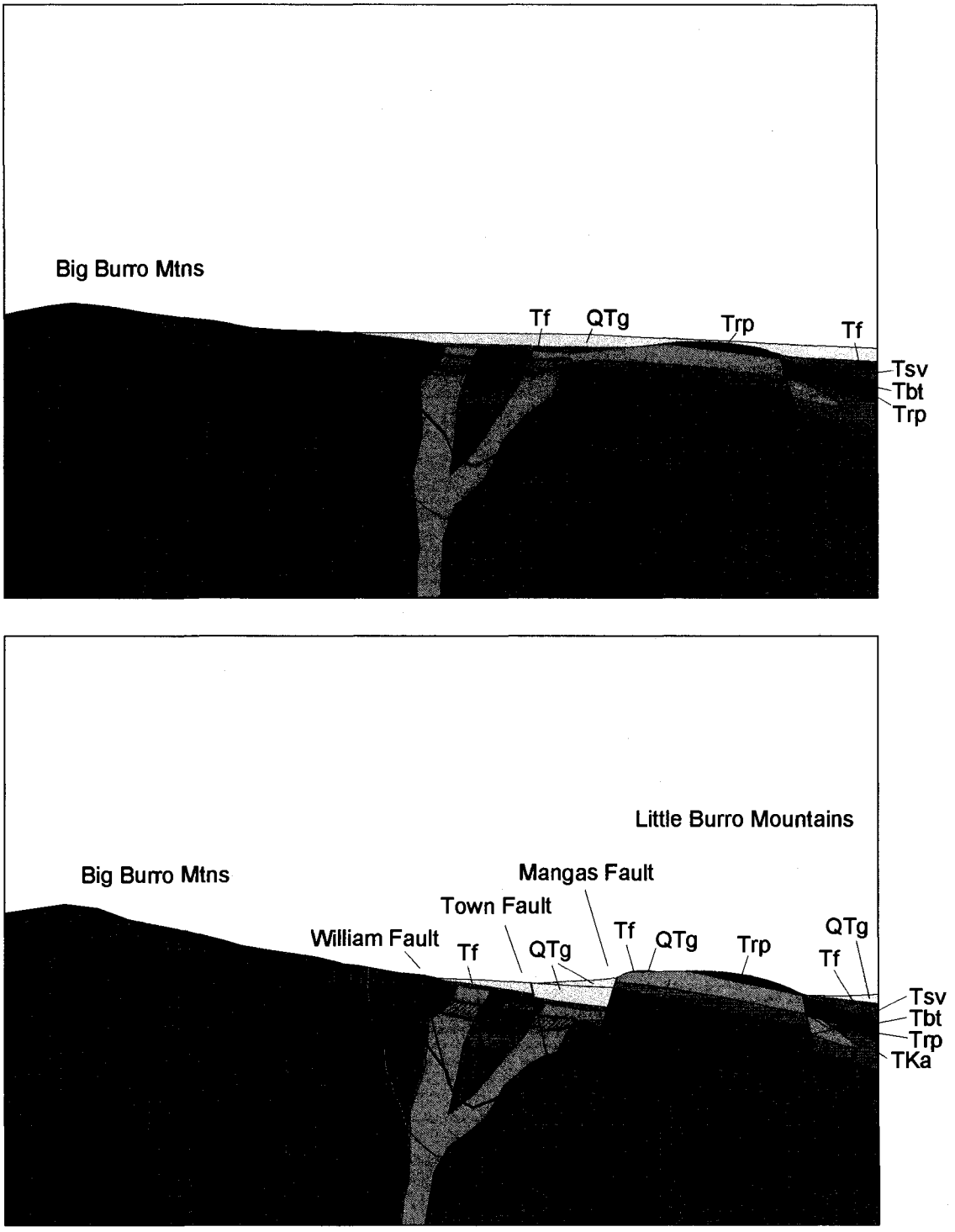

Figure 53, continued. **Tectonic development of the Tyrone supergene system.**

CHAPTER 13: SEQUENTIAL DEVELOPMENT OF THE ZONED SUPERGENE SYSTEM

Figure 54 is a series of schematic cross sections, prepared by the author, that depict the development of the irregular, laterally-zoned supergene system at Tyrone. The sections are intended to illustrate how the laterally-zoned hypogene system and faults controlled the lateral and vertical distributions of chalcocite and copper oxide zones. The cross sections represent the area from the Copper Mountain pit in the southwestern part of the district to the Main pit in the northeastern part of the district, a distance of approximately 3.2 km (2 mi). The vertical direction is exaggerated on the sections, but no vertical scale is implied. Cross sections were constructed using the Phelps Dodge Tyrone ore mineral types (Table 4).

Figure 54A shows the hypogene deposit prior to supergene enrichment. In the Main pit, the hypogene deposit has high hypogene sulfide content (2-5 vol. %), high pyrite:chalcopyrite (~11:1), and is dominated by phyllic alteration assemblages. The Copper Mountain pit has lower hypogene sulfide content (0.5-2.5 vol. %), lower pyrite:chalcopyrite (~7:1), and potassic alteration assemblages.

The three main stages of oxidation and enrichment described above are represented in Figure 54B-D. Each period of renewed uplift through the Miocene produced a relative lowering of the groundwater table, and rejuvenated supergene enrichment. Permeable zones such as faults played a major role in the downward movement of oxidized solutions. In the southwestern part of the district, solutions were neutral or alkaline, allowing formation of black copper oxides in the leached zone during first cycle leaching and a copper oxide zone at the top of the chalcocite blanket. In the northeastern part of the district, consumption of pyrite in the oxidizing zone and transition to more alkaline conditions may not have occurred until after 10 Ma except locally along faults that were conduits for dilute meteoric solutions. However, copper oxide ghost zones

may have formed at the top of the chalcocite blanket during some enrichment cycles resulting in perched cuprite and native copper zones (ore mineral type 8) in the leached cap upon renewed uplift and supergene enrichment. Finally, in-situ oxidation of chalcocite and replacement of earlier-formed copper oxides/sulfates by chrysocolla and malachite (ore mineral type 2) occurred in a weathering environment after complete oxidation of pyrite and depression of the groundwater table below the top of the chalcocite blanket in an arid climate.

Late Eocene (first stage, 45-35 Ma, Fig. 54B) oxidation and enrichment accompanied the erosional event that followed the Laramide orogeny. In the Main pit area, acidic conditions resulted in a well-developed chalcocite enrichment blanket and jarositic leached cap. In the Copper Mountain area, near-neutral to alkaline conditions resulted in a goethitic leached cap containing black copper oxides over a thin, low-grade chalcocite enrichment blanket. Ash-flow tuff deposition commenced at ~36 Ma and lasted until ~24 Ma (McIntosh et al., 1992).

Early Miocene, main-stage enrichment (second stage, 22-16 Ma, Fig. 54C) followed initiation of Basin and Range faulting/uplift and erosional removal of ash-flow tuffs from the deposit. Acidic conditions were maintained in the oxidizing column in the area of the Main pit. A hematitic leached cap occured in the position of the Eocene enrichment blanket, and a new chalcocite blanket formed below the groundwater table which had fallen to a new base level. Leaching of the intervening rock produced a lower jarosite zone. In the Copper Mountain area, a copper oxide zone containing cuprite and native copper was formed above the chalcocite enrichment blanket. The surface at the time was topographically high, and erosion dominated.

Subsequent Miocene erosion, leaching, and enrichment (second stage, 16-6 Ma, Fig. 54D) accompanied slowed but continued episodic uplift and a descending groundwater table during the middle to late Miocene. The earlier-formed Miocene enrichment blanket(s) in the Main pit were leached and oxidized to hematite, and a thick chalcocite blanket developed below. The leached Eocene blanket was eventually completely removed by erosion. In the Copper

Mountain pit, a thick copper oxide zone formed at the expense of the chalcocite blanket. Lateral flux of iron and copper resulted in deposition of ferricrete in paleochannels. Ferricrete was subsequently eroded and overlain by lower alluvial fan gravel.

At post-6 Ma (third stage, Fig. 54E), deposition of the lower semiconsolidated alluvial fan gravel unit continued until faulting on the Mangas fault. Uplift and tilting on the Mangas and Knight Peak faults again resulted in lowering of the groundwater table, but with the onset of more arid conditions, supergene enrichment diminished. The chalcocite blanket was tilted intact 7-9° to the northeast (not shown on Fig. 54). Pyrite was totally consumed above the chalcocite blanket. In-situ oxidation of copper sulfides and replacement of earlier-formed copper oxides by chrysocolla and malachite produced copper oxide zones across the district. Chalcanthite has locally developed where chalcocite is exposed in the present pit benches.

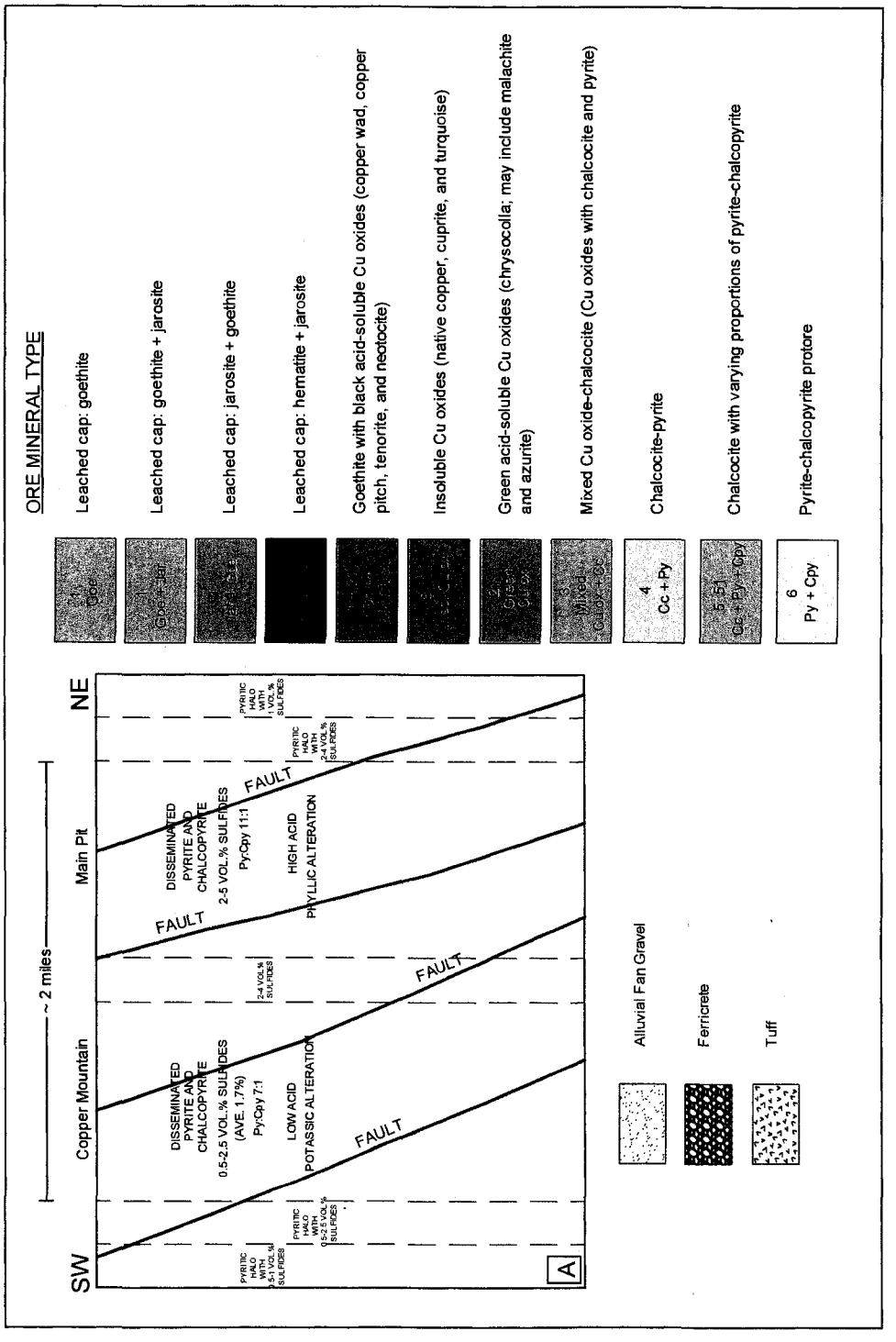

Figure 54. Development of the Tyrone supergene profile. A. Hypogene deposit. See text for discussion.

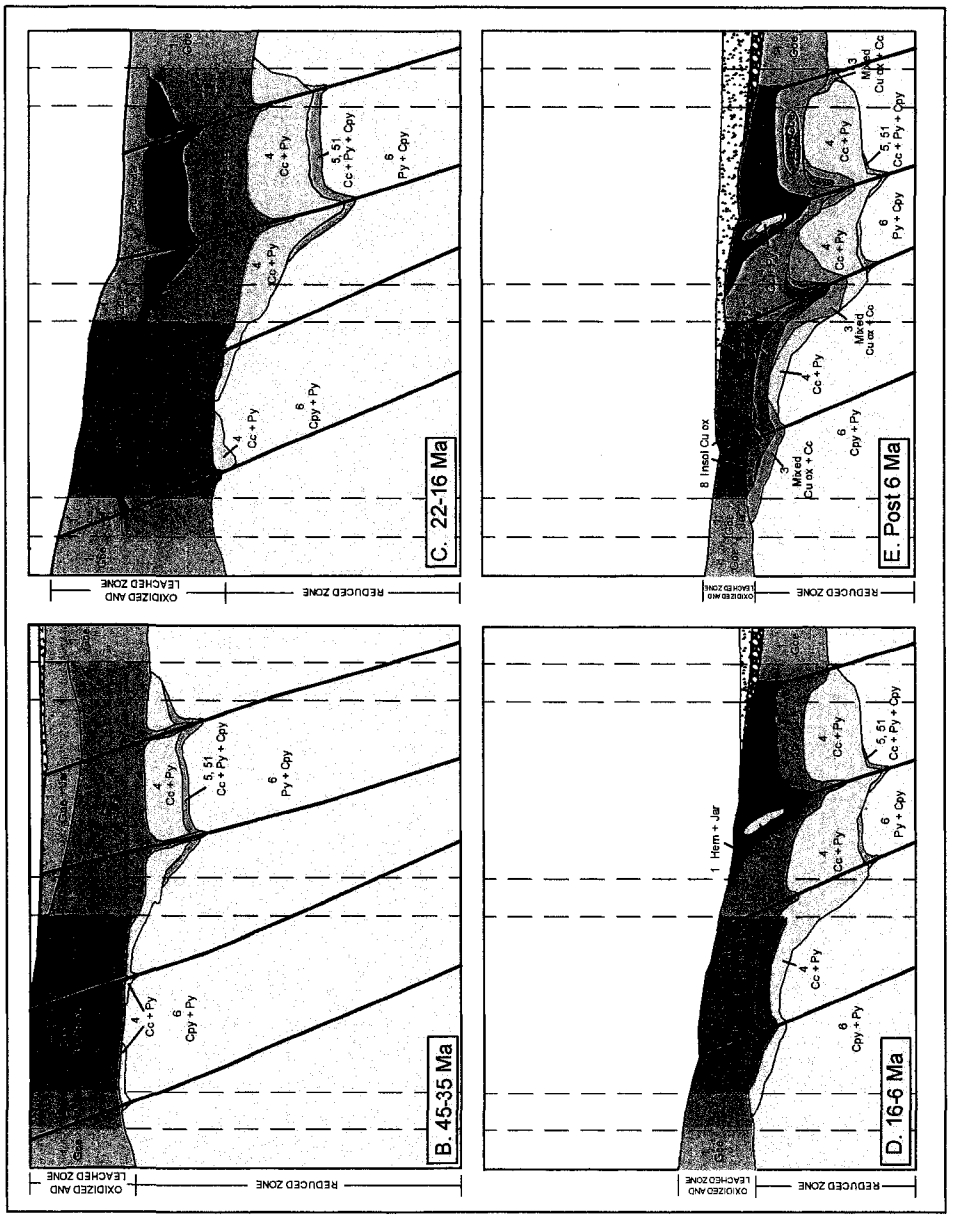

Figure 54. Development of the Tyrone supergene profile, continued. B. 45-35 Ma: First-stage supergene enrichment with major erosion; deposit eventually covered by ash-flow tuff. C. 22-16 Ma: Second, "main-stage" supergene enrichment with uplift, minor tilting and erosion. D. 16-6 Ma: Continued second-stage supergene enrichment with renewed uplift, minor tilting and erosion. Deposition and erosion of ferricrete. Lower alluvial fan gravel onlapped the deposit as uplift slowed. E. Post-6 Ma: Third-stage enrichment. Faulting and tilting on Mangas fault (not shown). Renewed uplift. Local chalcocite enrichment. Late-stage in-situ oxidation.

CHAPTER 14: SUMMARY AND CONCLUSIONS

This study has helped clarify the Cenozoic tectonic history of southwestern New Mexico, and has placed supergene events at Tyrone into the framework of tectonic events and the development of the Mogollon-Datil volcanic field. Geologic mapping in the southern part of the Little Burro Mountains and detailed $^{40}Ar/^{39}Ar$ dating of supergene minerals have led to the recognition of two major erosional unroofing/supergene enrichment events at Tyrone. The first event occurred in the late Eocene and is represented by the copper-bearing ferruginous conglomerate unit in the southern Little Burro Mountains. The ferruginous conglomerate overlies an unconformity between ash-flow tuff units erupted at 35.7 Ma (Bell Top Formation) and 31.6 Ma (Caballo Blanco Tuff). This supergene enrichment event took place during regional erosion that followed the Laramide orogeny. No chalcocite enrichment blanket or alunite veins remain from the late Eocene event, and the chalcocite blanket was probably entirely leached and removed by erosion during the Miocene. Dip fanning was not observed in the volcanic section in the Little Burro Mountains, indicating that extensional deformation and tilting did not occur in the Tyrone area until the onset of Basin and Range deformation in the early Miocene. However, minor renewed Eocene uplift of the Tyrone horst on northeast-striking Laramide faults may have kept the deposit elevated through the late Miocene.

The second erosional unroofing/supergene enrichment event took place in the early to late Miocene, and included formation of ferricrete in northeast-trending paleochannels. The Miocene event was the dominant supergene enrichment event at Tyrone. Ten $^{40}Ar/^{39}Ar$ dates on alunite from the Miocene event range from 22.2 to 8.7 Ma, and cryptomelane from the ferricrete yielded a date of 12.1 Ma, indicating a duration of at least 13.5 million years for main stage Miocene enrichment. The Miocene event probably consisted of a number of enrichment cycles of short duration related to episodic uplift of the Big Burro Mountains. Alunite and cryptomelane

dates in the later part of the Miocene (16-6 Ma) are separated by 2-3.5 Ma gaps that may represent diminished supergene enrichment due to slowing uplift and the drying Miocene climate. Alternating hematite and lower jarosite horizons logged in the leached cap, and calcic paleosols in basin-fill gravels suggest episodic uplift and supergene enrichment (Griffin, 2001; Mack and Stout, 2005).

The Miocene event was related to extensional faulting on the Treasure Mountain and Knight Peak faults, major northwest-striking Basin and Range normal faults that bound the Big Burro Mountains uplift and the San Vicente half graben (Mack, 2004). These faults have been active since the early Miocene, as evidenced by thick but poorly-dated basin-fill deposits in the San Vicente half graben (Mack, 2004). Some older, northeast-striking Laramide faults within the Big Burro Mountains horst were also reactivated at this time and formed local grabens that preserved the upper Eocene-Oligocene volcanic rocks from erosion.

A third, minor supergene enrichment event occurred in the Pliocene-Pleistocene and was related to uplift of the Little Burro Mountains and formation of the Mangas half graben along the Mangas fault. This event is represented by a single alunite date of 4.6 Ma from the southern Little Burro Mountains, and took place as supergene enrichment was waning. The chalcocite enrichment blanket was tilted 7-9° to the northeast by displacement on the Mangas fault.

The Miocene and Pliocene-Pleistocene supergene enrichment events at Tyrone can be clearly related to displacements on specific Basin and Range normal faults. The Tyrone district lies within the Basin and Range province but near its poorly defined boundary with the southern Transition Zone (Fig. 3). Mack (2004) placed the beginning of Basin and Range normal faulting in the southern Transition Zone at ~20 Ma and in the Basin and Range province at ~26 Ma. Alunite dates from Tyrone indicate that uplift and unroofing of the deposit began before 22 Ma, and possibly much earlier to allow time for erosion of volcanic rocks from the deposit before oxidation and supergene enrichment began. Thus, 26 Ma may be close to the beginning of uplift

of the Big Burro Mountains horst and the Tyrone deposit. Supergene alunite and cryptomelane dates have been shown here to be valuable pieces of information in deciphering the timing of faulting in areas where sulfide ore deposits are being uplifted and oxidized, and the regional structural geology is well understood.

The history of erosional unroofing and supergene enrichment events at Tyrone may be summarized as follows. Regional Eocene erosion produced and low-relief erosional surface and probably a supergene blanket before ~35 Ma. The Eocene supergene enrichment event ended in the late Eocene-Oligocene when the deposit was buried by volcanic rocks. Basin and Range extension in this part of New Mexico and uplift of the Big Burro Mountains began shortly before 22 Ma and was more or less vigorous until at least 12 Ma as evidenced by strong early-mid Miocene supergene enrichment blanket and ferricrete deposits. Faulting and uplift then slowed in the late Miocene and the deposit was buried by alluvial fan gravel. Faulting and uplift were rejuvenated before 5 Ma with uplift of the Little Burro Mountains on the Mangas fault, resulting in tilting of the chalcocite and minor enrichment.

The southern part of the Little Burro Mountains contains a well-preserved section of upper Eocene-Oligocene volcanic and volcaniclastic rocks (710 m (2,300 ft)) associated with the Mogollon-Datil volcanic field. Tuff member 3 of the Bell Top Formation (31.6 ± 0.36 Ma) and the Caballo Blanco Tuff (35.73 ± 0.09 Ma) were dated by $^{40}Ar/^{39}Ar$ and identified as part of this study. The entire volcanic section has been correlated with rocks of the Mogollon-Datil volcanic field using lithologic characteristics and stratigraphic position of the various units. From bottom to top, the formations in the southern part of the Little Burro Mountains are the Rubio Peak Formation, Bell Top Formation, Sugarlump Tuff, basaltic andesite possibly correlative with the Rustler Canyon Basalt, Caballo Blanco Tuff, and basaltic andesite possibly correlative with the Razorback Formation. As a result of this study, the Little Burro Mountains section is one of the southwesternmost dated sections in the Mogollon-Datil volcanic field.

Drill hole logging through the Tyrone district has shown that the laterally-zoned supergene system, from a chalcocite-dominated enrichment blanket in the northeastern part of the district to copper oxide-dominant blanket in the southwest, was strongly controlled by lateral variations in hypogene pyrite:chalcopyrite ratios, total hypogene sulfide content, and alteration assemblages. In the northeastern part of the district, the hypogene system is characterized by strong phyllic alteration, high pyrite:chalcopyrite (~11:1), and high hypogene sulfide content (2-5 vol. %). Strong acid generation and nonreactive host rocks in that area resulted in deep oxidation, strong copper leaching, and a well-developed chalcocite enrichment blanket. The chalcocite blanket in the graben between the Burro Chief-West Main and Virginia-Racket fault zones is generally overlain by a thick, hematite-dominant leached cap. However, because of the erosion of the leached cap and lateral copper flux, the strength and thickness of the hematitic leached cap cannot always be used to predict how well developed the underlying chalcocite blanket will be in a given location. Interlayering of hematite horizons and lower jarosite horizons can be distinguished in only a few drill holes, and hematite horizons cannot be reliably correlated between drill holes at 370 m (1200 ft) spacing because of the strong structural control on supergene enrichment in the district. Some of the strong hematite horizons represent former chalcocite blankets, but others were formerly enriched, steeply-dipping structural zones such as faults and fractures. Dip fanning could not be distinguished in the hematite horizons, again because of the difficulty in making correlations. Correlation of hematite horizons between drill holes may be a useful tool in porphyry copper deposits that have less structural complexity.

The hypogene system in the southwestern part of the district is characterized by a reactive potassic alteration assemblage, low pyrite:chalcopyrite (~7:1), and low hypogene sulfide content (0.5-2.5 vol. %). Weak acid generation in that area and strongly reactive host rocks resulted in poor copper leaching, a thin, low-grade chalcocite blanket, and a well-developed copper oxide zone. Much of the copper oxide material in the southwestern part of the district (ore

mineral types 21 and 8, both 0.18% Cu) is low grade and may have formed by incomplete leaching during active enrichment. Copper oxides mainly in the central and northeastern parts of the district are higher grade (ore mineral type 2, 0.34%), and may have been produced dominantly by in-situ oxidation of chalcocite.

The unusual distribution of hydrothermal alteration zones and copper mineralization at Tyrone is due in part to northeast tilting of the deposit during Basin and Range faulting along the Mangas fault. Tilting of the deposit depressed and protected the thick phyllic alteration zone in the northeastern part of the system from erosion, while elevating and exposing the potassic zone in the southwestern part of the district.

Mass balance calculations involved untilting the chalcocite blanket to find the elevation of the top of the blanket. The top of the hypogene copper-bearing system was calculated at an average elevation of 2,150 m (7,050 ft), or 250 m (820 ft) above the average pre-mine surface elevation. North and northeast-trending copper flux contours and the presence of copper-bearing ferricrete deposits in northeast-trending paleochannels show that copper flux was preferentially to the northeast. Northeast-striking faults and lithologic contacts (i.e., the granite/porphyry contact), probably served as conduits for supergene fluids, but fluid flow was largely controlled by the northeast-sloping hydrologic gradient established during uplift and tilting of the deposit during active supergene enrichment. Copper flux resulted in the strongest enrichment in the graben between the Burro Chief-West Main and Virginia-Racket fault zones. As much as 370,000 metric tons of copper were provided by areas of negative copper flux in the northern part of the deposit, and although some of this copper exited the deposit in northeast-trending paleochannels, most was probably captured by internal drainage into the sink between the Burro Chief-West Main and Virginia-Racket fault zones.

Hydrogen and sulfate oxygen stable isotopes from alunite indicate that the supergene system was well oxygenated and that alunite formed under unsaturated conditions. Groundwater

was recharged during seasonal precipitation, and the deposit experienced alternating wet and dry periods. Sulfur isotopes from alunite show that sulfur was derived from precursor hypogene sulfide minerals. The carbon and oxygen isotopes of malachite reveal isotopic signatures similar to speleothems. Carbon was probably derived from plant-respired CO_2. Late-stage oxidation of the deposit took place largely in unsaturated conditions above the groundwater table.

IMPLICATIONS FOR TIMING OF SUPERGENE ENRICHMENT AND EXPLORATION FOR LARAMIDE PORPHYRY COPPER DEPOSITS

Figure 55 summarizes published and unpublished K-Ar and $^{40}Ar/^{39}Ar$ dates for supergene alunite and jarosite for some porphyry copper deposits in the southwestern U.S. The alunite and cryptomelane dates from this study are also shown on the diagram. The arrow at Tyrone indicates the minimum age of Eocene enrichment based on the age of the Sugarlump Tuff which unconformably overlies the ferruginous conglomerate unit and underlies the Caballo Blanco Tuff (Fig. 12). The age data suggest that in most of the deposits, main-stage supergene enrichment occurred in the Miocene. For Morenci (Enders, 2000) and Tyrone (this study), the two deposits with timing of supergene enrichment most tightly constrained by $^{40}Ar/^{39}Ar$ dates, dominant supergene enrichment occurred between 14-3 Ma and 22-5 Ma, respectively. Livingston et al. (1968) noted evidence for Eocene enrichment in some Arizona deposits, but the K-Ar alunite dates presented by Cook (1994) indicate that most preserved supergene profiles in Arizona are also Miocene in age. It is significant that, although regional Eocene erosion affected most if not all of the deposits in the Laramide porphyry copper province (Scarborough, 1989), Eocene supergene enrichment is poorly represented in the radiometric data in Figure 55.

Chino and Tyrone both exhibit evidence for Eocene enrichment, and the difference in enrichment histories of the two deposits shown on Figure 55 can be explained by the degree of preservation beneath volcanic rocks of the Mogollon-Datil volcanic field. In the Chino deposit,

the leached cap contains supergene alunite veins as old as 48.1 Ma (R. Stegen, 2003, pers. comm.). The Eocene supergene profile has been preserved at Chino because of the Kneeling Nun tuff (34.9 Ma), which partially overlies the deposit (Cook, 1994). In contrast, at Tyrone, Miocene uplift of the Big Burro Mountains led to complete erosion and removal of volcanic cover and destruction of the Eocene leached cap and enrichment blanket. As noted above, the Eocene ferruginous conglomerate at Tyrone was preserved by burial within the San Vicente half graben, and later exposed by uplift of the Little Burro Mountains. Tyrone may be one of few deposits in the Laramide porphyry copper province in which both Eocene and Miocene supergene enrichment events can be clearly documented and dated. Although no vestige of the Eocene blanket remains within the Tyrone deposit itself, $^{40}Ar/^{39}Ar$ dating of the ferruginous conglomerate and supergene minerals combined with a mass balance estimate of the amount of leached material that has been removed by erosion provides evidence of an Eocene supergene enrichment event that was overprinted by a Miocene enrichment event. It is possible that in many deposits of the Laramide porphyry copper province, Eocene supergene profiles were destroyed by Miocene uplift and erosion.

Mapping in the southern Little Burro Mountains has shown that thin Eocene ferricrete or ferruginous conglomerate horizons may be poorly exposed and easily overlooked. The ferricrete deposits are valuable both for dating supergene enrichment events and as guides for exploration, particularly in buried porphyry copper deposits. Ferricretes may be exposed in mountain ranges (horst blocks) surrounding porphyry copper deposits that were downfaulted and buried during Miocene Basin and Range extension. The ferricrete deposits and their paleocurrent indicators could be used to identify areas within basins that are favorable for buried porphyry copper deposits and to direct exploration efforts such as geophysical and geochemical surveys and drilling. However, Scarborough (1989) noted that Eocene sedimentary rocks are rare in the Basin and Range province of southern Arizona because the Eocene was marked by erosion or

nondeposition. Some Eocene sedimentary rocks (Whitetail Assemblage of Scarborough (1989), Fig. 55) were deposited in local basins and occur as tilted and beveled fault-block remnants under mid-Tertiary volcanic cover.

Mass balance analyses should be routinely conducted along with structural mapping during exploration/development of porphyry copper deposits to answer questions such as: How much erosion of the protore is indicated? How much copper cannot be accounted for in the supergene blanket, and in what directions was copper transported? Where are the possible copper sinks and exotic deposits? The last two questions are especially relevant in deposits that were tilted and possibly dismembered during extensional faulting. Sink areas such as local grabens may be very important in exploration for economic copper deposits. Mass balance analysis can be easily done with basic copper assay and density data collected during exploration drilling.

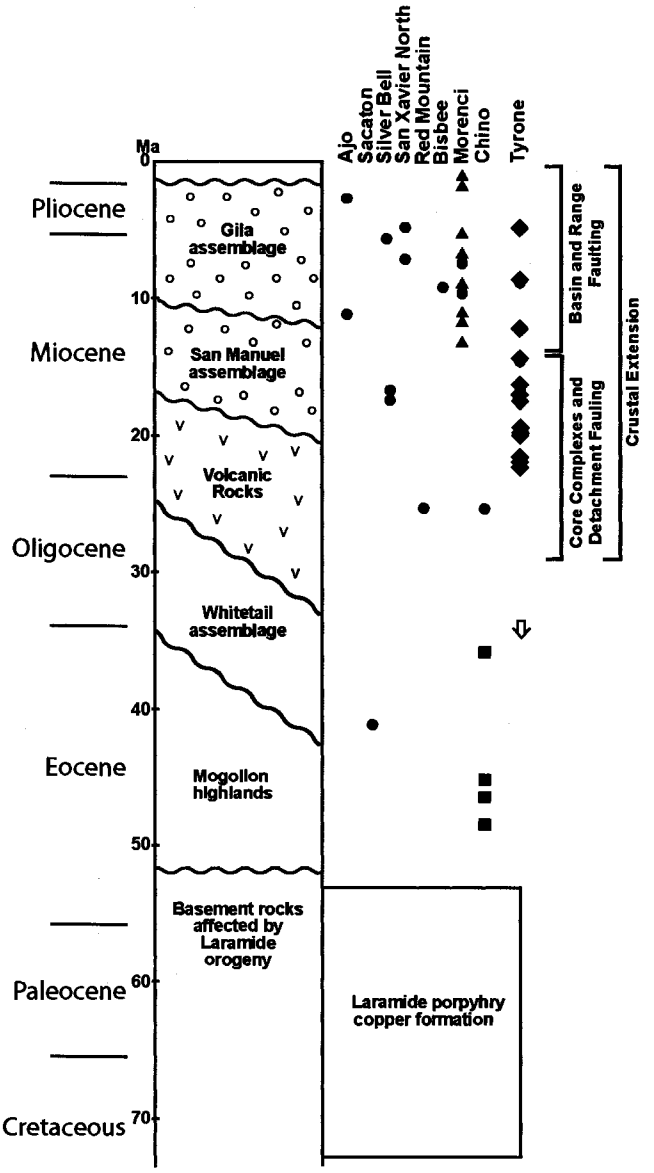

Figure 55. Ages of supergene activity at several porphyry copper deposits in southern Arizona and southwestern New Mexico. The timing of formation of Laramide porphyry copper deposits is indicated by the height of the box; Cenozoic sedimentary assemblages of Scarborough (1989) and tectonic styles/timing defined by Dickinson (2002) are also shown. Supergene enrichment of the copper deposits predates and spans mid-Tertiary extension. Supergene alunite and jarosite dates are as follows: K-Ar dates from Cook (1994) are shown as black circles; $^{40}Ar/^{39}Ar$ dates for Morenci from Enders (2000) are shown as black triangles; unpublished K-Ar and $^{40}Ar/^{39}Ar$ total gas ages for the Chino deposit from R. Stegen (pers. comm., 2003) are shown as black squares; $^{40}Ar/^{39}Ar$ dates for Tyrone from this study and R. Stegen (pers. comm., 2003) are shown as red diamonds. The arrow at Tyrone is the minimum age of Eocene supergene activity based on the age of Sugarlump Tuff overlying the ferruginous conglomerate in the southern Little Burro Mountains. Diagram modified from Sillitoe (2005).

REFERENCES

Ague, J.J., and Brimhall, G.H., 1989, Geochemical modeling of steady state fluid flow and chemical reaction during supergene enrichment of porphyry copper deposits: Economic Geology, v. 84, p. 506-528.

Alpers, C.N, and Brimhall, G.H., 1988, Middle Miocene climate change in the Atacama Desert, northern Chile: Evidence from supergene mineralization at La Escondida: Geological Society of America Bulletin, v. 100, p. 1640-1656.

Alpers, C.N, and Brimhall, G.H., 1989, Paleohydrologic evolution and geochemical dynamics of cumulative supergene metal enrichment at La Escondida, Atacama Desert northern Chile: Economic Geology, v. 84, p. 229-255.

Anderson, C.A., 1955, Oxidation of copper sulfides and secondary sulfide enrichment: Economic Geology 50th Anniversary Volume, Part I, p. 324-340.

Anderson, J. A., 1982, Characteristics of leached capping and techniques of appraisal, *in* Titley, S.R., ed., Advances in geology of the porphyry copper deposits, southwestern North America: University of Arizona Press, p. 275-295.

Arehart, G.B., and O'Neil, J.R., 1993, D/H ratios of supergene alunite as an indicator of paleoclimate in continental settings, *in* Swart, P.K., Lochman, K.C., McKenzie, J., and Savin, S., eds., Climate change in continental isotopic records: American Geophysical Union Geophysical Monograph 78, p. 277-284.

Banfield, J.F., and Nealson, K.H., eds., 1997, Geomicrobiology: interactions between microbes and minerals: Mineralogical Society of America, Reviews in Mineralogy, v. 35, 448 p.

Bladh, K.W., 1982, The formation of goethite, jarosite, and alunite during the weathering of sulfide-bearing felsic rocks: Economic Geology, v. 77, p. 176-184.

Blanchard, R., 1968, Interpretation of leached outcrops: Nevada Bureau of Mines Bulletin 66, 196 p.

Brimhall, G.H., Alpers, C.N., and Cunningham, A.B., 1985, Analysis of supergene ore-forming processes and groundwater solute transport using mass balance principles: Economic Geology, v. 80, p. 1227-1256.

Cather, S.M., and Johnson, B.D., 1986, Eocene depositional systems and tectonic framework of west-central New Mexico and eastern Arizona, *in* Peterson, J.A., ed., Paleotectonics and sedimentation in the Rocky Mountain region, United States: American Association of Petroleum Geologists Memoir 41, p. 623-652.

Cerling, T.E., 1984, The stable isotopic composition of modern soil carbonate and its relationship to climate: Earth and Planetary Science Letters, v. 71, p. 229-240.

Chapin, C.E., McIntosh, W.C., and Chamberlin, R.M., 2004, The late Eocene –Oligocene peak of

Cenozoic volcanism in southwestern New Mexico, *in* Mack, G.H., and Giles, K.A., eds., The Geology of New Mexico, A Geologic History: New Mexico Geological Society Special Publication 11, p. 271-293.

Chávez, W.X., Jr., 2000, Supergene oxidation of porphyry copper deposits: zoning and distribution of copper oxide minerals: SEG Newsletter, no. 42, April 2000.

Chávez, W.X., Jr., 2005, Salient geologic and geochemical features characterizing economically-significant supergene copper sulfide development from porphyry-type protoliths: Geological Society of Nevada 2005 Symposium, Field Trip No. 9- Porphyry deposits of the Great Basin.

Clemons, R.E., and Mack, G.H., 1988, Geology of southwestern New Mexico: New Mexico Geological Society Guidebook 39, p. 45-57.

Cook, S.S., 1994, The geologic history of supergene enrichment in the porphyry copper deposits of southwestern North America: unpublished PhD dissertation, University of Arizona, 163 p.

Danley, W.M., 1976, Summary of 1975 work and Phase II Proposal for drilling Bald Mountain prospect, Grant County, New Mexico: Amax Exploration, Inc. internal report, 17 p.

Danley, W.M., 1978, Drilling summary 1976-1977 Bald Mountain Project 698, Grant County, New Mexico: Amax Exploration, Inc. internal report, 16 p.

Dickinson, W.R., 1989, Tectonic setting of Arizona through geologic time, *in* Jenney, J.P., and Reynolds, S.J., eds., Geologic evolution of Arizona: Tucson, Arizona Geological Society Digest 17, p 1-16.

Dickinson, W.R., 1991, Tectonic setting of faulted Tertiary strata associated with the Catalina core complex in southern Arizona: Geological Society of America Special Paper 264, 106 p.

Dickinson, W.R., 2002, The Basin and Range province as a composite extensional domain: International Geology Review, v. 44, p. 1-38.

Drewes, H., Houser, B.B., Hedlund, D.H., Richter, D.H., Thorman, C.H., and Finnell, T.L., 1985, Geologic map of the Silver City 1° x 2° quadrangle New Mexico and Arizona: U.S. Geological Survey Map I-1310-C, scale1:125,000.

DuHamel, J.E., 1986, Recommendations for drilling in the vicinity of the Tyrone mine, Grant County, New Mexico, Quadrangle 411, Phelps Dodge internal report, 9 p.

DuHamel, J.E., 1991, 1990 Annual Progress Report Tyrone project, Grant County, New Mexico, Phelps Dodge internal report, 11 p.

DuHamel J.E., and Cook, S.S., 1992, Results of investigation May 1990 through April 1992, Tyrone Project, New Mexico 411, Phelps Dodge internal report, 44 p.

DuHamel, J.E., Cook, S.S., and Kolessar, J., 1995, Geology of the Tyrone porphyry copper deposit, New Mexico, *in* Pierce, F.W., and Bolm, J.G., eds., Porphyry copper deposits of the American Cordillera: Arizona Geological Society Digest 20, p. 464-472.

Edwards, G.H., 1961, Geology of the central Little Burro Mountains, Grant County, New Mexico: unpublished MS thesis, University of Kansas, 60 p.

Elston, W.E., 1957, Geology and mineral resources of the Dwyer quadrangle, Grant, Luna, and Sierra Counties, New Mexico: New Mexico Bureau of Mines and Mineral Resources Bulletin 38, 86 p.

Elston, W.E., 1976, Glossary of stratigraphic terms of the Mogollon-Datil volcanic province, New Mexico, *in* Elston, W.E., and Northrop, S.A., eds., Cenozoic volcanism in southwestern New Mexico: New Mexico Geological Society Special Pub. No. 5, p. 131-151.

Emmons, W.H., 1917, The enrichment of ore deposits: U.S. Geological Survey bulletin 625, 530 p.

Enders, S.B., 2000, The evolution of supergene enrichment in the Morenci porphyry copper deposit, Greenlee County, Arizona: unpublished PhD dissertation, University of Arizona, 516 p.

Ehrlich, H.L., 1998, Geomicrobiology: its significance for geology: Earth-Science Reviews, v. 45, p. 45-60.

Field, C.W., 1966, Sulfur isotopic method for discrimination between sulfates of hypogene and supergene origin: Economic Geology, v. 61, p. 1428-1435.

Fortin, D., and Beveridge, T.J., 1997, Microbial sulfate reduction within sulfidic mine tailings: formation of diagenetic Fe sulfides: Geomicrobiology Journal, v. 14, p. 1-21.

Garrels, R.M., 1954, Mineral species as functions of pH and oxidation-reduction potentials, with special reference to the zone of oxidation and secondary enrichment of sulphide ore bodies: Geochimica et Cosmochimica Acta, v. 5, p. 153-168.

Garrels R.M., and Thompson, M.E., 1960, Oxidation of pyrite by iron sulfate solutions: American Journal of Science, v. 258A, p. 57-67.

Gillerman, E.C., 1952, Fluorspar deposits of Burro Mountains and vicinity, New Mexico: U.S. Geological Survey Bull. 973-F, p. 261-290.

Gillerman, E.C., 1964, Mineral deposits of western Grant County, New Mexico: New Mexico Bureau of Mines and Mineral Resources Bulletin 83, 213 p.

Gillerman, E.C., 1967, Structural framework and character of mineralization, Burro Mountains, New Mexico: Economic Geology, v. 62, p. 370-375.

Gillerman, E.C., 1970, Mineral deposits and structural pattern of the Burro Mountains, New Mexico, *in* Woodward, L.A., ed., Guidebook of the Tyrone-Big Hatchet Mountains-Florida Mountains Region: New Mexico Geological Society Guidebook 21, p. 115-121.

Gilmour, P., 1995, A field guide to leached capping interpretation, *in* Pierce, F.W., and Bolm, J.G., eds., Porphyry copper deposits of the American Cordillera: Arizona Geological Society Digest, v. 20, p. 169-179.

Griffin, J.D., 2001, Alluvial architecture and tectonic setting of the Mangas Conglomerate, Tyrone mine area, Grant County, New Mexico: unpublished MS thesis, University of Texas at Austin, 121 p.

Guilbert, J.M., and Park, C.F., Jr., 1986, The geology of ore deposits: W. H. Freeman, 985 p.

Hayes, T.S., 2004, Ferricretes, manganocretes, and exotic Cu deposits formed in weathering and dispersion of porphyry Cu deposits, Arizona [abs.]: Geological Society of America Abstracts with Programs, v. 36, no. 5, p. 517.

Hedlund, D.C., 1978a, Geologic map of the Burro Peak quadrangle, Grant County, New Mexico: U.S. Geological Survey Misc. Field Studies Map MF-1040, scale 1:24,000.

Hedlund, D.C., 1978b, Geologic map of the Tyrone quadrangle, Grant County, New Mexico: U.S. Geological Survey Misc. Field Studies Map MF-1037, scale 1:24,000.

Hedlund, D.C., 1978c, Geologic map of the White Signal quadrangle, Grant County, New Mexico: U.S. Geological Survey Misc. Field Studies Map MF-1041, scale 1:24,000.

Hedlund, D.C., 1978d, Geologic map of the Wind Mountain quadrangle, Grant County, New Mexico: U.S. Geological Survey Misc. Field Studies Map MF-1031, scale 1:24,000.

Hedlund, D.C., 1985, Geology, mines, and prospects of the Tyrone stock and vicinity, Grant County, New Mexico: U.S. Geological Survey Open-File Report 85-0232, 31 p.

Heidrick, T.L., and Titley, S.R., 1982, Fracture and dike patterns in Laramide plutons and their structural and tectonic implications, *in* Titley, S.R., ed., Advances in geology of the porphyry copper deposits, southwestern North America: University of Arizona Press, p. 73-92.

International Commission on Stratigraphy, 2008, International Stratigraphic Chart.

Jones, W.R., Hernon, R.M., and Moore, S.L., 1967, General geology of the Santa Rita quadrangle, Grant County, New Mexico: U.S. Geological Survey Professional Paper 555, 144 p.

Jones, W.R., Moore, S.L., and Pratt, W.P., 1970, Geologic map of the Fort Bayard quadrangle, Grant County, New Mexico: U.S. Geological Survey Geologic Quadrangle Map GQ-865, scale 1:24,000.

Karlstrom, K.E., Amato, J.M., Williams, M.L., Heizler, M., Shaw, C.A., Read, A.S., and Bauer, P., 2004, Proterozoic tectonic evolution of the New Mexico region: A synthesis, *in* Mack, G.H., and Giles, K.A., eds., The Geology of New Mexico, A Geologic History: New Mexico Geological Society Special Publication 11, p. 1-34.

Keller, G.R., 2004, Geophysical constraints on the crustal structure of New Mexico, *in* Mack, G.H., and Giles, K.A., eds., The Geology of New Mexico, A Geologic History: New Mexico Geological Society Special Publication 11, p. 439-456.

Kemp, J.F., 1905, Secondary enrichment of ore-deposits of copper: Economic Geology, v. 1, p. 11-25.

Kolessar, J., 1970, Geology and copper deposits of the Tyrone district, *in* Woodward, L.A., ed., Guidebook of the Tyrone-Big Hatchet Mountains-Florida Mountains Region: New Mexico Geological Society Guidebook 21, p. 127-132.

Kolessar, J., 1982, The Tyrone copper deposit: Grant County, New Mexico, *in* Titley, S.R., ed., Advances in geology of the porphyry copper deposits, southwestern North America: University of Arizona Press, p. 327-333.

Kues, B.S., and Giles, K.A., and Lawton, T.F., 2004, The late Paleozoic Ancestral Rocky Mountains system in New Mexico, *in* Mack, G.H., and Giles, K.A., eds., The Geology of New Mexico, A Geologic History: New Mexico Geological Society Special Publication 11, p. 153-168.

Kwong, Y.T.J., Brown, T.H., and Greenwood, H.J., 1982, A thermodynamic approach to the understanding of the supergene alteration of the Afton copper mine, south-central British Columbia: Canadian Journal of Earth Science, v. 19, p. 2378-2386.

Lawton, T.F., 2004, Upper Jurassic and Lower cretaceous strata of southwestern New Mexico and northern Chihuahua, Mexico, *in* Mack, G.H., and Giles, K.A., eds., The Geology of New Mexico, A Geologic History: New Mexico Geological Society Special Publication 11, p. 153-168.

Lichtner, P.C., and Biino, G.G., 1992, A first principles approach to supergene enrichment of a porphyry copper protore: I. Cu-Fe-S subsystem: Geochimica et Cosmochimica Acta, v. 56, p. 3987-4013.

Livingston, D.E., Mauger, R.L., and Damon, P.E., 1968, Geochronology of the emplacement, enrichment, and preservation of Arizona porphyry copper deposits: Economic Geology, v. 63, p 30-36.

Locke, A, 1926, Leached outcrops as guides to copper ore: Baltimore, Williams and Wilkins, 175 p.

Loghry, J.D., 1972, Characteristics of favorable cappings from several southwestern porphyry copper deposits: unpublished M.S. thesis, University of Arizona, 112 p.

Mack, G.H., 2004, Middle and late Cenozoic crustal extension, sedimentation, and volcanism in

the southern Rio Grande rift, Basin and Range, and southern Transition Zone of southwestern New Mexico, *in* Mack, G.H., and Giles, K.A., eds., The Geology of New Mexico, A Geologic History: New Mexico Geological Society Special Publication 11, p. 389-406.

Mack G.H., and Clemons, R.E., 1988, Structural and stratigraphic evidence for the Laramide (early Tertiary) Burro uplift in southwestern New Mexico: New Mexico Geological Society Guidebook 39, p. 59-66.

Mack, G.H., and Stout, D.M., 2005, Unconventional distribution of facies in a continental rift basin: the Pliocene-Pleistocene Mangas basin, southwestern New Mexico, USA: Sedimentology, v. 52, p. 1187-1205.

Mack G.H., Galemore, J.A., and Kaczmarek, E.L., 1988, The Cretaceous foreland basin in southwestern New Mexico: New Mexico Geological Society Guidebook 39, p. 135-141.

Mack, G.H., Cole, D.R., James, W.C., Giordano, T.H., and Salyards, S.L., 1994a, Stable oxygen and carbon isotopes of pedogenic carbonates as indicators of Plio-Pleistocene paleoclimate in the southern Rio Grande rift, south-central New Mexico: American Journal of Science, v. 294, p. 621-640.

Mack, G.H, Seager, W.R., and Kieling, J., 1994b, Late Oligocene and Miocene faulting and sedimentation, and evolution of the southern Rio Grande rift, New Mexico, USA, Sedimentary Geology, v. 92, p. 79-96.

McCrea, J.M., 1950, on the isotopic chemistry of carbonates and a paleotemperature scale: Journal of Chemical Physics, v.18, p. 849-857.

McIntosh, W.C., Kedzie, L.L., and Sutter, J.F., 1991, Paleomagnetism and $^{40}Ar/^{39}Ar$ ages of ignimbrites, Mogollon-Datil volcanic field, southwestern New Mexico: New Mexico Bureau of Mines and Mineral Resources Bulletin 135, 99 p.

McIntosh, W.C., Chapin C.E., Ratte, J.C., and Sutter, J.F., 1992, Time-stratigraphic framework for the Eocene-Oligocene Mogollon-Datil volcanic field, southwest New Mexico: Geological Society of America Bulletin, v. 104, p. 851-871.

McIntosh, W.C., Sutter, J.F., Chapin C.E., and Kedzie, L.L., 1990, High-precision $^{40}Ar/^{39}Ar$ sanidine geochronology of ignimbrites in the Mogollon-Datil volcanic field, southwestern New Mexico: Bulletin of Volcanology, v. 52, p. 584-601.

McLemore, V.T., McIntosh, W.C., and Appelt, R.., 2000, Volcanic stratigraphy, geochemistry, and structure of the Steeple Rock district, Grant County, New Mexico, and Greenlee County, Arizona: New Mexico Geological Society Guidebook 51, p. 127-140.

McMillan, N.J., 2004, Magmatic record of Laramide subduction and the transition to Tertiary extension: Upper Cretaceous through Eocene igneous rocks of New Mexico, *in* Mack, G.H., and Giles, K.A., eds., The Geology of New Mexico, A Geologic History: New Mexico Geological Society Special Publication 11, p. 249-270.

Melchiorre, E.B., and Enders, S.M., 2003, Stable isotope geochemistry of copper carbonates at the Northwest Extension deposit, Morenci district, Arizona: Implications for conditions of supergene oxidation and related mineralization: Economic Geology, v. 98, p. 607-621.

Melchiorre, E.B., Criss, R.E., and Rose, T.P., 1999, Oxygen and carbon isotope study of natural and synthetic malachite: Economic Geology, v. 94, p. 245-260.

Menges, C.M., and McFadden, L.D., 1981, Evidence for a latest Miocene to Pliocene transition from basin-range tectonic to post-tectonic landscape evolution in southeastern Arizona: Arizona Geological Society Digest, v. 13, p. 151-160.

Menges, C.M., and Pearthree, P.A., 1989, Late Cenozoic tectonism in Arizona and its impact on regional landscape evolution, *in* Jenney, J.P., and Reynolds, S.J., eds., Geologic evolution of Arizona: Tucson, Arizona Geological Society Digest 17, p 649-680.

Mote, T.I., Brimhall, G.H., Tidy-Finch, E., Muller, G., and Carrasco, P., 2001, Application of mass-balance modeling of sources, pathways and sinks of supergene enrichment to exploration and discovery of the Quebrada Turquesa exotic copper orebody, El Salvador District, Chile: Economic Geology, v. 96, p. 367-386.

Münchmeyer, C., 1996, Exotic deposits – Products of lateral migration of supergene solutions from porphyry copper deposits, *in* Camus, F., Sillitoe, R.H., and Petersen, R., eds., Andean copper deposits: new discoveries, mineralization, styles, and metallogeny: Society of Economic Geologists Special Publication No. 45, p. 43-58.

Nations, D., Wilt, J.C., and Hevly, R.H., 1985, Cenozoic paleogeography of Arizona, *in* Flores, R.M., and Kaplan, S.S., eds., Cenozoic paleogeography of the west-central United States: Rocky Mountain Section, Society of Economic Paleontologists and Mineralogists, p. 335-355.

Newberg, D.W., 1967, Geochemical implications of chrysocolla-bearing alluvial gravels: Economic Geology, v. 62, p. 932-956.

Ohmoto, H., and Goldhaber, M.B., 1997, Sulfur and carbon isotopes, *in* Barnes, H.L., ed., Geochemistry of hydrothermal deposits, 3rd edition: John Wiley & Sons, p.517-611.

Paige, S., 1911, Metalliferous ore deposits near the Burro Mountains, Grant County, New Mexico: U.S. Geological Survey Bulletin 470, p. 131-150.

Paige, S., 1922, Copper deposits of the Tyrone district, New Mexico: U.S. Geological Survey Prof. Paper 122, 53 p.

Penrose, R.A.F., 1894, Superficial alteration of ore deposits: Journal of Geology, v. 2, p. 288-317.

Phelps Dodge Tyrone Geological Services, 2002, Drill log memo: Phelps Dodge Tyrone internal memorandum, 36 p.

Phelps Dodge Tyrone Geological Services, 2003, Unpublished interpretive geologic map of the Tyrone mine, scale 1"=600'.

Phelps Dodge Mining Company, 2002, Unpublished map of portions of the Little Burro Mountains, scale 1"=400'.

Ross, C.A., and Ross, J.R.P., 1986, Paleozoic paleotectonics and sedimentation in Arizona and New Mexico, *in* Peterson, J.A., ed., Paleotectonics and sedimentation in the Rocky Mountain region, United States: American Association of Petroleum Geologists Memoir 41, p. 653-668.

Rye, R.O., Bethke, P.B., and Wasserman, M.D., 1992, The stable isotope geochemistry of acid sulfate alteration: Economic Geology, v. 87, p. 225-262.

Sato, M., 1960a, Oxidation of sulfide ore bodies; I. Geochemical environments in terms of Eh and pH: Economic Geology, v. 55, p. 928-961.

Sato, M., 1960b, Oxidation of sulfide ore bodies; II. Oxidation mechanism of sulfide minerals at 25°C: Economic Geology, v. 55, p. 1202-1231.

Scarborough, R., 1989, Cenozoic erosion and sedimentation in Arizona, *in* Jenney, J.P., and Reynolds, S.J., eds., Geologic evolution of Arizona: Tucson, Arizona Geological Society Digest 17, p 515-537.

Schippers, A., Jozsa, P-G, and Sand, W., 1996, Sulfur chemistry in bacterial leaching of pyrite: Applied and Environmental Microbiology, v. 62, n. 9, p. 3424-3431.

Schmidt, K.-H., 1991, Tertiary paleoclimate history of the southeastern Colorado Plateau: Palaeogeography, Palaeoclimatology, Palaeoecology, v. 86, p. 283-296.

Seager, W.R., 1995, Geology of southwest quarter of Las Cruces and northwest El Paso 1° x 2° sheets (scale 1:125,000), New Mexico: New Mexico Bureau of Mines and Mineral Resources Geologic Map 60.

Seager, W.R., 2004, Laramide (Late Cretaceous-Eocene) tectonics of southwestern New Mexico, *in* Mack, G.H., and Giles, K.A., eds., The Geology of New Mexico, A Geologic History: New Mexico Geological Society Special Publication 11, p. 183-202.

Seager, W.R., and Mack, 1986, Laramide paleotectonics of southern New Mexico, *in* Peterson, J.A., ed., Paleotectonics and sedimentation in the Rocky Mountain region, United States: American Association of Petroleum Geologists Memoir 41, p. 669-685.

Seager, W.R., and Morgan, P., 1979, Rio Grande rift in southern New Mexico, west Texas, and northern Chihuahua, *in* Riecker, R.E., ed. Rio Grande rift: tectonics and magmatism: American Geophysical Union, p. 87-106.

Seager, W.R., Shafiqullah, M.., Hawley, J.W., and Marvin, R.F., 1984, New K-Ar dates from basalts and the evolution of the southern Rio Grande rift: Geological Society of America Bulletin v. 95, p. 87-99.

Seedorff, E., Dilles, J.H., Profett, J.M., Jr., Enaudi, M.T., Zurcher, L., Stavast, W.J.A., Johnson, D.A., and Barton, M.D., 2005, Porphyry deposits: Characteristics and origin of hypogene features, *in* Hedenquist, J.W., Thompson, J.F.H., Goldfarb, R.J., and Richards, J.P., eds., Economic Geology 100th Anniversary Volume, p. 251-298.

Sillitoe, R.H., 2005, Supergene oxidized and enriched porphyry copper and related deposits, *in* Hedenquist, J.W., Thompson, J.F.H., Goldfarb, R.J., and Richards, J.P., eds., Economic Geology 100th Anniversary Volume, p. 251-298.

Sillitoe, R.H., and McKee, E.H., 1996, Age of supergene oxidation and enrichment in the Chilean porphyry copper province: Economic Geology, v. 91, p. 164-179.

Sillitoe, R.H., Folk, R.L., and Saric, N., 1996, Bacteria as mediators of copper sulfide enrichment during weathering: Science, v. 272, p. 1153-1155.

Smith, G.A., 1994, Climatic influences on continental deposition during late-stage filling of an extensional basin, southeastern Arizona: Geological Society of America Bulletin v. 106, p. 1212-1228.

Smith, L.N., Lucas, S.G., and Elston, W.E., 1985, Paleogene stratigraphy, sedimentation and volcanism of New Mexico, *in* Flores, R.M., and Kaplan, S.S., eds., Cenozoic paleogeography of the west-central United States: Rocky Mountain Section, Society of Economic Paleontologists and Mineralogists, p. 293-315.

Smith, V.P., 1998, Evolution of hypogene veining and associated alteration in the Tyrone porphyry copper deposit, Grant County, New Mexico: unpublished M.S. thesis, University of Texas at Austin, 185 p.

Somers, R.E., 1915, Geology of the Burro Mountains copper district, New Mexico: AIME transactions., v. 52, p. 604-656.

Spencer, J.E., and Reynolds, S.J., 1989, Middle Tertiary tectonics of Arizona and adjacent areas, *in* Jenney, J.P., and Reynolds, S.J., eds., Geologic evolution of Arizona: Tucson, Arizona Geological Society Digest 17, p 539-574.

Stacey, J.S., and Hedlund, D.C., 1983, Lead-isotopic compositions of diverse igneous rocks and ore deposits from southwestern New Mexico and their implications for early Proterozoic crustal evolution in the western United States: Geological Society of America Bulletin, v. 94, p. 43-57.

Stoffregen, R.E., Rye, R.O., and Wasserman, D.M., 1990, Rates of alunite-water alkali and isotope exchange [abs.]: Geological Society of America Abstracts with Programs, v. 22, p. A162.

Stokes, H.N., 1906, Experiments of the solution, transportation, and deposition of copper, silver, and gold: Economic Geology, v. 1, p. 644-660.

Stokes, H.N., 1907, Experiments on the action of various solutions on pyrite and marcasite:

Economic Geology, v. 2, p. 14-23.

Titley, S.R., 1982a, Geologic setting of porphyry copper deposits, southeastern Arizona, in Titley, S.R., ed., Advances in geology of the porphyry copper deposits, southwestern North America: University of Arizona Press, p. 37-58.

Titley, S.R., 1982b, The style and progress of mineralization and alteration in porphyry copper Systems, American southwest, *in* Titley, S.R., ed., Advances in geology of the porphyry copper deposits, southwestern North America: University of Arizona Press, p. 93-116.

Titley, S.R., 1995, Geological summary and perspective of porphyry copper deposits in southwestern North America, in Pierce, F.W., and Bolm, J.G., eds., Porphyry copper deposits of the American Cordillera: Arizona Geological Society Digest, v. 20, p. 6-20.

Titley, S.R., and Marozas, D.C., 1995, Processes and products of supergene copper enrichment, in Pierce, F.W., and Bolm, J.G., eds., Porphyry copper deposits of the American Cordillera: Arizona Geological Society Digest, v. 20, p. 156-168.

Trauger, F.D., 1972, Water resources and general geology of Grant County, New Mexico: New Mexico Bureau of Mines and Mineral Resources, Hydrologic Report 2, 211 p.

Trudinger, P.A., Chambers, L.A., and Smith, J.W., 1985, Low-temperature sulphate reduction: biological versus abiological: Canadian Journal of Earth Science, v. 22, p. 1910-1918..

Vasconcelos, P.M., 1999, $^{40}Ar/^{39}Ar$ geochronology of supergene processes in ore deposits, in Lambert, D.D., and Ruiz, J.R., eds., Application of radiogenic isotopes to ore deposit research and exploration: Reviews in Economic Geology, v. 12, p. 73-113.

Vasconcelos, P.M., Brimhall, G.H., Becker, T.A., and Renne, P.R., 1994a, $^{40}Ar/^{39}Ar$ analysis of supergene jarosite and alunite: Implications to the paleoweathering history of the western USA and West Africa: Geochimica et Cosmochimica Acta, v. 58, p. 401-420.

Vasconcelos, P.M., Renne, P.R., Brimhall, G.H., and Becker, T.A., 1994b, Direct dating of weathering phenomena by $^{40}Ar/^{39}Ar$ and K-Ar analysis of supergene K-Mn oxides: Geochimica et Cosmochimica Acta, v. 58, no. 6, p. 1635-1665.

Wasserman, M.D., Rye, R.O., Bethke, P.M., and Arribis, A, Jr., 1992, Methods for separation and total stable isotope analyses of alunite: U.S. Geological Survey Open-File Report 92-9, 20 p.

Wilkins, Joe, Jr., and Heidrick, T.L., 1995, Post-Laramide extension and rotation of porphyry copper deposits, southwestern United States, *in* Pierce, F.W., and Bolm, J.G., eds., Porphyry copper deposits of the American Cordillera: Arizona Geological Society Digest 20, p. 109-127.

Zalinski, E.R., 1907, Turquoise in the Burro Mountains, New Mexico: Economic Geology, v. 2, p. 464-492.

APPENDIX A

Thompson-CREG, 61-7, sanidine, J = 0.001691 ± 0.95%

4 amu discrimination = 1.01636 ± 0.22%, 40/39K = 0.0001 ± 100.0%, 36/37Ca = 0.000262 ± 2.28%, 39/37Ca = 0.000659 ± 0.44%

Crystal	T (C)	t (min.)	36Ar	37Ar	38Ar	39Ar	40Ar	%40Ar*	Ca/K	40Ar*/39ArK	Age (ma)	1s.d.
1	1600	6	1.389	0.512	1.013	60.637	1112.460	64.1	0.05809363	11.7780	35.58	0.37
2	1600	6	1.149	0.695	1.319	88.912	1386.700	76.2	0.05377993	11.9161	35.99	0.36
3	1600	6	1.315	1.282	2.262	164.458	2291.820	83.5	0.05363259	11.6717	35.26	0.35
4	1600	6	0.669	0.712	1.247	89.871	1249.730	84.8	0.0545075	11.8185	35.70	0.36
5	1600	6	0.817	1.079	2.382	179.977	2180.020	89.3	0.04124761	10.8493	32.80	0.33
6	1600	6	0.314	0.860	1.445	109.585	1384.130	93.6	0.05399371	11.8522	35.80	0.36
7	1600	6	0.360	1.163	1.782	138.925	1779.000	94.3	0.05759642	12.1054	36.56	0.36
8	1600	6	0.256	0.557	0.889	70.540	923.594	92.2	0.05432698	12.1001	36.54	0.36
9	1600	6	0.086	0.225	0.515	38.877	482.280	95.1	0.03981842	11.7994	35.64	0.35
10	1600	6	2.678	1.672	1.987	120.543	2188.240	64.5	0.09543215	11.7346	35.45	0.37
11	1600	6	0.691	0.477	0.913	64.585	946.026	78.9	0.05081386	11.5751	34.97	0.35
12	1600	6	0.073	0.390	0.655	49.007	590.999	96.7	0.05475235	11.6647	35.24	0.35
										Mean ± s.d. =	35.46	0.93
										Mean ± s.d. = (omit # 5)	35.70	0.48
										wtd mean = (omit # 5)	35.72	0.33
										Isochron age = (5 out of 12 xtals)	35.73	0.09

note: isotope beams in mV rlsd = released, error in age includes J error, all errors 1 sigma

(36Ar through 40Ar are measured beam intensities, corrected for decay in age calculations)

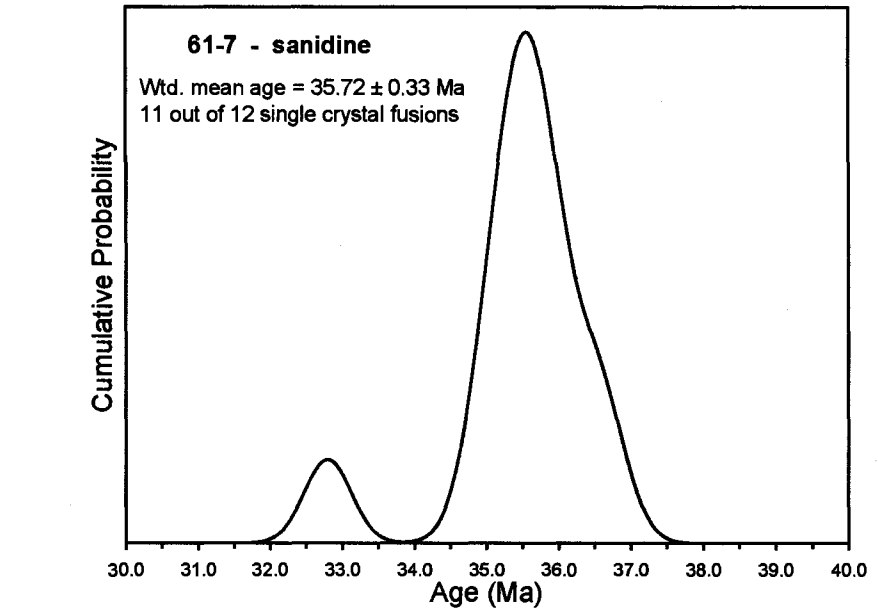
61-7 - sanidine
Wtd. mean age = 35.72 ± 0.33 Ma
11 out of 12 single crystal fusions
Cumulative Probability
30.0
31.0
32.0
33.0
34.0
35.0
36.0
37.0
38.0
39.0
40.0
Age (Ma)

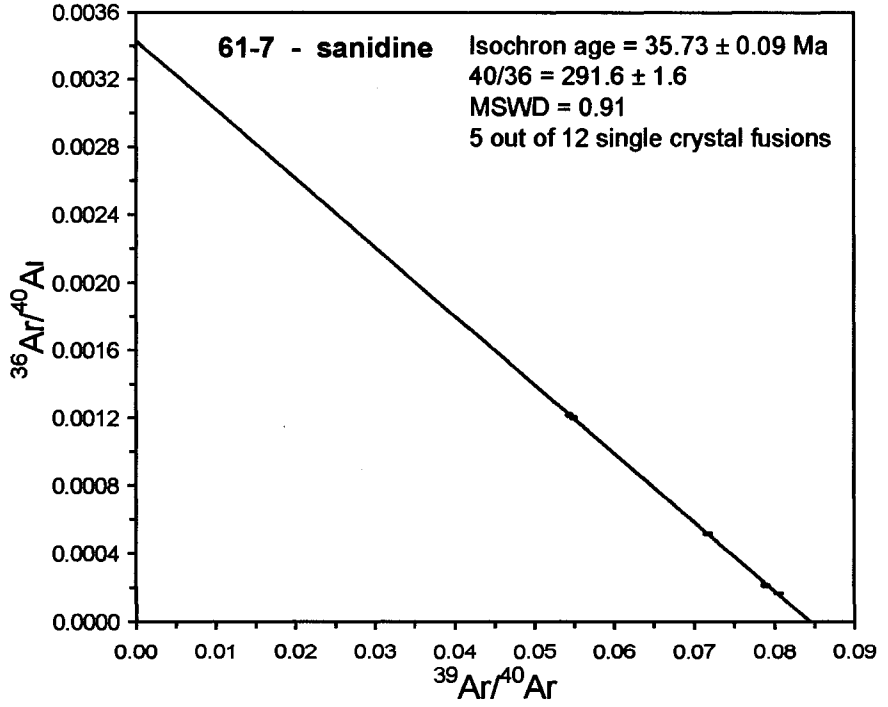
61-7 - sanidine
Isochron age = 35.73 ± 0.09 Ma
40/36 = 291.6 ± 1.6
MSWD = 0.91
5 out of 12 single crystal fusions
36Ar/40Al
0.0036
0.0032
0.0028
0.0024
0.0020
0.0016
0.0012
0.0008
0.0004
0.0000
0.00
0.01
0.02
0.03
0.04
0.05
0.06
0.07
0.08
0.09
39Ar/40Ar

Thompson-CREG, 89-5, plagioclase, 28.14 mg, J = 0.001679 ± 1.14%

4 amu discrimination = 1.01422 ± 0.18%, 40/39K = 0.0001 ± 100.0%, 36/37Ca = 0.000262 ± 2.28%, 39/37Ca = 0.000659 ± 0.44%

step	T (C)	t (min.)	36Ar	37Ar	38Ar	39Ar	40Ar	%40Ar*	% 39Ar rlsd	Ca/K	40Ar*/39ArK	Age (Ma)	1s.d.
1	650	12	9.668	2.383	1.894	6.894	2945.54	4.4	1.2	3.63526605	18.977191	56.59	2.84
2	730	12	1.618	4.802	0.449	12.460	702.489	33.5	2.2	4.05361168	18.805525	56.08	0.72
3	810	12	0.925	10.747	0.465	24.259	108.373	63.0	4.3	4.66048985	18.349343	54.74	0.65
4	890	12	0.942	16.878	0.648	37.683	948.74	72.2	6.7	4.71193658	18.144171	54.14	0.63
5	960	12	1.189	17.602	0.735	41.903	1102.01	69.5	7.4	4.41878201	18.244537	54.43	0.64
6	1020	12	0.469	13.271	0.522	35.003	764.754	83.4	6.2	3.98774901	18.138048	54.12	0.63
7	1080	12	0.431	13.114	0.584	38.657	821.411	85.9	6.8	3.56764509	18.177511	54.24	0.63
8	1150	12	0.832	11.434	0.635	38.782	937.733	75.3	6.9	3.10014196	18.120018	54.07	0.63
9	1220	12	3.353	18.681	1.456	65.299	2157.57	55.3	11.6	3.00812012	18.258487	54.48	0.64
10	1290	12	7.099	44.823	3.380	158.680	4938.32	58.5	28.1	2.97012928	18.256105	54.47	0.64
11	1400	12	5.310	40.157	2.322	104.881	3469.84	56.0	18.6	4.02716125	18.541306	55.31	0.66
							Cumulative %39Ar rlsd =		100.0		Total gas age =	54.61	0.81
note: isotope beams in mV, rlsd = released, error in age includes J error, all errors 1 sigma											Plateau age =	54.43	0.81
(36Ar through 40Ar are measured beam intensities, corrected for decay for the age calculations)											(steps 3-11)		
											Isochron age =	54.10	0.60
											(steps 3-11)		

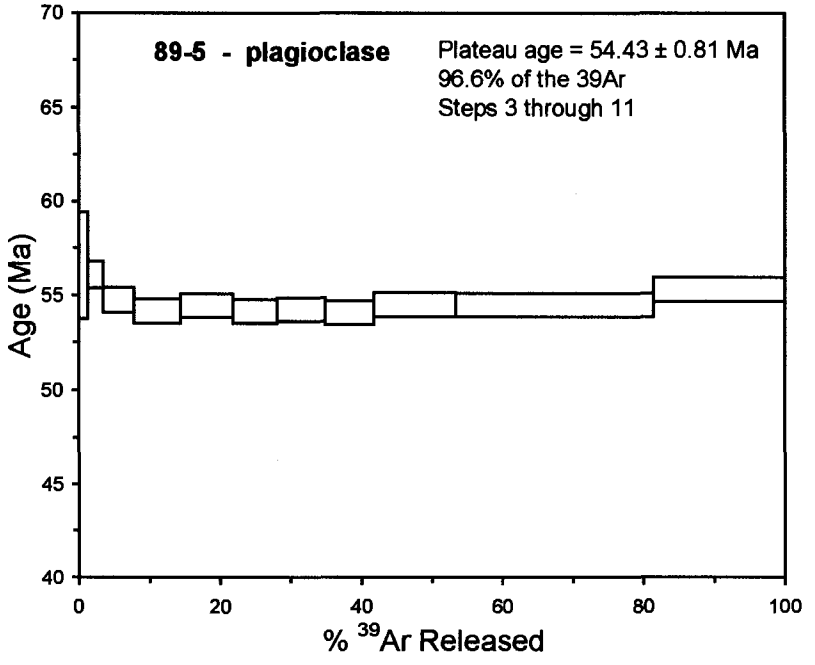
89-5 - plagioclase
Plateau age = 54.43 ± 0.81 Ma
96.6% of the 39Ar
Steps 3 through 11
Age (Ma)
% 39Ar Released
70
65
60
55
50
45
40
0
20
40
60
80
100

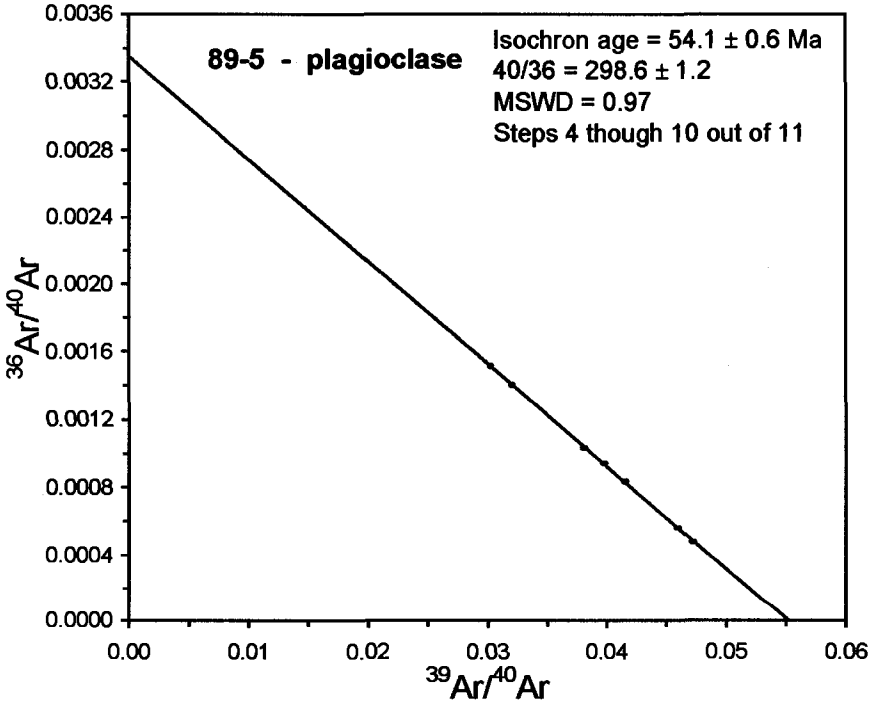
89-5 - plagioclase
Isochron age = 54.1 ± 0.6 Ma
40/36 = 298.6 ± 1.2
MSWD = 0.97
Steps 4 though 10 out of 11
36Ar/40Ar
39Ar/40Ar
0.0036
0.0032
0.0028
0.0024
0.0020
0.0016
0.0012
0.0008
0.0004
0.0000
0.00
0.01
0.02
0.03
0.04
0.05
0.06

Thompson-CREG, 89-8, plagioclase, 28.14 mg, J = 0.001679 ± 1.14%

4 amu discrimination = 1.01422 ± 0.18%, 40/39K = 0.0001 ± 100.0%, 36/37Ca = 0.000262 ± 2.28%, 39/37Ca = 0.000659 ± 0.44%

step	T (C)	t (min.)	36Ar	37Ar	38Ar	39Ar	40Ar	%40Ar*	% 39Ar rlsd	Ca/K	40Ar*/39ArK	Age (Ma)	1s.d.
1	650	12	2.763	0.513	0.707	15.592	945.779	15.0	0.5	0.34751748	9.104740	27.37	0.68
2	730	12	1.519	0.556	0.545	20.918	652.013	32.5	0.7	0.28074176	10.083933	30.29	0.40
3	810	12	1.272	0.984	0.654	36.233	740.083	50.4	1.2	0.28684282	10.256185	30.80	0.39
4	890	12	1.176	1.646	1.018	65.701	1026.83	67.1	2.1	0.26461114	10.457712	31.40	0.37
5	960	12	1.122	2.656	1.616	115.185	1522.46	78.9	3.7	0.24354526	10.422104	31.30	0.37
6	1020	12	0.950	2.896	1.971	144.335	1780.76	84.8	4.6	0.2119192	10.454016	31.39	0.37
7	1080	12	0.903	3.047	2.370	176.842	2111.79	87.8	5.7	0.1819812	10.487611	31.49	0.37
8	1150	12	1.188	3.401	3.804	291.237	3394.96	90.0	9.3	0.12333658	10.501049	31.53	0.37
9	1220	12	1.456	3.374	8.019	627.575	6985.85	94.1	20.1	0.05678094	10.488618	31.49	0.37
10	1290	12	1.200	4.428	13.959	1099.38	11883.58	97.1	35.1	0.04253839	10.523558	31.60	0.37
11	1290	12	0.456	2.719	5.439	433.68	4714.61	97.4	13.9	0.06621695	10.597812	31.82	0.37
12	1400	12	0.305	1.669	1.279	102.503	1174.86	93.4	3.3	0.17197208	10.632758	31.92	0.37
							Cumulative %39Ar rlsd =		100.0		Total gas age =	31.54	0.38
											Plateau age =	31.55	0.39
											(steps 4-12)		
											Isochron age =	31.60	0.36
											(steps 1-10)		

note: isotope beams in mV, rlsd = released, error in age includes J error, all errors 1 sigma
(36Ar through 40Ar are measured beam intensities, corrected for decay for the age calculations)

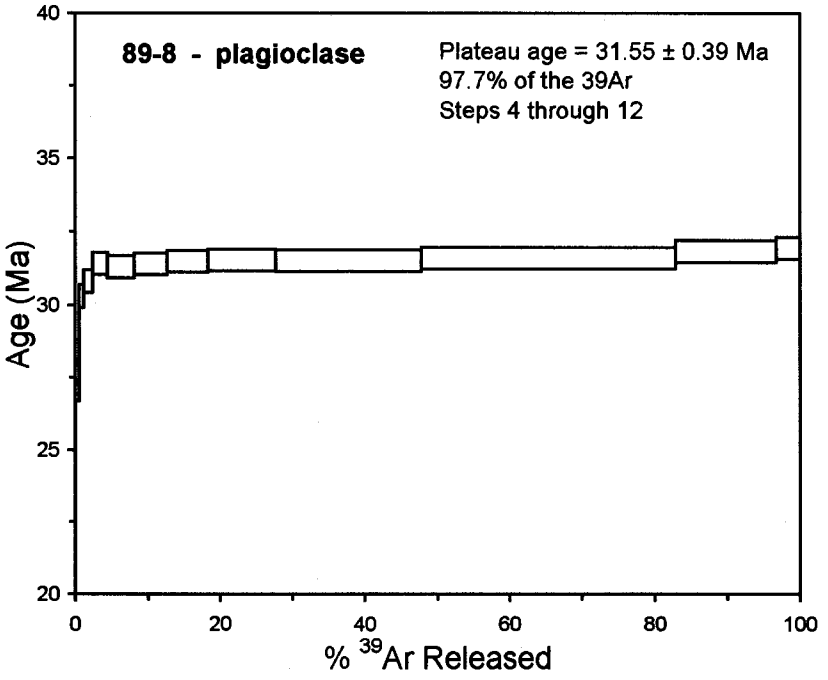
89-8 - plagioclase
Plateau age = 31.55 ± 0.39 Ma
97.7% of the 39Ar
Steps 4 through 12
Age (Ma)
% 39Ar Released
40
35
30
25
20
0
20
40
60
80
100

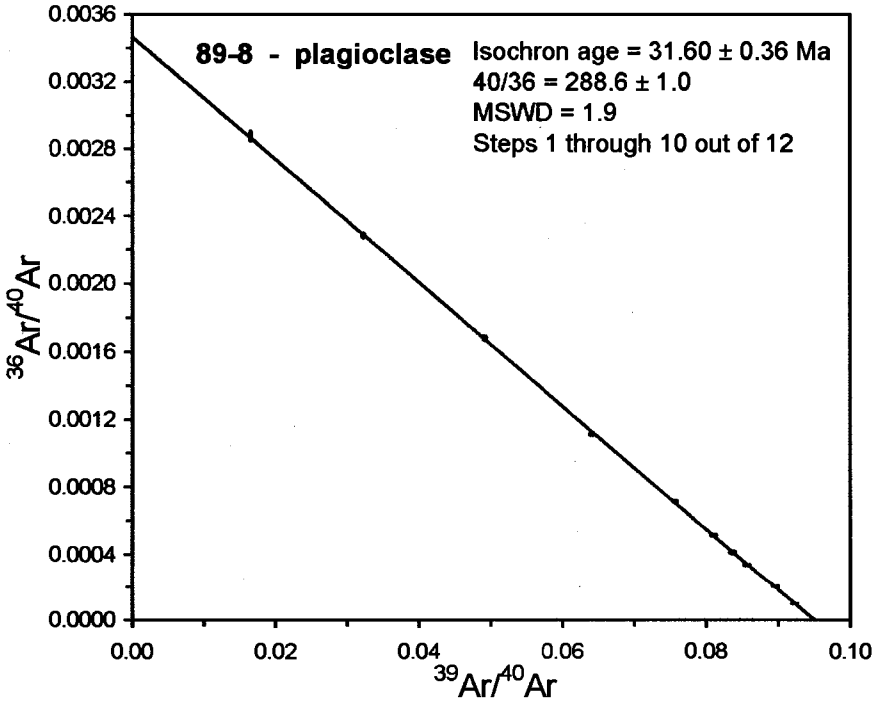
89-8 - plagioclase
Isochron age = 31.60 ± 0.36 Ma
40/36 = 288.6 ± 1.0
MSWD = 1.9
Steps 1 through 10 out of 12
36Ar/40Ar
39Ar/40Ar
0.0036
0.0032
0.0028
0.0024
0.0020
0.0016
0.0012
0.0008
0.0004
0.0000
0.00
0.02
0.04
0.06
0.08
0.10

Thompson-CREG, 817-1, cryptomelane, 14.74 mg, J = 0.001649 ± 1.02%
4 amu discrimination = 1.01422 ± 0.18%, 40/39K = 0.0001 ± 100.0%, 36/37Ca = 0.000267 ± 3.83%, 39/37Ca = 0.0007 ± 0.63%

step	T (C)	t (min.)	36Ar	37Ar	38Ar	39Ar	40Ar	%40Ar*	% 39Ar rlsd	Ca/K	40Ar*/39ArK	Age (Ma)	1s.d.
1	455	12	47.655	0.082	9.085	3.510	13979.39	0.7	0.4	0.27596387	26.479454	77.10	24.15
2	640	12	26.413	1.345	6.046	62.078	7894.88	2.5	6.6	0.25593368	3.166302	9.40	0.70
3	690	12	8.999	2.802	3.581	138.908	3110.52	15.7	14.9	0.23827663	3.516127	10.43	0.17
4	740	12	3.057	2.550	2.685	165.482	1587.68	44.1	17.7	0.18202148	4.230934	12.54	0.15
5	790	12	3.717	3.118	3.403	217.739	2053.61	47.5	23.3	0.16914978	4.138872	12.27	0.15
6	840	12	5.867	3.900	4.015	234.913	2716.58	37.2	25.1	0.19610679	4.306760	12.77	0.15
7	880	12	1.359	0.938	0.999	59.966	647.94	39.3	6.4	0.18476995	4.226872	12.53	0.14
8	950	12	0.867	0.554	0.524	25.586	327.549	23.2	2.7	0.25577037	2.925766	8.68	0.25
9	1050	12	0.737	0.517	0.483	26.666	300.402	29.0	2.9	0.22901927	3.210230	9.53	0.12
							Cumulative %39Ar rlsd =		100.0		Total gas age =	12.06	0.14
											no plateau		

note: isotope beams in mV, rlsd = released, error in age includes J error, all errors 1 sigma
(36Ar through 40Ar are measured beam intensities, corrected for decay for the age calculations)

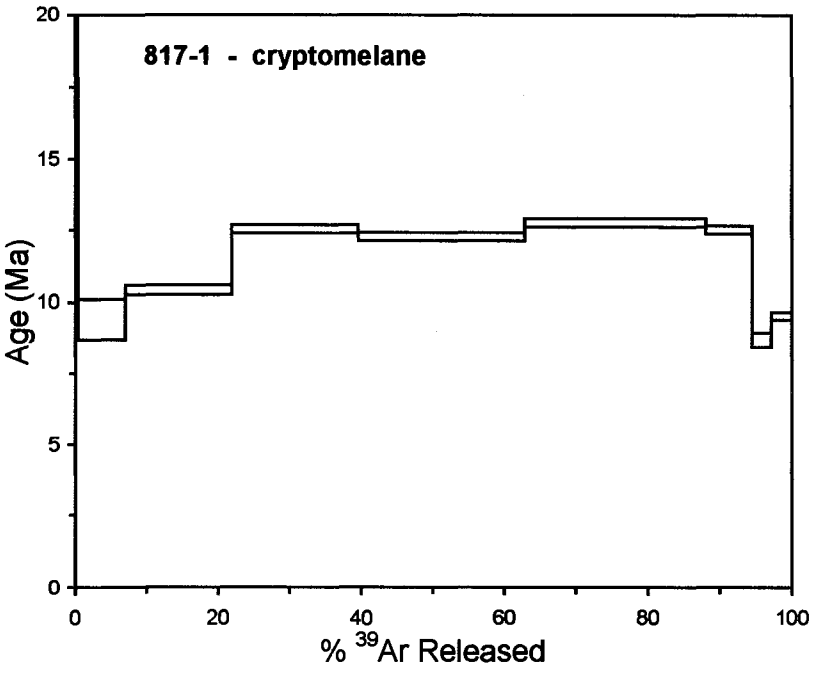
817-1 - cryptomelane
Age (Ma)
% 39Ar Released
0
5
10
15
20
0
20
40
60
80
100

Thompson-CREG, 1-12-03-2, sunite, 1.20 mg, J = 0.001632 ± 0.5%
4 amu discrimination = 1.02211 ± 0.26%, 40/39K = 0.0002 ± 0.0003, 36/37Ca = 0.00027 ± 2.46%, 39/37Ca = 0.00083 ± 0.98%

step	T (C)	t (min.)	36Ar	37Ar	38Ar	39Ar	40Ar	%40Ar*	% 39Ar rlsd	Ca/K	40Ar*/39ArK	Age (Ma)	1s.d.	anal err	37/39c	%39ArK	total39	mol 39Ar	Wmdata	Wtls	wfactor	WxX	37d
1	480	12	9.207	0.472	2.149	28.914	3027.650	12.1	31.2	0.06088413	12.6966	37.00	0.94	0.92569487	0.0285	99.99817	92.56	1.73E-15	37.00	0.925695	1.16698	43.17835	1.64
2	485	12	3.087	0.419	0.913	27.770	987.419	8.3	30.0	0.056274	2.9061	8.54	0.31	0.30704791	0.0245	99.99831		1.67E-15	8.54	0.307048	10.6069	90.54034	
3	490	12	1.064	0.312	0.492	20.868	359.288	12.8	22.5	0.05576285	2.1919	6.44	0.17	0.16488334	0.0242	99.99832		1.25E-15	6.44	0.164883	36.7829	236.9557	
4	495	12	0.16	0.155	0.174	11.044	63.101	27.5	11.9	0.05234491	1.4986	4.41	0.12	0.12101016	0.0228	99.99843		6.63E-16	4.41	0.12101	68.2899	300.9535	
5	515	12	0.042	0.062	0.050	3.844	17.816	36.4	4.2	0.08015594	1.3829	4.07	0.62	0.62166751	0.0262	99.99819		2.31E-16	4.07	0.621668	2.58752	10.52344	
6	600	12	0.060	0.028	0.009	0.124	20.463	15.9	0.1	0.8423813	22.1081	63.95	14.07	14.0643663	0.3662	99.97467		7.44E-18	63.95	14.06437	0.00506	0.323271	
							Cumulative	%39Ar rlsd =	100.0		Total gas age =	16.35	0.19							WtdMean	1sd	wJ	
note: isotope beams in mV, rlsd = released, error in age includes 0.5% J error, all errors 1 sigma											no plateau									5.713989	0.0915	0.185219	
(Not corrected for decay)											no isochron												

step	39/40c	39/40err	36/40c	36/40err	R2	36c	39c	40c	%36err	%39err	%40err	blank corr beam errors 36err	40err	%36err	%40err	WtdAge39Ar		Age (Ma) ± 2 sig err	
1	0.00951	0.2950	0.002975	0.3076	0.0728	9.20	28.91351	3024.36	0.10	0.05	0.02	0.0092	0.6056	0.100443	0.020025	11.55810285	1	35.15	38.85
2	0.02864	0.3043	0.003102	0.3001	0.0596	3.06	27.78957	964.13	0.07	0.09	0.02	0.0023	0.1936	0.074406	0.020096	2.560984443	2	7.92	9.15
3	0.05829	0.2985	0.002951	0.3303	0.0101	1.07	20.88788	356.00	0.14	0.07	0.01	0.0017	0.0373	0.157679	0.01049	1.45237312	3	6.11	6.77
4	0.18381	0.3283	0.002452	0.9004	0.0836	0.15	11.04384	59.82	0.64	0.12	0.09	0.0013	0.0577	0.846969	0.096454	0.525830899	4	4.16	4.65
5	0.263	0.4157	0.002152	8.5072	0.0020	0.03	3.843936	14.54	6.22	0.28	0.06	0.0027	0.0148	8.50168	0.101594	0.168901772	5	2.82	5.31
6	0.00718	1.8243	0.002846	3.9839	0.0046	0.05	0.123971	17.18	3.06	1.79	0.16	0.0020	0.0343	3.968299	0.199554	0.085665298	6	35.82	92.07

Sample run times

Start t	Step	T (C)	Step t	Inlet t	
12:56	1	480	0:12	13:16	
13:25	2	485	0:12	13:45	5
13:54	3	490	0:12	14:14	5
14:23	4	495	0:12	14:43	5
14:52	5	515	0:12	15:12	20
15:21	6	540	0:12	15:41	25
15:50	7	600	0:12	16:10	60
16:19					

Adjust ^{40}Ar & ^{36}Ar blanks for longer step times

step time =	45	New 40Ar and 36Ar blanks	
original blank time =	20	40Ar (mV)/min =	35.44
40Ar rate of rise (mV) =	0.95	36Ar (mV)/min =	0.12
36Ar rate of rise (mV) =	0.003		
40Ar blank =	11.69		
36Ar blank =	0.04		

Estimate of the %K_2O in sample

% K_2O	J factor	weight (mg)	exp. total mV $^{39}Ar_K$
3.00	1.632E-03	1.20	145.60

	enter data				cumulative	option	calc plateau age				spectrum plot			
step	Age	1s.d.	anal. Err.	%39Ar	^{39}Ar	frac.39Ar	step	%^{39}Ar	Age	anal. Err.	step	%^{39}Ar	Age	1s.d.
1	37.00	0.94	0.9256949	31.238	31.2	0.31	1	31.24	37.00	0.9256949	1	31.238	37.00	0.94
2	8.54	0.31	0.3070479	30.002	61.2	0.61	2	61.24	8.54	0.3070479	2	61.24	8.54	0.31
3	6.44	0.17	0.1648833	22.545	83.8	0.84	3	83.79	6.44	0.1648833	3	83.786	6.44	0.17
4	4.41	0.12	0.1210102	11.932	95.7	0.96	4	95.72	4.41	0.1210102	4	95.717	4.41	0.12
5	4.07	0.62	0.6216675	4.153	99.9	1.00	5	99.87	4.07	0.6216675	5	99.87	4.07	0.62
6	63.95	14.07	14.064366	0.134	100.0	1.00	6	100	63.95	14.064366	6	100	63.95	14.07

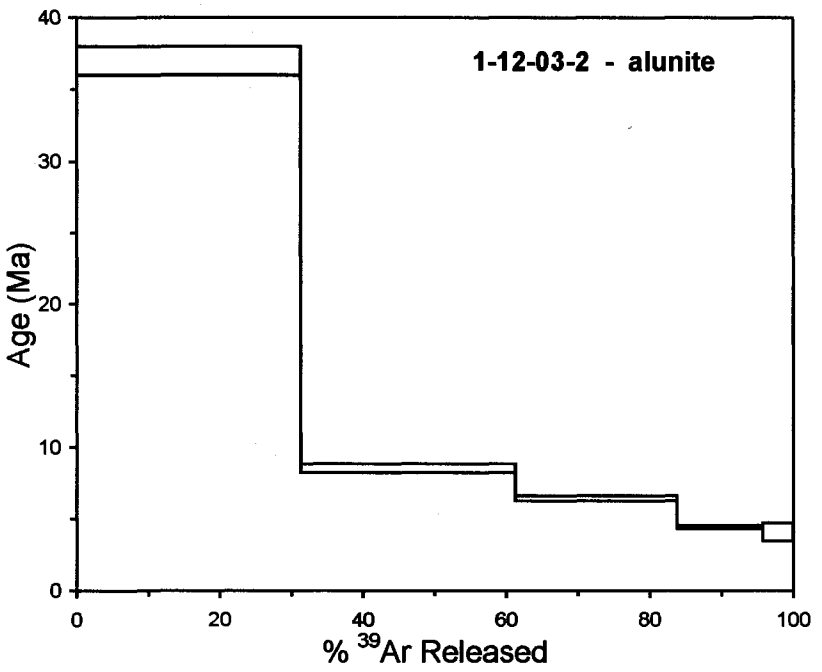
1-12-03-2 - alunite
Age (Ma)
% 39Ar Released
0
10
20
30
40
0
20
40
60
80
100

Thompson-CREG, 1-15-03-4, alunite, 1.57 mg, J = 0.001620 ± 0.5%
4 amu discrimination = 1.02211 ±0.29%, 40/39K = 0.0002 ± 0.0003, 36/37Ca = 0.00027 ± 2.46%, 39/37Ca = 0.00063 ± 0.98%

step	T (C)	t (min.)	36Ar	37Ar	38Ar	39Ar	40Ar	%40Ar*	% 39Ar rlsd	Ca/K	40Ar*/39ArK	Age (Ma)	1s.d.	anal err	37/39c	%39ArK	total39	mol 39Ar	Wmdata	WMs	wfactor	WxX	37d
1	480	12	14.397	1.544	3.366	35.628	4977.54	16.4	18.5	0.15902372	22.9841	65.95	1.23	1.18081796	0.0691	99.99522	192.55	2.14E-15	65.95	1.180818	0.71719	47.30082	1.61
2	485	12	5.660	1.342	1.620	40.284	2100.61	22.1	20.9	0.1222422	11.5747	33.52	0.50	0.46577207	0.0531	99.99632		2.42E-15	33.52	0.465772	4.60949	154.4871	
3	490	12	2.890	1.072	1.018	36.544	1194.1	30.1	19.0	0.10764108	9.8537	28.57	0.32	0.28634324	0.0468	99.99676		2.19E-15	28.57	0.286343	12.1962	348.4589	
4	495	12	1.130	0.801	0.621	31.527	575.279	43.4	16.4	0.09322821	7.9156	22.99	0.23	0.19342943	0.0405	99.9972		1.89E-15	22.99	0.193429	26.7273	614.3602	
5	500	12	0.359	0.579	0.352	23.968	255.139	60.0	12.4	0.08864283	6.3335	18.42	0.15	0.1196757	0.0385	99.99733		1.44E-15	18.42	0.119678	69.8213	1285.829	
6	505	12	0.119	0.374	0.214	15.567	118.525	72.7	8.1	0.08815835	5.4085	15.74	0.12	0.09190497	0.0383	99.99735		9.34E-16	15.74	0.091905	118.392	1863.607	
7	510	12	0.057	0.182	0.102	7.093	49.338	70.0	3.7	0.09415405	4.6041	13.41	0.23	0.22210578	0.0409	99.99717		4.26E-16	13.41	0.222106	20.2712	271.7562	
8	515	12	0.037	0.096	0.040	1.942	18.520	48.8	1.0	0.18139737	3.8524	11.22	0.49	0.48274895	0.0789	99.99454		1.17E-16	11.22	0.482749	4.29099	48.16205	
							Cumulative %39Ar rlsd =		100.0		Total gas age =	32.57	0.15							WtdMean	1sd	wJ	
note: isotope beams in mV, rlsd = released, error in age includes 0.5% J error, all errors 1 sigma											no plateau									18.02926	0.06238	0.153912	
(Not corrected for decay)											no isochron												

step	39/40c	39/40err	36/40c	36/40err	R2	36c	39c	40c	%36err	%39err	%40err	blank corr beam errors 36err	40err	%36err	%40err	WtdAge39Ar
1	0.00712	0.3082	0.00283	0.2977	0.1285	14.39	35.62643	4974.25	0.06	0.10	0.03	0.0087	1.4933	0.060271	0.030021	12.20344578
2	0.0191	0.2950	0.002835	0.3149	0.0611	5.85	40.28284	2097.32	0.12	0.05	0.02	0.0068	0.4202	0.120958	0.020037	7.011780109
3	0.03052	0.3063	0.002366	0.2967	0.2872	2.88	38.54291	1190.81	0.04	0.09	0.04	0.0014	0.4777	0.047873	0.04012	5.422480519
4	0.05481	0.3437	0.001915	0.4337	0.0276	1.12	31.52619	571.99	0.31	0.18	0.04	0.0038	0.2303	0.318975	0.040269	3.763755643
5	0.09484	0.3143	0.001355	0.5736	0.0478	0.35	23.98741	251.85	0.43	0.11	0.05	0.0017	0.1280	0.492243	0.050813	2.292363999
6	0.13433	0.2903	0.000924	0.8407	0.0284	0.11	15.56662	115.24	0.35	0.00	0.01	0.0009	0.0156	0.789035	0.013562	1.272805282
7	0.15318	0.2953	0.000997	3.5745	0.0007	0.05	7.092815	46.06	2.62	0.05	0.01	0.0017	0.0113	3.562803	0.024578	0.493839304
8	0.12872	0.6430	0.001731	3.2639	0.0000	0.03	1.941902	15.24	1.22	0.57	0.003	0.0009	0.0102	3.250295	0.066951	0.113201807

	Age (Ma) ± 2 sig err	
1	63.59	68.31
2	32.58	34.45
3	28.00	29.14
4	22.60	23.37
5	18.18	18.66
6	15.56	15.92
7	12.96	13.85
8	10.26	12.19

Sample run times

Start t	Step	T (C)	Step t	Inlet t	
11:40	1	480	0:12	12:00	
12:09	2	485	0:12	12:29	5
12:38	3	490	0:12	12:58	5
13:07	4	495	0:12	13:27	5
13:36	5	500	0:12	13:56	5
14:05	6	505	0:12	14:25	5
14:34	7	510	0:12	14:54	5
15:03	8	515	0:12	15:23	5
15:32	9	520	0:12	15:52	5
16:01	10	530	0:12	16:21	10
16:30	11	550	0:12	16:50	20
16:59					

Adjust ^{40}Ar & ^{36}Ar blanks for longer step times

step time =	45	New 40Ar and 36Ar blanks	
original blank time =	20	40Ar (mV)/min =	35.44
40Ar rate of rise (mV) =	0.95	36Ar (mV)/min =	0.12
36Ar rate of rise (mV) =	0.003		
40Ar blank =	11.69		
36Ar blank =	0.04		

Estimate of the $\%K_2O$ in sample

% K_2O	J factor	weight (mg)	exp. total mV $^{39}Ar_K$
0.25	3.736E-01	18.64	43146.95

	enter data				cumulative	option	calc plateau age				spectrum plot			
step	Age	1s.d.	anal. Err.	%39Ar	^{39}Ar	frac.39Ar	step	$\%^{39}Ar$	Age	anal. Err.	step	$\%^{39}Ar$	Age	1s.d.
1	65.95	1.23	1.180818	18.503	18.5	0.19	1	18.5	65.95	1.180818	1	18.503	65.95	1.23
2	33.52	0.50	0.4657721	20.921	39.4	0.39	2	39.42	33.52	0.4657721	2	39.425	33.52	0.50
3	28.57	0.32	0.2863432	18.979	58.4	0.58	3	58.4	28.57	0.2863432	3	58.404	28.57	0.32
4	22.99	0.23	0.1934294	16.373	74.8	0.75	4	74.78	22.99	0.1934294	4	74.777	22.99	0.23
5	18.42	0.15	0.1196757	12.448	87.2	0.87	5	87.22	18.42	0.1196757	5	87.225	18.42	0.15
6	15.74	0.12	0.091905	8.0847	95.3	0.95	6	95.31	15.74	0.091905	6	95.309	15.74	0.12
7	13.41	0.23	0.2221058	3.6837	99.0	0.99	7	98.99	13.41	0.2221058	7	98.993	13.41	0.23
8	11.22	0.49	0.4827489	1.0086	100.0	1.00	8	100	11.22	0.4827489	8	100	11.22	0.49

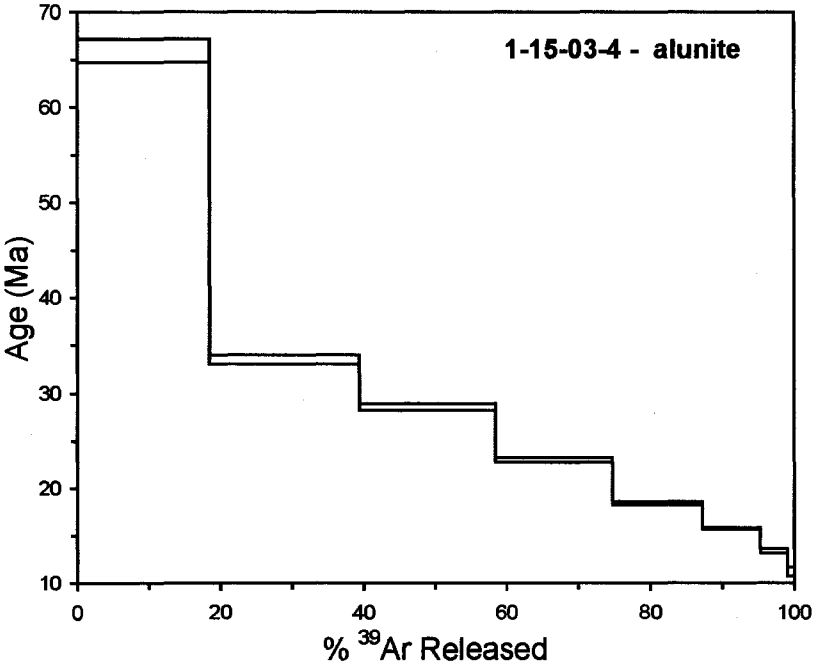
1-15-03-4 - alunite
Age (Ma)
70
60
50
40
30
20
10
0
20
40
60
80
100
% 39Ar Released

Thompson-CREG, 1-16-03-1, alunite, 1.57 mg, J = 0.001627 ± 0.5%
4 amu discrimination = 1.02211 ± 0.29%, 40/39K = 0.0002 ± 0.0003, 36/37Ca = 0.00027 ± 2.46%, 39/37Ca = 0.00063 ± 0.98%

step	T (C)	t (min.)	36Ar	37Ar	38Ar	39Ar	40Ar	%40Ar*	% 39Ar rlsd	Ca/K	40Ar*/39ArK	Age (Ma)	1s.d.	anal err	37/39c	%39ArK	total39	mol 39Ar	Wmdata	WMs	wfactor	WxX	37d
1	480	12	14.398	0.349	3.353	36.004	5004.710	16.8	18.1	0.03459816	23.4894	67.66	1.26	1.21165603	0.0150	99.99886	198.48	2.16E-15	67.66	1.211656	0.68115	46.08782	1.57
2	485	12	2.368	0.296	1.052	49.219	1105.070	38.1	24.8	0.02146523	8.5782	25.01	0.24	0.20016181	0.0093	99.99935		2.95E-15	25.01	0.200162	24.9596	624.1147	
3	490	12	1.193	0.228	0.761	42.139	671.971	48.9	21.2	0.01931199	7.7921	22.73	0.21	0.17181953	0.0084	99.99942		2.53E-15	22.73	0.17182	33.8731	769.8678	
4	495	12	0.815	0.147	0.564	32.447	480.065	51.2	16.3	0.01617033	7.5603	22.06	0.18	0.1384461	0.0070	99.99951		1.95E-15	22.06	0.138446	52.1721	1150.709	
5	500	12	0.646	0.093	0.416	21.125	346.774	48.5	10.6	0.01571311	7.5945	22.16	0.22	0.19123258	0.0068	99.99953		1.27E-15	22.16	0.191233	27.3449	605.8261	
6	510	12	0.627	0.068	0.262	10.818	272.049	33.6	5.5	0.02243565	8.3976	24.48	0.35	0.33109635	0.0098	99.99933		6.49E-16	24.48	0.331096	9.12202	223.3254	
7	530	12	0.72	0.053	0.200	3.388	263.597	21.1	1.7	0.05583591	16.3277	47.30	0.76	0.72121339	0.0243	99.99832		2.03E-16	47.30	0.721213	1.92253	90.93553	
8	600	12	1.277	0.087	0.334	3.336	470.070	21.5	1.7	0.0930849	30.2704	86.73	1.29	1.2191698	0.0405	99.9872		2E-16	86.73	1.21917	0.67278	58.35138	
							Cumulative	%39Ar rlsd =	100.0		Total gas age =	32.86	0.20							WtdMean	1sd	wJ	
											no plateau									23.67668	0.08145	0.201368	
											Isochron age = (steps 1-3)	19.25	0.13									

note: isotope beams in mV, rlsd = released, error in age includes 0.5% J error, all errors 1 sigma
(Not corrected for decay)

step	39/40c	39/40err	36/40c	36/40err	R2	36c	39c	40c	%36err	%39err	%40err	blank corr beam errors 36err	40err	%36err	%40err	WtdAge39Ar
1	0.00716	0.2970	0.002615	0.3094	0.2320	14.39	36.00366	5001.42	0.10	0.05	0.04	0.0144	2.0019	0.100207	0.040027	12.27379407
2	0.04443	0.2943	0.002094	0.2994	0.2683	2.36	49.21871	1101.78	0.06	0.04	0.03	0.0016	0.3317	0.068158	0.030104	6.200731031
3	0.06267	0.3116	0.001731	0.4778	0.0213	1.18	42.13877	668.68	0.37	0.11	0.03	0.0045	0.2018	0.37852	0.030186	4.825348609
4	0.06766	0.3074	0.001652	0.3113	0.0620	0.80	32.44685	476.78	0.06	0.10	0.02	0.0009	0.0966	0.111334	0.020251	3.605658162
5	0.06116	0.3197	0.001811	0.5408	0.0618	0.84	21.12491	343.49	0.43	0.12	0.06	0.0029	0.2083	0.45247	0.060648	2.358043002
6	0.04003	0.3375	0.002246	0.5812	0.0108	0.62	10.81793	268.77	0.48	0.17	0.03	0.0031	0.0822	0.50276	0.030602	1.334372612
7	0.01294	0.3298	0.002668	0.3225	0.3395	0.71	3.387948	260.32	0.06	0.14	0.07	0.0009	0.1848	0.12203	0.07099	0.807398227
8	0.00711	0.3593	0.002655	0.3058	0.0557	1.27	3.335914	466.79	0.07	0.21	0.03	0.0012	0.1414	0.09215	0.03029	1.457768803

	Age (Ma) ± 2 sig err	
1	65.24	70.09
2	24.60	25.41
3	22.38	23.07
4	21.78	22.33
5	21.77	22.54
6	23.82	25.14
7	45.86	48.74
8	84.29	89.17

Sample run times

Start t	Step	T (C)	Step t	Inlet t	
8:14	1	480	0:12	8:34	
8:43	2	485	0:12	9:03	5
9:12	3	490	0:12	9:32	5
9:41	4	495	0:12	10:01	5
10:10	5	500	0:12	10:30	5
10:39	6	510	0:12	10:59	10
11:08	7	530	0:12	11:28	20
11:37	8	600	0:12	11:57	70
12:06					

Adjust ^{40}Ar & ^{36}Ar blanks for longer step times

step time =	45	New 40Ar and 36Ar blanks	
original blank time =	20	40Ar (mV)/min =	35.44
40Ar rate of rise (mV) =	0.95	36Ar (mV)/min =	0.12
36Ar rate of rise (mV) =	0.003		
40Ar blank =	11.69		
36Ar blank =	0.04		

Estimate of the $\%K_2O$ in sample

% K_2O	J factor	weight (mg)	exp. total mV $^{39}Ar_K$
0.25	3.736E-01	18.64	43146.95

step	Age	1s.d.	anal. Err.	%39Ar	cumulative ^{39}Ar	option frac.39Ar
	enter data					
1	67.66	1.26	1.211656	18.14	18.1	0.18
2	25.01	0.24	0.2001618	24.798	42.9	0.43
3	22.73	0.21	0.1718195	21.231	64.2	0.64
4	22.06	0.18	0.1384461	16.348	80.5	0.81
5	22.16	0.22	0.1912326	10.643	91.2	0.91
6	24.48	0.35	0.3310963	5.4504	96.6	0.97
7	47.30	0.76	0.7212134	1.707	98.3	0.98
8	86.73	1.29	1.2191698	1.6808	100.0	1.00

step	calc plateau age $\%^{39}Ar$	Age	anal. Err.
1	18.14	67.66	1.211656
2	42.94	25.01	0.2001618
3	64.17	22.73	0.1718195
4	80.52	22.06	0.1384461
5	91.16	22.16	0.1912326
6	96.61	24.48	0.3310963
7	98.32	47.30	0.7212134
8	100	86.73	1.2191698

step	spectrum plot $\%^{39}Ar$	Age	1s.d.
1	18.14	67.66	1.26
2	42.938	25.01	0.24
3	64.169	22.73	0.21
4	80.516	22.06	0.18
5	91.16	22.16	0.22
6	96.61	24.48	0.35
7	98.317	47.30	0.76
8	99.998	86.73	1.29

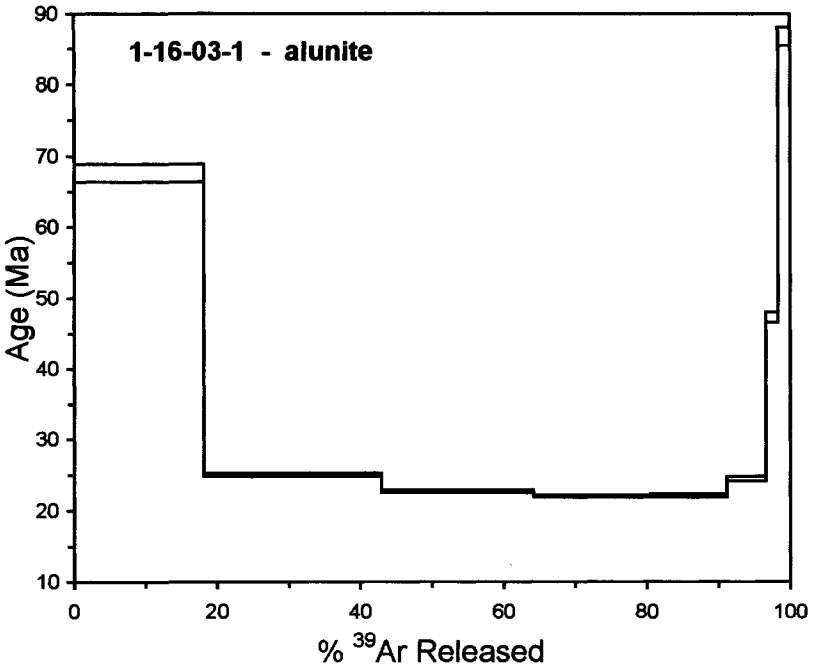
1-16-03-1 - alunite
Age (Ma)
% 39Ar Released
90
80
70
60
50
40
30
20
10
0
20
40
60
80
100

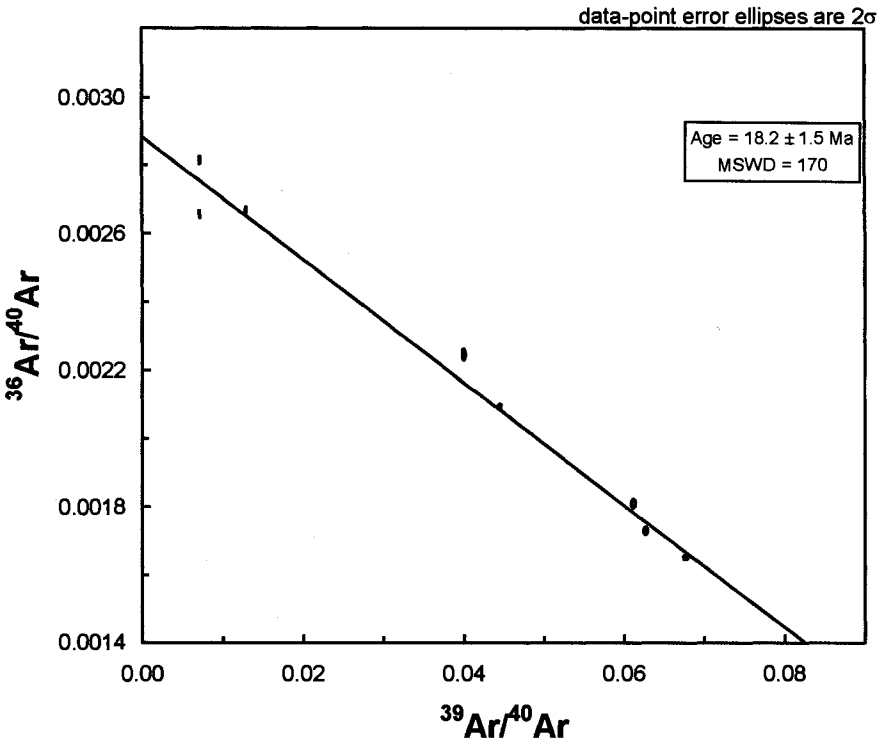
data-point error ellipses are 2σ
Age = 18.2 ± 1.5 Ma
MSWD = 170
0.0030
0.0026
0.0022
0.0018
0.0014
0.00
0.02
0.04
0.06
0.08
36Ar/40Ar
39Ar/40Ar

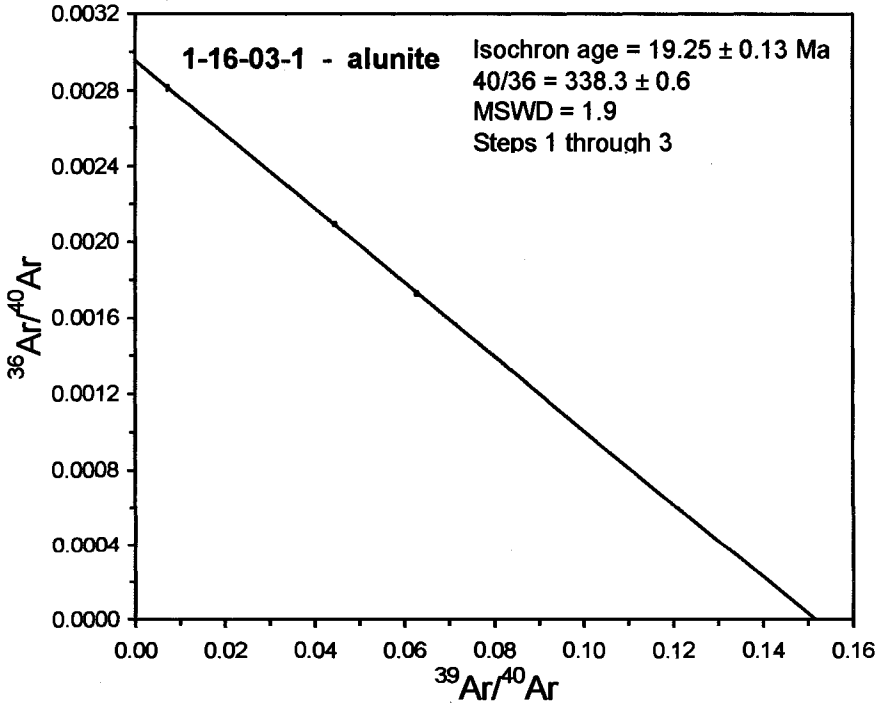
1-16-03-1 - alunite
Isochron age = 19.25 ± 0.13 Ma
40/36 = 338.3 ± 0.6
MSWD = 1.9
Steps 1 through 3
0.0032
0.0028
0.0024
0.0020
0.0016
0.0012
0.0008
0.0004
0.0000
0.00
0.02
0.04
0.06
0.08
0.10
0.12
0.14
0.16
36Ar/40Ar
39Ar/40Ar

Thompson-CREG, 3-20-03-1, alunite, 1.64 mg, J = 0.0016135 ± 0.5%
4 amu discrimination = 1.02211 ± 0.29%, 40/39K = 0.0002 ± 0.0003, 36/37Ca = 0.00027 ± 2.46%, 39/37Ca = 0.00063 ± 0.98%

step	T (C)	t (min.)	36Ar	37Ar	38Ar	39Ar	40Ar	%40Ar*	% 39Ar rlsd	Ca/K	40Ar*/39ArK	Age (Ma)	1s.d.	anal err	37/39c	%39ArK	total39	mol 39Ar	Wmdata	Wtls	wfactor	WtX	37d
1	490	12	4.312	0.111	1.673	61.017	1642.790	24.1	19.0	0.00864821	6.5156	18.87	0.26	0.24013519	0.0029	99.9998	320.47	3.66E-15	18.87	0.240135	17.3416	327.1834	1.61
2	500	12	0.398	0.137	1.033	75.380	427.708	73.6	23.5	0.00864197	4.1625	12.08	0.08	0.05694959	0.0029	99.9998		4.52E-15	12.08	0.05695	308.332	3723.419	
3	510	12	0.143	0.133	1.095	81.209	410.951	90.6	25.3	0.00598522	4.5686	13.25	0.09	0.05483555	0.0026	99.99982		4.87E-15	13.25	0.054836	332.564	4408.477	
4	520	12	0.048	0.111	0.866	67.319	341.632	96.8	21.0	0.00802584	4.8668	14.17	0.09	0.058694	0.0028	99.99982		4.04E-15	14.17	0.058694	290.277	4112.934	
5	525	12	0.018	0.055	0.345	27.618	144.355	98.4	8.6	0.00727785	5.0488	14.64	0.11	0.07529247	0.0032	99.99978		1.66E-15	14.64	0.075292	176.399	2581.957	
6	530	12	0.02	0.029	0.081	6.108	34.436	90.7	1.9	0.01735133	4.6500	13.49	0.22	0.20625923	0.0075	99.99948		3.66E-16	13.49	0.206259	23.5057	316.9744	
7	535	12	0.011	0.025	0.028	1.564	11.558	98.5	0.5	0.05841744	5.1330	14.88	0.54	0.53787883	0.0254	99.99824		9.38E-17	14.88	0.537879	3.45646	51.43207	
8	545	12	0.009	0.019	0.009	0.250	4.733	98.0	0.1	0.27776756	5.7235	16.58	4.01	4.00514173	0.1208	99.99164		1.5E-17	16.58	4.005142	0.06234	1.03384	
							Cumulative %39Ar rlsd =		100.0		Total gas age =	14.37	0.09							WtdMean	1sd	wJ	
note: isotope beams in mV, rlsd = released, error in age includes 0.5% J error, all errors 1 sigma											no plateau									13.47416	0.02946	0.089505	
(Not corrected for decay)											no isochron												

step	39/40c	39/40err	36/40c	36/40err	R2	36c	39c	40c	%36err	%39err	%40err	blank corr beam errors 36err	40err	%36err	%40err	WtdAge39Ar
1	0.03701	0.2989	0.002567	0.3073	0.4992	4.30	61.01689	1639.50	0.08	0.04	0.06	0.0035	0.9857	0.082065	0.060124	3.59224807
2	0.17683	0.3004	0.000894	0.3689	0.2863	0.39	75.37986	424.41	0.10	0.06	0.05	0.0008	0.2141	0.219091	0.050445	2.840480794
3	0.19811	0.3026	0.000319	0.8918	0.0499	0.13	81.20887	407.65	0.58	0.07	0.05	0.0011	0.2057	0.641833	0.050466	3.357628639
4	0.19787	0.2984	0.00011	4.9152	0.0000	0.04	67.31889	338.34	3.55	0.07	0.003	0.0019	0.0145	4.906622	0.004271	2.976387528
5	0.1947	0.3116	5.53E-05	19.3509	0.0119	0.01	27.61794	141.07	7.49	0.05	0.10	0.0015	0.1447	19.34842	0.102584	1.261411883
6	0.19497	0.2948	0.000314	13.0104	0.0005	0.01	6.107971	31.15	5.30	0.04	0.01	0.0013	0.0108	13.00713	0.034519	0.257017443
7	0.1879	0.4883	0.000117	78.1115	0.0888	0.00	1.563975	8.28	0.48	0.34	0.11	0.0008	0.0163	76.11071	0.196821	0.07261934
8	0.1711	0.8675	6.18E-05	1198.0484	0.0021	0.00	0.249981	1.45	8.92	0.33	0.08	0.0011	0.0109	1198.048	0.748055	0.012937248

step	Age (Ma)	± 2 sig err
1	18.39	19.35
2	11.96	12.19
3	13.14	13.36
4	14.05	14.29
5	14.49	14.79
6	13.07	13.90
7	13.80	15.98
8	8.57	24.59

Sample run times

Start t	Step	T (C)	Step t	Inlet t	
11:40	1	490	0:12	12:00	
12:09	2	500	0:12	12:29	10
12:38	3	510	0:12	12:58	10
13:07	4	520	0:12	13:27	10
13:36	5	525	0:12	13:56	5
14:05	6	530	0:12	14:25	5
14:34	7	535	0:12	14:54	5
15:03	8	545	0:12	15:23	10
15:32	9	555	0:12	15:52	10
16:01	10	570	0:12	16:21	15
16:30					

Adjust ^{40}Ar & ^{36}Ar blanks for longer step times

step time =	45	New 40Ar and 36Ar blanks	
original blank time =	20	40Ar (mV)/min =	35.44
40Ar rate of rise (mV) =	0.95	36Ar (mV)/min =	0.12
36Ar rate of rise (mV) =	0.003		
40Ar blank =	11.69		
36Ar blank =	0.04		

Estimate of the %K_2O in sample

% K_2O	J factor	weight (mg)	exp. total mV $^{39}Ar_K$
0.25	3.736E-01	18.64	43146.95

step	Age	1s.d.	anal. Err.	%39Ar	cumulative ^{39}Ar	option frac.39Ar
		enter data				
1	18.87	0.26	0.2401352	19.04	19.0	0.19
2	12.08	0.08	0.0569496	23.522	42.6	0.43
3	13.25	0.09	0.0548355	25.341	67.9	0.68
4	14.17	0.09	0.058694	21.006	88.9	0.89
5	14.64	0.11	0.0752925	8.618	97.5	0.98
6	13.49	0.22	0.2062592	1.906	99.4	0.99
7	14.88	0.54	0.5378788	0.488	99.9	1.00
8	16.58	4.01	4.0051417	0.078	100.0	1.00

step	%^{39}Ar	Age	anal. Err.
	calc plateau age		
1	19.04	18.87	0.2401352
2	42.56	12.08	0.0569496
3	67.9	13.25	0.0548355
4	88.91	14.17	0.058694
5	97.53	14.64	0.0752925
6	99.43	13.49	0.2062592
7	99.92	14.88	0.5378788
8	100	16.58	4.0051417

step	%^{39}Ar	Age	1s.d.
	spectrum plot		
1	19.04	18.87	0.26
2	42.562	12.08	0.08
3	67.902	13.25	0.09
4	88.908	14.17	0.09
5	97.526	14.64	0.11
6	99.432	13.49	0.22
7	99.92	14.88	0.54
8	99.998	16.58	4.01

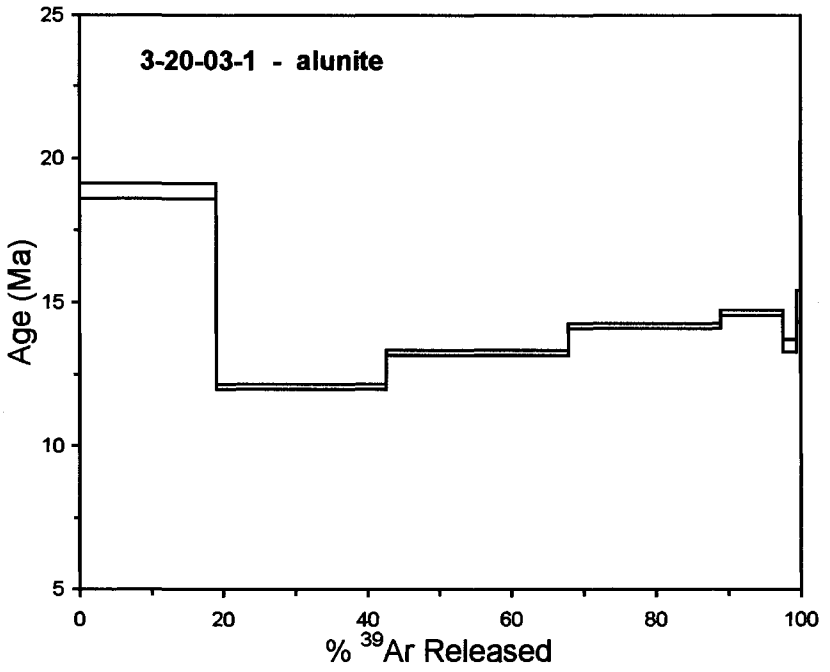
3-20-03-1 - alunite
Age (Ma)
25
20
15
10
5
0
20
40
60
80
100
% 39Ar Released

Thompson-CREG, 712-3A, alunite, 1.54 mg, J = 0.001680 ± 1.01%
4 amu discrimination = 1.01463 ± 0.28%, 40/39K = 0.0001 ± 100.0%, 36/37Ca = 0.000267 ± 3.83%, 39/37Ca = 0.0007 ± 0.63%

step	T (C)	t (min.)	36Ar	37Ar	38Ar	39Ar	40Ar	%40Ar*	% 39Ar rlsd	Ca/K	40Ar*/39ArK	Age (Ma)	1s.d.	anal err	37/39c	%39ArK	total39	mol 39Ar	Wmdata	WMs	wfactor	WxX	37d	start d	end d
1	1000	12	6.357	0.454	3.747	175.002	2832.74	34.7	100.0	0.03532179	5.622842	16.96	0.23	0.14586213	0.0154	99.99894	175.00	1.05E-14	16.96	0.145862	47.00185	797.2453	5.96	5.963	5.963
note: isotope beams in mV, rlsd = released, error in age includes J error, all errors 1 sigma											Total gas age =	16.96	0.34							WtdMean	1sd	wJ			
(36Ar through 40Ar are measured beam intensities, corrected for decay for the age calculations)																				16.962	0.145862	0.338308			

step	39/40c	39/40err	36/40c	36/40err	R2	T (C)	38c	39c	40c	%36err	%39err	%40err	blank corr beam errors 36err	40err	%36err	%40err	WtdAge39Ar
1	0.0617	0.2809	0.00221	0.3055	0.0371	1000	6.34	175.0001	2825.96	0.12	0.02	0.01	0.0077	0.2833	0.121776	0.010025	16.962

	39/40c	37/40c
	1.01463	1.01463
	0.01463	0.01463
	0.00366	0.00731
	1.00366	1.00732

	Age (Ma)	± 2 sig err
1	16.67	17.25

Sample run times

Start t	Step	T (C)	Step t	Inlet t	
8:27	1	600	0:12	8:47	
8:56	2	670	0:12	9:16	70
9:25	3	740	0:12	9:45	70
9:54	4	810	0:12	10:14	70
10:23	5	890	0:12	10:43	80
10:52	6	970	0:12	11:12	80
11:21	7	1060	0:12	11:41	90
11:50	8	1140	0:12	12:10	80
12:19	9	1400	0:12	12:39	260
12:48					

Adjust ^{40}Ar & ^{36}Ar blanks for longer step times

step time =	23	New 40Ar and 36Ar blanks	
original blank time =	12	40Ar (mV)/min =	8.53
40Ar rate of rise (mV) =	0.53	36Ar (mV)/min =	0.03
36Ar rate of rise (mV) =	0.002		
40Ar blank =	2.70		
36Ar blank =	0.01		

Estimate of the $\%K_2O$ in sample

% K_2O	J factor	weight (mg)	exp. total mV $^{39}Ar_K$
0.55	1.655E-03	23.71	534.9

Thompson-CREG, 712-3A, alunite, 1.54 mg, J = 0.001680 ± 1.01%

4 amu discrimination = 1.01463 ± 0.28%, 40/39K = 0.0001 ± 100.0%, 36/37Ca = 0.000267 ± 3.83%, 39/37Ca = 0.0007 ± 0.63%

step	T (C)	t (min.)	36Ar	37Ar	38Ar	39Ar	40Ar	%40Ar*	% 39Ar rlsd	Ca/K	40Ar*/39ArK	Age (Ma)	1s.d.
1	1400	12	6.357	0.454	3.747	175.002	2832.74	34.7	100.0	0.03667828	5.622842	16.96	0.23
note: isotope beams in mV, rlsd = released, error in age includes J error, all errors 1 sigma											Total gas age =	16.96	0.34
(36Ar through 40Ar are measured beam intensities, corrected for decay for the age calculations)													

Thompson-CREG, 712-3B, sunite, 1.17 mg, J = 0.001666 ± 0.99%
4 amu discrimination = 1.01483 ± 0.28%, 40/39K = 0.0001 ± 100.0%, 36/37Ca = 0.000267 ± 3.83%, 39/37Ca = 0.0007 ± 0.63%

step	T (C)	t (min.)	36Ar	37Ar	38Ar	39Ar	40Ar	%40Ar*	% 39Ar rlsd	Ca/K	40Ar*/39ArK	Age (Ma)	1s.d.	anal err	37/39c	%39ArK	total39	mol 39Ar	Wmdata	WMs	wfactor	WtX	37d	start d	end d
1	1000	12	0.348	0.117	0.223	11.058	165.975	40.0	100.0	0.14394247	5.732761	17.29	0.22	0.1317183	0.0626	99.99567	11.06	6.63E-16	17.29	0.131718	57.63795	996.6737	5.96	5.958	5.959
											Total gas age =	17.29	0.31							WtdMean	1sd	wJ			
																				17.292	0.131718	0.314174			

note: isotope beams in mV, rlsd = released, error in age includes J error, all errors 1 sigma
(36Ar through 40Ar are measured beam intensities, corrected for decay for the age calculations)

step	39/40c	39/40err	36/40c	36/40err	R2	T (C)	36c	39c	40c	%36err	%39err	%40err	blank corr beam errors 36err	40err	%36err	%40err	WtdAge39Ar	Age (Ma) ± 2 sig err	
1	0.08924	0.2800	0.002031	0.4512	#DIV/0!	1000	0.33	11.05751	159.11				0.0012	0.0019	0.353859	0.001213	17.292	1	17.03	17.56

39/40c	37/40c
1.01483	1.01483
0.01483	0.01483
0.00386	0.00731
1.00386	1.00732

Sample run times

Start t	Step	T (C)	Step t	Inlet t	
8:27	1	600	0:12	8:47	
8:56	2	670	0:12	9:16	70
9:25	3	740	0:12	9:45	70
9:54	4	810	0:12	10:14	70
10:23	5	890	0:12	10:43	80
10:52	6	970	0:12	11:12	80
11:21	7	1060	0:12	11:41	90
11:50	8	1140	0:12	12:10	80
12:19	9	1400	0:12	12:39	260
12:48					

Adjust ^{40}Ar & ^{38}Ar blanks for longer step times

step time =	23	New 40Ar and 36Ar blanks	
original blank time =	12	40Ar (mV)/min =	8.53
40Ar rate of rise (mV) =	0.53	36Ar (mV)/min =	0.03
36Ar rate of rise (mV) =	0.002		
40Ar blank =	2.70		
36Ar blank =	0.01		

Estimate of the $\%K_2O$ in sample

% K_2O	J factor	weight (mg)	exp. total mV $^{39}Ar_K$
0.55	1.655E-03	23.71	534.9

Thompson-CREG, 728-5A, alunite, 3.29 mg, J = 0.001662 ± 0.91%

4 amu discrimination = 1.01422 ± 0.18%, 40/39K = 0.0001 ± 100.0%, 36/37Ca = 0.000267 ± 3.83%, 39/37Ca = 0.00070 ± 0.63%

step	T (C)	t (min.)	36Ar	37Ar	38Ar	39Ar	40Ar	%40Ar*	% 39Ar rlsd	Ca/K	40Ar*/39ArK	Age (Ma)	1s.d.
1	470	12	8.010	0.487	2.068	40.807	2581.82	9.4	11.6	0.12849838	5.919450	17.66	0.54
2	480	12	1.054	0.418	0.819	42.118	581.287	47.1	11.9	0.1068585	6.462606	19.27	0.21
3	490	12	0.646	0.391	0.745	47.595	526.952	64.4	13.5	0.0884532	7.083517	21.12	0.22
4	500	12	0.548	0.435	0.930	62.965	629.055	74.8	17.8	0.07438517	7.435569	22.16	0.22
5	510	12	0.428	0.424	1.120	78.910	713.326	82.8	22.4	0.05785327	7.448737	22.20	0.22
6	520	12	0.158	0.296	0.828	60.100	492.242	91.2	17.0	0.05302867	7.406533	22.07	0.22
7	540	12	0.076	0.099	0.304	20.075	164.414	87.9	5.7	0.05309739	6.996801	20.86	0.22
8	600	12	0.101	0.024	0.023	0.307	33.408	6.3	0.1	0.84191726	5.850074	17.46	2.87
							Cumulative %39Ar rlsd =		100.0		Total gas age =	21.07	0.21
											Plateau age =	22.15	0.23
											(steps 4-6)		
											no isochron		

note: isotope beams in mV, rlsd = released, error in age includes J error, all errors 1 sigma
(36Ar through 40Ar are measured beam intensities, corrected for decay for the age calculations)

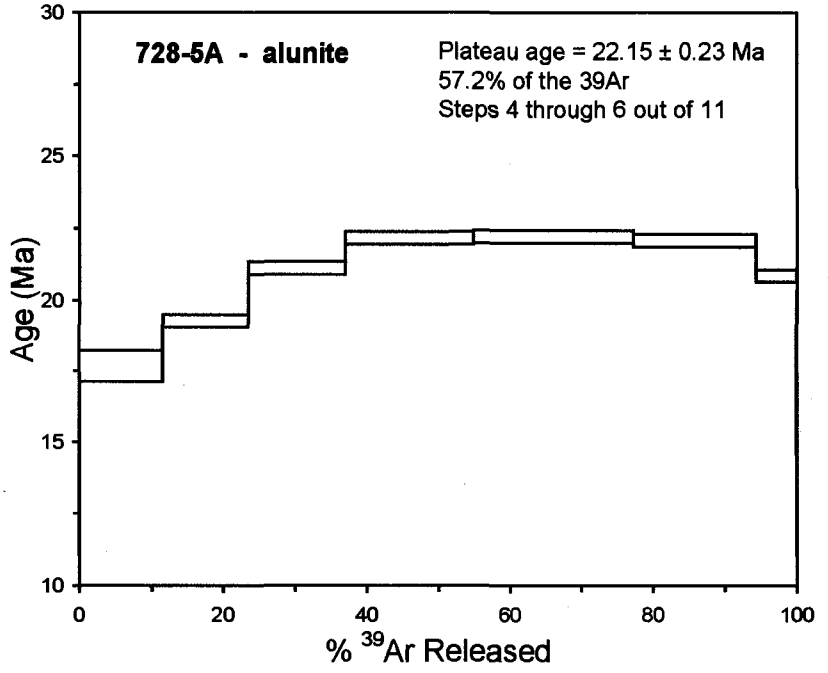
728-5A - alunite
Plateau age = 22.15 ± 0.23 Ma
57.2% of the 39Ar
Steps 4 through 6 out of 11
Age (Ma)
30
25
20
15
10
0
20
40
60
80
100
% 39Ar Released

Thompson-CREG, 728-5B, alunite, 3.48 mg, J = 0.001660 ± 0.87%

4 amu discrimination = 1.01463 ± 0.28%, 40/39K = 0.0001 ± 100.0%, 36/37Ca = 0.000267 ± 3.83%, 39/37Ca = 0.0007 ± 0.63%

step	T (C)	t (min.)	36Ar	37Ar	38Ar	39Ar	40Ar	%40Ar*	% 39Ar rlsd	Ca/K	40Ar*/39ArK	Age (Ma)	1s.d.
1	470	12	5.779	0.112	1.680	43.978	1973.13	14.7	8.6	0.03472409	6.609122	19.69	0.47
2	480	12	0.665	0.108	0.754	47.654	510.569	62.4	9.3	0.03090098	6.652671	19.81	0.23
3	490	12	0.355	0.098	0.838	61.409	535.328	81.1	12.0	0.02175909	7.041038	20.96	0.20
4	500	12	0.265	0.100	1.094	81.841	668.502	88.8	16.0	0.01666	7.236329	21.54	0.21
5	510	12	0.209	0.116	1.426	107.278	848.287	93.1	20.9	0.01474324	7.353939	21.89	0.21
6	520	12	0.149	0.087	1.411	106.263	832.980	95.1	20.7	0.01116304	7.444527	22.16	0.21
7	540	12	0.101	0.049	0.839	62.889	503.853	94.7	12.3	0.01062347	7.552372	22.48	0.21
8	600	12	0.106	0.02	0.024	0.828	47.810	36.3	0.2	0.37878328	19.562494	57.65	4.09
							Cumulative %39Ar rlsd =		100.0		Total gas age =	21.53	0.20
											no plateau		

note: isotope beams in mV, rlsd = released, error in age includes J error, all errors 1 sigma
(36Ar through 40Ar are measured beam intensities, corrected for decay for the age calculations)

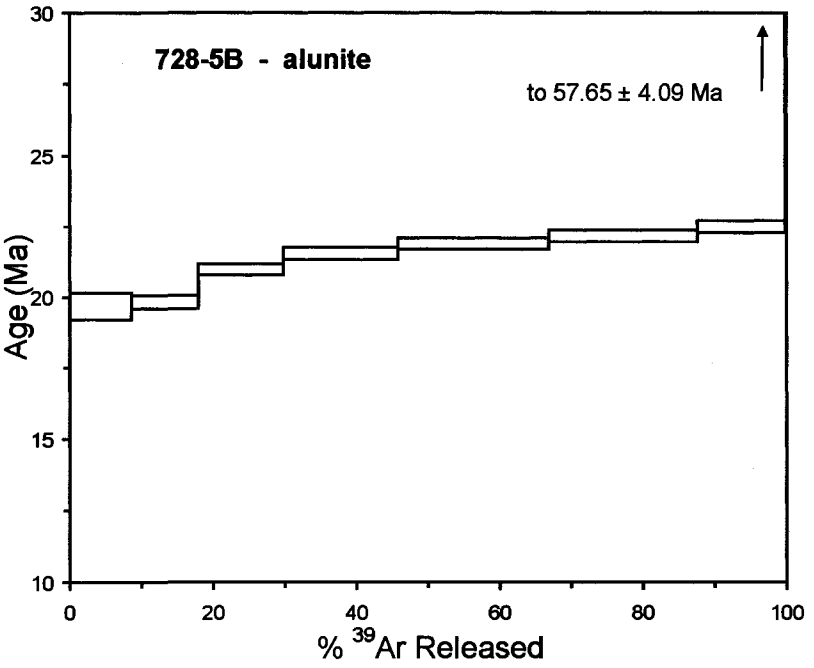
728-5B - alunite
to 57.65 ± 4.09 Ma
Age (Ma)
30
25
20
15
10
0
20
40
60
80
100
% 39Ar Released

Thompson-CREG, 728-6A, alunite, 1.64 mg, J = 0.001658 ± 0.83%

4 amu discrimination = 1.01159 ± 0.26%, 40/39K = 0.0001 ± 100.0%, 36/37Ca = 0.000267 ± 3.83%, 39/37Ca = 0.00070 ± 0.63%

step	T (C)	t (min.)	36Ar	37Ar	38Ar	39Ar	40Ar	%40Ar*	% 39Ar rlsd	Ca/K	40Ar*/39ArK	Age (Ma)	1s.d.
1	470	12	1.747	0.125	0.623	24.148	647.384	21.6	10.8	0.0525812	5.736600	17.08	0.41
2	480	12	0.519	0.119	0.419	21.649	291.728	49.7	9.7	0.0558356	6.544431	19.47	0.24
3	490	12	0.380	0.101	0.413	27.570	307.632	65.9	12.4	0.0372121	7.195325	21.40	0.27
4	500	12	0.301	0.115	0.533	36.656	350.257	76.9	16.5	0.03186777	7.210549	21.44	0.21
5	510	12	0.191	0.153	0.653	46.032	395.168	87.9	20.7	0.0337622	7.421694	22.06	0.21
6	520	12	0.097	0.136	0.586	43.257	347.809	94.3	19.4	0.03193607	7.435570	22.11	0.22
7	530	12	0.420	0.066	0.294	21.313	168.835	29.3	9.6	0.03145562	2.218931	6.63	1.04
8	540	12	0.016	0.018	0.028	1.985	20.495	97.7	0.9	0.09211255	6.266703	18.65	0.53
							Cumulative %39Ar rlsd =		100.0		Total gas age =	19.58	0.21
											no plateau		
											no isochron		

note: isotope beams in mV, rlsd = released, error in age includes 0.83% J error, all errors 1 sigma
(36Ar through 40Ar are measured beam intensities, corrected for decay for the age calculations)

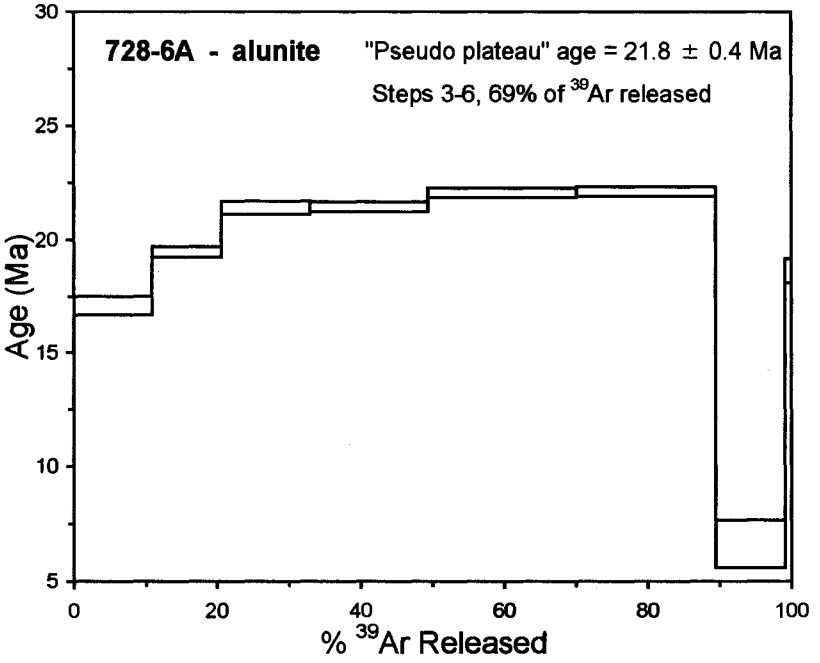
728-6A - alunite
"Pseudo plateau" age = 21.8 ± 0.4 Ma
Steps 3-6, 69% of ^{39}Ar released
Age (Ma)
30
25
20
15
10
5
0
20
40
60
80
100
% ^{39}Ar Released

Thompson-CREG, 728-6B, alunite, 0.80 mg, J = 0.001654 ± 0.81%

4 amu discrimination = 1.01159 ± 0.26%, 40/39K = 0.0001 ± 100.0%, 36/37Ca = 0.000267 ± 3.83%, 39/37Ca = 0.00070 ± 0.63%

step	T (C)	t (min.)	36Ar	37Ar	38Ar	39Ar	40Ar	%40Ar*	% 39Ar rlsd	Ca/K	40Ar*/39ArK	Age (Ma)	1s.d.
1	470	12	2.110	0.184	0.640	16.954	708.261	13.3	21.1	0.11174553	5.507612	16.36	0.41
2	480	12	0.500	0.150	0.311	14.282	239.733	40.8	17.8	0.10813998	6.649359	19.73	0.33
3	490	12	0.308	0.158	0.267	16.332	198.385	57.4	20.3	0.09960948	6.718142	19.94	0.21
4	500	12	0.160	0.158	0.262	16.865	164.957	75.9	21.0	0.09646134	7.087601	21.03	0.22
5	510	12	0.082	0.129	0.175	12.030	111.714	85.4	15.0	0.11041001	7.396898	21.94	0.23
6	520	12	0.034	0.056	0.068	3.913	40.417	96.4	4.9	0.14735584	8.062484	23.90	0.62
							Cumulative %39Ar rlsd =		100.0		Total gas age =	19.87	0.23

note: isotope beams in mV, rlsd = released, error in age includes 0.81% J error, all errors 1 sigma
(36Ar through 40Ar are measured beam intensities, corrected for decay for the age calculations)

no plateau
no isochron

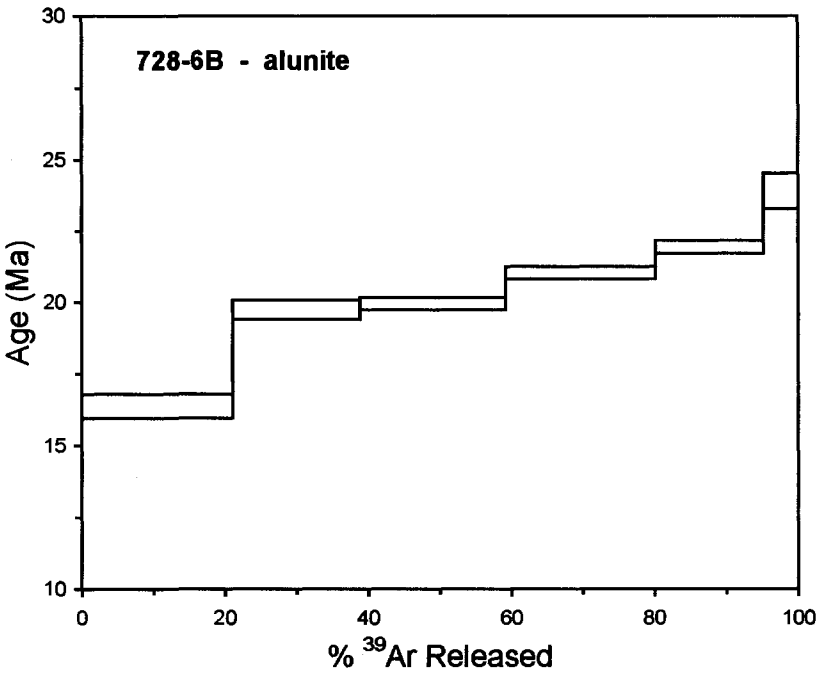
728-6B - alunite
Age (Ma)
30
25
20
15
10
0
20
40
60
80
100
% 39Ar Released

APPENDIX B

ALS Chemex
EXCELLENCE IN ANALYTICAL CHEMISTRY
ALS USA Inc.
994 Glendale Avenue, Unit 3
Sparks Nevada 89431-5730 USA
Phone: 775 356 5395 Fax: 775 356 0179

UNIVERSITY OF NEVADA RENO, CENTER FOR RESEARCH IN
MAIL STOP 169
RENO NV 89557-0232

Page # : 1
Date: 8-Oct-2003
Account: QXE

CERTIFICATE RE03038081

Project : Tyrone

P.O. No:

This report is for 20 - samples submitted to our lab in Sparks, Nevada, USA on 26-Sep-2003.

The following have access to data associated with this certificate:

CRAIG MACH

SAMPLE PREPARATION

ALS CODE	DESCRIPTION
WEI-21	Received Sample Weight
CRU-31	Fine crushing - 70% <2mm
LOG-22	Sample login - Rcd w/o BarCode
PUL-31	Pulverize split to 85% <75 um
SPL-21	Split sample - riffle splitter

ANALYTICAL PROCEDURES

ALS CODE	DESCRIPTION	INSTRUMENT
Cu-AA62	Ore grade Cu - four acid / AAS	AAS
Zn-AA62	Ore grade Zn - four acid / AAS	AAS
ME-MS61	47 element four acid ICP-MS	

To: UNIVERSITY OF NEVADA RENO, CENTER FOR RESEARCH IN
ATTN: CRAIG MACH
MAIL STOP 169
RENO NV 89557-0232

This is the Final Report and supersedes any preliminary report with this certificate number. Results apply to samples as submitted. All pages of this report have been checked and approved for release.

Signature:

ALS Chemex
EXCELLENCE IN ANALYTICAL CHEMISTRY
ALS USA Inc.
994 Glendale Avenue, Unit 3
Sparks Nevada 89431-5730 USA
Phone: 775 356 5395 Fax: 775 355 0179

UNIVERSITY OF NEVADA RENO, CENTER FOR RESEARCH IN
MAIL STOP 169
RENO NV 89557-0232

Page # : 2 - A
Total # of pages : 2 (A - D)
Date : 8-Oct-2003
Account: QXE

Project : Tyrone

CERTIFICATE OF ANALYSIS RE03038081

Sample Description	Method Analyte Units LOR	WEI-21 Recvd Wt kg 0.02	ME-MS61 Ag ppm 0.01	ME-MS61 Al % 0.01	ME-MS61 As ppm 0.2	ME-MS61 Ba ppm 10	ME-MS61 Be ppm 0.05	ME-MS61 Bi ppm 0.01	ME-MS61 Ca % 0.01	ME-MS61 Cd ppm 0.02	ME-MS61 Ce ppm 0.01	ME-MS61 Co ppm 0.1	ME-MS61 Cr ppm 1	ME-MS61 Cs ppm 0.05	ME-MS61 Cu ppm 0.2	ME-MS61 Fe % 0.01
5-31-03-3 Tips		0.17	0.22	8.08	12.8	310	3.02	0.31	0.42	0.30	136.5	6.0	10	5.92	186.5	2.69
6-7-03-1 Tips		0.57	0.13	6.79	8.4	680	2.04	0.18	0.58	0.22	64.2	10.8	61	15.85	22.5	3.39
6-7-03-2 Tips		0.39	0.39	7.72	5.7	740	1.84	0.27	0.24	0.15	32.2	5.6	6	3.85	30.3	11.00
6-9-03-3 QTgf		0.83	0.14	5.36	4.3	620	1.42	0.69	0.09	1.32	57.4	1.2	237	2.09	704	13.45
7-20-03-1 QTgf		0.50	0.22	5.69	24.7	580	1.32	0.64	0.11	3.94	30.0	1.1	4	1.66	1815	12.55
7-25-03-1 Emma		0.47	0.39	7.03	3.6	760	5.10	0.76	0.69	8.47	136.5	137.0	95	3.99	>10000	1.82
7-25-03-2 Emma		0.41	0.58	6.46	4.2	530	5.17	0.40	0.77	10.95	115.5	125.5	<1	4.11	>10000	2.60
7-25-03-3 Tyrone Pk		0.43	5.81	7.74	13.6	1440	2.17	0.75	0.22	101.5	34.2	10.4	60	1.12	6040	2.27
7-25-03-4 Tyrone Pk		0.39	5.63	7.92	14.5	990	2.01	0.76	0.32	64.1	36.4	53.0	5	0.93	3570	2.91
8-8-03-1 Tips		0.58	0.14	8.26	5.9	640	2.46	0.39	0.71	0.56	52.8	9.5	46	14.05	61.2	3.30
8-8-03-3 QTgf		1.42	1.56	5.88	4.4	450	1.30	0.88	0.16	1.11	31.1	1.4	15	3.47	237	16.60
8-8-03-4 Tips		0.92	0.14	8.39	1.8	530	1.79	0.20	0.22	0.26	130.0	5.2	34	8.99	222	2.29
8-8-03-5 Tips		0.95	0.15	8.42	9.3	460	2.73	0.23	0.24	0.39	81.5	3.7	9	7.10	467	3.34
8-8-03-8 QTgf		1.74	0.39	6.06	4.9	740	1.62	0.92	0.12	3.90	33.2	4.8	170	5.51	900	11.95
8-9-03-6 QTgf		2.04	0.26	5.86	109.0	760	6.64	0.83	0.19	8.31	30.9	20.5	7	2.35	2290	16.55
8-10-03-1 QTgf		1.06	0.33	6.19	8.4	530	2.85	0.27	0.22	2.29	37.2	5.1	32	1.79	1710	17.40
8-13-03-1 QTgf		1.10	0.36	5.01	7.3	620	0.92	0.42	0.16	0.96	46.0	1.3	12	1.32	267	13.05
8-15-03-1 QTgf		0.43	0.47	5.55	5.0	760	2.22	0.70	0.11	2.10	48.9	0.9	98	2.58	2120	11.40
8-15-03-2 QTgf		0.33	0.17	7.59	2.3	830	1.42	0.70	0.12	0.27	44.9	2.3	4	3.20	440	2.28
8-15-03-3 QTgf		0.70	1.14	7.24	4.5	820	1.92	1.82	0.19	1.36	159.0	1.5	70	5.71	558	2.99

Comments: Interference: Mo>400ppm on ICP-MS Cd,ICP-AES results shown. REE's may not be totally soluble in MS61 method.

ALS Chemex
EXCELLENCE IN ANALYTICAL CHEMISTRY
ALS USA Inc.
994 Glendale Avenue, Unit 3
Sparks Nevada 89431-5730 USA
Phone: 775 356 5395 Fax: 775 355 0179

UNIVERSITY OF NEVADA RENO, CENTER FOR
RESEARCH IN
MAIL STOP 169
RENO NV 89557-0232

Date : 8-Oct-2003
Account: QXE

Project : Tyrone

CERTIFICATE OF ANALYSIS RE03038081

Sample Description	Method / Analyte / Units / LOR	ME-MS61 Ga ppm 0.05	ME-MS61 Ge ppm 0.05	ME-MS61 Hf ppm 0.1	ME-MS61 In ppm 0.005	ME-MS61 K % 0.01	ME-MS61 La ppm 0.5	ME-MS61 Li ppm 0.2	ME-MS61 Mg % 0.01	ME-MS61 Mn ppm 5	ME-MS61 Mo ppm 0.05	ME-MS61 Na % 0.01	ME-MS61 Nb ppm 0.1	ME-MS61 Ni ppm 0.2	ME-MS61 P ppm 10	ME-MS61 Pb ppm 0.5
5-31-03-3 Tips		21.6	0.51	2.6	0.048	6.66	41.2	20.6	0.41	243	1.21	0.36	9.6	13.2	230	26.5
6-7-03-1 Tips		19.05	0.29	0.6	0.059	6.68	26.7	16.6	0.36	940	1.37	0.73	7.5	10.6	1300	17.2
6-7-03-2 Tips		20.3	0.31	0.6	0.063	2.78	19.0	10.5	0.30	278	4.23	0.06	2.9	2.6	1760	14.4
6-9-03-3 QTgf		17.85	0.38	1.0	1.395	3.42	31.2	7.5	0.14	158	184.5	0.11	5.0	3.2	1210	151.5
7-20-03-1 QTgf		16.40	0.51	0.9	0.844	2.48	20.4	8.1	0.23	217	718	0.08	2.8	3.1	1060	74.8
7-25-03-1 Emma		18.25	0.37	1.0	0.112	3.48	78.6	10.1	0.32	6760	85.0	1.80	14.4	25.7	410	25.4
7-25-03-2 Emma		15.40	0.33	1.3	0.105	3.02	48.6	9.0	0.57	9730	159.5	1.26	9.2	41.3	630	26.7
7-25-03-3 Tyrone Pk		27.0	0.23	0.5	0.791	3.15	22.3	20.6	0.30	>10000	10.85	0.27	2.6	37.0	970	935
7-25-03-4 Tyrone Pk		26.5	0.22	1.5	0.602	2.61	21.7	14.6	0.31	>10000	5.01	0.73	4.2	23.6	990	775
8-8-03-1 Tips		16.05	0.32	0.6	0.059	7.37	23.9	12.6	0.30	1110	1.38	0.60	6.2	10.2	700	17.6
8-8-03-3 QTgf		17.60	0.39	1.3	1.485	2.44	20.1	9.4	0.25	454	74.1	0.05	3.0	2.6	1550	182.0
8-8-03-4 Tips		17.30	0.53	0.5	0.041	6.87	58.7	14.4	0.23	307	4.83	0.62	7.0	8.8	710	29.3
8-8-03-5 Tips		17.55	0.43	0.7	0.063	7.22	37.3	12.5	0.21	380	6.84	0.64	9.3	6.9	670	32.6
8-8-03-5 QTgf		18.70	0.34	0.3	0.779	3.49	21.1	11.6	0.24	930	322	0.10	3.3	3.2	1140	59.9
8-8-03-6 QTgf		18.80	0.44	0.4	1.215	2.11	18.3	9.9	0.25	1940	149.5	0.05	3.0	10.1	1200	106.6
8-10-03-1 QTgf		20.9	0.40	0.2	2.38	1.64	25.0	8.5	0.26	745	78.0	0.04	3.3	5.8	1500	38.2
8-13-03-1 QTgf		19.95	0.32	0.2	2.14	1.86	26.9	5.3	0.23	245	31.3	0.04	2.9	2.0	1750	117.0
8-15-03-1 QTgf		16.10	0.38	0.6	0.643	2.83	23.1	7.7	0.16	324	226	0.09	2.6	2.4	1420	122.0
8-15-03-2 QTgf		20.5	0.25	1.3	0.397	3.50	24.2	10.6	0.21	304	31.7	0.46	4.3	3.7	500	135.5
8-15-03-3 QTgf		22.0	0.36	0.8	0.648	3.25	75.6	16.4	0.36	545	61.3	0.09	3.7	4.4	1260	284

Comments: Interference: Mo>400ppm on ICP-MS Cd,ICP-AES results shown. REE's may not be totally soluble in MS61 method.

ALS Chemex
EXCELLENCE IN ANALYTICAL CHEMISTRY
ALS USA Inc.
994 Glendale Avenue, Unit 3
Sparks Nevada 89431-5730 USA
Phone: 775 356 5395 Fax: 775 355 0179

UNIVERSITY OF NEVADA RENO, CENTER FOR RESEARCH IN
MAIL STOP 169
RENO NV 89557-0232

Page # : 2 - C
Total # of pages : 2 (A - D)
Date : 8-Oct-2003
Account: QXE

Project : Tyrone

CERTIFICATE OF ANALYSIS RE03038081

Sample Description	Method Analyte Units LOR	MS-MS61 Rb ppm 0.1	MS-MS61 Re ppm 0.002	MS-MS61 S % 0.01	MS-MS61 Sb ppm 0.05	MS-MS61 Se ppm 1	MS-MS61 Sn ppm 0.2	MS-MS61 Sr ppm 0.2	MS-MS61 Ta ppm 0.05	MS-MS61 Te ppm 0.05	MS-MS61 Th ppm 0.2	MS-MS61 Tl % 0.01	MS-MS61 Tl ppm 0.02	MS-MS61 U ppm 0.1	MS-MS61 V ppm 1	MS-MS61 W ppm 0.1
5-31-03-3 Tlpe		285	0.004	0.03	3.27	9	2.1	108.5	0.34	<0.05	12.8	0.24	0.84	6.4	30	1.2
6-7-03-1 Tlpe		239	0.003	0.01	0.91	1	1.5	108.0	0.15	0.12	11.8	0.35	2.24	2.0	73	1.6
6-7-03-2 Tlpe		130.5	0.004	0.14	0.62	4	1.3	1200	0.07	0.97	4.2	0.32	0.58	1.1	134	1.4
6-8-03-3 QTgf		154.0	0.003	0.74	0.67	2	3.7	447	0.31	0.51	10.3	0.14	1.03	3.3	46	2.9
7-20-03-1 QTgf		91.2	0.014	0.16	2.69	3	3.8	720	0.08	0.65	9.0	0.08	1.02	2.5	37	4.9
7-25-03-1 Emma		243	0.004	0.04	0.47	7	4.6	139.0	1.32	0.10	29.9	0.17	0.97	27.7	27	2.4
7-25-03-2 Emma		209	0.004	0.02	1.59	7	2.8	121.0	0.82	0.09	19.9	0.23	0.96	69.1	42	2.7
7-25-03-3 Tyrone Pk		137.0	0.002	0.19	0.89	3	1.0	491	0.07	2.35	4.9	0.20	1.79	3.2	38	0.4
7-25-03-4 Tyrone Pk		114.5	0.003	0.34	1.20	2	1.3	377	0.12	3.43	5.0	0.22	1.42	4.5	36	0.5
8-8-03-1 Tlpe		290	0.008	0.01	0.54	1	1.8	88.1	0.11	0.22	9.7	0.34	2.34	2.0	77	1.4
8-8-03-3 QTgf		100.5	0.003	0.88	0.60	<1	2.3	1225	0.11	1.40	5.0	0.16	0.99	1.5	76	1.5
8-8-03-4 Tlpe		302	0.003	0.04	0.57	1	1.7	552	0.12	<0.05	12.2	0.25	0.91	2.9	34	0.7
8-8-03-5 Tlpe		312	0.003	0.03	1.06	2	1.8	290	0.15	0.06	13.8	0.24	0.90	3.9	49	3.3
8-8-03-8 QTgf		155.5	0.004	0.16	0.55	1	3.1	846	0.10	0.77	6.9	0.11	1.57	5.0	46	12.3
8-9-03-6 QTgf		83.3	0.004	0.31	1.88	3	1.8	956	0.07	1.35	4.9	0.17	1.00	5.0	83	44.7
8-10-03-1 QTgf		50.5	0.003	0.18	0.26	1	0.8	834	0.07	1.74	6.5	0.16	0.58	6.9	70	0.8
8-13-03-1 QTgf		56.7	0.002	0.53	0.51	1	1.0	1570	0.08	1.08	4.5	0.16	0.65	2.1	47	0.8
8-15-03-1 QTgf		116.5	0.003	0.56	0.32	5	2.3	650	0.10	1.47	6.8	0.13	1.00	5.0	78	4.1
8-15-03-2 QTgf		158.5	0.002	0.06	1.16	1	3.5	462	0.14	0.87	8.1	0.14	1.27	2.1	27	3.0
8-15-03-3 QTgf		190.5	0.005	0.43	0.52	1	3.7	998	0.13	3.78	18.6	0.20	1.74	4.2	64	3.2

Comments: Interference: Mo>400ppm on ICP-MS Cd,ICP-AES results shown. REE's may not be totally soluble in MS61 method.

ALS Chemex
EXCELLENCE IN ANALYTICAL CHEMISTRY
ALS USA Inc.
994 Glendale Avenue, Unit 3
Sparks Nevada 89431-5730 USA
Phone: 775 356 5395 Fax: 775 356 0179

UNIVERSITY OF NEVADA RENO, CENTER FOR
RESEARCH IN
MAIL STOP 169
RENO NV 89557-0232

Date : 8-Oct-2003
Account: QXE

Project : Tyrone

CERTIFICATE OF ANALYSIS RE03038081

Sample Description	Method	ME-MS61	ME-MS61	ME-MS61	Zn-AAS2	Cu-AAS2
	Analyte	Y	Zn	Zr	Zn	Cu
	Units	ppm	ppm	ppm	%	%
	LOR	0.1	2	0.5	0.01	0.01
5-31-03-3 Tips		193.0	288	94.2		
6-7-03-1 Tips		21.5	54	31.9		
6-7-03-2 Tips		9.4	40	25.5		
6-9-03-3 QTgf		5.7	48	27.7		
7-20-03-1 QTgf		3.1	243	21.3		
7-25-03-1 Emma		128.0	865	17.4		2.97
7-25-03-2 Emma		115.0	1235	29.4		4.67
7-25-03-3 Tyrone Pk		20.5	>10000	24.0	1.01	
7-25-03-4 Tyrone Pk		13.9	5880	44.5		
8-8-03-1 Tips		16.5	86	26.1		
8-8-03-3 QTgf		3.6	88	44.0		
8-8-03-4 Tips		12.8	79	30.3		
8-8-03-5 Tips		17.0	113	31.1		
8-8-03-8 QTgf		5.6	118	16.3		
8-9-03-6 QTgf		20.5	1295	17.8		
8-10-03-1 QTgf		7.0	739	5.8		
8-13-03-1 QTgf		2.7	102	9.2		
8-15-03-1 QTgf		4.0	218	25.4		
8-15-03-2 QTgf		5.1	535	40.8		
8-15-03-3 QTgf		7.8	261	25.1		

Comments: Interference: Mo>400ppm on ICP-MS Cd,ICP-AES results shown. REE's may not be totally soluble in MS61 method.